S-wave and P-wave velocity model estimation from surface waves

Ph.D. in

Civil and Environmental Engineering

(XXXIII cycle)

S-wave and P-wave velocity model estimation from surface waves

Author:

Farbod Khosro Anjom

Advisors:

Prof. Laura Valentina Socco

Dr. Frank Adler

June 2021

Acknowledgment

I would like to thank TOTAL E&P for supporting my Ph.D. and providing the industrial data sets. I would like to thank Frank Adler for all the time and help he offered, as well as, for his comments that helped improving the thesis. I am also grateful to Jules Browaeys, Jean-Luc Boelle, Peigen Xie, and Isabella Masoni for their support and insight.

I would like to express my sincere gratitude to my Ph.D. advisor Prof. Valentina Socco for her invaluable guidance. Her knowledge and intuition of geophysics and science in general, motivated most breakthroughs of my work.

I am very grateful to my wife, Camellia, for her support every step of the way, and also to my family for motivating and supporting me, as always.

I would like to thank Prof. Cesare Comina for the countless times he humbly helped me to overcome challenging scientific issues. I want to express my gratitude to Prof. Alberto Godio for his constant review of my thesis evolution during the whole Ph.D. period and also for making the department a friendlier place for me.

Finally, I would also like to thank Myrto and Karim for their modest opinion and help in developing the thesis, and for their moral support during difficult times.

List of Symbols and Acronyms

VS	S-wave velocity
VP	P-wave velocity
VSZ	Time-average S-wave velocity
VPZ	Time-average P-wave velocity
DC	Dispersion curve of surface waves
W/D	Wavelength-depth
LCI	Laterally constrained inversion
SWT	Surface wave tomography
MCI	Monte Carlo inversion
FWI	Full-waveform inversion
λ	Wavelength
c	Phase velocity
f	Frequency
ω	Angular frequency
k	Wavenumber
σ	Standard deviation
S	Frequency-phase velocity spectrum

U	Phase component of the Fourier transform
V_z	Time-average velocity
h	Layer thickness
V_t	Interval velocity
ν_z	Apparent Poisson's ratio
ν	Poisson's ratio
Δt	Interval transit time
$t_{one-way}$	One-way arrival time
ε	Model difference
r	Residual misfit
r_{norm}	Normalized residual misfit
p	slowness
Q	Misfit function

Table of Contents

1. Introduction

1.1 Motivation

Seismic methods are the leading techniques in oil and gas exploration. Even though the deep subsurface is the target of these surveys, the reconstruction of the elastic properties of the near-surface is crucial for two main reasons: (1) surface waves (ground-roll) damping. (2) statics corrections. Surface waves are usually dominant in the seismic data, obscuring the reflection data (McMechan and Sun, 1991; Henley, 2003; Halliday et al., 2015), which raises the necessity to remove them from the raw data. Through the years, many acquisition designs and filtering methods have been developed to suppress the surface wave. The primary filtering methods, such as low-pass or band-pass filters, are often effective in removing surface waves but can also eliminate the reflection data's essential low-frequency elements common with surface waves (Saatcilar and Canitez,1988; Coruh and Costain, 1983). The $f-k$ and $\tau-p$ filtering techniques (Treitel et al., 1967; Yilmaz, 2001; March and Bailey, 1983; Embree et al., 1963; Kelamis and Mitchell, 1989) are the other popular surface wave elimination methods. However, they can significantly distort the reflection data when the surface wave is the dominant event or is scattered in the crossline direction (Liu, 1999; Halliday et al., 2010). The alternative surface wave suppression method are the model-based techniques, in which the near-surface structure is constructed to estimate and subtract the surface wave data from the records (Blonk and Herman, 1994; Blonk, 1995; Ernst, 1998; Ernst et al., 2002; Halliday et al., 2010).

The complex low-velocity shallow layers of the subsurface (weathered layers) create inconsistencies in the deep reflection data (Marsden, 1993; Cox, 1999). Static correction (statics) is an essential step of the seismic reflection surveys, in which the data are corrected for a specific datum depth below the weathered layers. The successful surface wave suppression and static corrections require knowledge of the near-surface S-wave and P-wave velocity (VS and VP) models.

The full-waveform inversions (FWIs) applied to near-surface data provide both VS and VP models (Brossier et al., 2009; Masoni et al., 2014; Perez Solano et al., 2014; Yuan et al., 2015). These methods have the advantage of considering the topography and provide good lateral resolution in obtaining the velocity models.

Despite many attempts to start FWI from crude initial models (Warner and Guasch, 2016; van Leeuwen and Herrmann, 2013), cycle-skipping in the near-surface environment, especially for high frequencies, is a challenging issue. As a result, FWI applied to near-surface environment needs a good initial guess of the media's properties to avoid cycle-skipping issues (Borisov et al., 2018). The traveltime tomography of the first breaks is common for near-surface VP estimation. However, the picking of the first arrivals could be time-consuming. Also, the low-velocity layers embedded in the shallow subsurface cannot be detected by the refraction tomography (Whiteley and Greenhalgh, 1979; Schmoller, 1982).

Surface waves travel along the free surface and decay exponentially in depth. As a result, they contain important information regarding the shallow subsurface and are good candidates for near-surface model reconstruction. In this thesis, we aim at answering the question whether both VS and VP models can be estimated from surface wave methods. We present four surface wave methods and show their applications to data sets recorded with various acquisition techniques from the sites with different geological properties. Two of these methods (laterally constrained inversion and surface wave tomography) are well-known in retrieving VS model and are modified to also estimate VP models.

The phase velocities of the surface wave propagation in layered media are characterized by geometrical dispersion. The so-called surface wave dispersion curves (DCs, phase velocity versus frequency) are estimated and inverted to estimate the velocity model. The DCs are considered to be very sensitive to VS (Nazarian, 1984; Xia et al., 1999; Foti et al., 2018). As a result, most surface wave methods focus on estimating the VS model only, and they require a priori VP or Poisson's ratio for the inversion step. Few researchers investigated the possibility of estimating VP from surface waves (Xia et al., 2003; Socco and Comina, 2017; Bergamo and Socco, 2016). Socco et al. (2017) discovered a strong correlation between DC and the time-average VS (VSZ). They showed that there exists a relationship between the wavelength of DCs and the investigation depth of surface waves (Wavelength-Depth relationship, W/D relationship). To construct the W/D relationship, a reference DC and the corresponding VSZ model is required. This relationship represents the wavelength and depth couples corresponding to equal surface wave phase velocity and VSZ, and can be used to transform the DC at different locations into VSZ. Socco and Comina (2017) proved that the W/D relationship is highly sensitive to Poisson's ratio. They developed a method to estimate time-average VP (VPZ), exploiting only the W/D relationship.

Based on Socco et al. (2017) and Socco and Comina (2017) studies, we develop a W/D workflow to estimate interval VS and VP, which is valid even in the presence of significant lateral variations. The proposed W/D method requires only the local DCs and demands no prior information. We also develop a joint inversion method in scheme of Monte Carlo that considers both surface wave DC and W/D relationship to estimate the VS and VP models. In this thesis, we use the W/D method to estimate the a priori Poisson's ratio required by well-established surface wave methods, laterally constrained inversion (LCI) and surface wave tomography (SWT), to enable the estimation of both VS and VP using these methods.

In the context of the LCI, the parameters of the 1D models are connected laterally and vertically through certain constraints level, which controls the variations between layers and adjacent model points. As a result, consistent and smooth estimated quasi 2D or 3D models are obtained from the LCI applications. The earliest applications of LCI were applied to resistivity data (Auken and Christiensen, 2004; Wisén et al., 2005; Auken et al., 2005). Later, Wisén and Christiensen (2005) applied LCI method to surface wave data.

The W/D and LCI methods require the local DCs as inputs, which are estimated through wavefield transform applied to an array of receiver records and are assigned to the receiver array center (known as the multi-channel method). Different receiver arrays are usually selected across the 2D seismic line, and the corresponding local DCs are estimated. Similarly, for classical 3D data where multiple parallel and perpendicular lines of receivers and sources are deployed, many local DCs along each line are estimated and used for the model estimations. A significant fraction of onshore oil and gas deposits are in remote areas with extreme environment and challenging topography such as foothills, forests, and deserts. The difficulty in transporting and deploying the acquisition equipment, as well as the natural hazards associated with these unmarked regions, make the seismic acquisition very challenging. The recent technological developments, such as the capability to deliver the receivers from the sky, have facilitated these acquisitions. However, the limited sky access and constraints for source locations usually result in full 3D acquisition layouts instead of classical 3D acquisition setting, where the receivers and sources are irregularly spaced and scattered across the investigated area. For such data sets, the DC estimation method from array receivers aligned with sources leads to erroneous and inconsistent DCs: Various receiver arrays aligned with sources with different azimuthal angles, as a result, with different propagation paths, can be used to estimate the DC of the same location. To mitigate this issue

for 3D data sets, we propose multi-channel analysis of the receiver records over an area instead of along an array.

SWT is a suitable alternative for model estimations from 3D data sets, which supports the irregular acquisition layout and results in high-resolution model estimation. SWT is a well-established method in earthquake seismology for VS reconstruction of the crust and upper mantel (Wespestad et al., 2019; Bao et al., 2015; Boiero, 2009; Yao et al., 2006; Shapiro et al., 2005). Recently, a few authors showed the SWT applications for the near-surface characterization, using active (Da Col et al., 2019; Socco et al., 2014) and passive data (Badal et al., 2013; Picozzi et al., 2009). Boiero (2009) developed a two-step SWT method, where, first, the path-averaged DCs are estimated and then inverted using a tomographic inversion algorithm to estimate the VS model. The path-averaged DCs are estimated using the records of receiver couples aligned with a source (also known as the two-station method).

Surface wave propagation is a multi-modal phenomenon. Although usually, the fundamental mode of the surface wave is solely excited or dominant in the whole bandwidth, under certain conditions of the site and the source, multiple modes of surface waves can be created. The higher modes travel with larger wavelengths. As a result, including them in the inversion increases the investigation depth (MacBeth and Burton, 1985; Yoshizawa and Kennet, 2004; Xia et al., 2003; Ganji et al., 1998; Khosro Anjom et al., 2021). Unlike the multi-channel method, the two-station method does not provide enough resolution to estimate various surface wave modes. We propose a two-station DC estimation method that includes the muting in *x-t* domain and enables the estimation of multiple modes of surface waves. The proposed method focuses on estimating a specific surface wave mode at each attempt, where a proper mute based on the preliminary multi-channel analysis of the data is used to damp the other modes. We modify the SWT inversion algorithm by Boiero (2009) to support the multi-modal DCs.

1.2 Thesis outline

A review of the surface wave's properties is provided in chapter 2. The surface wave dispersion, multi-modal propagation, and DC forward model are explained. Then, the steps involving the common surface wave methods are reviewed, focusing on the ones used in this thesis.

A total of 5 data sets are processed, which are described in chapter 3. The data sets are recorded in different environments with different acquisition techniques. The data are divided into vintage data sets, for which prior information about the characteristics of the site are available, and industry data sets. For each data set, the main properties are explained, and the key aspects necessary for the surface wave method application are discussed.

In chapter 4, we outline the workflow used for the direct transform method (W/D method) to estimate the interval VS and VP models. The method is applied to a vintage data set from a controlled test site and two industry data sets from stiff sites. When available, we compare the results with the previously estimated models from other studies. In chapter 4, we also describe the technique based on the W/D method to estimate Poisson's ratio required for the inversion methods in chapters 6 and 7.

In chapter 5, we explain the Monte Carlo joint inversion algorithm aimed at estimating high-resolution VS and VP models. We apply the method to two synthetic examples to evaluate the performance of the method in unsaturated and saturated environment. We also show the application of the method to a real example from one of the vintage data sets. We interpret the estimated VP based on the information from the previous seismic reflection survey, downhole test, and P-wave traveltime tomography studies.

In chapter 6, we briefly explain the laterally constrained inversion (LCI) developed by Boiero (2009) and describe the modifications made to the algorithm. We then show the method's application to an industry data set from a stiff site to estimate the VS and VP models.

In chapter 7, we describe the steps to estimate path-averaged multi-modal DCs and show the technique's performance on a synthetic example. Then, we describe the tomographic inversion method and the implemented modifications to the algorithm. We show the application of the multi-modal SWT to 3D data sets acquired by airdropped sensors in the foothills of Papua New Guinea (PNG). We also show the application of the tomographic inversion to the fundamental modes from two sites characterized by stiff material.

The W/D, LCI, and SWT methods are compared in chapter 8, using the estimated VS and VP models from one of the used data sets. We discuss the methods' pros and cons, considering the resolution, investigation depth, and computational costs.

In chapter 9, we provide the final remarks of the thesis and discuss the possible prospects.

2. Surface Waves

2.1 Introduction

In this chapter, the essential properties of surface waves for understanding this thesis are provided. We also briefly describe the forward model used for the synthetic DC simulation of all surface wave methods in this thesis. Finally, we review the common surface wave methods.

2.2 Features and Properties

2.2.1 Surface wave dispersion

The surface wave propagates horizontally and decays in depth. The surface waves with various frequencies (wavelength) penetrate different subsurface portions and create different particle displacement fields. The displacement field can be computed numerically and in homogenous isotropic half-space the vertical displacement becomes negligible roughly at depth equal to one wavelength. In Figure 2.1a, an example synthetic model is shown, and in Figure 2.1b, we show the relevant normalized vertical particle displacement for 20 Hz and 100 Hz surface wave fundamental modes, computed using Lai and Rix (2002) algorithm. It can be clearly observed that the 100 Hz (short wavelength) harmonic decays at shallower depth compared to the 20 Hz (large-wavelength) one.

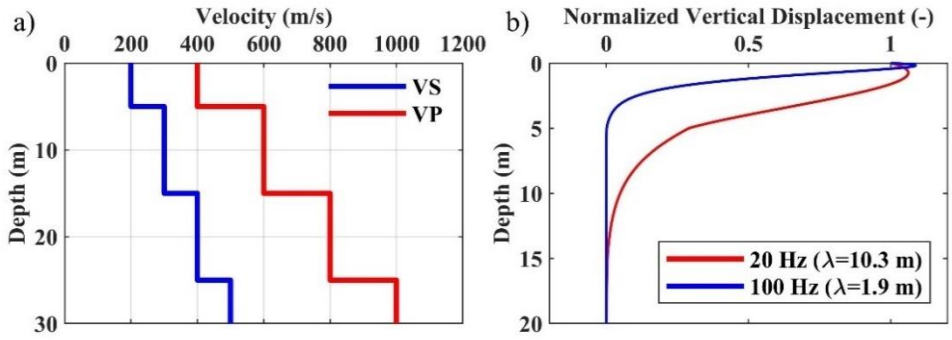

Figure 2.1: The normalized vertical displacement relevant to the propagation of the fundamental mode computed based on a synthetic example. (a) The VS and VP of the synthetic example. (b) The normalized vertical particle displacement at 20 and 100 Hz.

In a homogenous semi-infinite medium, the surface wave velocity is constant. However, in vertically varying models such as the example in Figure 2.1a, the phase velocity of the surface waves is dispersive. The geometrical dispersion of the surface waves is usually expressed with phase velocity as a function of frequency (dispersion curve, DC). Figure 2.2a shows the computed fundamental mode DC, corresponding to the example in Figure 2.1a. The DC can also be represented as a function of wavelength by computing wavelengths as:

$$\lambda = \frac{c}{f}, \tag{2.1}$$

where c and f are the phase velocity and frequency. In Figure 2.2b, we show the fundamental mode DC as a function of wavelength, corresponding to the example in Figure 2.1a.

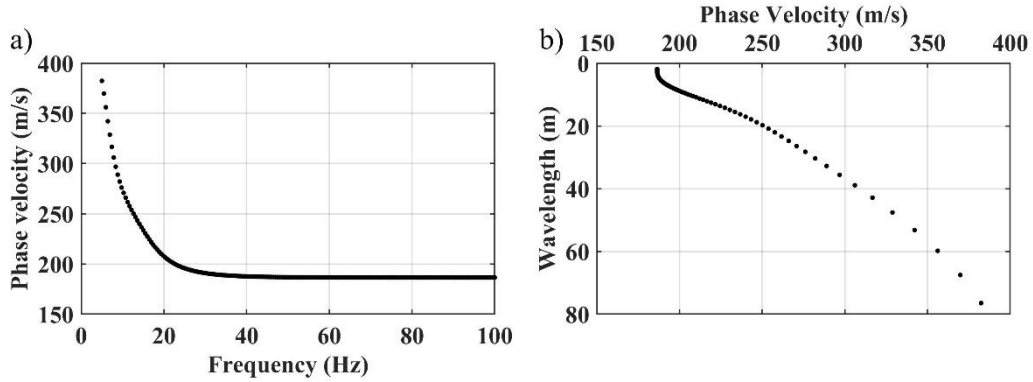

Figure 2.2: The computed DC corresponding to the synthetic model in Figure 2.1a, as a function of: (a) frequency. (b) wavelength.

The surface wave propagation and dispersion curve parameters are the VS, VP, density, and thicknesses. The DC exhibits strong sensitivity to VS while VP has a weaker effect and the density an even smaller influence on the DC (Foti and Strobbia 2002).

2.2.2 Multi-modal dispersion curves

The surface wave propagation in vertically heterogeneous media is a multi-modal phenomenon: Each frequency component can propagate at different phase velocities. The higher modes of surface waves are usually excited when VS of the media changes irregularly in depth, and low-velocity layers are embedded between

high-velocity layers (Parolai et al., 2005). The higher modes are faster than the fundamental mode, providing larger wavelengths and penetrating a deeper subsurface portion (MacBeth and Burton, 1985; Yoshizawa and Kennet, 2004; Xia et al., 2003; Ganji et al., 1998). Figure 2.3a shows the vertical displacement pattern of the fundamental and 1st higher modes at 20 Hz corresponding to the example in Figure 2.1a, where the 1st higher mode is affected by a deeper portion of the subsurface. In Figure 2.3b, we show the multi-modal DC of the synthetic example in Figure 2.1a, which includes the fundamental and first 9 higher modes.

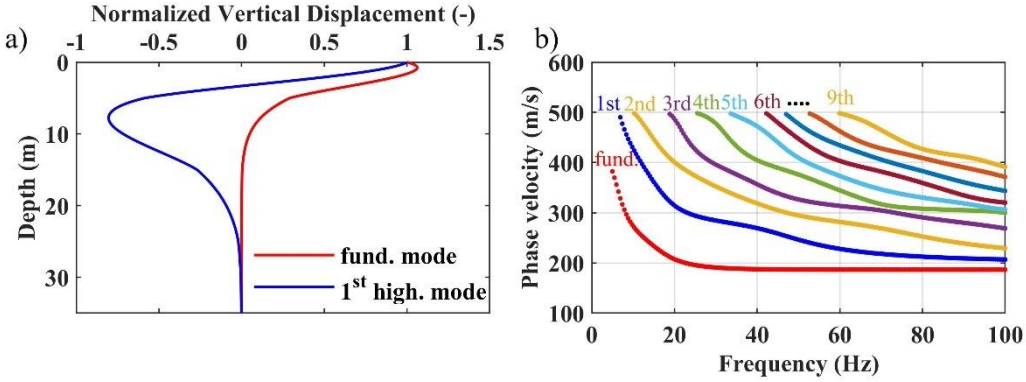

Figure 2.3: The multi-modal diplacement pattern and DC corresponding to the example in Figure 2.1a. (a) The comparison between the normalized vertical particle displacement of the fundamental and 1st higher modes at 20 Hz. (b) The simulated fundamental and first 9 higher mode DCs.

2.2.3 Forward Model

Thomson (1950) provided an algorithm to compute the synthetic DC of the multi-layered laterally invariant model, which was later modified by Haskell (1953). The method involves the computation of transfer matrices that describe the stress and displacement field at the bottom and top of the layers. The continuity of the stress and displacement fields at the interface of the layers are considered to eliminate the equations of the intermediate interfaces and achieve a single matrix (system matrix) that describes the fields within all layers based on the external boundary conditions. For the surface wave modes to exist, the determinant of the system matrix, also known as Haskell and Thomson matrix determinant, should be zero. The Haskell and Thomson determinant is a function of angular frequency and wavenumber and its roots give the modal solution of surface wave. Many numerical methods have been developed to find the roots and compute modal DCs.

The early forward algorithms for computing the synthetic DCs were unstable when the model contained large layers, and the high frequencies were considered (Lowe, 1995; Cercato, 2005). Dunkin (1965) slightly modified the method so that the equations do not become ill-conditioned for modal solutions at high frequencies. Herrmann developed the surface wave forward model in Fortran based on Dunkin's mathematical derivations (Herrmann, 2002). Maraschini (2008) translated and modified Hermmann's routine in MATLAB. We implemented modifications (e.g., pre-allocation of variables, vectorization of mathematical operations and etc) to Maraschini's algorithm aiming at optimizing the MATLAB routine to expedite the DC computation. The current algorithm is at least ten times faster than Maraschini's original algorithm, depending on the number of layers.

2.3 Common Surface Wave Methods

The conventional surface wave methods usually include data acquisition, a processing technique to estimate the DCs, and an inversion method to estimate the near-surface 1D VS velocities. In the following, we introduce certain aspects of these steps.

2.3.1 Data Acquisition

The seismic surface waves are excited in almost all types of seismic acquisitions, enabling the use of the surface wave methods regardless of the acquisition design. However, the lateral resolution and investigation depth of the estimated models from surface wave methods are significantly affected by the acquisition outline and equipment. The short spacing of receivers allows the estimation of dense, high-quality DCs, increasing the lateral resolution of the obtained 2D or 3D models.

In addition, the frequency band of the seismic source and the receiver type directly affect the frequency band of the records. As explained in section 2.2, the penetration depth of the surface waves is related to the wavelength (frequency) of the DCs. The broadband DCs, including both high and low frequencies, ensure both shallow and deep model estimation. Traditionally, in the oil and gas exploration context, 10 Hz geophones are used. In Figure 2.4, with a synthetic example, we highlight the impact of using geophones characterized by various natural frequencies. In Figure 2.4a and b, we show the VS and VP models and the corresponding DC. If we consider DC's low-cutoff frequency equal to the geophone's natural frequency (equal attenuation at all frequencies), using 10 Hz geophones, the red portion of the DC can be retrieved. Employing 4.5 and 2 Hz geophones in the acquisition allow

also the estimation of the low frequency DCs highlighted in green and blue in Figure 2.4b.

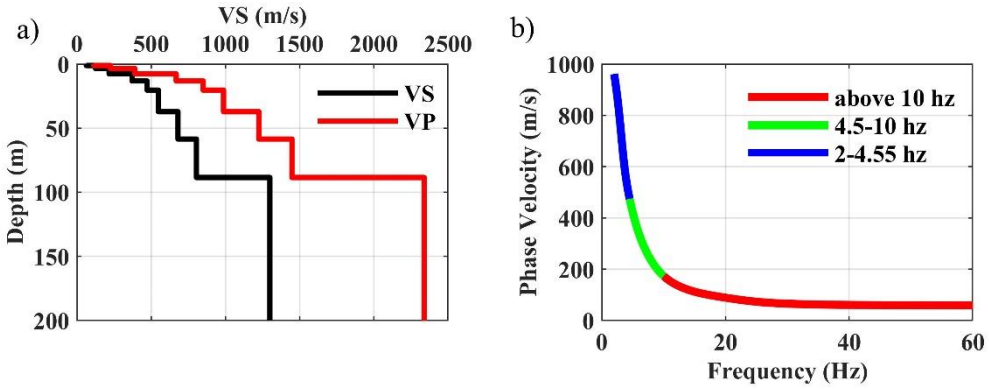

Figure 2.4: (a) The VS and VP model of the synthetic example. (b) The computed DC corresponding to the synthetic models in (a), segmented according to the low cut-off frequency of the 10 Hz, 4.5 Hz, and 2 Hz geophones.

In Figure 2.5, we show the same DC from Figure 2.4b as a function of wavelength: The part of the DC obtained by 10 Hz geophones corresponds to very short wavelengths, and allows the estimation of the shallowest part of the model only. However, using the 2 Hz geophone allows the estimation of the wavelengths up to 400 m. The investigation depth of surface wave methods almost linearly increases with the maximum registered wavelength. So, it is highly recommended to use receivers with low natural frequencies to enhance the surface wave investigation depth. This recommendation is valid provided that long enough receiver arrays are deployed to capture large wavelengths when the source provides the low-frequency waves.

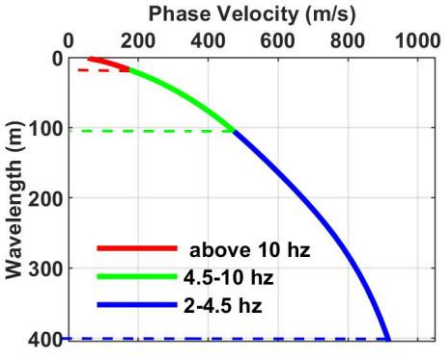

Figure 2.5: The DC from Figure 2.4b represented as a function of wavelength. The segments of the DC are according to the low cut-off frequency of the 10 Hz, 4.5 Hz, and 2 Hz geophones.

2.3.2 Local DC estimations

Usually, the records from segments of receiver arrays are considered to estimate the DCs corresponding to the segment centers. We refer to such estimated curves as local DCs. There are many methods available in literature for estimating the local DCs. Most of these methods use spectral estimators to measure the phase differences of the surface wave harmonics at multiple locations (Nolet and Panza, 1976; McMechan and Yedlin, 1981; Park et al., 1998). These methods are commonly known as multi-channel approaches, as more than two receivers' records are used to compute the spectrum.

If possible, the spectra computed from recordings of the same receiver locations, but different source positions are stacked to improve the signal-to-noise ratio. Also, the DCs from individual spectra are estimated for the uncertainty analysis. At each frequency, a phase velocity standard deviation is obtained based on the estimated phase velocity of the non-stacked spectra. In the following, we briefly explain the two processing methods used in this thesis.

2.3.2.1 f-k method

One of the most popular local DC estimation techniques is the *f-k* method, which involves the computation of the 2D Fourier transform of recordings. The raw *f-k* technique requires the recording from an array of receivers evenly spaced. We use the *f-k* method developed by Bergamo et al. (2012), in which the traces are spatially windowed using a moving Gaussian window before the computation of the spectrum. The 2D Fourier transform is employed to transform the data into the *f-k*

domain. The local maxima on the *f-k* spectrum are picked and transformed to phase velocity (phase velocity = $\frac{2\pi f}{k}$). The spatial windowing provides estimated DCs focused on a specific portion of the subsurface. The standard deviation of the spatial Gaussian window is defined as:

$$\sigma = \frac{N}{2\alpha}, \tag{2.2}$$

where N is the number of the receivers and α is the parameter inversely proportional to the standard deviation. Depending on the number of the receivers, a large α results in a very narrow window. The data's spatial windowing creates a compromise between the spectral resolution and the lateral resolution retrieved by the estimated DCs, which is determined by the standard deviation. A very narrow window well localizes the data and results in the computation of the spectrum corresponding to the property beneath the array center. However, the data windowed this way leads to poor spectral resolution. Bergamo et al. (2012) provide recommendations for selecting α based on the number of receivers and the required spectral resolution to properly separate different propagating modes.

2.3.2.2 Phase shift method

The phase-shift method (Park et al., 1998) provides the frequency-phase velocity spectrum that helps visualization of the velocity trend during the DC picking. It can be applied to receiver layouts with irregular spacing. The frequency-phase velocity spectrum is obtained by integrating the Fourier transform of the traces over the offset:

$$s(\omega, c) = \int e^{-i\left(\frac{\omega}{c}\right)x} u(x, \omega) dx, \tag{2.3}$$

where u is the phase component of the Fourier transform. ω and c are the angular frequency and phase velocity, respectively. The DC is then picked as the local maxima at each frequency.

2.3.3 Inversion

The inversion is the process of finding a realistic model that produces a synthetic DC similar enough to the experimental one. The challenging task of optimizing an inversion problem has led to the development of many inversion algorithms. Most conventional inversion methods focus on the estimation of a VS model

corresponding to a single DC. The inversion algorithms can be classified into two main categories: (i) Deterministic methods. (ii) Stochastic methods.

2.3.3.1 Deterministic inversion methods

The deterministic methods are based on Newtonian or similar iterative approaches, in which an initial guess of the model is provided to the algorithm, and its corresponding DC is compared with the experimental DC. Based on the synthetic DC's sensitivity to the model parameters (usually only VS), the model is updated iteratively until a satisfactory misfit between the synthetic and experimental DC is achieved. The deterministic inversion of the surface wave is a convex problem, and the solution is non-unique: A good guess of the model is required so that the inversion converges to the global minimum (Sambridge and Kennett, 2001; Luke et al., 2003; Wathelet et al., 2005). The possibility of imposing constraints or a priori information to least-square inversion methods can reduce the degree of non-uniqueness (Cercato, 2009).

2.3.3.2 Stochastic inversion methods

Many of the surface wave stochastic inversion approaches are based on the Monte Carlo method (e.g., Sambridge and Mosegaard, 2002; Tarantola, 2005). In these methods, the parameters of the models are randomly sampled within a model space, and the best-fitting models are selected as the solution. The stochastic approaches partially solve the non-uniqueness issue of the deterministic inversions, which is caused by assumption of the linear relation between the DCs and the model unknowns.

Here, in specific steps of the proposed methods, we use Monte Carlo inversion developed by Socco and Boiero (2008). The inputs of the method are the boundaries of the model space and experimental local DC. All surface wave model parameters can be defined as a variable in the method. The model parameters are randomly sampled within the homogenous boundaries. The modal solutions of the surface wave are scalable: If the velocities of all layers are equally scaled, the phase velocity of the DC will scale to the same extent (Socco and Strobbia, 2004). The algorithm developed by Socco and Boiero (2008) takes advantage of this principle; the synthetic DCs of the random models are computed and shifted as close as possible to the experimental DC; the scaling factor is obtained from the level of the shift and the models are scaled. These scaling steps which are performed fully automatic, provide more realistic models within the model space, and reduce the number of

required simulations to find the inversion results. The best fitting models are then selected according to a statistical Fisher test with a certain level of confidence.

We use the Monte Carlo inversion in chapter 4 to estimate the reference model required for W/D relationship estimation. Also, in chapter 5, we develop a Monte Carlo joint inversion method based on the principles explained here.

3. Data Sets

We will test the application of the surface wave methods on five field data sets, out of which two are vintage data sets recorded in controlled sites, and three are industry data sets provided by TOTAL E&P. In this chapter, we introduce the site locations and describe essential characteristics of the field and the recorded data.

3.1 Vintage data sets

3.1.1 CNR

The data were acquired in a test site at CNR (National Research Council) headquarter in Turin, Italy. The properties of the site are well-known. The site contains an artificial loose sand body embedded in more compacted geological formations (i.e., sand and gravel). The sand body occupies an area of 5×5 m^2 and extends to 2.5 m in depth. The target of the surface wave experiment is to recover the lateral variation created by the sand body. The VP model from the traveltime P-wave tomography is available for the site, facilitating the evaluation of the estimated model from the surface wave method.

The 2D acquisition was carried out along a line crossing the sand body. The acquisition parameters of the 2D acquisition line are given in Table 3.1. Four cross-line acquisitions were also carried out using the same hammer source shooting externally to 18 geophones, evenly spaced every 0.5 m.

Table 3.1: The acquisition parameters of the CNR's 2D seismic line

Receivers	Receiver spacing (m)	Sources	Number of receivers	Number of shots	Sampling rate (ms)	Recording time window (s)
4.5 Hz geophones	0.3	8 kg Hammer	72 (every 0.3 m)	11 (various spacings)	0.152	0.512 s

For each source position, 8 to 10 shots were stroke and stacked to improve the recordings' signal-to-noise ratio. The aerial view of the site and acquisition outline are reported in Figure 3.1. The sand body's extent can be observed in Figure 3.1c, where we show the main receiver array superimposed with the vertical section of the sand body. More details about CNR seismic acquisition can be found in Teodor et al. (2017).

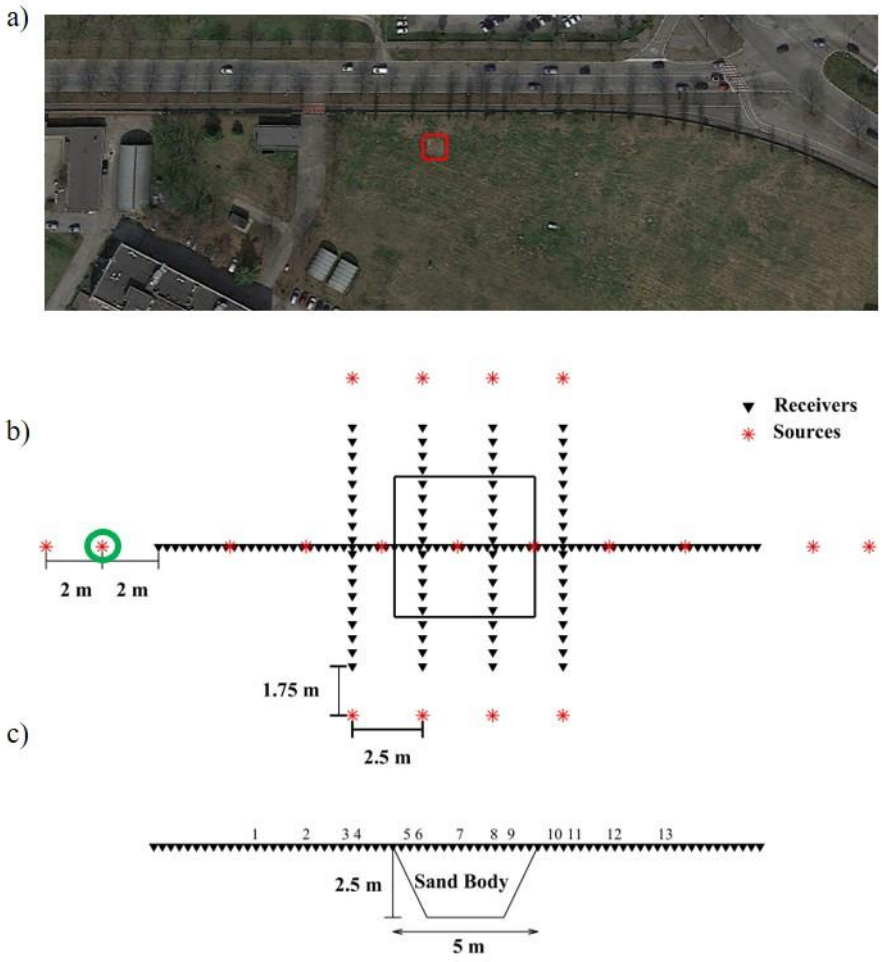

Figure 3.1 The acquisition outline of the CNR data set. (a) Aerial view of the site with the sand body highlighted with red square. (b) The top view of the acquisition layout. (c) The cross-section of the main 2D acquisition line. The indices 1-13 show the location of the estimated DCs in chapter 4.5.1.

In Figure 3.2a, we show the first 0.3 s recordings of the main line's receivers from the shot location circled in green in Figure 3.1b; the arrival times and pattern of the recorded data significantly change when the surface waves enter the sand body area. This is mainly due to the unconsolidated sand body that is expected to have lower

VS than the surrounding areas. This velocity contrast can also be observed in the DCs from the two environments. We separately performed the phase-shift method on the first 10 m of the data (outside the sand body) and the portion of the data inside the sand body area. In Figure 3.2b and c, we show the estimated spectra corresponding to the area outside and inside the sand body, respectively. The estimated fundamental mode of Figure 3.2b shows a much higher phase velocity compared to the estimated one in Figure 3.2c. The examples' frequency band is limited between 18 to 80 Hz (wavelengths between 1 to 20 m), suggesting a surface wave investigation depth of up to a few meters.

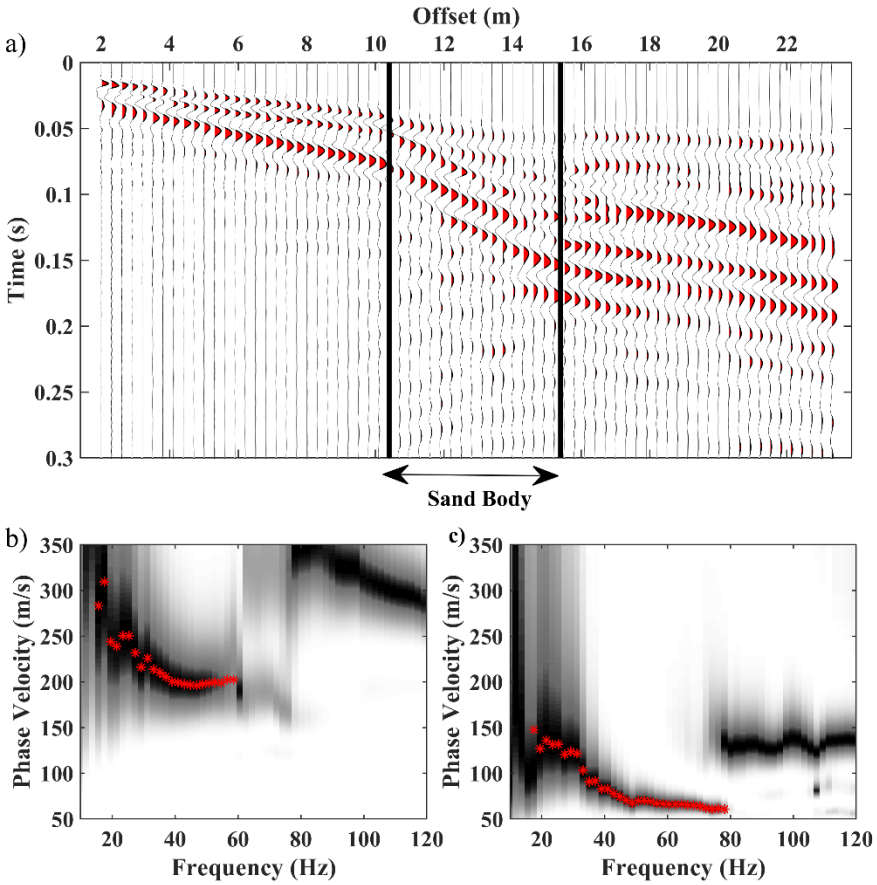

Figure 3.2 Example recordings and frequency-phase velocity spectra from the CNR data set. (a) The main receiver line's recordings from the shot location highlighted in Figure 3.1b. (b) The spectrum and estimated fundamental mode corresponding to the first 10 m of the recordings in Figure 3.2a. (c) The spectrum and estimated fundamental mode corresponding to the sand body area highlighted in Figure 3.2a.

3.1.2 La Salle

The data were acquired in La Salle, a small village in the north-west of Italy. The town is located on a 1.5 × 2.5 km^2 triangular alluvial fan, mainly consisting of medium to coarse gravelly deposits. The site is interesting for surface wave applications since it is well-characterized by two high-resolution reflection surveys and VP model from P-wave traveltime tomography. Also, the VS and VP at two locations are available from downhole tests.

Active and passive seismic acquisitions were performed at five selected locations. The active data were collected along multiple receiver arrays with varying lengths (48 to 75 m). The passive data were acquired using circular receiver arrays with even receiver spacings. The details of the acquisition parameters are given in Table 3.2.

Table 3.2: The parameters of active and passive acquisitions in La Salle site.

	Receivers	Sources	Sampling rate (ms)	Recording time window (s)
Active Data	4.5 Hz geophones	sledgehammer	0.5	4.096
Passive Data	2 Hz geophones	Ambient noise	16	522

Socco et al. (2008) separately processed the active and the passive data to estimate the local DCs, using the *f-k* and frequency domain beamformer (FDBF) methods. They then merged the estimated DCs from the active and passive data to obtain broadband DCs at the five site locations. In the map in Figure 3.3a, the locations of the estimated local DCs (A to E), the downhole tests, and the two seismic lines used for the reflection surveys are shown. In Figure 3.3b, we plot these estimated DCs. A full description of the acquisition and the site's characteristics are available in Socco et al. (2008).

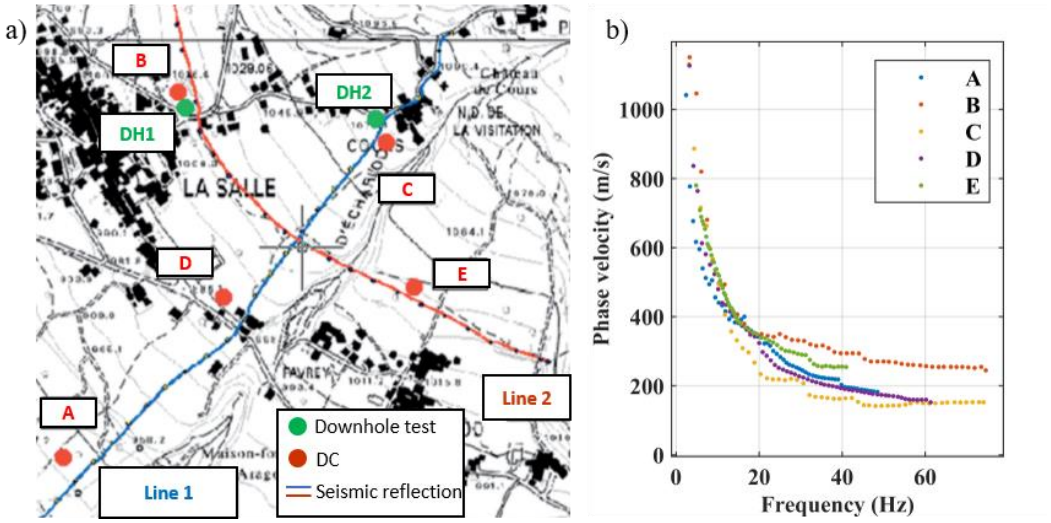

Figure 3.3: (a) The La Salle site's map shown with the location of the estimated DCs, downhole tests, and seismic reflection lines (reproduced from Socco et al., 2008). (b) Estimated local DCs, labeled according to the locations highlighted in (a).

3.2 Industry data sets

3.2.1 PNG: METIS's first pilot

The data were acquired in the foothills of Papua New Guinea (PNG) as the first pilot of METIS (Multiphysics Exploration Technologies Integrated System), over an area of about 0.2 km^2. The acquisition in remote areas such as PNG is very challenging as transporting and deploying acquisition equipment are hard to achieve. Also, the violent rains, intense humidity, high temperature, and dense vegetation make PNG an extreme environment for acquiring seismic data. In the age of technological developments and innovations, the METIS research project was created to reform the conventional acquisition methods and enable seismic imaging of remote areas (Lys et al., 2018). In the scheme of METIS, the sensors are placed in 40 cm DARTs (downfall air receiver technology), and drones are used to deliver and drop them to predefined positions. The DARTs are equipped with radio transmitters that enable real-time recording (Pagliccia et al., 2018). The sources and receivers' deployment geometry are based on the so-called carpet recording, where a fine grid of receivers is deployed, and the number of sources is limited only to the accessible locations (Lys et al., 2018). The data acquired with the novel acquisition technique from such unmarked areas require innovative processing tools. We

exploit the surface wave available in the data to reconstruct the near-surface VS and VP models.

In the densely vegetated environment of the site, the DARTs were expected to safely land only into the gaps between the trees (sky holes). So, before the acquisition days, the location and the size of the sky-holes were identified using an airborne lidar survey. Also, 25 holes (approximately 2 to 3 m) were drilled for mud-gun sources. In Figures 3.4a and b, we show the prototype drone and DART. An aerial view of a drone dropping a DART in a sky-hole is given in Figure 3.4c.

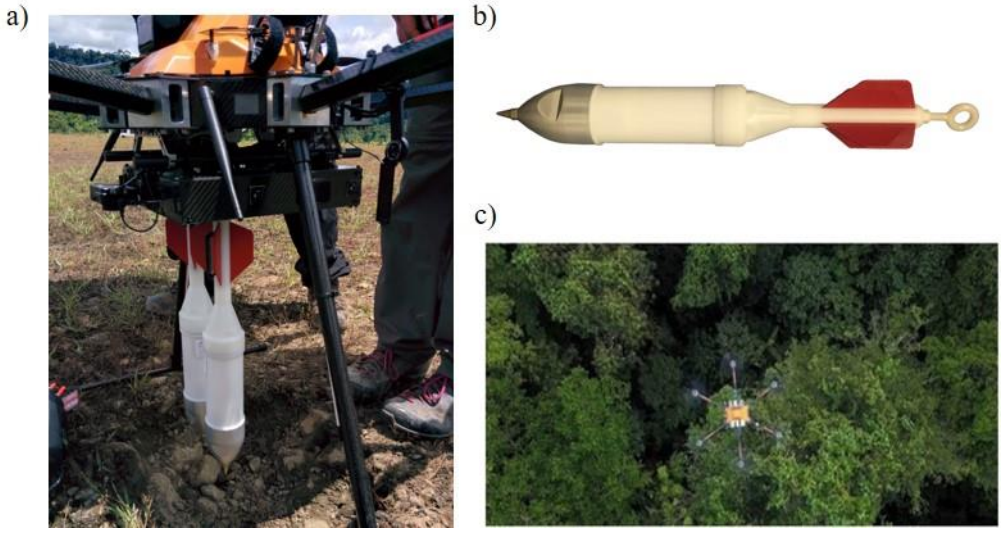

Figure 3.4 (a) The drone and 2 DARTs installed on the drone. (b) a DART (c) An aerial view of a drone dropping a DART into a sky-hole (Pagliccia et al., 2018).

Among 81 deployed DARTs, 38 geophones' data were recovered. The full description of the acquisition parameters is given in Table 3.3.

Table 3.3: Acquisition parameters of the PNG data set

Receivers	Sources	Number of receivers	Number of shots	Sampling rate (ms)	Recording time window (s)
10 Hz geophones	Mud gun (2000 psi)	38 (irregular layout)	25 (irregular layout)	4	6

In Figure 3.5a, we show the deployment geometry of the receivers and the sources. At each source's location, between 5 to 8 shots were stroke; the saturated signals were detected and removed before the stacking of the traces. In Figure 3.5b, we show the first 3 s of the normalized recordings from the shot location highlighted in Figure 3.5a. The records are displayed on a single spatial axis, considering only the source-receiver offset. The first breaks are available for all receivers; although, they are less evident in the far offset. In Figure 3.5b, the solid red lines show the boundaries of the surface wave's time panel. The data show the excitation of the fundamental and 1st higher modes of the surface wave; the separation of the two surface wave modes is evident in the offset beyond 300 m. The two surface wave modes can also be observed in the frequency-phase velocity spectrum in Figure 3.5c, where the estimated fundamental and 1st higher modes are shown in blue and red, respectively. The spectrum of the records in Figure 3.5c shows that surface waves are available between 5 to 20 Hz. However, depending on the source-receiver offset, the surface wave is present up to 55 Hz.

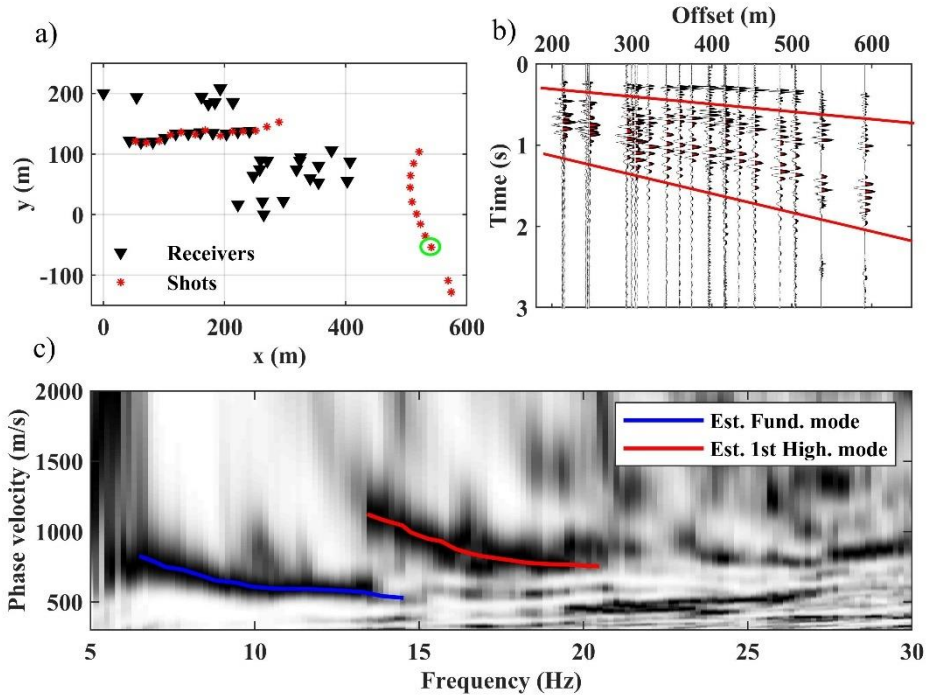

Figure 3.5: (a) The deployment geometry of the sources and receivers for the PNG data set. (b) The recordings from the highlighted shot in (a) plotted on a single spatial axis, which represents the distance between the source position and receivers. (c) The frequency-phase velocity spectrum, corresponding to the seismic data in (b).

3.2.2 Aurignac

The data were acquired and licensed by Gallego Technic Geophysics in a mining site in the province of Aurignac, south France, characterized by stiff materials. The surface wave applications to mining sites characterized by stiff material are very challenging and rare (Papadopoulou et al., 2020). We consider various surface wave methods to reconstruct the near-surface VS and VP of the area.

The data set is considered a test data set, which was acquired in the direction of the METIS's acquisition scheme to evaluate the carpet recording and real-time wireless recording, using various types of sources. The acquisition was performed inside and outside the two active open mining pits. Similar to the PNG data set in section 3.2.1, the carpet acquisition layout was adopted for the Aurignac data set. Many receivers were deployed within regular grids (area 2 km × 1 km), and several source locations were limited to access roads, resulting in a 3D large scale acquisition layout. The data were acquired using various source types, such as vibrator truck, electromagnetic sources (Storm and Lightning) from Seismic Mechatronics, and weight drop. We compared the surface wave in the different sources' recordings and concluded that the data from the vibrator truck is the most promising for the surface wave applications. The Birdwagen Mark IV off-road trucks equipped with 24-ton vibrator generated seismic waves at various locations within 3 to 110 Hz. The data were recorded remotely using the RT2 wireless system. The position of the shooting locations and the receivers, as well as the topographic map of the area, were obtained with 0.01 m accuracy, thanks to the real-time kinematic GPS system. The full description of the acquisition parameters is given in Table 3.4.

Table 3.4: Acquisition parameters of the Aurignac data set.

Receivers	Sources	Number of receivers	Number of shots	Sampling rate (ms)	Recording time window (s)
5 Hz geophones	Vibroseis truck	918 (spacing 25 to 50 m)	1077 (irregular layout)	2	5

The site is characterized by significant natural and human-made elevation contrast, which can cause highly scattered surface waves. Figure 3.6a shows the map of the area superimposed with the acquisition outline and the topography. We split the data into four sub data sets, each with relatively flat topography, to minimize the

effect of scattered surface waves. In Figure 3.6b, we show the sub data sets with different colors; in the pit zones, the sources and receivers at the pits' benches were excluded. In this thesis, we apply surface wave methods to the two sub data sets from outside the pits.

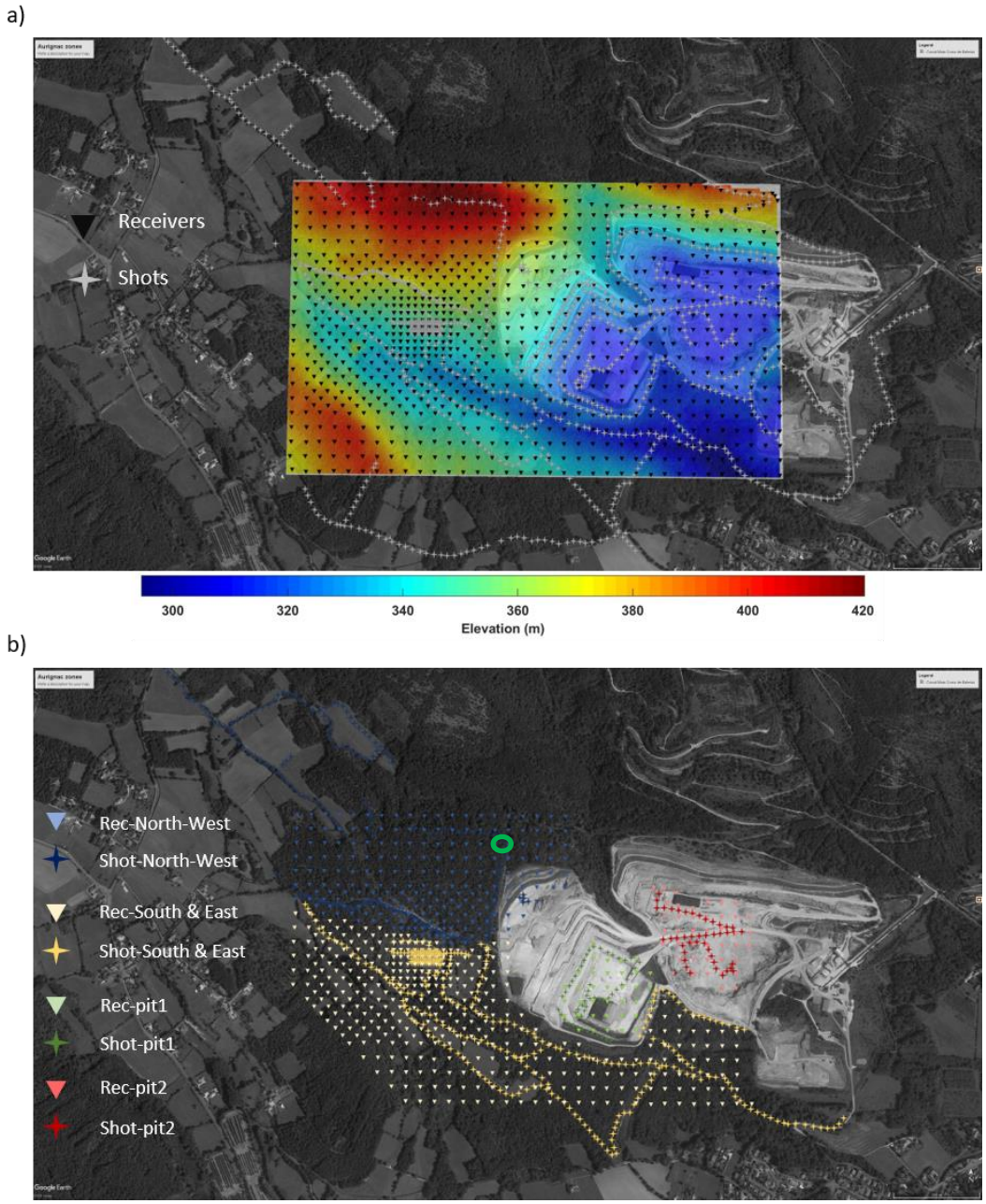

Figure 3.6: (a) The aerial map of the Aurignac site superimposed with the acquisition geometry and the elevation map. (b) The data divided into four sub data sets shown with different colors, each within relatively flat area.

In Figure 3.7, we show the first 2 s of the recordings from the shot location highlighted in Figure 3.6b, in which only 20 % of the traces from the north-west zone are shown for better visualization.

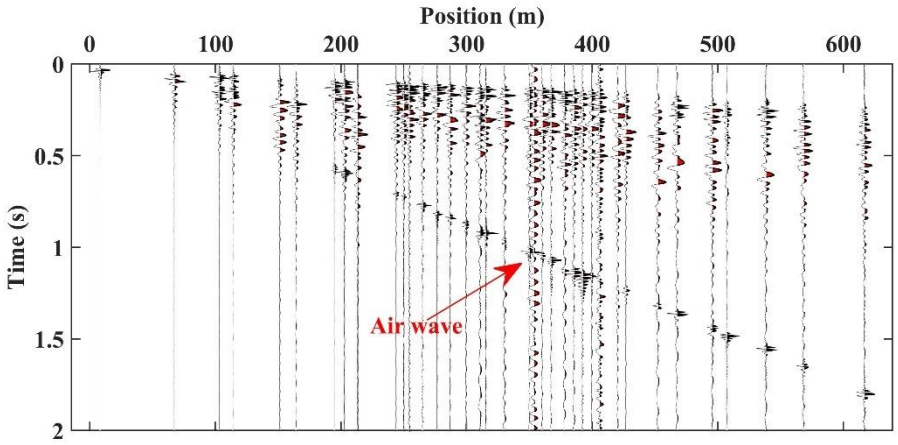

Figure 3.7: A sample seismogram from the north-west zone of the Aurignac site, highlighted with green circle in Figure 3.6b.

The surface wave is available in a broad time panel, suggesting multi-modal propagation of the surface waves. Our preliminary study of the data confirmed this observation. In Figure 3.8, we show an example estimation of the frequency-phase velocity spectrum, which was estimated from the recordings of a receiver spread highlighted in Figure 3.8a; the individual spectra corresponding to each source within 250 m of the receiver spread were computed and stacked to increase the signal-to-noise ratio. The spectrum in Figure 3.8b shows the excitation of at least two higher modes of surface waves in addition to the fundamental mode. We limit our surface wave analysis within the 4 to 55 Hz frequency range to avoid contamination of the data by airwaves and other correlated noises.

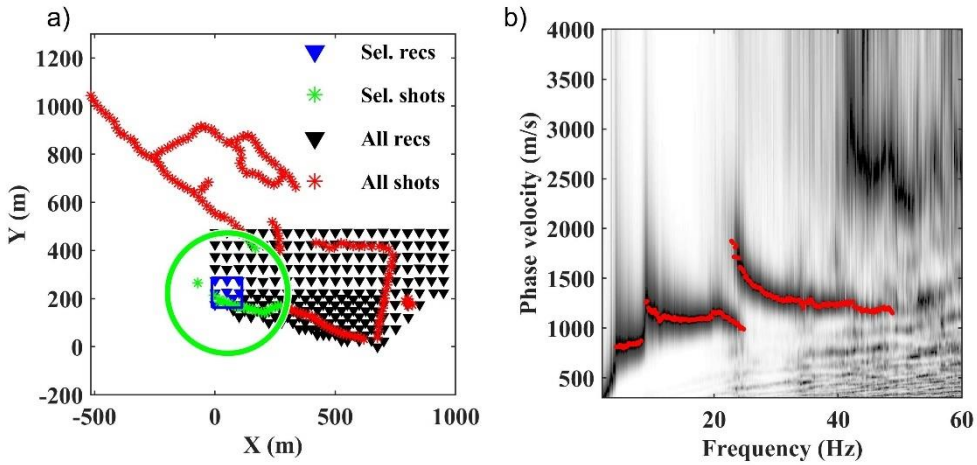

Figure 3.8: An example of the obtained spectrum for the Aurignac data set using the phase-shift method. (a) The geometry of the selected sources and receivers. (b) The obtained frequency-phase velocity spectrum, where the red dots show the estimated modes of surface waves.

3.2.3 Oil and gas exploration data set

The data were acquired at the bottom of the mountainside along a 12 km 2D seismic line. The area is characterized by recent alluvial deposits on top of the sedimentary bedrock. The data were acquired for oil and gas exploration; the recordings from receiver groups were stacked to damp the surface waves. We evaluate and process the residual surface waves in the data to estimate near-surface VS and VP models.

The vibroseis truck sources with a sweeping profile between 4 to 90 Hz were used at various locations. For each receiver station, the recorded data from the 12 geophones were stacked to improve the signal-to-noise ratio of the reflection data and damp the surface waves. The acquisition parameters of the data set are provided in Table 3.5. A thorough description of the data and the site's geology is given in Masoni (2016).

Table 3.5: The acquisition parameters of the oil and gas exploration data set

Receivers	Sources	Number of receivers	Number of shots	Sampling rate (ms)	Recording time window (s)
10 Hz geophones	Vibroseis truck	601 (every 20 m)	600 (every 20 m)	2	6.002

A schematic view of the acquisition location is given in Figure 3.9. The area's topography is relatively flat, except for the two canyons, each with a maximum depth of 30 m over the 500 m of the acquisition line.

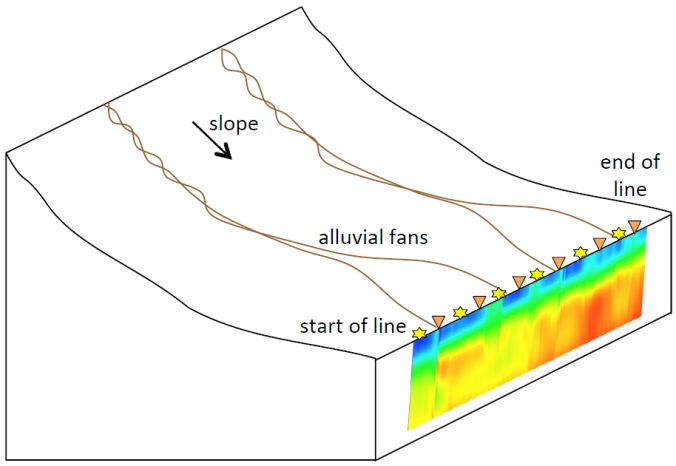

Figure 3.9: Schematic view of the acquisition location for the oil and gas exploration data set (Masoni, 2016).

In Figure 3.10a, we show an example shot from the data set, in which we highlighted the different events. The preliminary analysis of the data showed the excitation of the fundamental mode. In Figure 3.10b, we show the frequency-phase velocity spectrum corresponding to the area highlighted in Figure 3.10a. Despite the use of receiver groups in the acquisition to damp the surface waves, they are still strongly available in the data. In Figure 3.10c, we show the amplitude spectrum of the traces in Figure 3.10a. The data are available in a broad frequency band; however, the surface waves are limited to the first low-frequency peak. While the maximum amplitude of surface waves is observed within 15 to 20 Hz, they are available between 8 to 30 Hz.

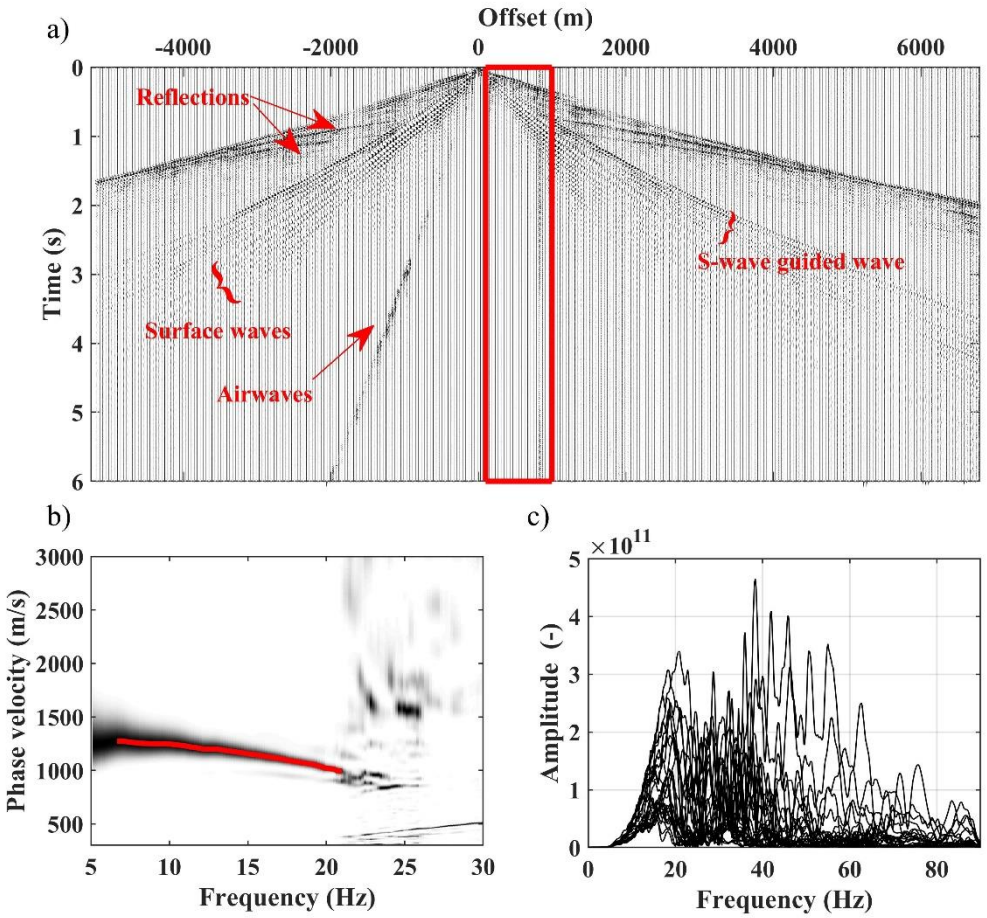

Figure 3.10: (a) An example shot gather from the oil and gas exploration data set, where various observed events are highlighted. (b) The estimated frequency-phase velocity spectrum using the recordings highlighted in (a) with a red rectangle. (c) The amplitude spectrum of the recordings from the highlighted area in (a).

3.3 Conclusion

We introduced five data sets and explained the essential properties of the site and acquisition. Each data set provides unique characteristics that we consider interesting for surface wave applications. We process these data sets using various surface wave methods to estimate the near-surface VS and VP models.

4. Wavelength – Depth method (W/D)

The wavelength-depth method (W/D) was initially introduced to estimate near-surface VSZ and VPZ models. We develop a stable W/D workflow that estimates interval VS and VP and can be used for the sites characterized by significant lateral variations. We also develop an uncertainty workflow to evaluate the estimated VS and VP models' reliability from the W/D method. The proposed method and its application to CNR data set is available also in Khosro Anjom et al. (2019). In the following, we describe the W/D workflow and uncertainty estimation. Then, we show the method's application to the CNR, Aurignac, and oil and gas exploration data sets. We evaluate the estimated models based on the information available for the site and the models provided by other methods.

4.1 W/D method's background: advantages and pitfalls

Socco et al. (2017) showed that local DC as a function of wavelength, and the corresponding time-average VS (VSZ) are highly correlated. Time-average velocity (either for S-wave or P-wave) can be obtained from the layered velocity model as:

$$V_z = \frac{\sum_{i=1}^{n} h_i}{\sum_{i=1}^{n} \frac{h_i}{V_{t,i}}}, \tag{4.1}$$

where V_z is the time-average velocity at depth z and n is the number of layers down to depth z, and the thickness and interval velocity of the ith layer are denoted by h_i, and $V_{t,i}$. Socco et al. (2017) developed a method to estimate a relationship between the investigation depth and the surface wave wavelength. The W/D relationship is an ensemble of the depth and wavelength data points satisfying the expression:

$$\left((\lambda_i, z_i) \in \mathrm{W/D}\right) \leftrightarrow c(\lambda_i) = VSZ(z_i), \tag{4.2}$$

where i is the index of the W/D data points at each depth level. The only pieces of information required to estimate a W/D relationship are the VSZ and DC from the same location. In sites with no sharp lateral variations, the estimated W/D relationship at a reference location can be used at different locations to directly transform the DCs (phase velocity as a function of wavelength) into local VSZ models (Socco et al., 2017), considering equation (4.2). In Figure 4.1, we show the process of obtaining the W/D relationship for a synthetic example. The dashed lines in Figure 4.1a are instances of wavelength-depth couples with equal phase velocity and VSZ. The wavelength-depth couples are assembled to build the W/D relationship in Figure 4.1b.

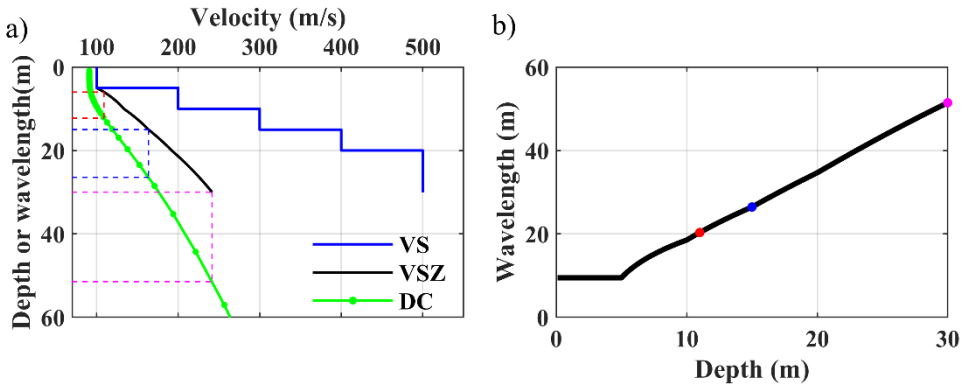

Figure 4.1: Example estimation of the W/D relationship. (a) The VS and VSZ models in blue and black, and DC in green. The dashed lines highlight three example depth-wavelength couples that demonstrate equal VSZ and phase velocity. (b) The estimated W/D relationship. The colored dots correspond to the wavelength-depth couples highlighted in (a).

Socco and Comina (2017) showed that the W/D relationship is highly sensitive to Poisson's ratio. They developed a method to estimate a reference apparent Poisson's ratio from the reference W/D relationship. The apparent Poisson's ratio relates the VSZ and VPZ as:

$$\nu_{app} = \frac{1}{2}\left[\frac{\left(\frac{VPZ}{VSZ}\right)^2 - 2}{\left(\frac{VPZ}{VSZ}\right)^2 - 1}\right]. \tag{4.3}$$

According to the method, first, the reference location's VS model is considered for computing a set of synthetic DCs, each from a specific constant Poisson's ratio.

Then, the synthetic DCs and the reference VSZ are used to estimate synthetic W/D relationships. The experimental W/D relationship is compared with the synthetic ones to obtain the apparent Poisson's ratio at each depth as:

$$\forall z \in \text{W/D}: \ \nu_{app}(z) = \nu_{syn}(z) \leftrightarrow \lambda_{\exp}(z) = \lambda_{syn}(z), \tag{4.4}$$

where ν_{syn} is the Poisson's ratio of the synthetic W/D relationships. In practice, at each depth, the discrete values of λ_{syn} from a set of synthetic W/D relationships are interpolated to find the λ_{syn} that satisfies equation (4.4) and the corresponding ν_{syn} is considered as the apparent Poisson's ratio at depth z.

In Figure 4.2, we show the steps of apparent Poisson's ratio estimation for the example introduced in Figure 4.1. The synthetic DCs and reference VSZ in Figure 4.1a are used to compute the synthetic W/D relationships in Figure 4.2b. Finally, the apparent Poisson's ratio at each depth (Figure 4.2c) is estimated by linear interpolation between the synthetic W/D relationships and comparing them with the experimental one.

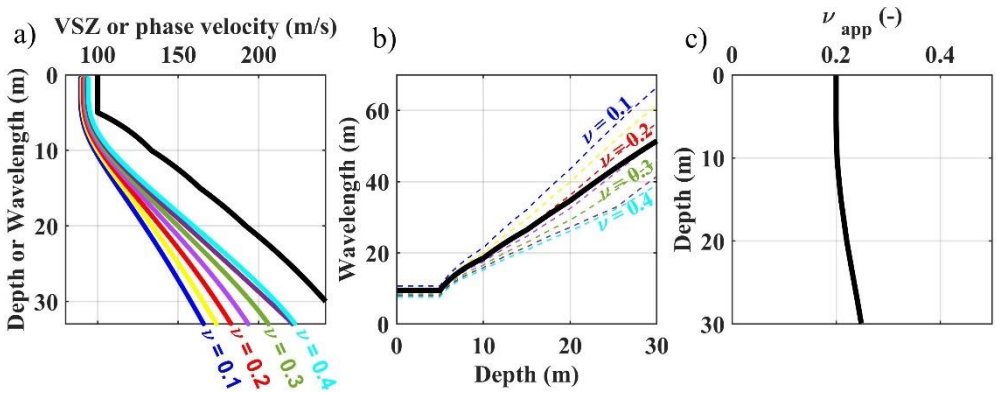

Figure 4.2: The estimation of apparent Poisson's ratio for the example in Figure 4.1. (a) The synthetic DCs computed from true model parameters but each with the indicated Poisson's ratio. The VSZ model is shown in black. (b) The experimental W/D relationship compared with the synthetic ones. The color scale of the synthetic W/Ds matches the ones used for the DCs in (a). (c) The estimated apparent Poisson's ratio as a function of depth.

For smoothly laterally varying sites, the estimated apparent Poisson's ratio at a reference location is used to transform the estimated VSZ models at various locations into VPZ (Socco and Comina, 2017) as:

$$VPZ = VSZ\sqrt{\frac{2\left(\nu_{app}-1\right)}{2\nu_{app}-1}}. \tag{4.5}$$

Socco et al. (2017) and Socco and Comina (2017) successfully tested the method on multiple synthetic and real data sets. The method directly estimates the VSZ and VPZ from the local DCs without the need for extensive inversion. However, it requires the VSZ and VS models at a reference location to estimate the experimental W/D and apparent Poisson's ratio, respectively. Moreover, the W/D relationship is valid for a site where no sharp lateral variations exist. Here, we address these limitations: We develop a W/D workflow that accounts for the lateral variations in a site and requires no known VSZ and VS model to estimate the experimental W/D relationship and apparent Poisson's ratio. Also, we provide a method to estimate the interval VS and VP velocities from the VSZ and VPZ models. Since the W/D method is a data transformed method, the estimated models' uncertainty is highly data-driven and noise dependent. We develop an uncertainty propagation workflow that obtains the standard deviation of the estimated VS and VP models based on the uncertainty of the input DCs. We also provide a method to estimate the interval Poisson's ratio at the reference location.

4.2 The Method

The only inputs of the proposed W/D method are the local DCs from different locations at a site. Let us assume that a set of DCs has been obtained along a seismic line (2D geometry) or over an acquisition area (3D geometry) using the methods explained in section 2.3.2. We use these DCs to build the quasi 2D or 3D velocity models, following the workflow described in Figure 4.3.

The DCs are grouped into clusters of relatively homogeneous sets (a). For each cluster: A reference DC is selected and inverted with a Monte Carlo inversion (MCI) algorithm to obtain VS and VSZ models as reference models (b). The estimated VSZ and the corresponding DC are used to estimate a reference W/D relationship for the cluster (c). The reference W/D relationship is employed to transform all DCs of the cluster into VSZ models (d). An apparent Poisson's ratio for the cluster is estimated utilizing the reference W/D relationship and the

reference VS model (e). Each VSZ profile is transformed into a VPZ profile, thanks to the estimated apparent Poisson's ratio (f). All the reconstructed VSZ and VPZ 1D models are then transformed into interval VS and VP profiles using specific differentiation rules (g). In the following, we consider each step of this workflow for a more detailed description.

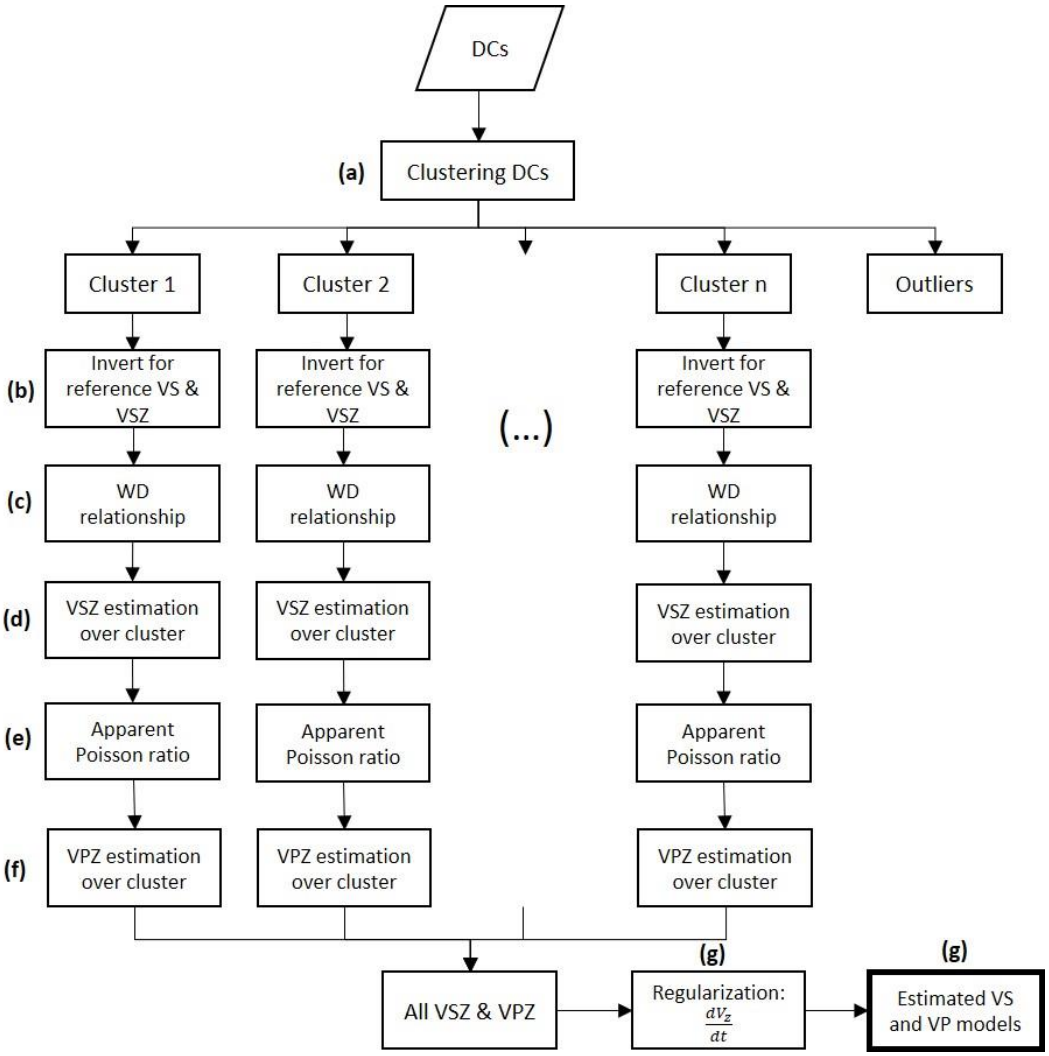

Figure 4.3: The full workflow of the W/D method to estimate the local 1D VS and VP models. The DCs are divided into clusters and the W/D steps are performed individually for each cluster to estimate local VSZ and VPZ models. These models are transformed to interval VS and VP models through differentiation process.

4.2.1 Local DC clustering

Given a data set of DCs, a hierarchical clustering algorithm (Rokach and Maimon, 2005) is applied to divide the data set into homogeneous sets of DCs (Khosro Anjom et al., 2017). Hierarchical clustering algorithms do not require prior information regarding, for example, possible lateral velocity variations. Moreover, the number of clusters does not need to be defined, and they are obtained from the algorithm. The distinction between the clusters is based on the dissimilarity between DCs and is obtained by defining appropriate metrics and linkage criteria. We use the Euclidean distance between each two DCs as metrics, which is expressed as:

$$d(\mathbf{c}_1, \mathbf{c}_2) = \left[\sum_{i=1}^{n} (c_1(i) - c_2(i))^2 \right]^{0.5}, \tag{4.6}$$

where $\mathbf{c}_1$ and $\mathbf{c}_2$ are the phase velocity vectors of two DCs corresponding to frequencies within the common frequency band. The i is the index of the frequency elements, where $i=1$ and $i=n$ are the indices of the minimum and maximum frequencies within the frequency band. Wide frequency common band between the DCs ensures reliable clustering. As a result, to maximize the frequency band between all DCs, it is necessary to remove the short banded DCs before the clustering.

We use the average linkage criterion, in which the distance between two clusters is computed as the average distance between any element of one cluster to the other cluster. This allows all elements of each DC to contribute to the clustering process. The hierarchical clustering outcome is a dendrogram used to identify the DC clusters.

4.2.2 Reference VS, VSZ, and W/D estimation

The reference VS and VSZ models and their corresponding DC are needed for estimation of the W/D relationship. For each cluster, the DC with the broadest frequency band is selected as the reference DC and inverted using a Monte Carlo inversion (MCI) algorithm (Socco and Boiero, 2008; section 2.3.3.2) to estimate reference 1D VS and VSZ models. Vast model space is defined by selecting ranges for each model parameter (VS, thicknesses, and the Poisson ratio for each layer). A large population of random models is generated, and their relevant fundamental

modes are computed using the Haskell and Thomson forward modeling (Haskell, 1953; Thomson, 1950; Maraschini, 2008). The final result of the MCI is a set of accepted VS models, according to the imposed level of confidence in a statistical one-tailed Fisher test. We use a low level of confidence to accept a set of models that their DCs show a good fitting with respect to the experimental one. The selected models are then transformed into their corresponding VSZ models using equation (4.1). The reference VS and VSZ models are computed by averaging the models at each depth. The reference DC and VSZ are used to estimate the reference W/D relationship, following the method proposed by Socco et al. (2017) and explained in section 4.1.

4.2.3 VSZ estimation over a cluster

Socco et al. (2017) showed that given a homogenous set of DCs, where no significant lateral variations exist, the reference W/D relationship is valid for all DCs to obtain the local VSZs at the position of each DC. The reference W/D relationship for the cluster is used for all DCs of the cluster to retrieve the associated VSZ profiles (equation 4.2).

4.2.4 Reference apparent Poisson's ratio and VPZ estimation

We compute the synthetic W/D relationships required to estimate the reference apparent Poisson's ratio of each cluster, thanks to the reference VS model of the cluster. Then, we estimate the apparent Poisson's ratio by comparing the synthetic and experimental W/D relationships according to equation (4.4). Assuming negligible variation of the apparent Poisson's ratio inside each cluster area, we use the reference apparent Poisson's ratio to transform all estimated VSZs into VPZ models using equation (4.5).

4.2.5 Interval VS and VP estimation

The time-average velocity models can be useful for computing static corrections, but an interval velocity model is needed for most applications. Equation (4.1) expresses the computation of the time-average velocity from interval velocity. We develop a stable approach for inverting this equation to transform time-average velocities into interval velocities and apply it to the VSZ and VPZ models relevant to all the DCs.

Considering interval velocity (either for P-wave or S-wave) as a set of elements corresponding to different intervals, let us define the interval transit time Δt_i inside the i-th interval. Considering that interval's thickness is equal to $V_i \Delta t_i$, we can rewrite the time-average velocity (equation 4.1) as a function of time:

$$V_z(t) = \frac{\sum_{i=1}^{n} \left(V_i \Delta t_i \right)}{\sum_{i=1}^{n} \Delta t_i}, \tag{4.7}$$

and, by moving to a continuous depth description, we can express the time-average velocity under the integral form:

$$V_z(t) = \frac{\int_0^t V_t dt}{\int_0^t dt} = \frac{\int_0^t V_t dt}{t}, \tag{4.8}$$

where the quantity V_t is the interval velocity defined within each interval dt. Equation (4.8) is the continuous analog of the discrete equation (4.1): an illustration of why the quantity V_z is called time-average velocity. This relation is unique between the time and depth variables. The differentiation of equation (4.8) gives $V_t dt = d(t \; . \; V_z(t))$ from which we can obtain the interval velocity V_t through the expression:

$$V_t(t) = V_z + t \frac{dV_z}{dt}. \tag{4.9}$$

Based on equation (4.9), the interval velocity V_t consists of a time-average velocity term and a derivative term. The difference dV_z can be discretized at each depth and divided by the stepwise Δt to get a numerical value of the derivative; however, small perturbations in the time-average velocity leads to massive relative changes in the derivative estimation (Khosro Anjom et al., 2019). Hence, a different approach must be applied for the derivative calculation, especially for noisy data.

Many methods are available in literature to differentiate noisy data, such as least-squares polynomial approximation, Tikhonov regularization, and total-variation regularization (Knowles and Renka, 2014). The estimated VSZ and VPZ carry noise because they are directly obtained through data transform. On the other hand, abrupt but realistic variations in the velocity profile produce discontinuities in the derivative trend. So, the method to calculate the derivative term should intrinsically allow discontinuities in the derivative estimation to avoid too strong smoothing. We consider the total variation regularization for the estimation of the derivative term in equation (4.9). Total variation regularization was initially introduced by Rudin et al. (1992) to remove the noise from images without smearing the edges. In this method, given a discrete set of data points V_z, the first derivative $\left(\frac{dV_z}{dt}\right)$ is approximated by the solution u of the minimization of the function:

$$F(u) = \alpha \int_0^T \left| u(t)' \right| dt + \frac{1}{2} \int_0^T \left| Au(t) - V_z(t) \right|^2 dt, \tag{4.10}$$

where $Au(t) = \int_0^t u(\tau) d\tau$ defines the smoothed V_z and the regularization parameter is denoted by the symbol α. The term $\int_0^T \left| Au(t) - V_z(t) \right|^2 dt$ minimizes the difference between the smoothed function $Au(t)$ and the input function $V_z(t)$. On the other hand, $\int_0^T |u(t)'| \, dt$ is the total variation of the first derivative u. The regularization parameter controls the balance between the two terms. The numerical implementation in MATLAB to be used in our application is provided by Chartrand (2011).

In Figure 4.4, we show an example transformation of a noisy and noise-free VSZ to interval VS. In Figure 4.4a, the noisy VSZ (noise level ±2 m/s) is plotted in blue, and the noise-free VSZ is represented in black. The difference between these two VSZ models is almost unnoticeable, given the low noise level. In Figure 4.4c, the derivative term $\left(\frac{dV_z}{dt}\right)$ of noisy data is evaluated either by numerical differentiation in green or by the total variation technique of equation (4.10) in red, while Figure 4.4b provides the wanted interval velocity: a minor amount of noise, present in the VSZ, has a significant impact on the interval VS estimation. The total variation

regularization provides an acceptable reconstruction of the true model (shown in red).

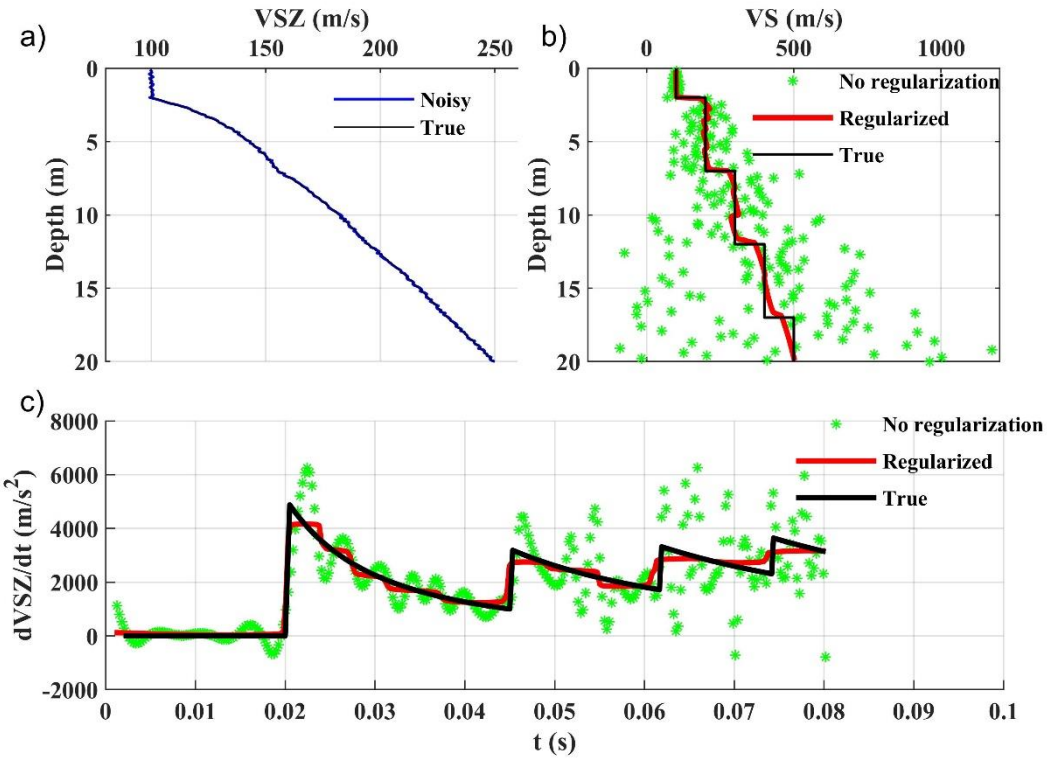

Figure 4.4: The application of equations (4.9) and (4.10) to transform noisy synthetic VSZ example into interval VS models. (a) True and noisy VSZ models in black and blue. (b) Estimated VS profiles without (green) and with regularization (red) compared to the true profile (black). (c) Estimated $\left(\frac{dVSZ}{dt}\right)$ without (green) and with regularization (red) compared to the true derivative (black).

To estimate the interval VS and VP models from the time-average velocities at different positions, we use equation (4.9), in which we perform total variation regularization (equation 4.10) for the computation of the derivative term. This procedure is applied to all estimated VSZ and VPZ models to obtain interval VS and VP. These interval velocity models can be laterally interpolated for obtaining quasi 2D or 3D velocity models.

4.3 Uncertainty propagation

We start from the uncertainties associated with the estimated local DCs, and we translate this uncertainty to the estimated VS and VP models. In section 2.3.2, we

explained how the uncertainties of the DCs are usually obtained. However, sometimes, in particular when small scale data sets are being processed, there are not enough data to estimate uncertainties of the experimental DCs. Passeri (2019) investigated the uncertainty of 52 sites, and he obtained an empirical equation with which we can approximate the standard deviations of the phase velocities as:

$$\sigma_c = \left(0.2822\, e^{-0.1819 f} + 0.0226\, e^{0.0077 f}\right) \times c, \tag{4.11}$$

where f is the frequency, and the c is the phase velocity at *f*. We use this equation to approximate DC's uncertainty when it is not possible to estimate the experimental uncertainties using the seismic data.

To propagate the uncertainty to the VS and VP models, we follow the same workflow steps shown in Figure 4.3. We divide the steps into two main blocks: (1) obtaining the uncertainty of the reference W/D and apparent Poisson's ratio of each cluster, and (2) propagating the uncertainty to each estimated 1D VS and VP models.

4.3.1 Reference W/D and apparent Poisson's ratio uncertainty

Considering *g* as a function of *h* and *k*, and assuming no correlation between the error of *h* and *k*, we can propagate the variance of *h* and *k* to *g(h,k)* as:

$$\sigma_g^2 = \left(\frac{\partial g}{\partial h}.\sigma_h\right)^2 + \left(\frac{\partial g}{\partial k}.\sigma_k\right)^2, \tag{4.12}$$

where σ_g, σ_h and σ_k are the standard deviations of *g*, *h,* and *k*, respectively. We start from the standard deviation of the reference DC. As the first step, knowing that wavelength is phase velocity divided by frequency and considering negligible uncertainty for the frequency, we use equation (4.12) to translate the standard deviation of the phase velocity to the wavelength as:

$$\sigma_\lambda = \frac{\sigma_c}{f}. \tag{4.13}$$

The reference VSZ is estimated from the MCI, as explained in section 4.2.2. We know that the solutions of the inversion are non-unique. As a result, the uncertainty of the reference VSZ model should be included in the uncertainty workflow. We estimate a standard deviation for the reference VSZ at each depth by considering

the distribution of the selected VSZ models from the MCI. Given that depth is VSZ multiplied by one-way arrival time and considering negligible standard deviation for time measurement (sampling rate), we estimate the standard deviation for depth using equation (4.12), which gives:

$$\sigma_z = \sigma_{VSZ} \cdot t_{one-way}, \tag{4.14}$$

where $t_{one-way}$ is the one-way traveltime, and σ_{VSZ} is the estimated standard deviation of the reference VSZ.

We directly translate the estimated standard deviations for the wavelength (obtained from equation 4.13) and depth (obtained from equation 4.14) to the reference W/D relationship. The next step is to estimate the standard deviation of the reference apparent Poisson's ratio. As explained in section 4.2.4, the reference apparent Poisson's ratio is obtained by comparing the synthetic W/D relationships, each from a constant Poisson's ratio, with the reference W/D relationship. First, we randomly sample the W/D relationship points, considering the normal Gaussian distribution of the error. Then, we compare the randomly sampled data points with the synthetic W/D relationships to estimate an ensemble of experimental apparent Poisson's ratio at each depth. Finally, we estimate the standard deviations of the reference apparent Poisson's ratio, considering the distribution of the obtained data points at each depth.

At the end of this step, we obtain the standard deviation of the reference W/D relationships and apparent Poisson's ratios of each cluster.

4.3.2 Uncertainty of the estimated VS and VP models.

The first step is to estimate the uncertainty of the local VSZ models. The VSZ's uncertainty is governed by the uncertainties of the corresponding local DC and the reference W/D relationship which transforms it to VSZ model. To estimate the latter, we consider the same random samples of the reference W/D relationship to perform the direct transformation method and estimate a set of estimated VSZ at each depth. We consider the distribution of the VSZ data points at each depth to estimate the standard deviation related to the application of W/D workflow. Each local DC is associated with phase velocity uncertainty, either from the data or computed from equation (4.11). To include the local DC's uncertainty for the estimation of the VSZ, we use the reference W/D relationship to transform the standard deviation of phase velocity into the standard deviation of VSZ as a function

of depth. We compute the total standard deviation of the estimated VSZ model at the position of each DC as the summation of the standard deviations from the application of the W/D workflow and the standard deviation from the DC.

We now consider the estimation of the VPZ at the position of each DC. Considering equation (4.5) and following the uncertainty propagation method explained in equation (4.12), we translate the uncertainty associated with the estimated VSZ model and the reference apparent Poisson's ratio to the estimated VPZ as:

$$\sigma_{VPZ}^2 = \left(\sqrt{\frac{2\nu_{app}-2}{2\nu_{app}-1}}.\sigma_{VSZ} \right)^2 + \left(VSZ.\frac{\sigma_{\nu_{app}}}{\left(2\nu_{app}-1\right)^2 \sqrt{\frac{2\nu_{app}-2}{2\nu_{app}-1}}} \right)^2, \tag{4.15}$$

where σ_{VPZ}, σ_{VSZ}, and $\sigma_{\upsilon_{app}}$ are the standard deviations of VPZ, VSZ, and apparent Poisson's ratio, respectively.

The interval VS and VP are estimated using equations (4.9) and (4.10). To estimate the uncertainties associated with interval velocities, assuming normal Gaussian distribution of the error for time-average velocity estimates, we randomly sample, at each depth, the estimated 1D VSZ and VPZ models. Using the proposed workflow (equations 4.9 and 4.10), we transform time-average velocities into interval velocities. Then, we use the distribution of the estimated interval velocity at each depth to estimate the standard deviations of the interval VS and VP. We normalize the standard deviations to the velocities for a better understanding of the uncertainty level.

4.4 W/D method to estimate reference Poisson's ratio

The W/D method is a stand-alone method, which provides interval VS and VP models. However, when other surface wave methods, such as LCI, SWT and etc., are applied to estimate the VS model, they require a priori Poisson's ratio in the inversion stage. We use the W/D method to estimate the Poisson's ratio required for these methods. Also, using the same Poisson's ratio, we transform the estimated VS models from these methods into VP.

In chapter 4.1, it was described how we cluster the DCs to group them to more homogenous sets, and we estimate a reference W/D relationship and apparent

Poisson's ratio for each set (cluster). We go a step further to estimate an laterally invariant interval Poisson's ratio corresponding to the area of the cluster. We use the reference VSZ and apparent Poisson's ratio of each cluster to estimate the reference VPZ, using equation (4.5). Then, we estimate the reference interval VP from the reference VPZ, thanks to equations (4.9) and (4.10). Then, we use the reference VS and VP models to estimate the Poisson's ratio of the cluster, using the expression:

$$\nu = \frac{1}{2}\left[\frac{\left(\frac{VP}{VS}\right)^2 - 2}{\left(\frac{VP}{VS}\right)^2 - 1}\right]. \tag{4.16}$$

We use this method in sections 6 and 7 to estimate a priori Poisson's ratio required for LCI and SWT.

4.5 Application to field data sets

4.5.1 CNR

4.5.1.1 Local DCs and clusters

The local DCs were estimated along the 2D seismic line in different positions by spatially windowing the data and performing *f–k* wavefield transform (Bergamo et al. 2012; section 2.3.2.1), which was designed according to equation (2.2). Having 72 receivers along the main seismic line, we used an α number of 6, which corresponds to a standard deviation of 1.8 m and a wavenumber resolution of 0.9 rad/m. For each window position, the spectra from the four sources external to the line were stacked to improve the signal-to-noise ratio before extracting the DC. We estimated nine DCs, each 1.8 m apart. We also estimated four DCs using cross-line acquisitions. The location of the 13 retrieved DCs are indicated in the Figure 3.1c of the section 3.1.

The estimated DCs were continuous and smooth, and since the site is characterized by a smooth velocity gradient, we assume that the DCs correspond to the fundamental mode of surface wave propagation without any contamination by higher modes. In Figures 4.5a and b, we show the estimated DCs as a function of frequency and wavelength, respectively. The extracted DCs were analyzed by the hierarchical clustering strategy (Figure 4.5c). Two main clusters were detected: six

DCs for the blue cluster (cluster A) and five for the green cluster (cluster B). Two DCs were identified as outliers by the clustering process (indicated in red); therefore, they were excluded from the workflow. In Figures 4.5a and b, the same colors are used to distinguish the clusters and the outliers.

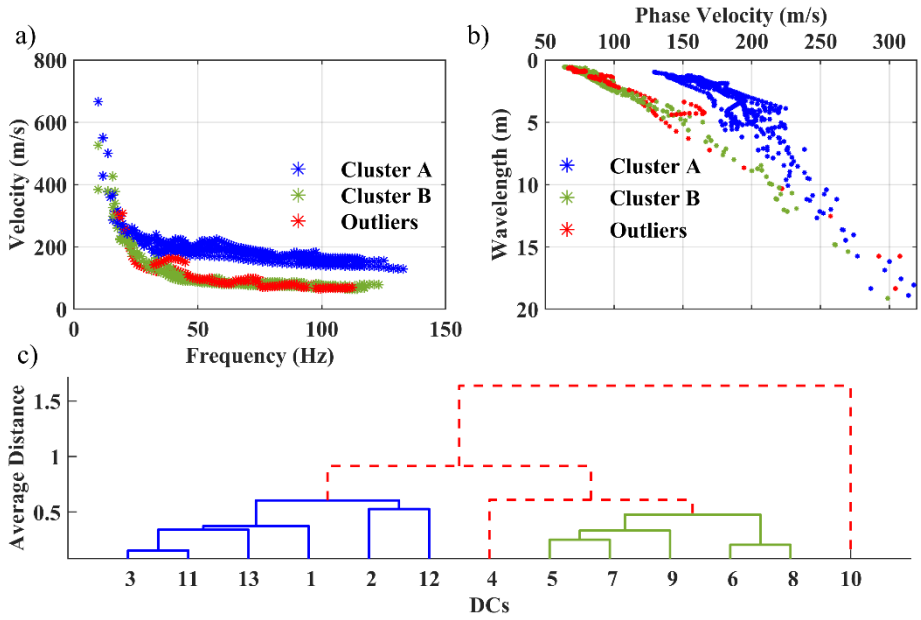

Figure 4.5: The estimated DCs from the processing of the CNR data set using the f-k method. (a) Estimated DCs as a function of frequency, indicated with different colors based on the obtained clusters in (c). (b) Estimated DCs as a function of wavelength, indicated with different colors based on the obtained clusters in (c). (c) The dendrogram obtained through hierarchical clustering; two main clusters are shown in blue and green, and the two outlier DCs are shown in red .

As was mentioned in section 3.1.1, an area of the site was excavated and filled with loose sand (sand body), creating sharp lateral variations. The two selected clusters correspond to DCs located inside and outside the sand body, and the outliers are located at the sand body boundaries. Thus, the clustering was effective in identifying different zones along the survey line and positions where sharp lateral variations occur.

4.5.1.2 The reference W/Ds and apparent Poisson's ratios

In Figures 4.6a to c and Figures 4.6d to f, we show the results of the MCI to estimate reference VSZ models from the reference DCs of clusters A and B, respectively. In Figures 4.6 a and d, we show the experimental DCs with the uncertainties computed

according to equation (4.11). The selected VS models (Figures 4.6b and e) were then transformed into VSZ models (Figures 4.6c and f), which we averaged to obtain the reference VSZ models. When comparing the VS results shown in Figures 4.6b and e, the different velocities between loose sand and stiffer material of the background corresponding to cluster A and B can be observed.

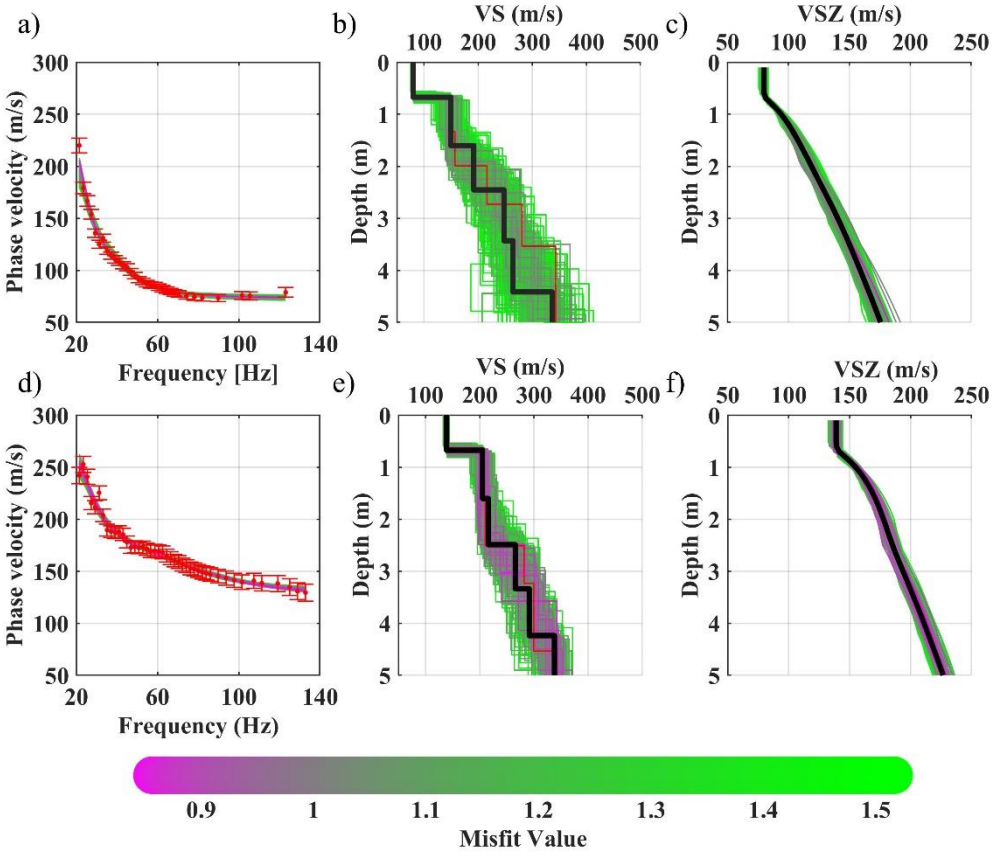

Figure 4.6: The results of the MCI applied to the reference DCs of the CNR data set. (a) to (c) are related to cluster A and (d) to (f) are related to cluster B. (a,d) The experimental DC with the uncertainties and the selected synthetic DCs. (b,e) The selected VS models. The black model shows the average of the selected models. (c,f) The selected VSZ models and the averaged reference VSZ models.

In Figures 4.7a and b, we show the reference DCs of clusters A and B as a function of wavelength, where the horizontal and vertical bars are the standard deviation of the phase velocity and wavelength (equation 4.13). We estimated the standard deviation of the reference VSZ models (section 4.3.1) using the selected VSZ models in Figures 4.6c and f. We propagated the VSZ uncertainty to depth uncertainty using equation (4.14). In Figures 4.7a and b, we also show the reference

VSZ models (in black), where the horizontal and vertical bars are the standard deviation of the VSZ and depth, respectively. Next, we used the reference DCs and corresponding VSZ models to estimate the reference W/D relationships. In Figure 4.8a and b, we show the reference W/D relationships with the corresponding depth and wavelength uncertainties (black bars).

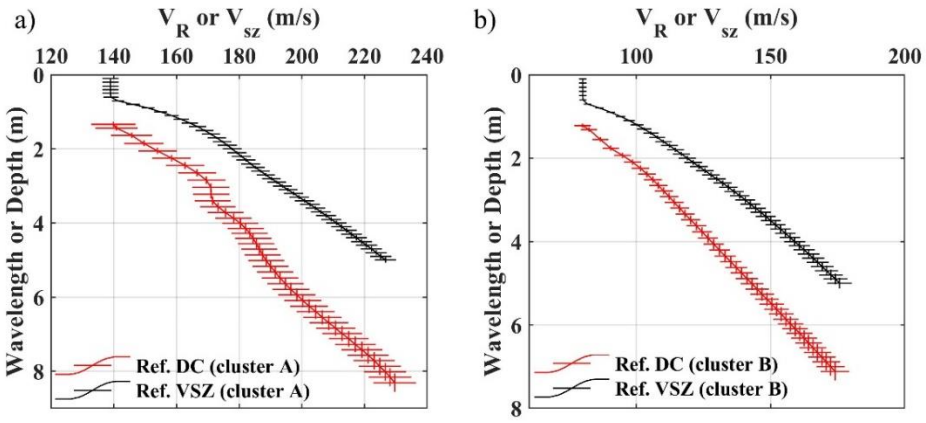

Figure 4.7: The reference DC and VSZ models in red and black with the uncertainties, corresponding to: (a) cluster A, and (b) cluster B.

the synthetic W/D relationships in Figures 4.8a and b were compared with the experimental ones to estimate the reference apparent Poisson's ratio of cluster A and B in Figures 4.8c and d. At each depth, 10,000 random samples based on the standard deviations of the W/D relationships (gray dots in Figures 4.8a and b) were generated, and the standard deviations of the reference apparent Poisson's ratios were estimated (horizontal bars in Figures 4.8c and d) following the uncertainty propagation method explained in section 4.3.1.

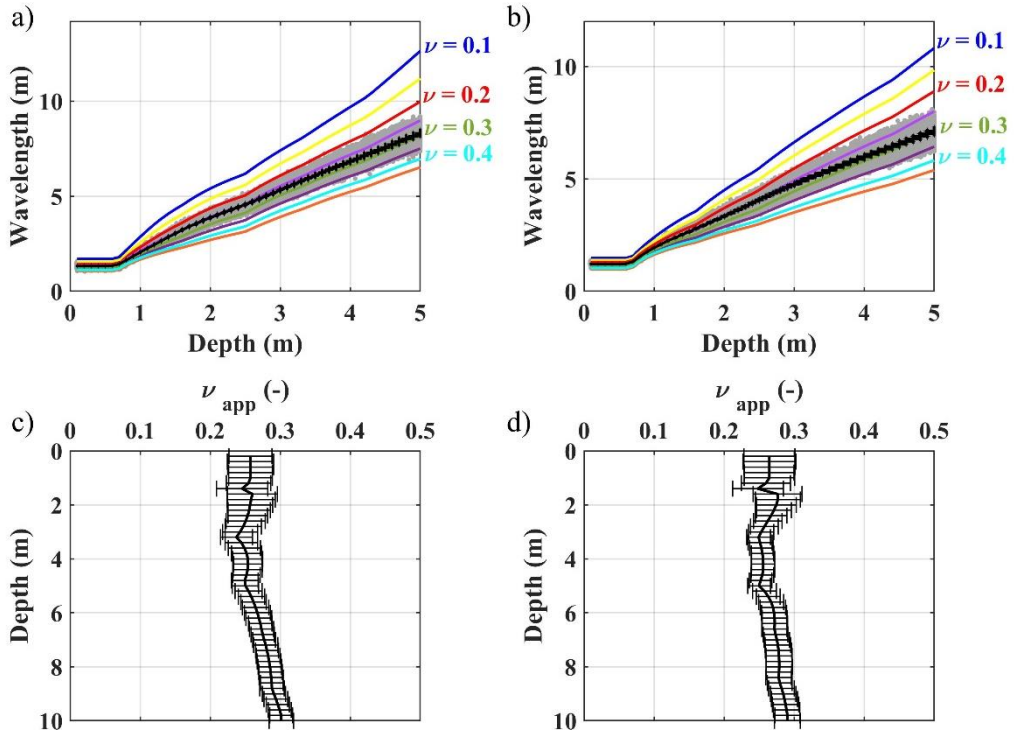

Figure 4.8: The estimated reference W/D and apparent Poisson's ratios for the CNR data set. (a) and (c) are related to cluster A. (b) and (d) belong to cluster B. (a,b) The estimated reference W/D relationship in black with depth and wavelength standard deviations shown as horizontal and vertical bars, and the random samples of the reference W/D relationship in gray dots. The synthetic W/D relationships for Poisson's ratio analysis are highlighted in different colors. (c,d) The estimated apparent Poisson's ratios with the uncertainties as the standard deviations.

4.5.1.3 Results

All DCs inside each cluster were transformed into VSZ profiles using the reference W/D relationship of the cluster (Figures 4.8a and b). These VSZ profiles were converted into interval VS profiles by applying equations (4.9) and (4.10). From the 11 DCs, 11 VS profiles were estimated and linearly interpolated to create a quasi 2D section of the VS. In Figure 4.9a, we show the estimated interval VS model with the sand body shape superimposed. The estimated VS shows lower velocity inside the loose sand region, as expected. In Figure 4.9a (black dots), we show the DC data points after the W/D transform, which can be considered as the vertical resolution of the data. Figure 4.9b shows the normalized uncertainty of the estimated 2D section of the S-wave velocity (Figure 4.9a). The uncertainties are

below 10 % in most regions except for the small portion below and inside the sand body, where it gets as high as 20%.

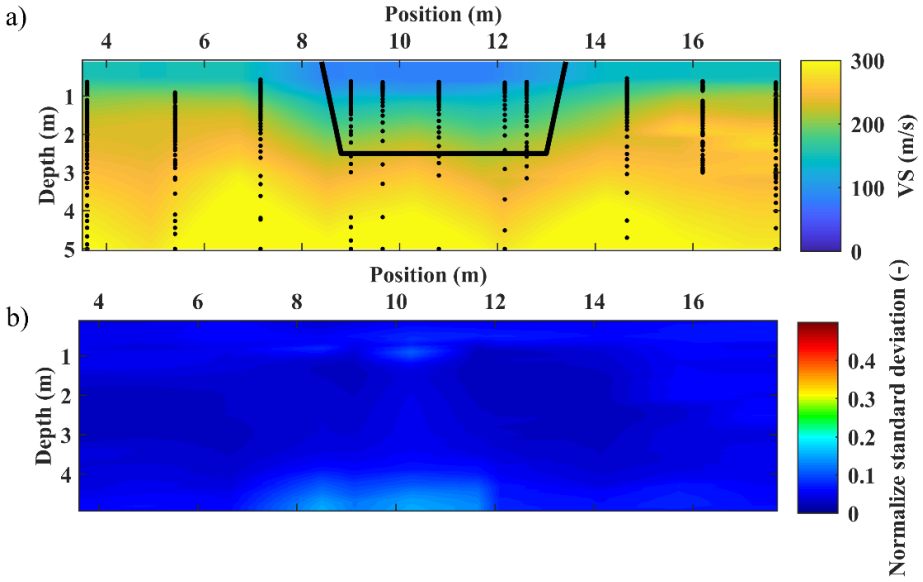

Figure 4.9: (a) The estimated quasi 2D VS model from the application of the W/D method to the CNR data set superimposed with the sand body; the black dots represent the DC data distribution along the profile. (b) The normalized uncertainty of the estimated VS model in (a).

We estimated the VP model (Figure 4.10a), following the method explained in section 4.2.4 and 4.2.5. In Figure 10b, we compare the estimated VP with the VP model obtained from a benchmark P-wave traveltime tomography (Khosro Anjom et al., 2019). At each point, the difference ε between these two models is calculated as:

$$\varepsilon = \frac{VP_{tomo} - VP_{WD}}{VP_{tomo}} \,. \tag{4.17}$$

In Figure 4.10c, we show the ε. In most parts of the 2D section, the difference between the estimated VP and the benchmark is less than 5%. The highest differences are registered at very shallow depths as well as at the bottom and below the sand body. The water table is not expected within the first 5 m of the site's subsurface, which is also confirmed by the depicted low P-wave velocities. We estimated the normalized uncertainty of the estimated VP (Figure 4.10d), following the method in section 4.3.2, which shows values of less than 10% except for parts of the sand body area.

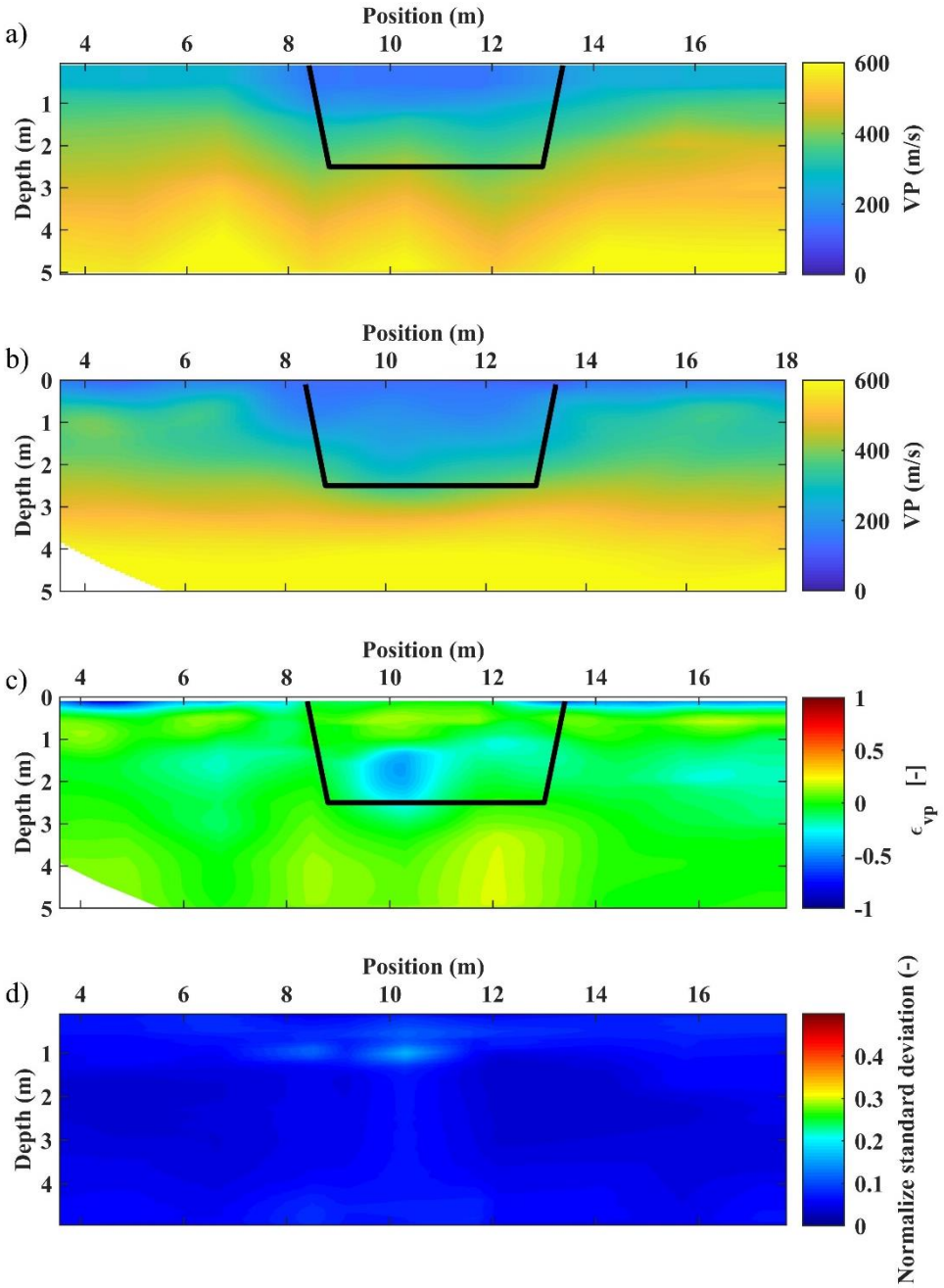

Figure 4.10: The estimated quasi 2D VP models from the application of the W/D method to the CNR data set compared with the benchmark VP from P-wave tomography: (a) Estimated VP model from the W/D method. (b) Benchmark VP from the P-wave traveltime tomography (Khosro Anjom et al., 2019). (c) The normalized difference between the models in (a) and (b) using equation (4.17). (d) The normalized uncertainty of the estimated VP from the W/D method in (a).

4.5.1.4 Full-waveform matching

In this section, using the estimated quasi 2D VS and VP models, we construct a full 3D model, representative of the site conditions, to numerically simulate the full-waveform propagation from the position of the sources and store the recordings at the position of the 72 receivers. These synthetic records are then compared with the observed (real) recordings for further evaluation of the results. Next, based on the similarity of the real and synthetic data, we investigate the possibility of using the estimated VS and VP models from the W/D method as the initial models for the FWI.

Full-waveform numerical simulations were performed using a 3D spectral-element method (Trinh et al., 2019). To construct the 3D simulation domain, we extended laterally the estimated 2D models to a 3D structure by symmetrically replicating the 2D section along the cross-line direction (y-direction). The extent of the sand body in the y-direction was kept equal to that observed one in the x-direction. Also, the models were extended laterally along the x-direction and in-depth, beyond the investigation limits of the method, with the aim of avoiding boundary artifacts during numerical simulations. The vertical extension was performed using a constant gradient, extrapolating the trend of the lower portion of the estimated models. In Figures 4.11a and c, we show the vertical sections of the extended VS and VP superimposed with the boundaries of the estimated VS and VP before the extension (dashed black line). In Figures 4.11b and d, we show the horizontal section of the 3D models at the surface, where the black line shows the position of the receivers along the main seismic line.

The model parameters required for the simulations are the estimated VP and VS, density, and quality factors (QP and QS). The density was assumed constant over the 3D space (1800 kg/m3), while QP and QS values were estimated from the velocity models according to Hauksson and Shearer (2006).

We performed the simulations considering the space and time numerical dispersion criteria. In agreement with the frequency band (10 -150 Hz) and velocity range (80 m/s – 1050 m/s), a mesh with a constant element size of 0.3 m (in the x, y, and z-direction) was used to honor the wavelength sampling and avoid numerical dispersion.

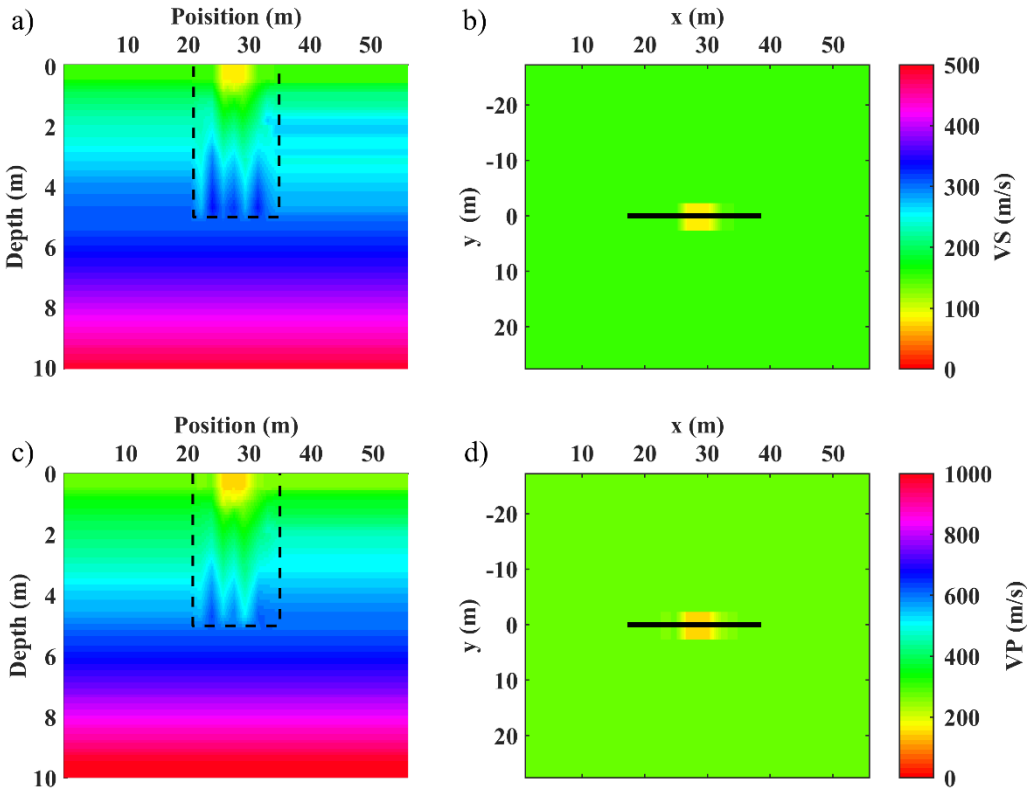

Figure 4.11: The extended estimated VS and VP models (from W/D method) of the CNR data set prepared for the full-waveform simulation. (a) The vertical section of the extended VS superimposed with the boundaries of the estimated VS before extension. (b) The horizontal section of the extended VS model at depth=0. (c) The vertical section of the extended VP superimposed with the boundaries of the estimated VP before extension. (d) The horizontal section of the extended VP model at depth=0 .

The simulation results together with the observed (real) records at one shot position (in Figure 3.1b, the 4th shot from left) are shown in Figure 4.12. The simulated data (in red) from the forward modeling show the same patterns of phases as the real data (in black), except for small diffracted phases. In Figures 4.12b and c, zoomed sections (shown as black boxes in Figure 4.12a) illustrate the in-phase shape of waveforms, which confirms the good accuracy of the estimated VS and VP models. Teodor et al. (2018) performed the similar approach to a synthetic data set similar to CNR geological properties. They applied the W/D method to the synthetic data to obtain the VS and VP models and then, they simulated the data based on the

estimated models. The true and simulated data well-matched except for the far-offset which exhibited small phase difference (figure 7 in Teodor et al., 2018).

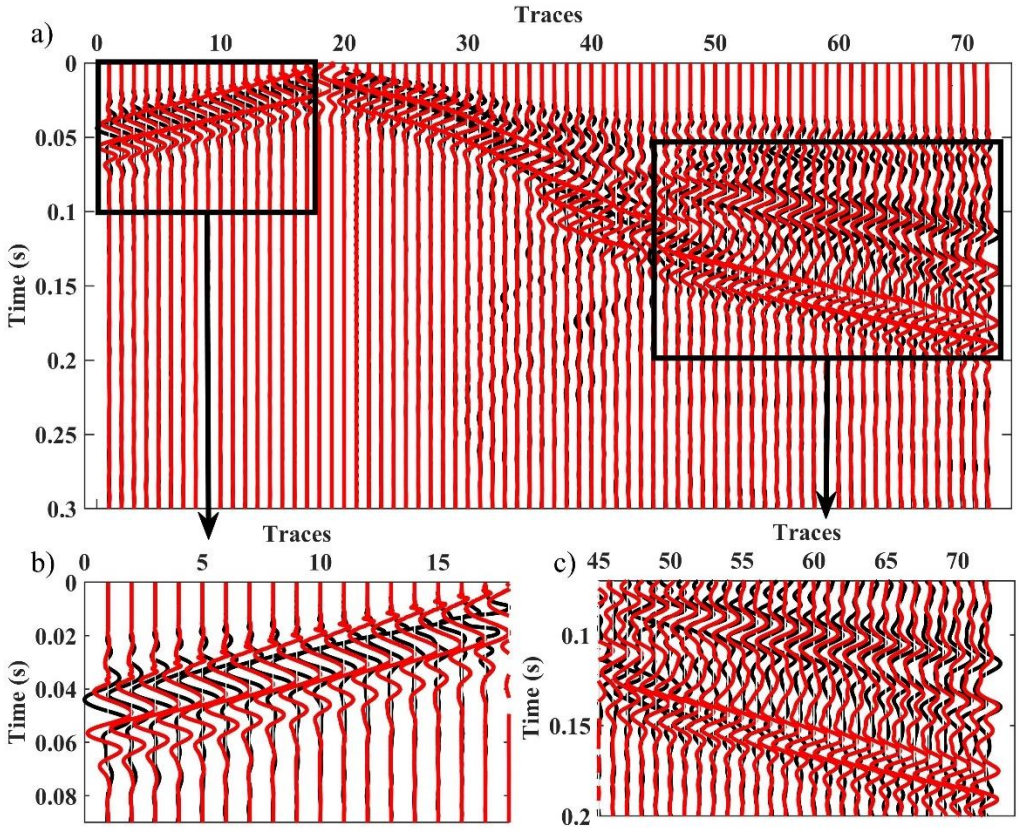

Figure 4.12: The comparison between the simulated and real data from one of the shot locations (4th shot from left in Figure 3.1b) of the CNR field test. In black, the traces of the recorded on the field. In red, the traces, for the same shot position, obtained by running forward simulations on the estimated VS and VP models from the application of the W/D method. (a) The whole recordings. (b) The zoomed view of the traces 0–17. (c) The zoomed view of the traces 45–72.

As further validation, DCs were extracted from the synthetic data and compared with those obtained from real data (Figure 4.13). Differences between phase velocities of these DCs were always less than 10%. In Figure 4.13, the two different phase velocity trends, inside and outside the sand body, can be observed both for the real DCs and those obtained from the simulated data.

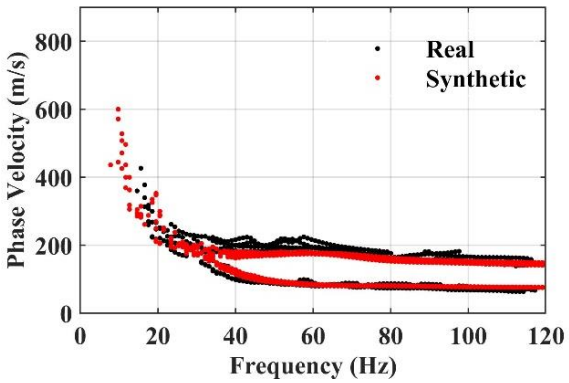

Figure 4.13: Comparison between the experimental DCs of the CNR data set and the DCs from synthetic seismograms of numerical simulations.

Cross-correlation between real and synthetic data can be a fair criterion for the goodness of the full-waveform matching, especially when cycle-skipping effects are considered. In Figure 4.14, we show the results of the cross-correlation of the synthetic and real recordings from Figure 4.12, where the solid red line shows the zero-time lag. To avoid the cycle-skipping in the FWI process, the error in matching the real and synthetic data should fall below half-the-period of the dominant frequency (Virieux and Operto, 2009). For CNR data set, at a dominant frequency of 60 Hz, the half-period corresponds to 8.33 ms. It can be observed in Figure 4.14 that the short-offset traces (0 to 52) show lower time-lag than half-the-period, while long offset traces (52 to 72) show a time lag higher than 8.33 ms, leading to possible cycle-skipping problems, relevant to long offsets and arrival times greater than 0.12 s (see Figure 4.12c). The high-frequency surface waves generated from the source are highly affected by the low velocity inside the sand body before reaching receivers 52 to 72; slight errors in the velocity or the sand body's size significantly affect the arrival time of the high-frequency phases. These effects, related to the interaction of the wavefront with the sand body anomaly, can be mitigated by hierarchical strategies from low-to-high frequencies and short offsets to large offsets. Dedicated FWI strategies should be designed for overcoming these cycle-skipping issues.

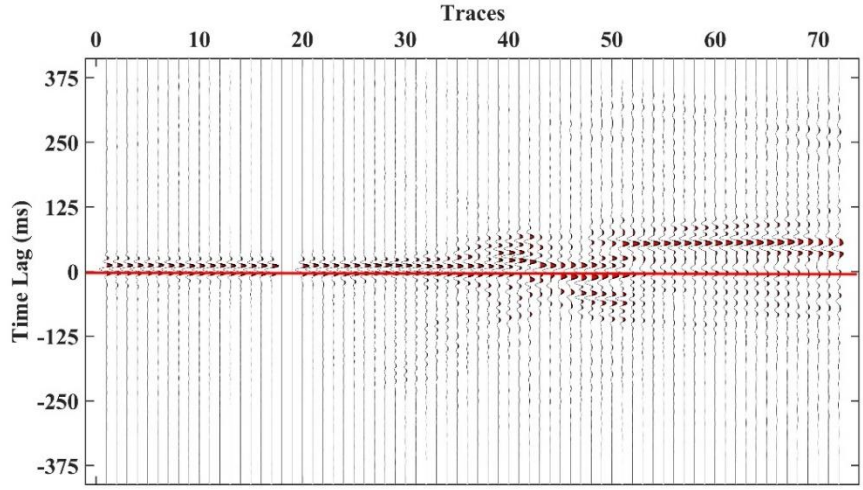

Figure 4.14: The cross-correlation of the experimental and synthetic data from Figure 4.12a.

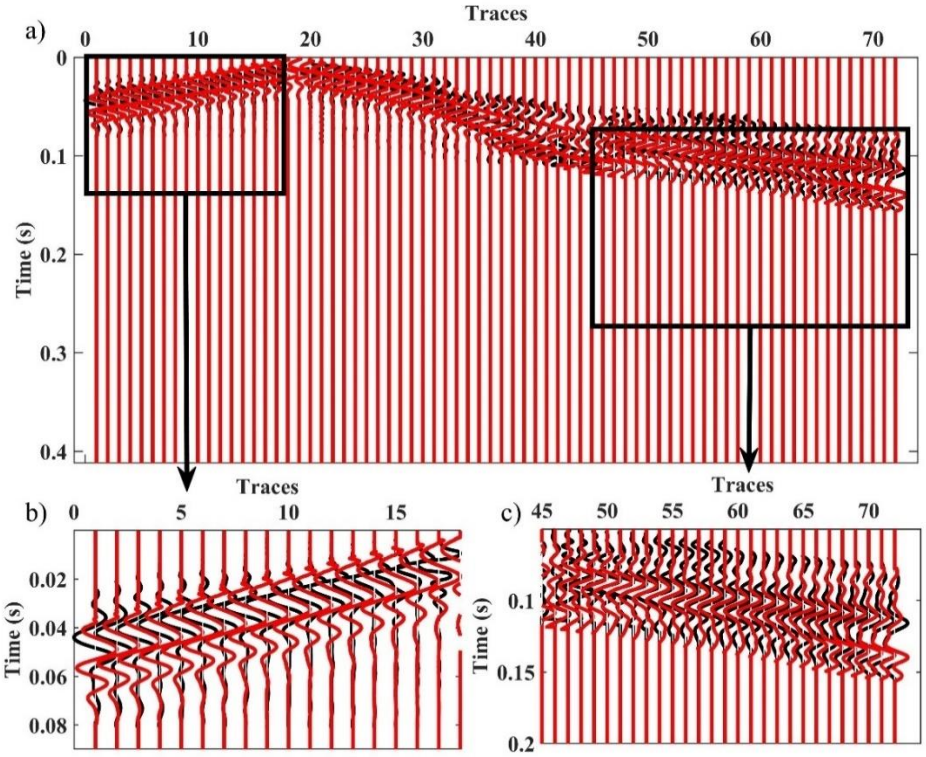

Figure 4.15: Full waveform comparison of the data from Figure 4.12 after muting. In black, the muted traces of the recorded on the field; In red, the traces, for the same shot position, obtained by running forward simulations on the 3D estimated VP and VS models and muted afterward. (a) The whole recordings. (b) Zoomed view of traces 0 to 17. (c) Zoomed view of traces 45 to 72.

As an illustration of such hierarchical strategy, we muted the out of phase portion of the recordings at far offsets. In Figure 4.15a, the muted real and synthetic recordings are shown in black and red. The muting impact on the cycle-skipping is illustrated by the cross-correlation of real and synthetic recordings in Figure 4.16. The cross-correlation shows an acceptable time-lag for the whole seismogram considering the recordings' main frequency as 60 Hz.

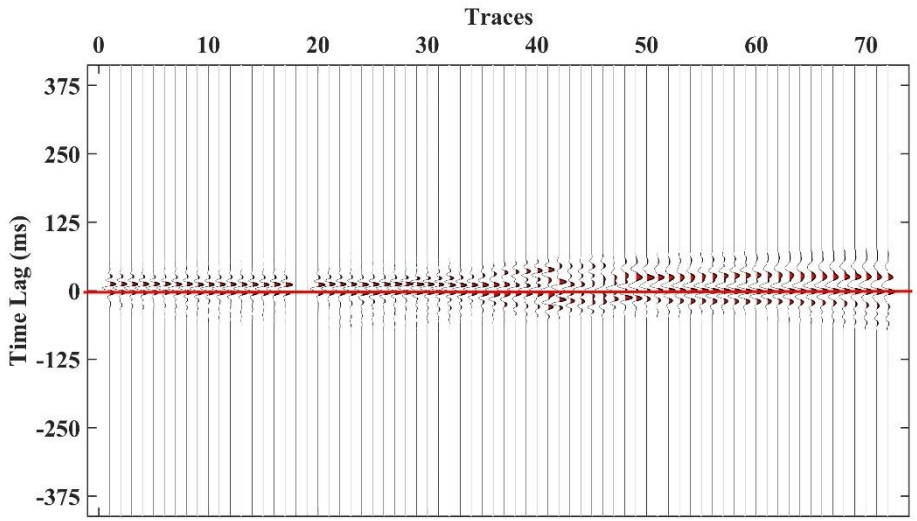

Figure 4.16: *The cross-correlation of the muted experimental data with the muted synthetic from Figure 4.15a.*

Teodor et al. (2021) compared the use of different initial models, including the estimated models from W/D method (Figures 4.9a and 4.10a), for the FWI of the CNR data. They concluded that the use of the initial models from W/D method significantly improves the final results of the inversion; the extent and velocities of sand body area were better resolved.

4.5.2 Aurignac

4.5.2.1 Local DC estimation

The classical 3D data sets usually consist of multiple parallel and perpendicular acquisition lines. The phase-shift processing method can be separately applied to various seismic lines to estimate reliable local DCs at different locations. For full 3D data sets, such as the Aurignac data set, the receivers aligned with the sources can be located, and the estimated DCs can be assigned to the center of the receiver arrays. However, application to a full 3D data set can lead to significant inconsistencies between the adjacent estimated local DCs: A DC at a particular

position can be obtained from receiver arrays with various azimuthal angles aligned with sources; the propagation paths from different angles can result in very different DCs. To better show this issue, we compare the estimation of local DC at a specific location of the Aurignac data set (green cross in Figure 4.17a) from two receiver arrays representing different angles (highlighted in blue and red in Figure 4.17a). The estimated DCs corresponding to the same location are more than 15% different in terms of phase velocity for the whole frequency band (Figure 4.17b). The two arrays have a single intersection point and a completely different surface wave propagation path, which leads to this significant difference.

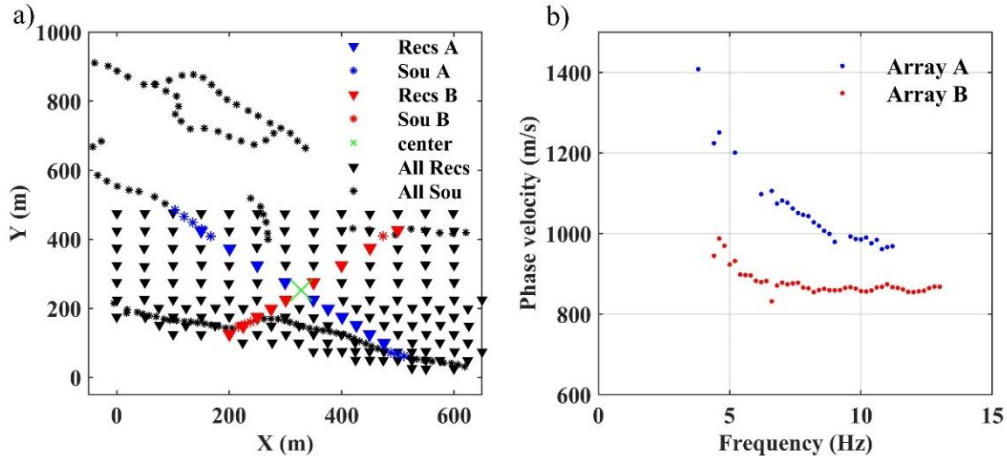

Figure 4.17: Two example receiver arrays from Aurignac data set to obtain the DC at the same location.(a) The acquisition layout in the north-west of the Aurignac data set. Two selected receiver arrays and shot locations highlighted in blue and red used to separately estimate the DC at the location of green cross. (b) The estimated fundamental mode DCs from the two sets of recordings from the receiver arrays in (a) using the phase-shift method.

To resolve arrays directionality for 3D data sets, we consider areal receiver spread instead of linear spreads. For each DC estimation, we select the receivers inside a square area, and we consider the recordings from sources within a specific range distance from the center of the square. We use the phase-shift method to estimate the DC, and we assign it to the center of the receiver spread. We estimate DCs corresponding to different locations by sliding the square.

For the Aurignac data set, we selected the receivers inside a 100×100 m^2 square and considered sources within 250 m from the square's center. We slid the square by one inter receiver distance to maximize the number of the estimated DCs. In the northern part of the field, the inter-receiver distance was 50 m, while this value was

25 m in the southern parts. We processed separately the two sub data sets (north-west and south-west) from the outside of mining pits to minimize the effect of the elevation difference on the propagation of surface waves from the north to the south and vice versa. Figure 4.18 shows two estimations of the fundamental mode DCs from the north-west area using the adopted DC estimation workflow. In Figures 4.18a and c, we show the selected receivers and sources. We stacked the computed spectra from different source locations to increase the signal-to-noise ratio. In Figures 4.18b and d, we show the obtained spectra and the fundamental mode corresponding to the records from the selected shots in Figures 4.18a and c. In Figure 4.18d, the excitation of at least one higher mode of the surface wave is evident. We only consider the fundamental modes of the DCs for the application of the W/D method.

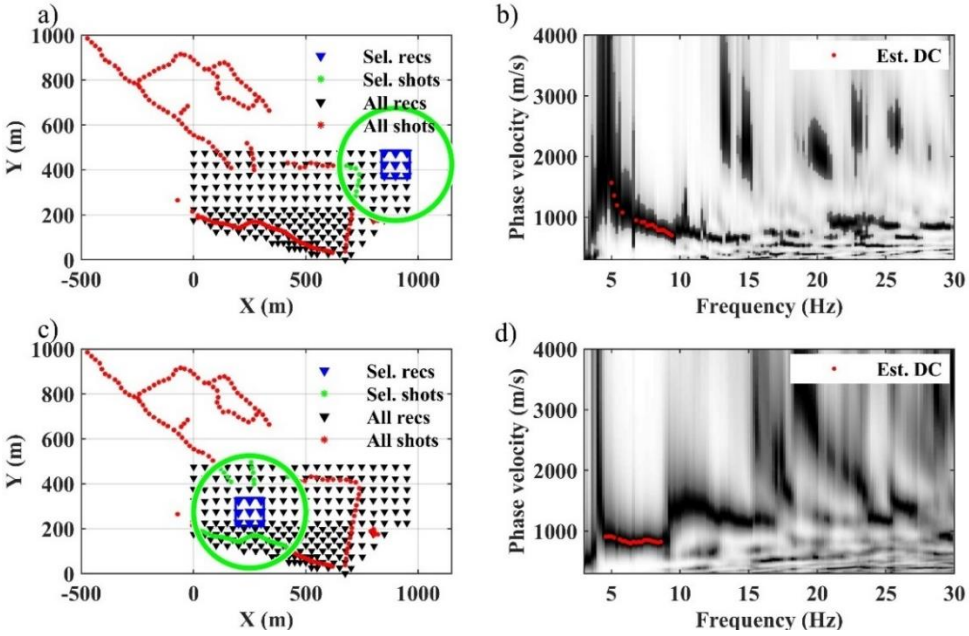

Figure 4.18: The example estimations of the fundamental mode of the surface waves for the Aurignac data set. (a,c) The selected receiver and sources for the phase-shift transform. (b,d) The estimated spectra and fundamental modes corresponding to the selected recordings in (a) and (c), respectively.

In total, we estimated 545 fundamental mode DCs for the considered two zones. In Figure 4.19a, we show the estimated DCs as a function of frequency. The next step from the W/D workflow is the clustering of DCs. The clustering algorithm requires DCs with a common frequency band. We excluded the short banded DCs from the clustering algorithm, but not the whole workflow, to increase the common band between the DCs. The circles in Figure 4.19b show the DCs used for the clustering

and the colors distinct the two obtained cluster. Based on the spatial location of the obtained clusters, we assigned the previously excluded DCs to the clusters. The DCs of the western cluster (cluster A shown in blue) presented lower phase velocities compared to the eastern DCs (cluster B shown in green).

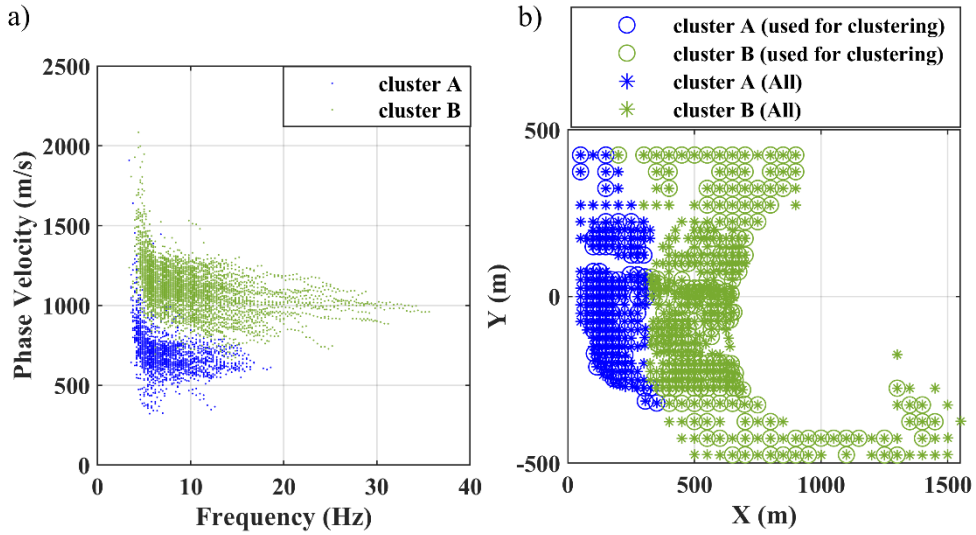

Figure 4.19: The estimated DCs and clustering of the Aurignac data set. (a) The estimated DCs, where the colors of obtained clusters in (b) are used to distinct the two velocity trends. (b) The spatial view of the obtained clusters. The circles present the DCs used for the clustering algorithm. The asterisks show all DCs divided into two clusters based on the spatial location of the two clusters.

To analyze the wavelength coverage of the estimated DCs, in Figure 4.20, we plot the pseudo-slices within different wavelength ranges, where the color scale shows the average phase velocity within the wavelength range. A limited portion of data are available for wavelengths below 40 m (Figure 4.20a). The coverage increases for the wavelengths above 40 m until it reaches the maximum at 160 to 220 m (Figure 4.20e). Then, the coverage declines. The velocity contrast detected by the clustering algorithm between the west and east of the area can be seen in the pseudo-slices in Figure 4.20.

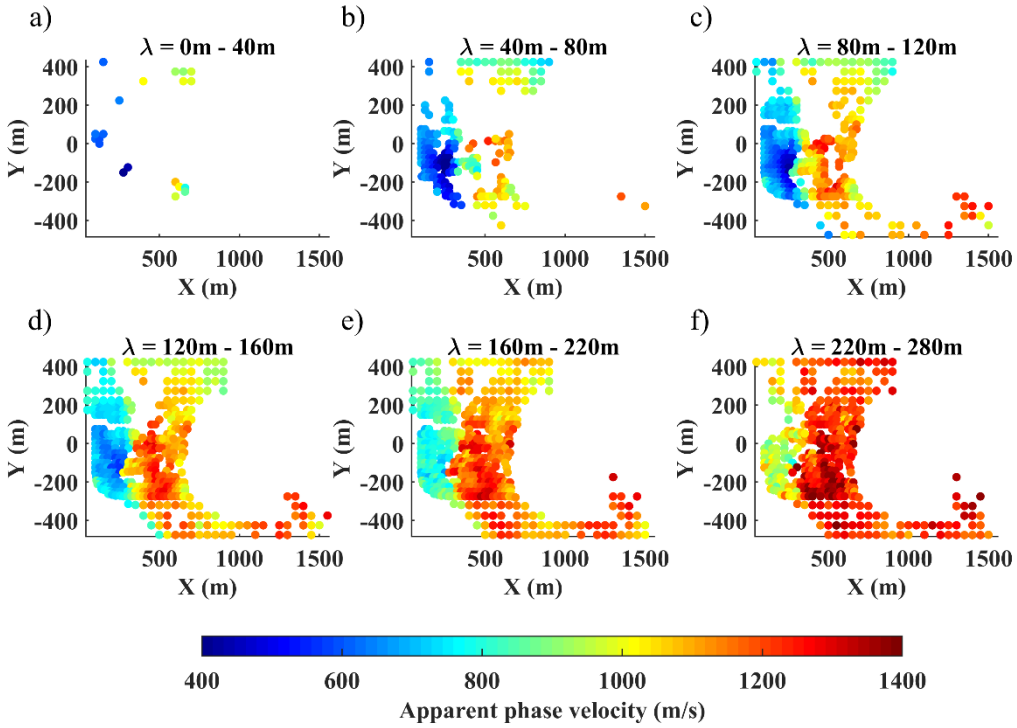

Figure 4.20: Wavelength coverage of the estimated DCs for the Aurignac data set plotted as pseudo-slices within different wavelength ranges: (a) 0 to 40m. (b) 40 to 80 m. (c) 80 to 120 m. (d) 120 to 160 m. (e) 160 to 220 m. (f) 220 to 280 m.

4.5.2.2 The reference W/D and apparent Poisson's ratios

Amongst the DCs of each cluster, a reference DC was selected as the reference DC. In Figures 4.21, we show the steps of estimating the reference W/D relationship and apparent Poisson's ratio for cluster A. We inverted the reference DC of cluster A (Figure 4.21a) using the MCI; we considered variable Poisson's ratio between 0.1 and 0.45 and a vast model space for the VS. We used density of 2000 kg/m^3 for the first layer and constant density of 2200 kg/m^3 for the rest of the layers. We imposed a 0.05 level of confidence for the Fisher test to select the best fitting models. Figure 4.21a shows the reference DC of cluster A with phase velocity uncertainty estimated from the seismic data and the synthetic DCs corresponding to the selected VS models in Figure 4.21b. The selected and reference VSZ models are shown in Figure 4.21c. We used the reference VSZ and experimental DC to estimate the W/D relationship in Figure 4.21d. Then, we estimated the reference apparent Poisson's ratio (Figure 4.21e), following the method explained in sections 4.2.4. In Figures 4.21d and e, we also show the uncertainty associated with the reference W/D and

apparent Poisson's ratio of the cluster A, following the steps explained in section 4.3.1.

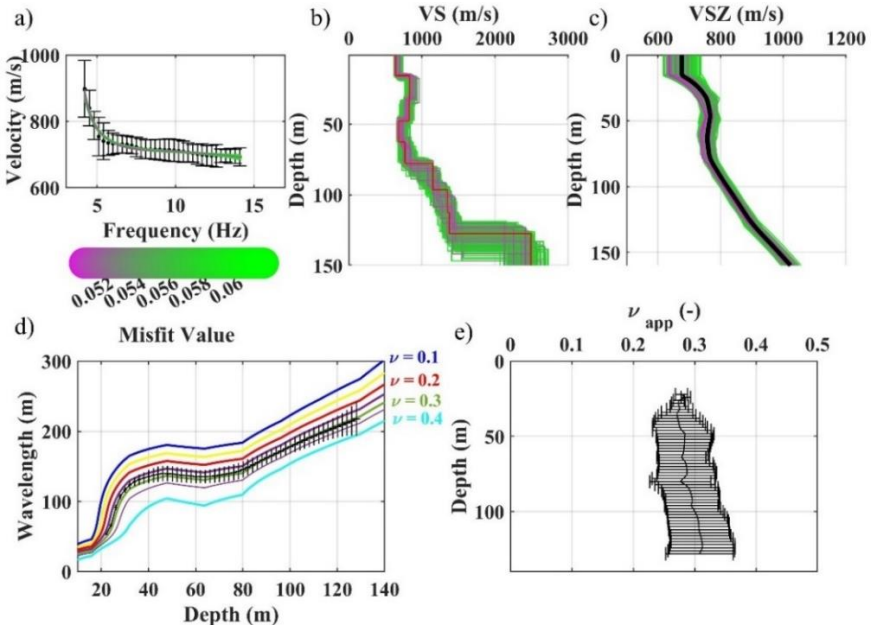

Figure 4.21: The steps of estimating the reference W/D relationship and apparent Poisson's ratio of the Aurignac data set for the area labeled as ***cluster A*** *in Figure 4.19b. (a) The reference DC with the uncertainty and the synthetic selected DCs from the MCI. (b) The selected VS models from the MCI. (c) The selected VSZ models from the MCI; the solid black line is the reference VSZ model computed by averaging the selected VSZ models. (d) Estimated reference W/D relationship in black with the vertical and horizontal bars showing the depth and wavelength standard deviations. The colored W/D relationships are the synthetic ones, each with constant Poisson's ratio, used for Poisson's ratio sensitivity analysis. (e) The estimated reference apparent Poisson's ratio with the standard deviation at each depth.*

In Figure 4.22, we show the steps of estimating the W/D relationship and apparent Poisson's ratio for cluster B in the same order explained for cluster A. The uncertainties of the estimated W/D relationship and apparent Poisson's ratio of cluster A are higher than the observed ones for cluster B. This is mainly due to the higher uncertainties of the reference DC of cluster A (Figure 4.21a) compared to cluster B (Figure 4.22a). The depth range of the estimated W/D relationship and apparent Poisson's ratio for cluster A are limited to 20 to 128 m (Figures 4.21d and e), while the depth ranges are increased to 20 to 140 m for cluster B (Figures 4.22d and e): The higher phase velocities of DCs of cluster B resulted in larger wavelengths, providing a deeper subsurface investigation depth.

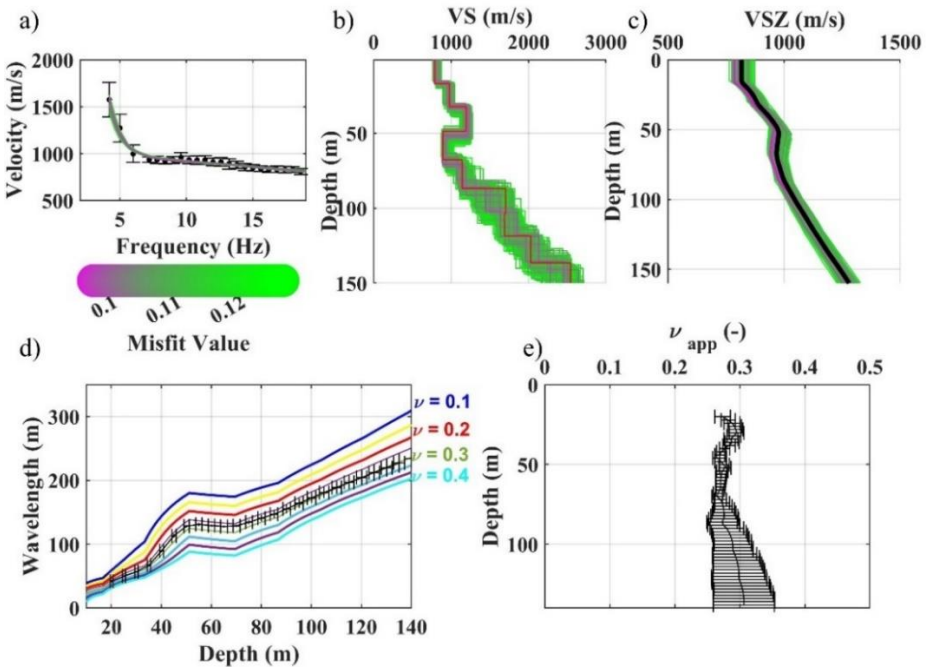

Figure 4.22: The steps of estimating the reference W/D relationship and apparent Poisson's ratio of the Aurignac data set for the area labeled as ***cluster B*** *in Figure 4.19b. (a) The reference DC with the uncertainty and the synthetic selected DCs from the MCI. (b) The selected VS models from the MCI. (c) The selected VSZ models from the MCI; the solid black line is the reference VSZ model computed by averaging the selected VSZ models. (d) Estimated reference W/D relationship in black with the vertical and horizontal bars showing the depth and wavelength standard deviations. The colored W/D relationships are the synthetic ones, each with constant Poisson's ratio, used for Poisson's ratio sensitivity analysis. (e) The estimated reference apparent Poisson's ratio with the standard deviation at each depth.*

4.5.2.3 Results

We estimated the 1D VSZ models from the local DCs of each cluster, thanks to the W/D relationships in Figures 4.21d and 4.22d. Then, we used equation (4.9) and (4.10) to estimate the interval VS models at every 10 cm depth step. In Figure 4.23a to i, we show the horizontal slices of the estimated local VS models averaged over the depth intervals indicated on top of each plot. Also, the 1D VS models at every 10 cm steps were laterally interpolated (linear) to form the quasi 3D model in Figure 4.23j. In Figure 4.23k, we show the isosurfaces of the estimated VS model at various plains in x, y, and z directions, which was obtained from the quasi 3D model in Figure 4.23j.

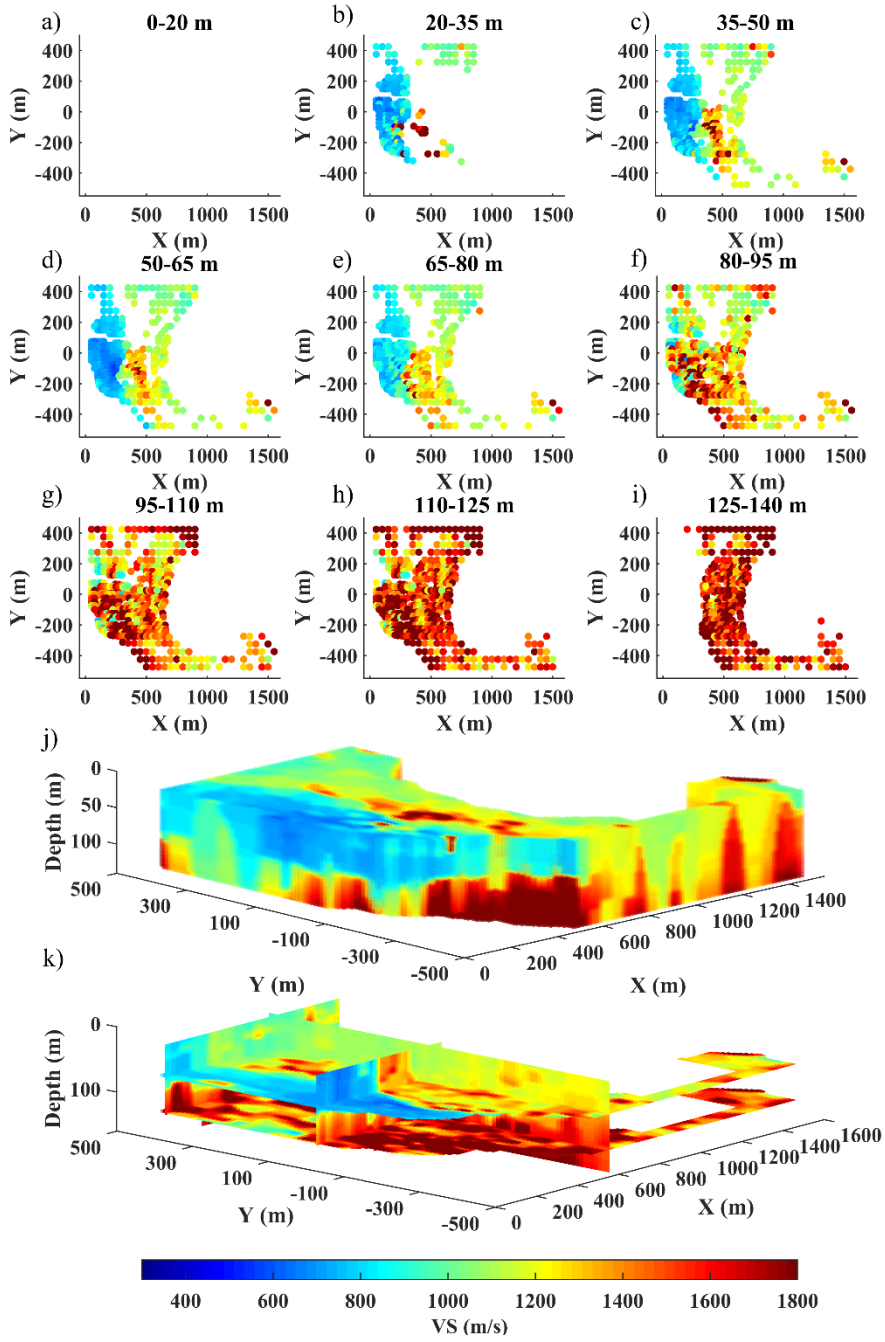

Figure 4.23: The estimated VS model for the Aurignac site using the W/D method. (a to i) The horizontal slices within various depth intervals indicated on top of each figure. (j) The pseudo 3D view of the estimated VS after linear interpolation of the 1D models. (k) Isosurfaces obtained from the 3D model in (j) at plains x=600 m, y=0 and 400 m, and z=70 and 125 m.

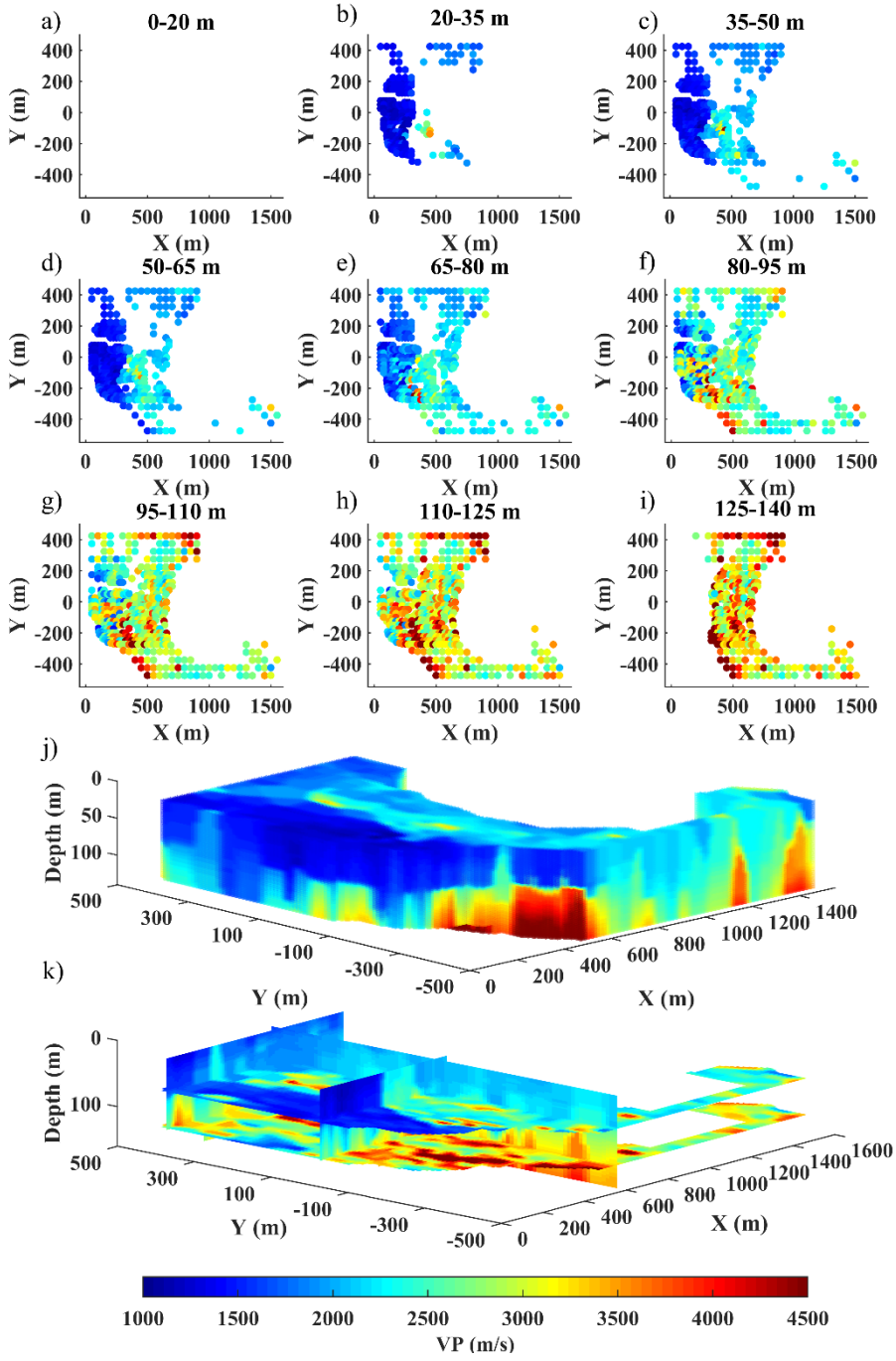

Figure 4.24: The estimated VP model for the Aurignac site using the W/D method. (a to i) The horizontal slices within different depth intervals indicated on top of each figure. (j) The pseudo 3D view of the estimated VP after linear interpolation of the 1D models. (k) Isosurfaces obtained from the 3D model in (j) at plains x=600 m, y=0, and 400 m, and z=70 and 125 m.

Using equation (4.5) and thanks to the reference Poisson's ratio of the two clusters (Figures 4.21e and 4.22e), we transformed the estimated 1D VSZ models into VPZ models. Then, we transformed the VPZ model into interval VP models (equations 4.9 and 4.10). In Figures 4.24a to i, we show the horizontal slices of the interval VP models within the same depth interval as shown in Figures 4.23a to i. Similar to the estimated 1D VS models, we linearly interpolated the 1D VP models to obtain the pseudo 3D view in Figure 4.24j. In Figure 4.24k, we show the isosurfaces of the estimated VP model obtained from Figure 4.24j. The estimated VS and VP models do not contain velocity values between 125-140 m for the west side (Figures 4.23i and 4.24i), since the W/D relationship and apparent Poisson's ratio of the cluster A provided estimations only up to the depth 128 m (Figures 4.21d and e). The estimated VS and VP models show a significant velocity contrast between the east and west. However, this contrast reduces in the deeper portion of the model.

We estimated the associated uncertainty to the estimated VS and VP models, following the method explained in section 4.3. In Figure 4.25 and 4.26, we show the 3D view of the normalized standard deviation for the estimated VS and VP models, respectively. In the majority of the 3D volume, the uncertainty is lower than 15%. However, for both models, the uncertainty of the west side is higher than the east; this is mainly because of the more complex geology of the west side which led to higher uncertainties of the DCs.

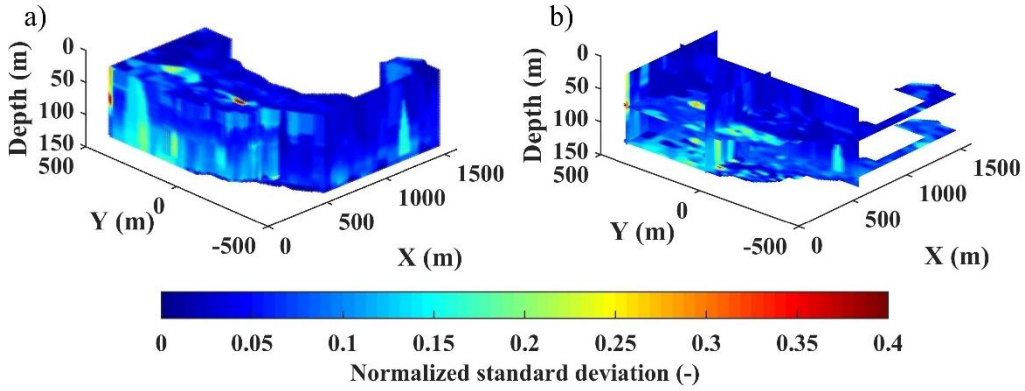

Figure 4.25: The normalized standard deviation of the estimated VS model for Aurignac site using the W/D method (Figure 4.23). (a) The pseudo 3D representation of the standard deviations. (b) the isosurfaces obtained from the 3D plot in (a) at plains x=600 m, y=0 and 400 m, and z=70 and 125 m.

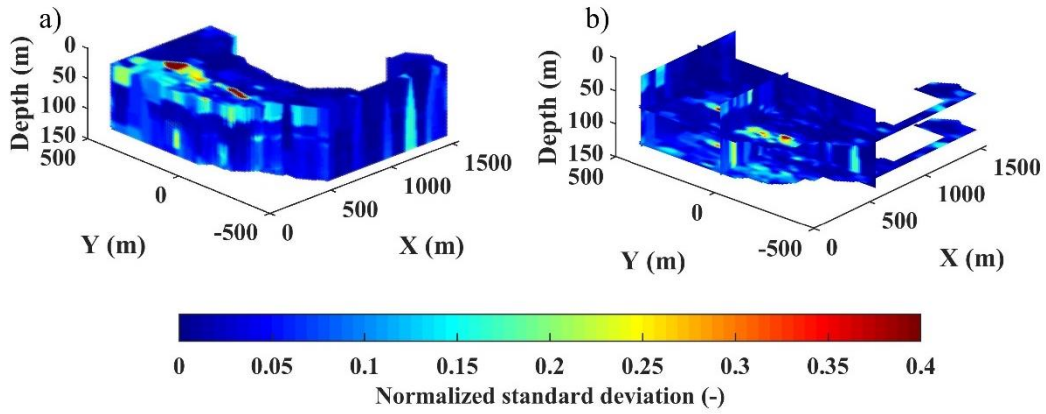

Figure 4.26: The normalized standard deviation of the estimated VP models for the Aurignac site using the W/D method (Figure 4.24). (a) The pseudo 3D representation of the standard deviations. (b) The isosurfaces obtained the 3D plot in (a) at plains x=600 m, y=0 and 400 m, and z=70 and 125 m.

4.5.3 Oil and gas exploration data set

4.5.3.1 Local DC estimation and clustering

The local DCs along the seismic 2D line were estimated by Karimpour (2018) in the *f-k* domain using the method proposed by Bergamo et al. (2012). The data were spatially windowed using Gaussian windows prior to wavefield transform. A DC for every 60 m of the 12 km 2D seismic line was estimated, giving a total of 198 DCs. A quality control method was used to locate the noisy and possibly erroneous DCs. 52 DCs were considered low quality, and they were discarded from the data. For more information regarding the estimation of the DCs and the quality control, please see Karimpour (2018). In Figure 4.27a, we show the estimated DCs as a function of frequency. The clustering of the DC data suggested two groups of DCs (dendrogram in Figure 4.27b). We show the spatial location of the clustered DCs in Figure 4.27c. The outlier DC (In Figure 4.28c at the position of around 5000 m) was removed from the DC data. In Figure 4.27a, the two trends of the DCs (cluster A and B) are distinct with different colors.

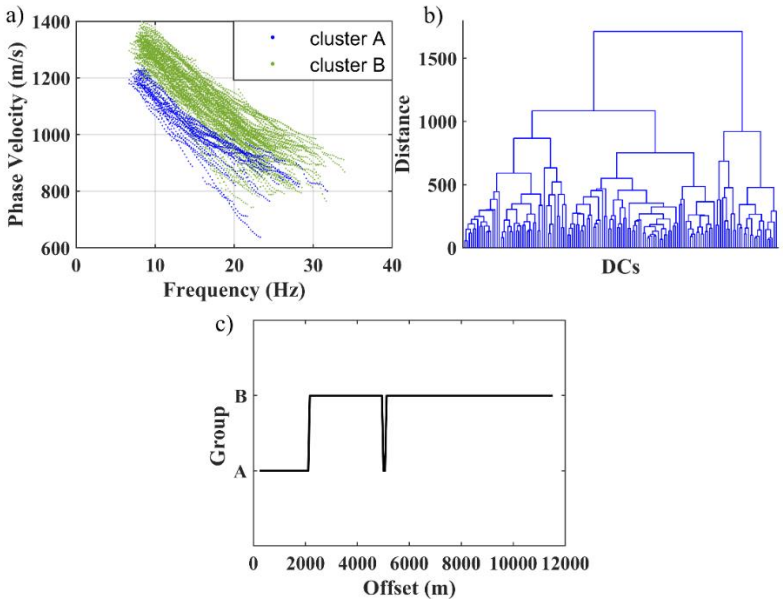

Figure 4.27: (a) The estimated DCs for oil and gas exploration data set using f-k wavefield method. The color scale separates the two clusters obtained in (b) and (c). (b) The dendrogram showing the clustering of the DCs in (a); two main clusters are detected. (c) The spatial location of the two clusters obtained from (b).

In Figure 4.28a, we show the pseudo-section of the estimated local DCs along the seismic line, where the y-axis and the color scale show the wavelength and phase velocity of the DCs, respectively. A significant change in the trend of the DCs can be seen at an approximated position of 2000 m; the DCs between 0 to 2000 m show lower phase velocities compared to the rest of the line, which was detected also by clustering algorithm (Figure 4.27c).

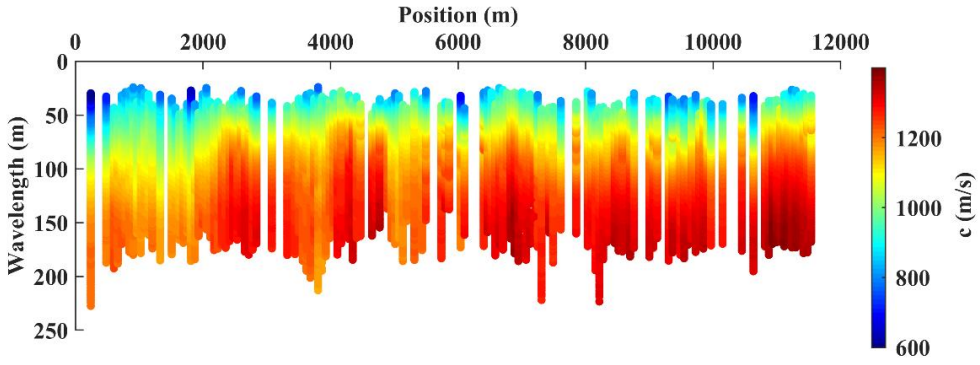

Figure 4.28: Pseudo-section of the estimated DCs for the oil and gas exploration data set. The y-axis and the color scale are the wavelength and phase velocity of the local DCs, respectively.

4.5.3.2 The reference W/Ds and apparent Poisson's ratios

For each cluster, we selected the reference DC based on the quality control performed by Karimpour (2018). In Figure 4.29 and 4.30, we show the steps of estimating the W/D relationship and apparent Poisson's ratio for clusters A and B, respectively. The velocity contrast between the west side and east side of the seismic line can also be observed by comparing the *VS* results of the MCI inversion for the cluster A and B (Figures 4.29b and 4.30b).

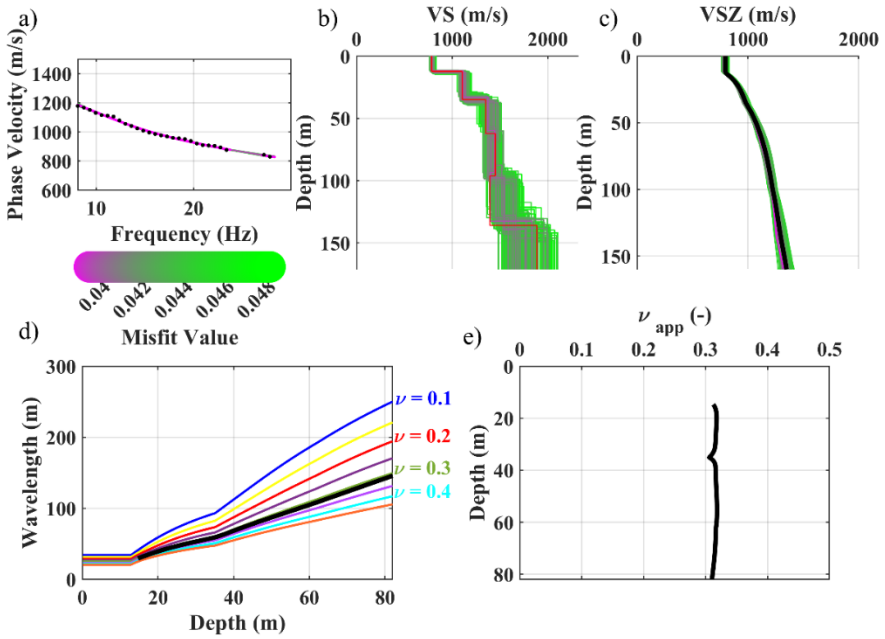

Figure 4.29: The steps of estimating the reference W/D relationship and apparent Poisson's ratio of the oil and gas exploration data set for the locations labeled as ***cluster A*** *in Figure 4.27c. (a) The reference DC and the synthetic selected DCs from the MCI. (b) The selected VS models from the MCI. (c) The selected VSZ models from the MCI; The solid black line is the reference VSZ model computed by averaging the selected VSZ models. (d) Estimated reference W/D relationship in black. The colored W/D relationships are the synthetic ones, each with constant Poisson's ratio, used for Poisson's ratio sensitivity analysis. (e) The estimated reference apparent Poisson's ratio.*

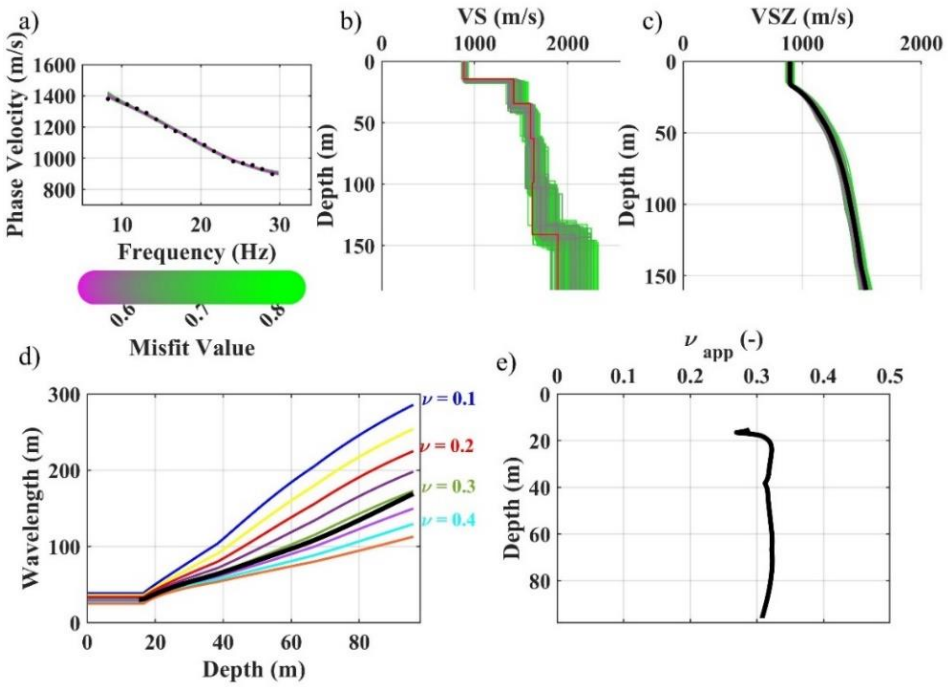

Figure 4.30: The steps of estimating the reference W/D relationship and apparent Poisson's ratio of the oil and gas exploration data set for the locations labeled as ***cluster B*** *in Figure 4.27c. (a) The reference DC and the synthetic selected DCs from the MCI. (b) The selected VS models from the MCI. (c) The selected VSZ models from the MCI; The solid black line is the reference VSZ model computed by averaging the selected VSZ models. (d) Estimated reference W/D relationship in black. The colored W/D relationships are the synthetic ones, each with constant Poisson's ratio, used for Poisson's ratio sensitivity analysis. (e) The estimated reference apparent Poisson's ratio.*

4.5.3.3 Results

In Figure 4.31a, we show the estimated VS models at the location of the local DCs using the method explained in sections 4.2.3 to 4.2.5. In Figure 4.31b, we compare the estimated VS with the VS model by CGG using "*surface wave 1D inversion*" (Masoni, 2016). Both estimated VS models show significant lateral variation at approximately position 2000 m. However, the VS model from the surface wave 1D inversion presents lower VS compared to the model from W/D method. Moreover, the estimated VS model from W/D method presents more lateral and vertical variability for the investigated area.

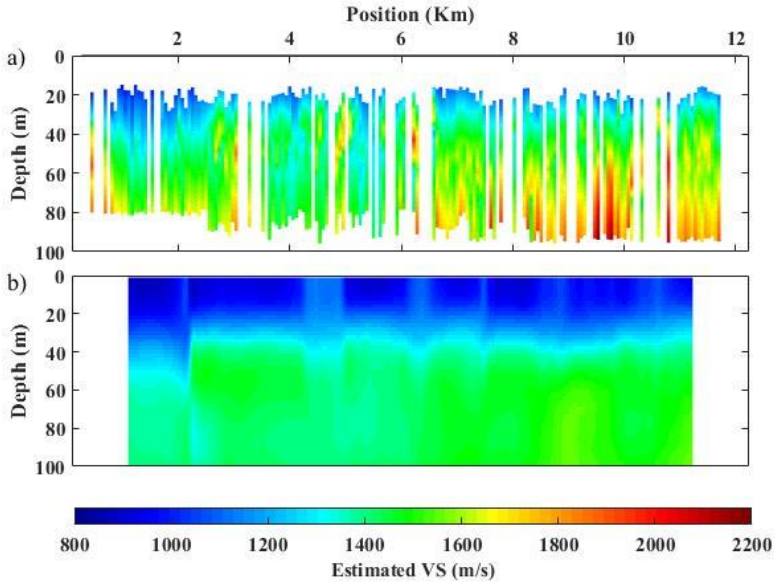

Figure 4.31: Estimated VS models for the oil and gas exploration data set using: (a) W/D method. (b) surface wave 1D inversion performed by CGG (reproduced from Masoni, 2016).

We also estimated the VP model following the method described in section 4.2.5. In Figure 4.32, we compare the estimated VP model from the W/D method (Figure 4.32a) with the VP model obtained by Masoni (2016) using P-wave traveltime tomography (Figure 4.32b).

The VP from the W/D method shows the same lateral discontinuity also observed by the estimated VS model. The VP from W/D method (Figure 4.32a) shows higher resolution of the lateral and vertical variability compared to the model from P-wave traveltime tomography.

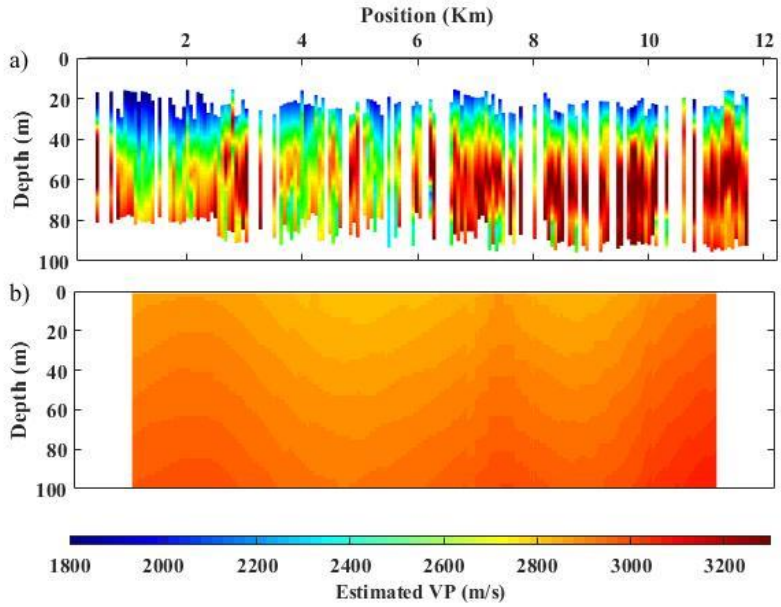

Figure 4.32: Estimated VP models for the oil and gas exploration data set (a) using the W/D method. (b) P-wave traveltime tomography (reproduced from Masoni, 2016).

4.6 Conclusion

We showed the application of the W/D method to three data sets to estimate the near-surface VS and VP models. The adopted hierarchical clustering of the DCs well detected the lateral discontinuities of the sites, which enables the method's application in the presence of sharp lateral variations. We reformulated the relationship between time-average velocity and interval velocity (equation 4.9), and by including total variation regularization (equation 4.10), we reached a stable mechanism to estimate the interval VS and VP models. Being the W/D method a direct transformation technique, the noise in DCs is inherently propagated to the estimated VS and VP models. We developed a method to compute the uncertainty of the estimated VS and VP models from the experimental uncertainty of the data. For the CNR data set, the comparison between field records and synthetic waveforms computed from the obtained velocity model showed a very good agreement. This makes the W/D data transform method a good candidate for a fast estimate of initial velocity models to be used in FWI.

5. Monte Carlo joint inversion

We develop a Monte Carlo joint inversion method to estimate high-resolution VS and VP models. While DCs are mainly sensitive to the VS model, W/D relationships are sensitive also to Poisson's ratio and VP. We perform the joint inversion in a Monte Carlo's scheme, based on two minimization objectives: (1) DC misfit. (2) W/D misfit. In the following, we explain the method. Then, we show its application to two synthetic examples and La Salle field data set. In the second synthetic example, we evaluate the performance of the proposed method in water saturated loose environment characterized by high Poisson's ratio. The proposed method is published in Khosro Anjom et al., (2018) and also its E-lecture is available on EAGE website (Khosro Anjom et al., 2021).

5.1 Method

The inputs of the method are the experimental W/D relationship and DC at the same location. In smooth laterally varying sites, where the DCs can be considered as a single cluster, the experimental W/D relationship is not expected to change drastically at different locations. As a result, the W/D relationship of the close-by positions can be used at the location of the joint inversion. We estimate the experimental W/D relationship following the MCI method explained in section 4.2.2. In Figure 5.1, we show the workflow of the joint inversion.

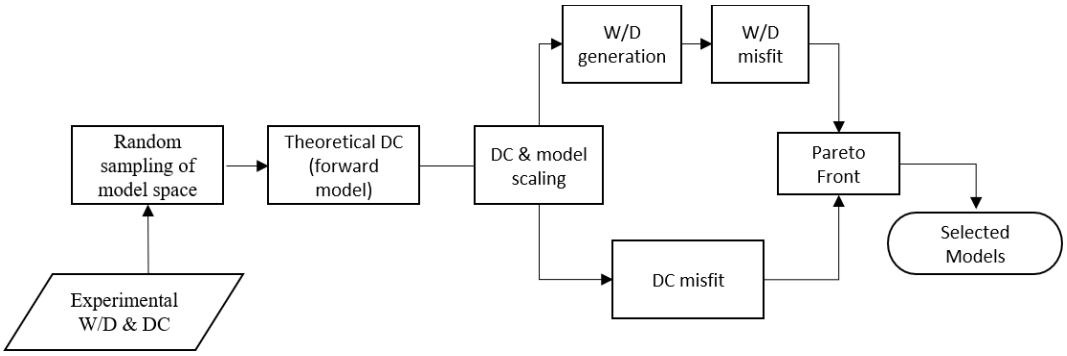

Figure 5.1: The Monte Carlo joint inversion workflow. The inputs of the workflow are the experimental DC and W/D relationship, while the outputs are a set of selected VS and VP models.

We consider both VS and VP as targets of the inversion. So, a set of VS models, thicknesses, and Poisson's ratios are uniformly sampled within the boundaries of the model space, which are chosen a priori. The number of layers selection involves a compromise between defining the system properly and the model over-parameterization. The unknowns of the inversion increase almost linearly with the number of layers. As a result, the number of the randomly sampled model should increase when more layers are considered. We consider a fixed density profile for the inversion, based on the geological information from the site. The DC for each randomly generated model is calculated using Haskell and Thomson DC forward model. At this stage, the random VS models are automatically optimized (scaled), thanks to the scaling property of the DCs explained in section 2.3.3.2. The scaling adjusts the randomly sampled models to better-fitting models and minimizes the impact of possible poor model space boundary selection. We use theoretical DCs and corresponding VSZ models to obtain theoretical W/D relationships. Next, we compute the misfit of the theoretical W/D relationships and DCs with respect to the experimental ones. Given the different units of the two misfits (i.e., velocity for DC and wavelength for WD), we consider normalized misfit. We estimate the misfits for the DCs and W/Ds as:

$$Q_{DC} = \frac{\sum_{i=1}^{l_{DC}} \left(\frac{c_{\exp,i} - c_{syn,i}}{c_{\exp,i}} \right)^2}{l_{DC} - (3n+2)}, \text{ and} \tag{5.1}$$

$$Q_{WD} = \frac{\sum_{i=1}^{l_{WD}} \left(\frac{\lambda_{\exp,i} - \lambda_{syn,i}}{\lambda_{\exp,i}} \right)^2}{l_{WD} - (3n+2)}, \tag{5.2}$$

where n is the number of the layers (half-space excluded). So, $3n + 2$ corresponds to the number of VS, Poisson's ratio, and thickness unknowns. l_{DC} and l_{wd} are the number of data points of the experimental DC and W/D. The $c_{\exp,i}$ and $c_{syn,i}$ are the experimental and synthetic phase velocity corresponding to ith frequency element, while the $\lambda_{\exp,i}$ and $\lambda_{syn,i}$ are the experimental and synthetic wavelength of the W/D relationships at each depth. If the uncertainties for the W/D relationship and experimental DC are available, the phase velocity and wavelength standard deviations can be used instead of $c_{\exp,i}$ and $\lambda_{\exp,i}$ to normalize equations (5.1) and (5.2).

The solution of multi-objective problems is non-trivial: a single solution that optimizes both misfits does not exist. We select the models that minimize the two misfits (Q_{DC} and Q_{WD}), according to Pareto optimality. Pareto optimality or efficiency is a situation for which it is not possible to find a solution with lower misfit for one of the misfit functions without, at least, making one other misfit worsen off (Edgeworth, 1881; Pareto, 1896). A solution is called dominated when there exist other solutions having lower misfit for at least one of the misfit terms, while the other misfits remain unchanged. The Pareto efficient solutions are those solutions that cannot be dominated by any other solution from the defined model space. The Pareto efficiency of the solutions are assessed by the Pareto dominance criterion. Given two possible model solutions $\mathbf{m}_A$ and $\mathbf{m}_B$, solution A dominates B if:

$$\forall j \in \{1,2\}, Q_j(\mathbf{m}_A) \leq Q_j(\mathbf{m}_B), \tag{5.3}$$

where Q_1 and Q_2 are the DC and W/D misfits. Usually, the result of applying Pareto dominance criterion is not a single but a set of Pareto efficient solutions. If these solutions are connected graphically on the cross-plot of the misfit, they create the front of optimum solutions, which is also known as the Pareto front (PF). For a small population of data, PF can be obtained graphically from the cross plot of the misfits. We developed a MATLAB routine that compares the model misfits in terms of Pareto dominance (equation 5.3) and automatically obtains the set of Pareto efficient models. We use this algorithm to select the Pareto efficient models that minimize the Q_{DC} and Q_{WD}, and we consider the VS and VP of these models as the solution of the joint inversion.

To evaluate the inversion results, we compare the estimated models with true models (for synthetic examples) or with the benchmark models (for real data). We discretized the VS and VP of the selected and true (or benchmark) models within the investigation depth. For each selected model i, we compute the model misfit as:

$$\varepsilon_{\text{model}_i} = \frac{1}{2n}\sum_{j=1}^{n}\left(\left|\frac{VS_{tr}(z_j) - VS_i(z_j)}{VS_{tr}(z_j)}\right| + \left|\frac{VP_{tr}(z_j) - VP_i(z_j)}{VP_{tr}(z_j)}\right|\right), \tag{5.4}$$

where VS_{tr} and VP_{tr} are the true model (or benchmark) values, while VS_i and VP_i are the velocities of the selected models. The misfit is computed at each discretized depth z_j and averaged over the n number of data points in depth.

5.2 Synthetic example 1

The parameters of the synthetic example 1 are summarized in Table 5.1, where 4 layers with gradually increasing VS are considered overlying the bedrock half-space.

Table 5.1: The model parameters of the synthetic example 1.

	Thickness (m)	VS (m/s)	Poisson's ratio (-)	Density (kg/m^3)
Layer 1	2	100	0.2	1800
Layer 2	5	200	0.2	1800
Layer 3	10	400	0.33	2200
Layer 4	20	500	0.33	2200
Half-space	-	1000	0.33	2200

In Figure 5.2a, we show the true VS model, as well as the VSZ and DC, which we used to estimate the experimental W/D relationship in Figure 5.2b.

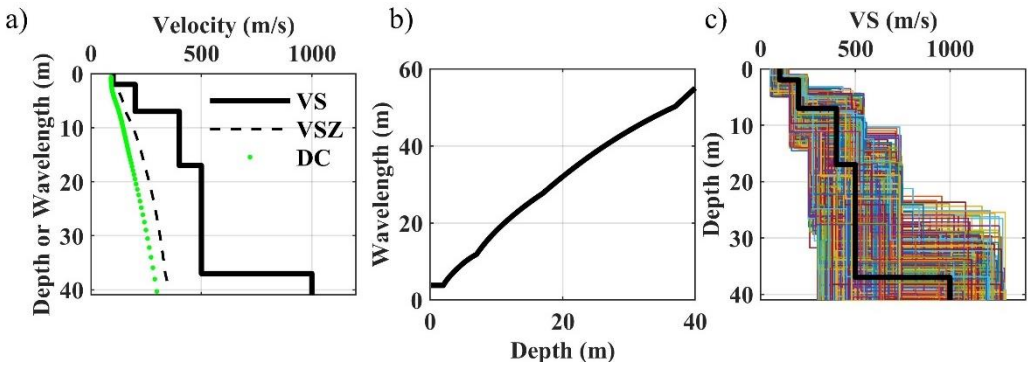

Figure 5.2: W/D relationship estimation and VS model sampling for the inversion of synthetic example 1. (a) The true VS, VSZ, and DC. (b) The estimated W/D relationship using the VSZ and DC in (a). (c) The generated 1,000,000 random VS models for the Monte Carlo inversion compared with the true VS in black.

The adopted model space boundaries for the Monte Carlo inversion are given in Table 5.2. We uniformly sampled 1,000,000 models within the defined boundaries. In Figure 5.2c, we show the *VS* of the sampled models. In the following, we compare the results of the inversion by considering the DC misfit with those from the joint inversion.

Table 5.2: The boundaries of the model space used for random sampling of the parameters for the inversion of synthetic example 1.

	Thickness (m)	*VS* (m/s)	Poisson's ratio (-)	Density (kg/m^3)
Layer 1	1 to 5	50 to 150	0.15 to 0.4	1800
Layer 2	2 to 10	150 to 250	0.15 to 0.4	1800
Layer 3	5 to 20	250 to 550	0.15 to 0.4	2200
Layer 4	10 to 30	300 to 750	0.15 to 0.4	2200
Half-space	-	800 to 1300	0.15 to 0.4	2200

5.2.1 Monte Carlo DC inversion

We computed the misfit between true DC and synthetic DCs from random models. We used the statistical Fisher test (section 2.3.3.2) with a high confidence level (0.15) to select the best fitting models. In Figure 5.3, we show the selected results of the inversion in blue and the curves relevant to the true model in black. In Figure 5.3b and c, we show in red the best matching VS and VP models among the 1,000,000 randomly sampled models with respect to the true ones, according to equation (5.4); the best-matching random VS and VP models were not selected by the inversion and are 3.8% different from the true VS and VP. The selected models from the inversion show a 10 to 32% difference with respect to the true models.

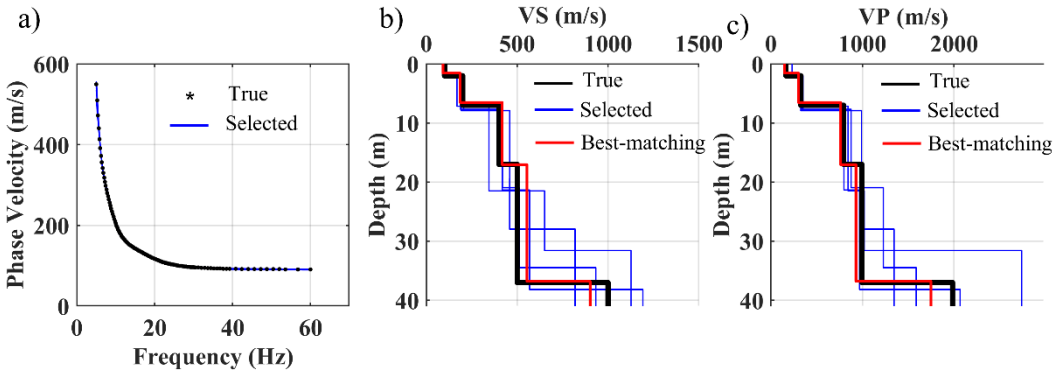

Figure 5.3: The result of Monte Carlo inversion applied to synthetic example 1, considering only the DC misfit as selection criterion. (a) The selected DCs compared with the true one. (b) The selected VS models in blue compared with the true VS model in black. (c) The selected VP models in blue compared with the true VP model in black. In (b) and (c), the red VS and VP models are the best-matching models among the random models according to equation (5.4).

5.2.2 Monte Carlo Joint inversion

In the previous section, we used the DC misfit to select the VS and VP models. Here, we consider both DC and W/D misfits for the inversion. In Figure 5.4a, we show the cross-plot of the W/D and DC misfits corresponding to each randomly sampled model, where the color scale associated with each point represents the model misfit computed from equation (5.4). Five models out of the 1,000,000 models were registered as Pareto efficient (asterisks in Figure 5.4a). The comparison between the DC and W/D relationship of these five models with respect to the true ones, are given in Figures 5.4b and c. In Figures 5.4d and e, we show the selected VS and VP models; the plots also include the true models and the best-

matching model amongst the randomly sampled models according to equation (5.4). The minimum difference of 7.3% was registered for the estimated joint inversion models with respect to the true model. This value was 3.8% for the best-matched randomly sampled models (red models in Figures 5.4d and e), which was not selected by the joint inversion. The estimated models show a better estimation of VS and VP in deeper layers than the obtained models from DC inversion only (Figure 5.3b and c).

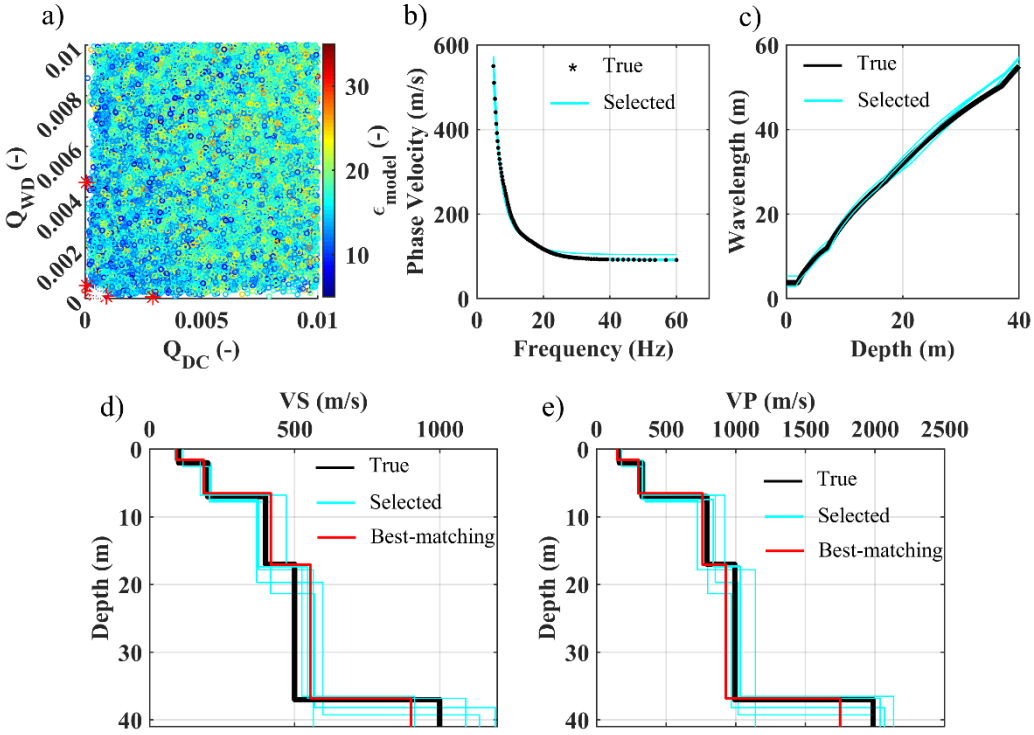

Figure 5.4: The Monte Carlo joint inversion result for the synthetic example 1. (a) The cross-plot showing the W/D and DC misfit of the random models. The color scale shows the misfit between each model with respect to the true one according to equation (5.4). (b) The DCs of the selected models compared with the true one. (c) The W/Ds of the selected models compared with the true one. (d) The selected VS models in light blue compared to the true one in black. (e) The selected VP models in light blue compared with the true one in black. In (d) and (e), the red VS and VP models are the best-matching models among the random models according to equation (5.4).

In the boxplot in Figure 5.5, we compare the model misfit of all randomly sampled models, the selected models from DC inversion, and the selected models from the

joint inversion. The box plot is defined by three lines showing the 25th percentile, median and 75th percentile of the residual's distribution, and whisker lines extending from the box's edges up to 1.5 times the distance between the edges of the box. The rest of the data are considered outliers and shown with "+". The median misfit of the estimated models, according to both inversions, is significantly less than all models' misfits. Yet, the joint inversion estimated more accurate models, which mostly were less than 15% different from true VS and VP models.

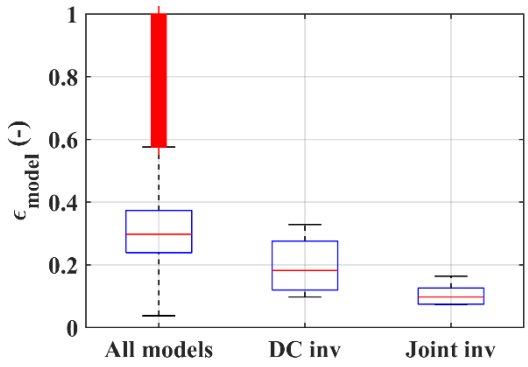

Figure 5.5: The model misfit of all 1,000,000 randomly sampled models, selected models using DC inversion (Figure 5.3), and selected models using joint inversion (Figure 5.4), with respect to the true VS and VP models of the synthetic example 1. These model misfits are computed using equation (5.4).

5.3 Synthetic example 2

We applied the joint inversion method to a 1D synthetic example composed of sand deposit overlying the half-space with the water table at depth 10 m. In Figure 5.6, we show the soil column of the synthetic example 2, in which we divided the sand deposit medium into unsaturated and saturated layers.

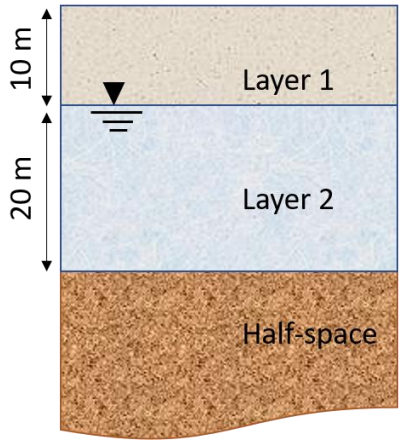

Figure 5.6: The geometry of the synthetic example. The sand deposit is divided into unsaturated and saturated layers, which overly the bedrock half space.

The petrophysical properties related to the sand deposit shown in Table 5.3 are taken from Garofalo (2014) and based on Comina et al. (2010) and Santamarina et al. (2001). In Table 5.3, $\nu_{skeleton}$, ϕ and ρ_s are the Poisson's ratio of the skeleton, porosity and density corresponding to the sand deposit, respectively. ρ_f and K_f are the density and bulk modulus of the fluid (water).

Table 5.3: The petrophysical properties adopted for the sand deposit and pore fluid (water) of the synthetic example 2 shown in Figure 5.6.

$\nu_{skeleton}$	0.227
ϕ	0.4
ρ_s	2650 kg/m^3
ρ_f	1000 kg/m^3
K_f	2.18 Gpa

Foti et al. (2002) proposed a relationship to estimate the porosity of the saturated granular material from the seismic velocities. We reorganized this equation to estimate VP as:

$$VP = \frac{4(\rho_s - \rho_f)k_f}{\rho_s - \left[\rho_s - 2\phi(\rho_s - \rho_f)\right]^2} + 2\left(\frac{1-\nu}{1-2\nu}\right)VS\,, \tag{5.5}$$

We used equation (5.5) to estimate the VP of the saturated portion of the sand deposit. We also computed the density of the saturated and unsaturated sand layer using:

$$\rho = (1-\phi)\rho_s + \phi\rho_f\,. \tag{5.6}$$

In Table 5.4, we report the seismic model parameters of the synthetic example, where the density of the layers 1 and 2 were computed from equation (5.6) and the VP of the saturated portion of the sand deposit (layer 2) was obtained from equation (5.5). The VS of the layers and also the parameters of the half-space were assumed according to Garofalo (2014).

Table 5.4: The model parameters of the synthetic example 2.

	H (m)	Density (kg/m$^{3)}$	VS (m/s)	VP (m/s)
Layer 1	10	1590	170	346
Layer 2	20	1990	200	1688
Half-space	-	2402	350	2000

In Figure 5.7a, we show the true VS, VSZ and DC of the synthetic example 2 which was used to estimate the experimental W/D relationship in Figure 5.7b. The adopted model space boundaries selected for the inversion of synthetic example 2 is reported in Table (5.5). We sampled 1,000,000 models uniformly within these boundaries (Figure 5.7c).

Table 5.5: The boundaries of the model space used for random sampling of the parameters for the inversion.

	Thickness (m)	VS (m/s)	Poisson's ratio	Density (kg/m^3)
Layer 1	6 to 14	100 to 250	0.1 to 0.495	1590
Layer 2	12 to 28	150 to 350	0.1 to 0.495	1990
Half-space	-	250 to 500	0.1 to 0.495	2402

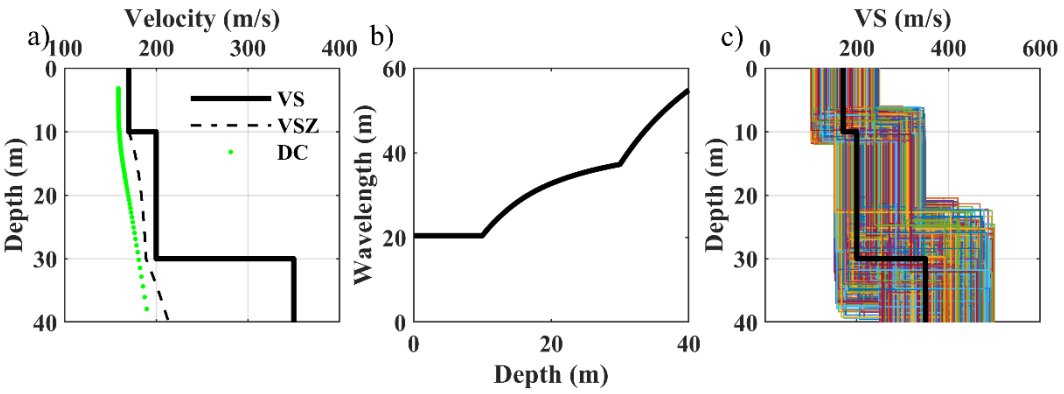

Figure 5.7: W/D relationship estimation and VS model sampling for the inversion of synthetic example 2. (a) The true VS, VSZ, and DC. (b) The estimated W/D relationship using the VSZ and DC in (a). (c) The generated 1,000,000 VS models for the Monte Carlo inversion compared with the true VS in black.

In the following, we first show the results of the inversion considering only the DC misfit. Then, we perform the joint inversion to estimate the models and compare the result with the DC inversion.

5.3.1 Monte Carlo DC inversion

The statistical Fisher test (section 2.3.3.2) with a high confidence level (0.15) was applied to select the models according to the DC misfit. In Figure 5.7, we show the results of the inversion, where, in Figure 5.7b and c, the selected VS and VP models are compared with the true (in black) and best-fitting model among the 1,000,000 generated models (in red) according to equation (5.4). The selected models do not include the best-matching model (red in Figures 5.7b and c) and show 23 to 35%

difference with respect to the true ones according to equation (5.4). This high difference is mainly caused by the significant inaccuracy in estimating the VP model.

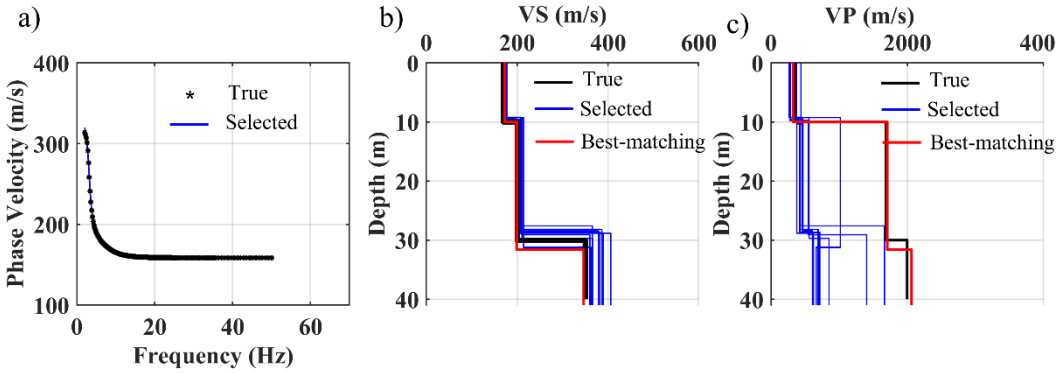

Figure 5.8: The result of Monte Carlo inversion applied to synthetic example 2, considering only the DC misfit as selection criterion. (a) The selected DCs compared with the true one. (b) The selected VS models in blue compared with the true VS model in black. (c) The selected VP models in blue compared with the true VP model in black. In (b) and (c), the red VS and VP models are the best-matching models among the random models according to equation (5.4).

5.3.2 Monte Carlo joint inversion

The application of the joint inversion (Figure 5.9) resulted in 11 Pareto efficient solutions, which are shown as red asterisks in the cross-plot of the misfits (Figure 5.9a). The VS of the selected models well depicted the true VS of the synthetic example 2 (Figure 5.9d). The selected VP models well recovered the unsaturated first layer (Figure 5.9e), however, the accuracy decreased in determining the saturated layer and the half-space, which is mainly due to the high Poisson's ratio at these levels.

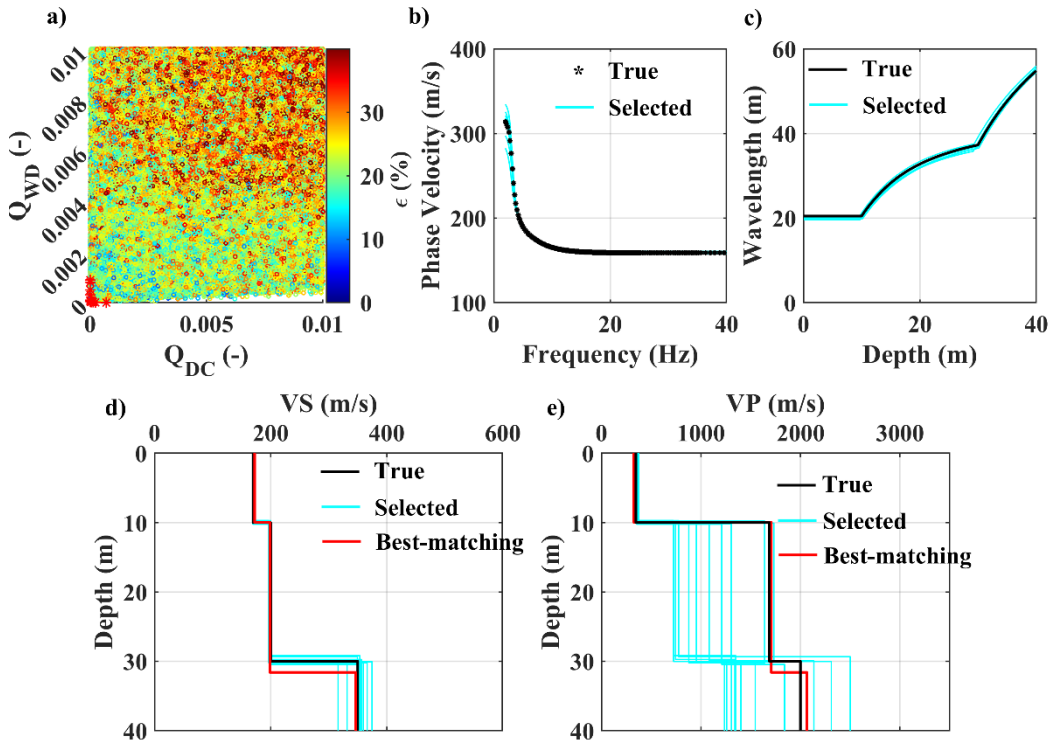

Figure 5.9: The Monte Carlo joint inversion result for the synthetic example 2. (a) The cross-plot showing the W/D and DC misfit of the random models. The color scale shows the misfit between each model with respect to the true one according to equation (5.4). (b) The DCs of the selected models compared with the true one. (c) The W/Ds of the selected models compared with the true one. (d) The selected VS models in light blue compared to the true one in black. (e) The selected VP models in light blue compared with the true one in black. In (d) and (e), the red VS and VP models are the best-matching models among the random models according to equation (5.4).

In Figure 5.10, we compare the estimated Poisson's ratio from the DC inversion and the joint inversion with the true profile. In Figure 5.10b, it can be observed that the selected Poisson's ratios from the joint inversion well recovered the true profile. However, small inaccuracy in Poisson's ratios estimation resulted in significant variation of the *VP* of the saturated layer and the half-space (Figure 5.9e).

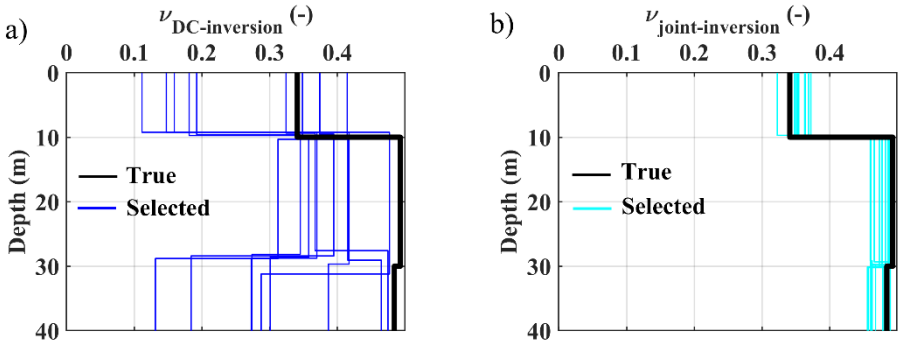

Figure 5.10: Selected (estimated) Poisson's ratio for the synthetic example 2, using: (a) DC Monte Carlo inversion. (b) Monte Carlo joint inversion.

The inaccuracy of VP estimation in high Poisson's ratio environment is due to the non-linear relationship between VP and Poisson's ratio (equation 4.16): The sensitivity of Poisson's ratio to VP/VS variations significantly decreases when high Poisson's ratio values are available. To better show the effect of this non-linearity on the W/D relationship, we performed sensitivity analysis of the W/D relationship with respect to Poisson's ratio (Figure 5.11a) and VP/VS (Figure 5.11b) variations. In Figure 5.11a, we show the W/D relationship obtained for synthetic example 2 using different Poisson's ratio ranging from 0 to 0.5, while, in Figure 5.11b the similar W/D relationships were obtained by changing the VP/VS ratio. Figure 5.11a shows that the W/D relationship is sensitive to the Poisson's ratio variation within various intervals of Poisson's ratio. On the other hand, when VP/VS ratio is considered (Figure 5.11b), most of the W/D variations are related to the range between the minimum VP/VS ratio ($\sqrt{2}$; $\nu = 0$) and VP/VS =3.5 ($\nu = 0.45$). Beyond this ratio range, the W/D relationship variations significantly decreases to a point that it almost collapses to a single relationship (Figure 5.11b in red) for VP/VS greater than 5 ($\nu > 0.48$).

The misfit of the joint inversion's selected models according to equation (5.4) ranged between 10 to 23%, which is more than the difference obtained for synthetic example 1 (7.3 to 18%). However, compared to the DC inversion of example 2 (Figure 5.8c), the joint inversion much better resolved the P-wave velocities (Figure 5.9e). This improvement can be better observed in the boxplot of the model misfit for synthetic example 2 (Figure 5.12), where we compare the model misfit of all

randomly sampled models, the selected models from DC inversion, and the selected models from the joint inversion.

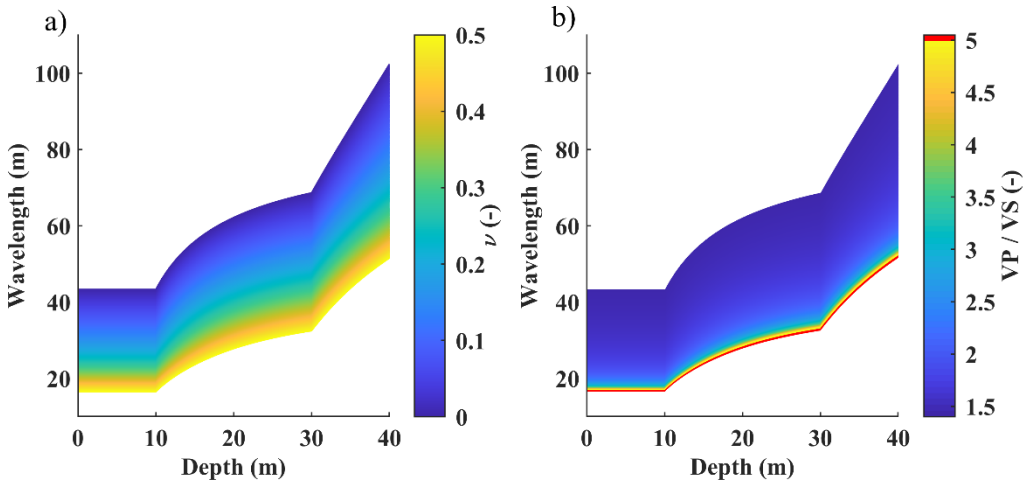

Figure 5.11: The W/D relationship variation of synthetic example 2 by changing: (a) Poisson's ratio, and (b) VP/VS ratio. In both cases the VS is fixed to the value used for synthetic example 2 (Table 5.4). The red portion in (b) is related to VP/VS greater than 5.

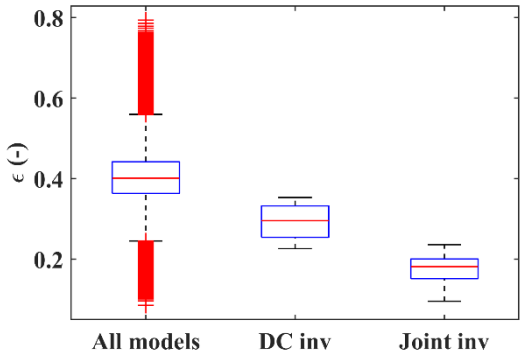

Figure 5.12: The model misfit of all 1,000,000 randomly sampled models, selected models using DC inversion (Figure 5.8), and selected models using joint inversion (Figure 5.9), with respect to the true VS and VP models of the synthetic example 2. These model misfits are computed using equation (5.4).

5.4 Field Example (La Salle data set)

We performed the joint inversion at location B of the La Salle site (Figure 3.3a). The site is known for smooth lateral variation. To further test the performance of

the method, we provided the W/D relationship needed for the joint inversion from location A.

We used the method explained in section 4.2.2 to estimate the experimental W/D relationship at location A of the site (location shown in Figure 3.3a). We randomly sampled 5,000,000 models within the model space boundary given in Table 5.6. We used the statistical Fisher test with a low level of confidence (0.05) to include all possible models with various geological properties best fitting the DC at position A.

Table 5.6: The selected model space for the inversion of the DC at location A.

	Thickness (m)	VS (m/s)	Poisson's ratio (-)	Density (kg/m^3)
Layer 1	1.5 to 3	170 to 240	0.1 to 0.45	1800
Layer 2	1.5 to 3	250 to 350	0.1 to 0.45	1800
Layer 3	3 to 5	350 to 400	0.1 to 0.45	1800
Layer 4	3 to 5	400 to 450	0.1 to 0.45	1800
Layer 5	7.5 to 11	430 to 480	0.1 to 0.45	2200
Layer 6	7.5 to 11	480 to 550	0.1 to 0.45	2200
Layer 7	12 to 17	550 to 650	0.1 to 0.45	2200
Layer 8	25 to 34	650 to 720	0.1 to 0.45	2200
Layer 9	25 to 34	720 to 800	0.1 to 0.45	2200
Half-space	-	800 to 900	0.1 to 0.45	2200

In Figure 5.13, we show the steps of estimating W/D relationship at point A of La Salle site. The selected VS models (Figure 5.13b) were transformed to VSZ models using equation (4.1); the VSZ models were averaged at each depth to estimate the

VSZ model required for the W/D relationship (Figure 5.13c). The estimated W/D relationship is shown in Figure 5.13d.

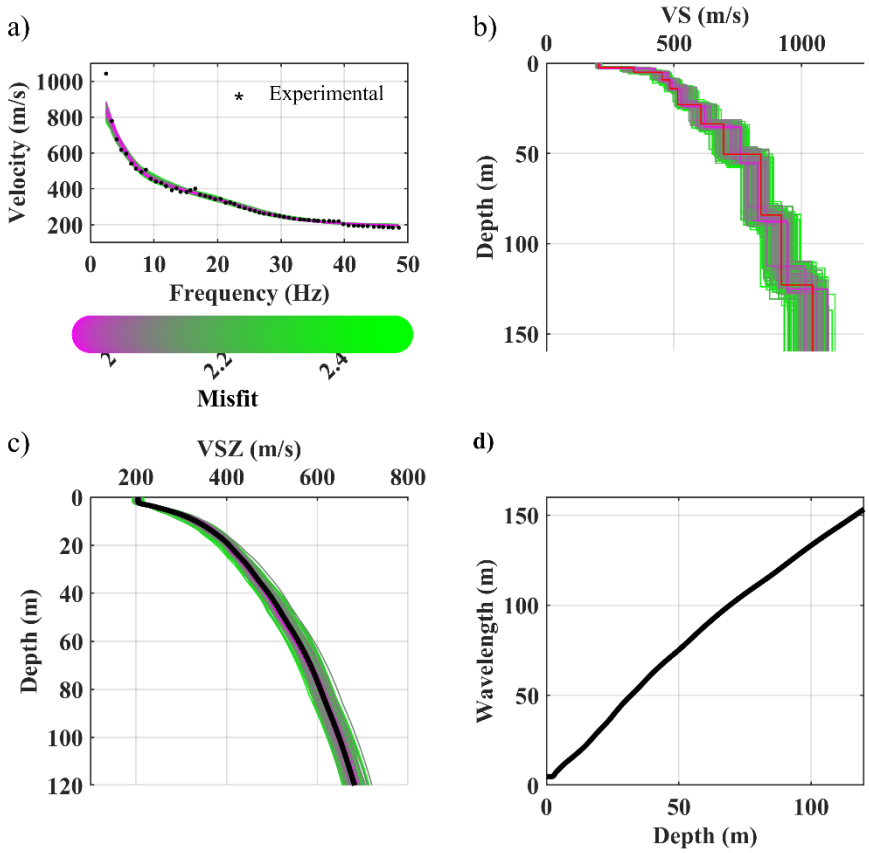

Figure 5.13: The W/D relationship estimation for location A of La Salle site (Figure 3.3a) using the Monte Carlo inversion. (a) The experimental DC of location A and the selected synthetic DCs. (b) The selected VS models. (c) The selected VSZ models. The reference VSZ in black. (d) The estimated W/D relationship.

We use the estimated W/D relationship (Figure 5.13d) at location B, where we perform the joint inversion. Similar to the synthetic examples, we first show the result of the inversion considering only DC misfit as a selection criterion of the Monte Carlo inversion. Then, we perform the joint Monte Carlo inversion. The adopted model space boundaries for both inversions are given in Table 5.7, which we used to randomly sample 5,000,000 models.

Table 5.7: The model space defined for the inversion of the experimental DC at location B of La Salle site.

	Thickness (m)	VS (m/s)	Poisson's ratio (-)	Density (kg/m^3)
Layer 1	1.5 to 3	230 to 300	0.1 to 0.45	1800
Layer 2	1.5 to 3	320 to 400	0.1 to 0.45	1800
Layer 3	3 to 5	350 to 450	0.1 to 0.45	1800
Layer 4	3 to 5	400 to 500	0.1 to 0.45	1800
Layer 5	7.5 to 11	500 to 650	0.1 to 0.45	2200
Layer 6	7.5 to 11	600 to 730	0.1 to 0.45	2200
Layer 7	12 to 17	700 to 900	0.1 to 0.45	2200
Layer 8	25 to 34	900 to 1100	0.1 to 0.45	2200
Layer 9	25 to 34	1000 to 1350	0.1 to 0.45	2200
Half-space	-	1200 to 1500	0.1 to 0.45	2200

5.4.1 Monte Carlo DC inversion

We applied a statistical Fisher test with a 0.15 confidence level to select the models according to DC misfit. In Figure 5.14a, we show the selected DCs and experimental DC at location B. In Figures 5.14b and c, we compare the estimated VS and VP models with the models obtained from the close-by downhole test (solid black lines obtained from Socco et al., 2008). The minimum difference between the selected models and the ones from downhole tests is 9.1% according to equation (5.4).

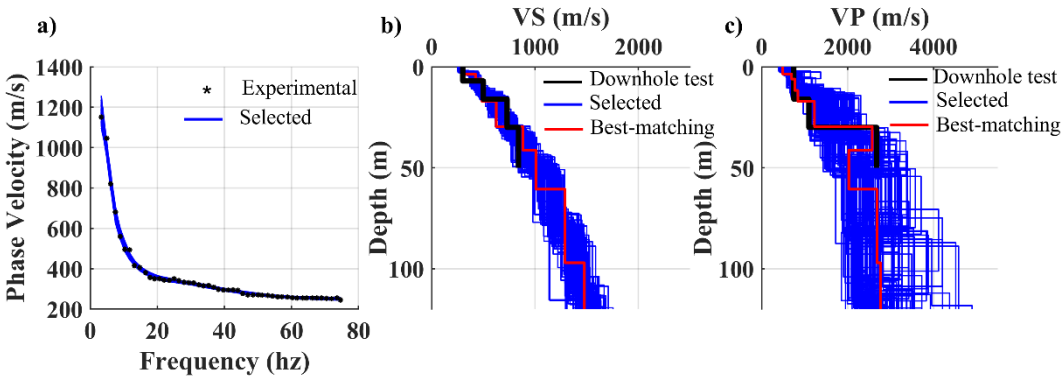

Figure 5.14: The results of the Monte Carlo inversion at location B of the La Salle site considering only the DC misfit. (a) The DCs of the selected models compared with the experimental one. (b) The selected VS models in blue compared with the one obtained from close-by down hole test in black (from Socco et al., 2008). (c) The selected VP models in blue compared with the one obtained from close-by downhole test in black (from Socco et al., 2008). In (b) and (c), the red VS and VP models are the best-matching models with respect to the ones from down hole tests (in black) according to equation (5.4).

5.4.2 Monte Carlo Joint inversion

We estimated the DC and W/D misfit of each randomly generated model, thanks to equations (5.1) and (5.2). Figure 5.15a shows the cross-plot of the DC and W/D relationships of the randomly sampled models. 11 models out of 5,000,000 models were found as Pareto efficient solutions. In Figures 5.15b and c, we compare the selected models' DCs and W/D relationships with the experimental ones. In Figure 5.15d and e, we compare the selected VS and VP models with the models obtained from the downhole tests (Socco et al., 2008) and the best-matching models according to equation (5.4). The selected models were 8.4% to 22% different from the models obtained from the downhole test.

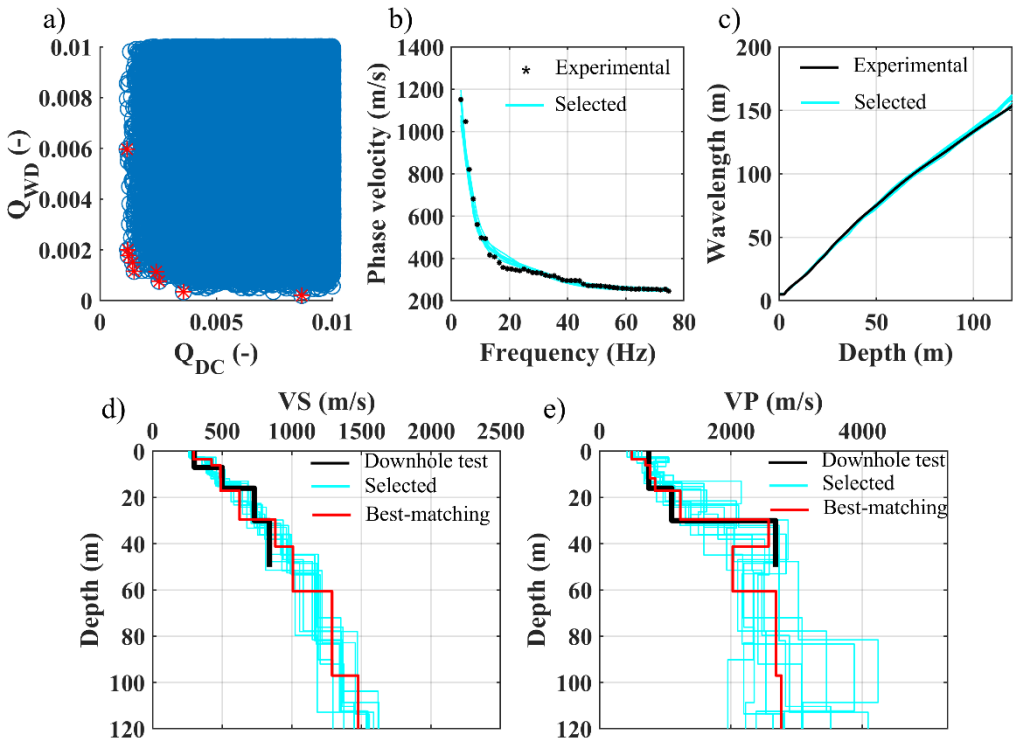

Figure 5.15: The results of the Monte Carlo joint inversion applied to the location B of the La Salle data set. (a) The cross-plot showing the W/D and DC misfit of the random models. (b) The DCs of the selected models compared with the experimental one. (c) The W/Ds of the selected models compared with the experimental one. (d) The selected VS models in light blue compared with VS model of the close-by downhole test in black (from Socco et al., 2008). (e) The selected VP models in light blue compared with the VP model of the close-by downhole test in black (from Socco et al., 2008). In (d) and (e), the red VS and VP models are the best-matching models with respect to the ones from down hole tests (in black) according to equation (5.4).

In Figure 5.16, we compare the model misfit of the selected models obtained from the two inversions and all randomly sampled models. Similar to the synthetic examples, the joint inversion provided better matching models with respect to the DC inversion.

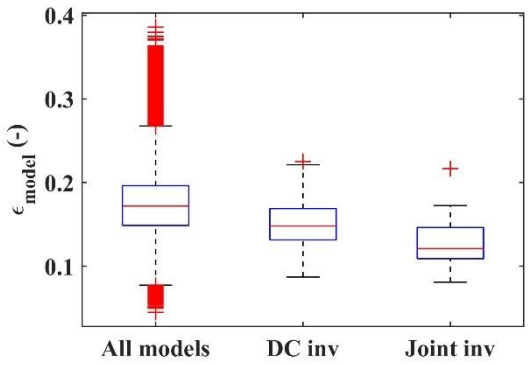

Figure 5.16:The model misfit of all 5,000,000 randomly sampled models, selected models using DC inversion (Figure 5.14) and selected models using joint inversion (Figure 5.15), with respect to the downhole test models within first 50 m of the subsurface (the black models in Figures 5.15d and e; from Socco et al., 2008). These model misfits were computed using equation (5.4).

5.5 Discussion and conclusion

We successfully tested the joint inversion method on two synthetic data sets (Figures 5.4 and 5.9). Including the W/D relationship in the inversion guaranteed more accurate VS and VP model estimations. Even though the accuracy of the VP estimation decreased for the synthetic example 2 below the water table, the joint inversion yet provided significantly better estimation of the P-wave velocity (Figure 5.9e) compared to the DC inversion (Figure 5.8c). We also applied the method to the La Salle data set. We compared the results of using only DC misfit with the results of the joint inversion. Although the estimated VS models of both methods were well supported by the near-by downhole test's VS model, the joint inversion resulted in a less number of estimated models and more confined velocity estimates (Figure 5.15d). The estimated VP models of the joint inversion showed satisfactory agreement with the VP from the downhole test.

In Figure 5.17, we compare the VS and VP results of the joint inversion with the results of the high-resolution reflection survey (Figure 5.17a, reproduced from Socco et al., 2008) and the P-wave traveltime tomography (Figure 5.17b, reproduced from Socco et al., 2008). In Figure 5.17e and f, we show the average of the selected VS and VP models by the joint inversion (computed from Figure 5.17c and d), for which we used the distribution of the velocities at each depth to obtain a standard deviation. Two primary reflections were observed (Socco et al., 2008)

from the seismic section in Figure 5.17a, which coincide with the location B of the La Salle site (inversion location) at depths 22 and 120 m.

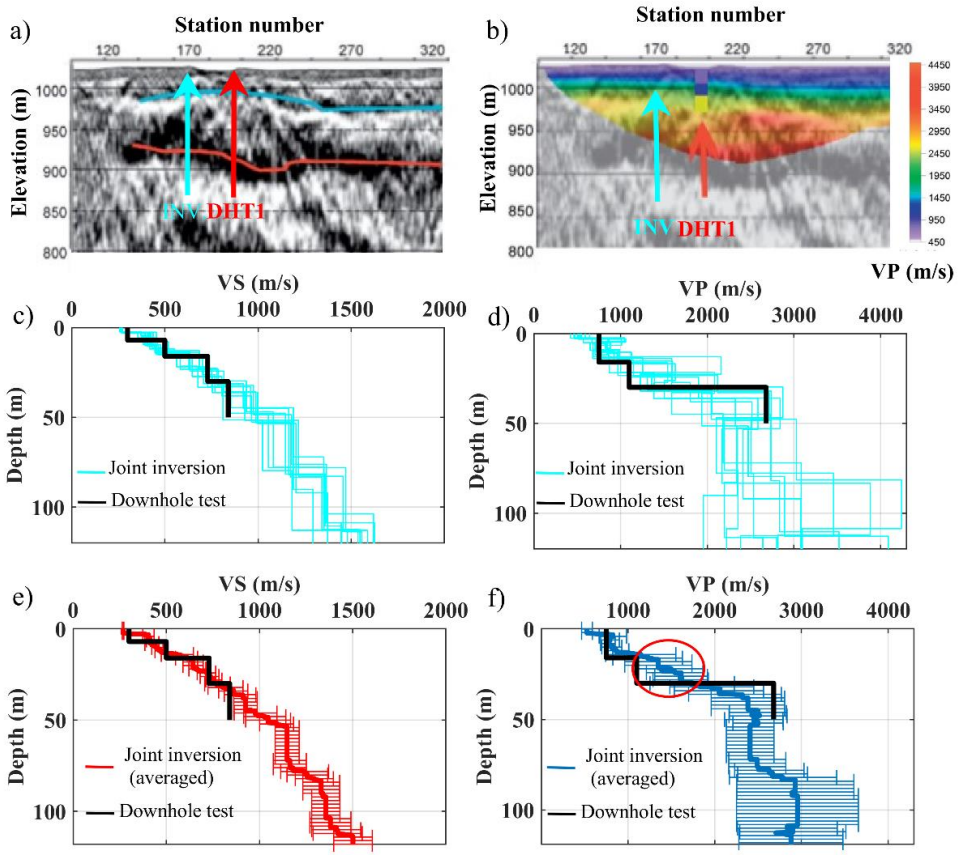

Figure 5.17: The comparison between the estimated models for the location B of the La Salle site with the benchmark seismic reflection survey, P-wave traveltime tomography and near-by downhole test. (a) The high-resolution reflection survey (reproduced from Socco et al., 2008). The location of the downhole test and the location of the joint inversion are highlighted with red and light blue arrows. (b) The VP model from P-wave traveltime tomography superimposed with the seismic reflection image of (a) (reproduced from Socco et al., 2008). (c) The selected VS models from the Monte Carlo joint inversion in light blue. In black the VS of the near-by downhole test (from Socco et al., 2008). (d) The selected VP models from the Monte Carlo joint inversion in light blue. In black the VP of the near-by downhole test (from Socco et al., 2008). (e) The average of the selected VS models from (c), where the bars are the standard deviations. (f) The average of the selected VP models from (d), where the bars are the standard deviations. The red circle in (f) highlights the portion that is interpreted as water table by benchmark seismic reflection survey in (a) and P-wave traveltime tomography in (b).

The shallow reflection (blue horizon in Figure 5.17a) was interpreted as the water table. The water table was also confirmed by P-wave traveltime tomography showing the VP of 1500 m/s at this level. The average VP of the selected models from Monte Carlo joint inversion (Figure 5.17f) shows values around 1500 m/s for depth between 18 to 27 m and the value of 1492 m/s at depth 22 m. Unlike the VS results of the joint inversion (Figure 5.17e), the estimated average VP from the joint inversion (Figure 5.17f) shows a substantial increase in the standard deviation below the water table, which indicates the challenges in determining the VP model in saturated environment.

The second reflection was interpreted as the bedrock (Socco et al., 2008), which is partially observed in the tomography result. Although the selected models of the joint inversion (Figure 5.17d in light blue) do not provide a well-confined estimation at the bedrock depth (120 m), the averaged VP model in Figure 5.17f depicts the high VP of this portion of the subsurface.

The joint inversion algorithm supports parallel computing, which significantly expedites the inversion. Compared to the DC Monte Carlo inversion, the joint inversion has two additional steps: The W/D estimations and the Pareto dominance check of the randomly generated models. The algorithm running time grows almost linearly with number of randomly generated models. The joint inversion of 5,000,000 sampled models takes about 12 hrs, employing 10 CPU cores.

6. Laterally Constrained Inversion (LCI)

We use the LCI to estimate the VS, for which we provide a priori Poisson's ratio using the W/D method explained in section 4.4. We then use the same Poisson's ratio to transform the VS results into VP. In the following, we first briefly explain the method. Then, we show the method's application to the Aurignac data set.

6.1 Background

The LCI is a well-established method in many geophysical applications, such as resistivity and EM data (Wisén et al., 2005; Auken et al., 2005; Mansoor et al., 2006). The first application of LCI to surface seismic wave data was introduced by Wisén and Christiansen (2005). Since then, many authors have applied LCI to surface wave data (Socco et al., 2009; Boiero, 2009; Bardainne et al., 2017). In the scheme of LCI, the lateral constraints link the adjacent model parameters to control the lateral variations (Figure 6.1). Similarly, the constraints can be imposed to connect parameters of different layers to limit the variations in depth. In the scheme of LCI, the DCs are inverted simultaneously, minimizing the non-uniqueness of single inversion.

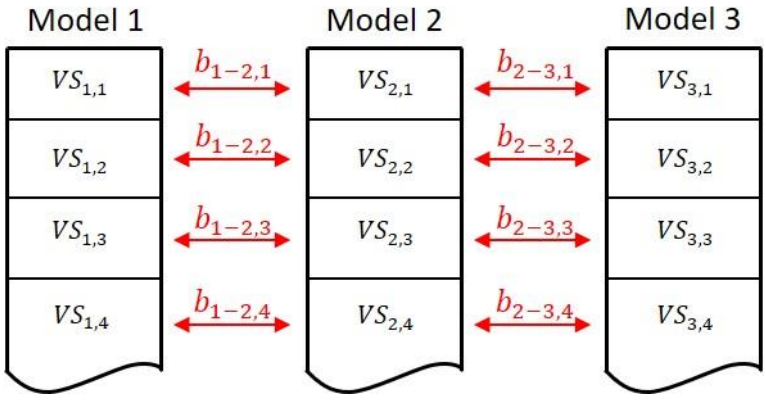

Figure 6.1: A schematic view of how the lateral constraints are imposed in LCI methods. The constraints are indexed according to the indices of the model points and layers.

The constrained inversion leads to a smoother and more consistent model estimation (Socco et al., 2009). Moreover, it diminishes the effect of erroneous DCs (outliers) that are significantly different from the close by DCs. The surface wave LCI methods' target is usually the VS model, demanding a priori Poisson's ratio.

6.2 The method

6.2.1 Inputs: the local DCs and reference model

The method's inputs are the local DCs and the reference model at their location. The DCs are estimated using any of the methods explained in section 2.3.2. The reference model is composed of the thickness, density, Poisson's ratio, and VS, where equal thicknesses are used by discretizing the investigation depth. The densities are set based on the geological properties of the site. We cluster the DCs and estimate 1D reference Poisson's ratio for each cluster using the W/D method explained in section 4.4. At each spatial location, the relevant Poisson's ratio according to the clustering of the DCs is associated with the reference model. We select the VS of the reference models according to the estimated VS models from the Monte Carlo inversion used for Poisson's ratio estimation explained.

6.2.2 Inversion algorithm

The LCI algorithm was developed by Socco et al. (2009) and Boiero (2009), based on the work of Auken and Christiansen (2004). We modified the algorithm to support parallel computing. The method is a deterministic least-square inversion method which minimizes the misfit Q as:

$$Q = \left[(\mathbf{d_{obs}} - \mathbf{d(m)})^{\mathbf{T}}\, \mathbf{C_{obs}^{-1}}\, (\mathbf{d_{obs}} - \mathbf{d(m)}\right] + \left[\left(-\mathbf{R_p m}\right)^{\mathbf{T}} \mathbf{C_{Rp}^{-1}} (-\mathbf{R_p m})\right], \tag{6.2}$$

where the first term determines the misfit between the experimental data $\mathbf{d_{obs}}$ and synthetic data $\mathbf{d(m)}$. $\mathbf{m}$ is the vector of the model parameters and $\mathbf{C_{obs}^{-1}}$ is the reciprocal of the covariance matrix. The second term defines the lateral regularization of the velocities and thicknesses, where $\mathbf{R_p}$ is the regularization matrix composed of values 1 and -1 for the constrained parameters and zeros elsewhere. The strength of the regularization is determined by the covariance matrix $\mathbf{C_{Rp}}$.

The model parameters VS and thickness are updated iteratively according to damping least-square algorithm (Marquart, 1963) until a local minimum of the misfit is reached. A thorough description of the method is available in Boiero (2009) and Socco et al. (2009).

We use the reference Poisson's ratio of each cluster to transform the related estimated VS models from the LCI to VP models.

6.2.3 Constraints selection criterion

The value (strength) of the constraints plays an important role in the inversion. The higher the constraints, the smoother the model will be. However, too strong constraints can result in an over-smoothed model estimation (Socco et al., 2009). We consider the residual misfit between the synthetic DCs of the last iteration and the experimental ones as an indicator for selecting the constraint level. We compute the residual misfit of each DC as:

$$r_{norm} = \frac{1}{n}\sum_{i=1}^{n}\frac{\left|c_{\exp,i} - c_{syn,i}\right|}{c_{\exp,i}}, \tag{6.2}$$

where $c_{\exp,i}$ and $c_{syn,i}$ are the experimental and synthetic phase velocities of the *i*th data point out of n data points of the DC. We also compute the total residual misfit as the average residual misfit of all DCs. The unconstrained inversion provides the lowest residual misfit. As a result, we first invert the data without imposing constraints to estimate a misfit baseline. Then, we repeat the inversion by gradually increasing the constraints' strength. For each inversion, we compare the misfit with the misfit baseline (unconstrained inversion misfit). We consider the VS model obtained from the constrained inversion with the highest level of constraints that is not significantly impacting the misfit.

6.3 Application to Aurignac data set

6.3.1 Estimated Local DCs

Previously, in section 4.5.2.1, a total of 545 DCs were estimated (Figure 4.19a), which were clustered into two groups (Figure 4.19b); the DCs of the west side (cluster A) showed slower phase velocity compared to the east side (cluster B) of the site (Figure 4.20).

6.3.2 Reference Model

We defined the reference model composed of 9 layers overlying half-space with constant thicknesses of 15 m, except for the first layer which was set 20 m, giving an investigation depth of about 140 m. We previously obtained the reference DC, W/D relationship, and apparent Poisson's ratio for each cluster (in section 4.5.2.2; Figures 4.21 and 4.22). We followed the method explained in section 4.3 to estimate the 1D Poisson's ratio corresponding to each cluster. In Figure 6.2a and b, we show the estimated VS and VP corresponding to cluster A and cluster B. We used equation (4.16) to estimate the Poisson's ratios of cluster A (Figure 6.2c) and cluster B (Figure 6.2d). The Poisson's ratios (blue lines) are obtained for every 0.1 m interval. We averaged the data points within the defined layers of LCI and also extrapolated the Poisson's ratios to cover the whole 140 m investigation depth required for the LCI. In Figures 6.2c and d, in red, we show the adopted Poisson's ratio used for the clusters A and B, respectively. We defined a constant density of 2400 kg/m^3, except for the first layer (2200 kg/m^3).

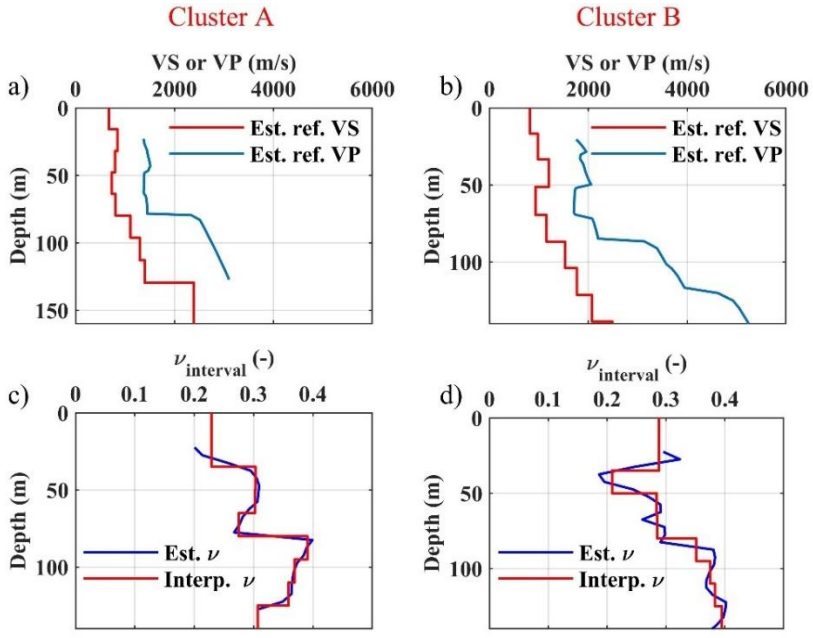

Figure 6.2: Estimated Poisson's ratios for the cluster A and Cluster B of the Aurignac data set using the W/D method explained in section 4.3. (a) The estimated VS and VP models corresponding to the reference DC of Cluster A. (b) The estimated VS and VP models corresponding to the reference DC of Cluster B. (c) The estimated Poisson's ratio for the cluster A in blue. In red, the obtained Poisson's ratio for LCI and later for SWT. (d) The estimated Poisson's ratio for cluster B in blue. In red, the obtained Poisson's ratio for LCI and later for SWT.

6.3.3 Results

We performed an unconstrained and several laterally constrained inversions to find the optimal level of constraints. The 50 m/s was the highest level of constraints that did not significantly impact the inversion's residual misfit. In Figure 6.3, we compare the residual misfits of the laterally constrained (50 m/s) and unconstrained inversion, which were computed by equation (6.2). In both inversions, the synthetic DCs are less than 10 % different from the experimental ones at all locations. Even though the constrained inversion shows a slight increase in the residuals on the west side, the total residual misfits are very similar (2.07% for the constrained and 1.82% for the unconstrained inversions).

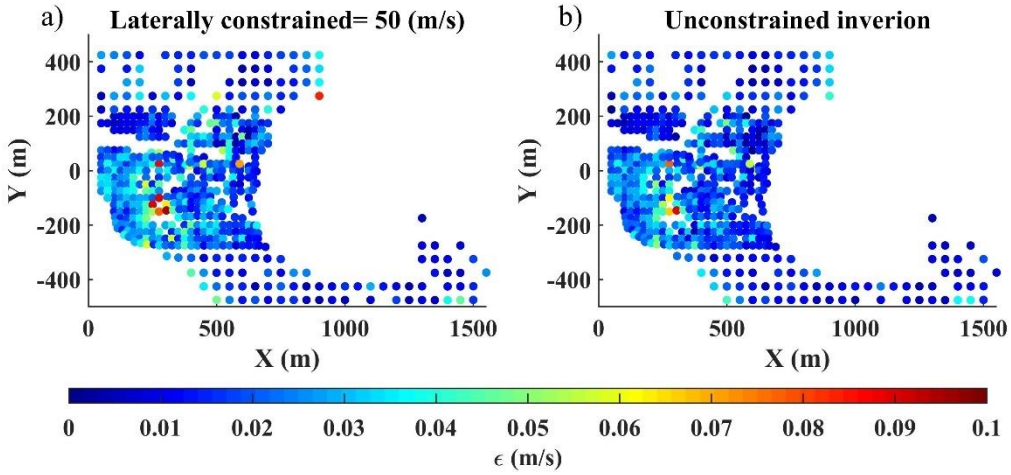

Figure 6.3: The residual misfit computed for the final models of LCI inversion using equation (6.2) for: (a) LCI with 50 m/s lateral constraints. (b) unconstrained inversion.

The selected inversion (50 m/s constraints) automatically stopped after 37 iterations. In Figure 6.4a to i, we show slices of the estimated VS model at various depths. We interpolated the estimated 1D models to obtain the quasi 3D VS model (Figure 6.4j). In Figure 6.4k, we show several isosurfaces of the 3D model in x, y, and z directions.

We used the estimated Poisson's ratio of the two clusters in Figures 6.2c and d (the blue lines) to estimate the subsurface's VP model. The estimated Poisson's ratios of cluster A and B were limited between depths 20 to 128 m (Figure 6.2c) and 20 to 140 m (Figure 6.2d), respectively. As a result, the estimated VP model in Figure

6.5 is also bounded by this limitation. We show the quasi 3D model and isosurfaces of the estimated VP in Figures 6.5j and k.

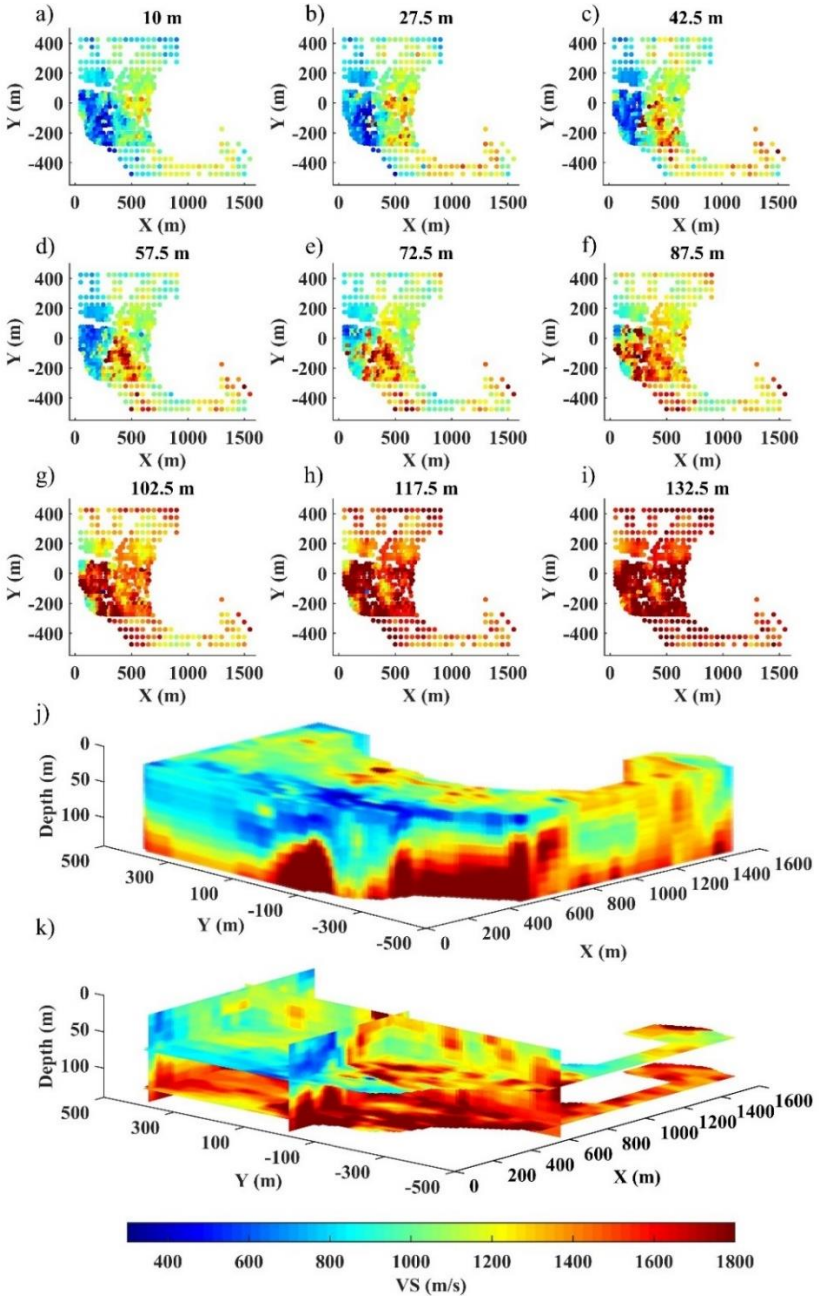

Figure 6.4: The estimated VS model for the Aurignac site using the LCI method. (a to i) The horizontal slices at different depths indicated on top of each figure. (j) The pseudo 3D view of the estimated VS after linear interpolation of the 1D models.(k) Isosurfaces obtained from the 3D model in (j) at plains x=600 m, y=0 and 400 m, and z=70 and 125 m.

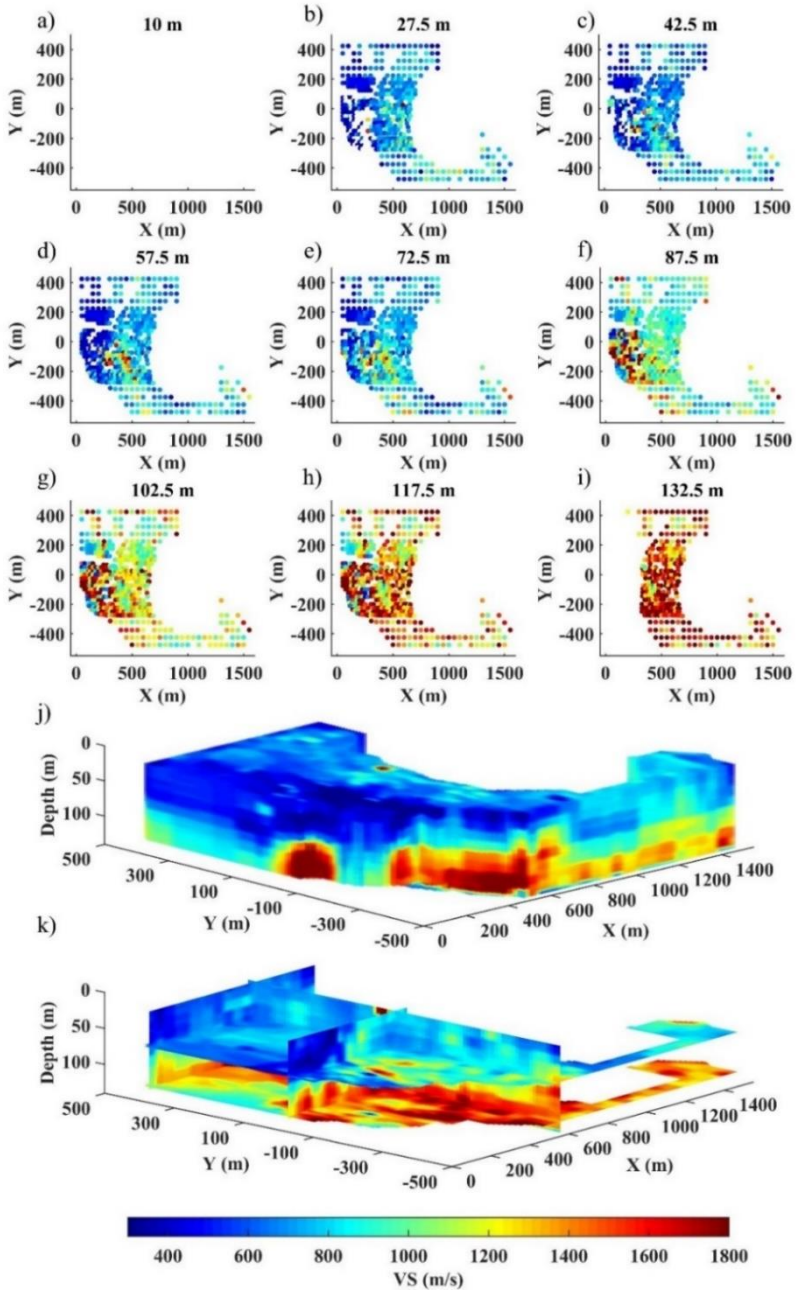

Figure 6.5: The estimated VP model for the Aurignac site obtained by converting the VS results of the LCI using the Poisson's ratios from W/D method in Figures 6.2c and d. (a to i) The horizontal slices at different depths indicated on top of each figure. (j) The pseudo 3D view of the estimated VP after linear interpolation of the 1D models.(k) Isosurfaces obtained from the 3D model in (j) at plains x=600 m, y=0 and 400 m, and z=70 and 125 m.

7. Surface Wave Tomography (SWT)

We develop an SWT workflow that enables the estimation and use of multi-modal surface waves. Also, we integrate the SWT with the W/D method, which enables the estimation of VP in addition to VS model. In the following, we introduce the method in detail and show its application to three industry data sets from section 3.2. The proposed method and its application to the PNG data set is also published in Khosro Anjom et al., (2021).

7.1 Background

The surface wave phase velocity and group velocity tomography are widely applied to reconstruct crust and upper mantle (Ritzwoller and Levshin, 1998; Kennet and Yoshizawa, 2002; Boiero, 2009; Yao et al., 2006; Shapiro et al., 2005; Sabra et al., 2005). Recently, the SWT tomography has become popular also for near-surface characterization using active (Da Col et al., 2019; Socco et al., 2014; Papadopoulou et al., 2018) and passive (Badal et al., 2013; Picozzi et al., 2009) data. Socco et al. (2014) applied SWT to the 2D data from a laterally varying site in New Zealand to estimate the 2D VS model of the first 50 m subsurface. Da col et al. (2020) evaluated the possibility of using the SWT for mineral exploration; they showed the application of the SWT to the data from a mining site in Finland and were able to reconstruct the first 270 m of the VS model of the area. Picozzi et al. (2009) applied the SWT to high-frequency ambient noise data from a test site in Nauen, Germany, and were able to recover the first 25 m of the near-surface model.

The SWT methods are generally composed of three steps (Yoshizawa and Kennett, 2004; Shapiro and Ritzwoller, 2002; Yao et al., 2008). First, many path-averaged DCs with various azimuthal angles are computed using the cross-correlation between records of the couple receivers aligned with a source. Then, the estimated path-averaged DCs are inverted to obtain the phase velocity maps corresponding to various frequencies. Finally, the phase velocity maps' elements at different locations are considered separately and inverted to estimate 1D VS models.

Alternatively, the inversion of the path-averaged DCs can be used to directly estimate the VS model, skipping the phase velocity map estimation (Boschi and Ekstrom, 2002; Boiero,2009; Fang et al., 2015). In particular, the method developed by Boiero (2009) involves the simultaneous tomographic inversion of all path-averaged DCs in the least-square laterally constrained scheme to estimate the VS model. He applied the method to data from Tibetan Plateau to estimate quasi 3D VS model of the crust and upper mantle; the estimated model was in agreement with the estimated model from the application of three-step SWT (Yao et al., 2008).

Surface wave fundamental mode is usually the dominant mode in the recordings and can be efficiently retrieved (e.g., Shapiro et al. 2005). In presence of energetic higher modes within the frequency band of fundamental mode, the higher modes can be damped by time windowing the recordings based on the group velocity of the fundamental mode (Yao et al., 2006). However, including the higher modes in the inversion instead of eliminating them can improve the investigation depth and resolution of the obtained model from surface wave analysis (MacBeth and Burton, 1985; Yoshizawa and Kennet, 2004; Xia et al., 2003; Beaty et al., 2002; Ganji et al., 1998). On the other hand, the separation of the modes using only two receivers recording at a time is not possible unless the modes are isolated prior to the processing stage for DC estimation (Halliday and Curtis, 2008). In the context of earthquake seismology, the separation of modes can be performed using band-pass filters (Båth and Crampin, 1965) or phase-match filtering (Hwang and Mitchell, 1986). However, accurate isolation of higher modes requires surface wave multi-channel analysis (e.g., Nolet, 1975; Nolet and Panza, 1976; Cara, 1978; Mitchel, 1980). We propose a muting strategy based on the multi-channel analysis of the DCs that allows the estimation of various modes of surface wave.

7.2 Method

The proposed workflow is composed of two main parts, one based on local DC analysis (multi-channel method) to estimate the velocity limit separating the different modes of surface wave in the site, and the other SWT. In the local DC analysis part, we also perform the W/D method to estimate a priori Poisson's ratio required for the SWT. The application of the W/D method to estimate a priori Poisson's ratio was explained in section 4.4.

In Figure 7.1, we show the detailed steps of the proposed workflow, where the SWT steps are highlighted in red, and the steps to obtain the velocity limit and Poisson's ratio are shown in green. The proposed method is valid for estimating and

employing various modes of surface waves in the SWT scheme. However, since our applications are restricted to the fundamental and 1st higher modes, the workflow in Figure 7.1 is limited to using the first two modes of surface waves.

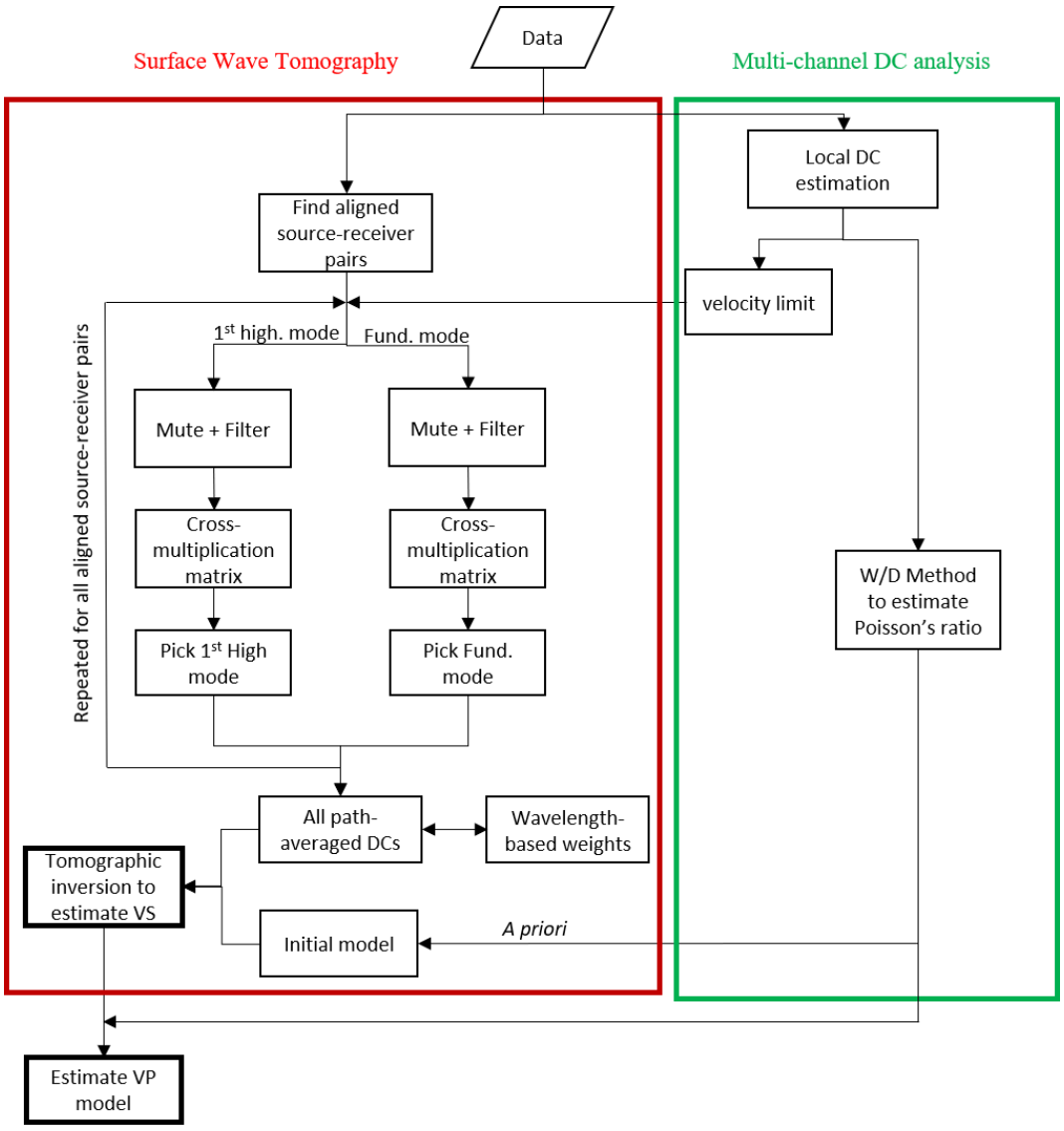

Figure 7.1: The detailed workflow of the SWT, where the steps involving the local DCs are highlighted in green and the SWT steps are shown in red. The local DC analysis provide the trend of various modes which will be used to design a frequency dependent velocity limit that separates them. Also, it is used to estimate the a priori Poisson's ratio. The SWT part is composed of two main steps that involves the path-averaged DC estimations and tomographic inversion to obtain the models. For details regarding various steps of the workflow refer to sections 7.2.1 to 7.2.3.

The method provides the VS and VP models at the location of model grids defined for the tomographic inversion. We use these 1D estimated models to build quasi 2D or 3D VS and VP models. In this section, we first explain the estimation of the velocity limit from the local DCs. Then, we introduce the various steps of path-averaged DC estimations, and we evaluate the path-averaged DC technique using a synthetic example. Finally, we describe various aspects of the tomographic inversion.

7.2.1 Local DC estimation and the Velocity Limit

To compute the DCs, we use the phase-shift method (section 2.3.2.2), with which it is possible to compute the frequency-phase velocity spectrum corresponding to receiver spreads with irregular spacing and separate the different propagation modes. We estimate various fundamental and 1st higher mode DCs corresponding to receiver spreads at different site locations. We then manually design a frequency-dependent velocity limit that best separates the fundamental and 1st higher modes of all DCs. The method is valid if the different modes of DCs are separated. In the presence of modes superpositions, this method can be applied to high frequencies, where the separation is expected. For the application of the SWT method using only the fundamental mode, this step should be neglected.

7.2.2 Path-averaged DC estimation

The first step of the SWT is to estimate the path-averaged DCs. These DCs are estimated using the recordings from receiver couples aligned with a source, in literature also known as the two-station or interferometry method. We implement an automatic algorithm to find the receiver couples aligned with the source at each azimuth angle, considering 1° tolerance for the deviation from a straight path. We filter the traces of the receiver couples, using a zero-phase Gaussian filters. Then, the filtered traces of the receiver couples are cross-correlated and assembled to form the cross-multiplication matrix. We use a 3rd order spline interpolator to convert the cross-multiplication matrix to the frequency-velocity domain. Finally, at each frequency, the phase velocity is picked as the maximum of the cross-multiplication matrix, closest to the reference DC.

Unlike local DC estimation methods that use the recordings from an array of receivers, the path-averaged DC estimation method from couple receivers does not deliver enough resolution to detect and pick multiple modes of surface waves. As a result, in the presence of multiple modes (such as the PNG data set; section 3.2.1),

it is imperative to isolate each mode before performing the recordings' cross-correlation (Halliday and Curtis, 2008). We propose a pre-processing technique based on which the dispersive velocity limit is used to automatically mute the seismic data and isolate multiple modes of the surface waves. We mute the recordings before the application of the two-station method and perform the two-station method separately for the computation of each mode of surface waves. Depending on whether the fundamental mode or the 1st higher mode estimation is intended, we apply the velocity limit as a half-Gaussian mute to the relevant time panel of the pair receivers' recordings.

7.2.2.1 Synthetic example: the path-averaged DC estimation

Here, we show how the path-averaged DCs are estimated in the presence of two modes, through the application of the method to synthetic signals at two locations. We created the two signals containing two events at the expected times of the fundamental and the 1st higher modes of surface waves for the 1D layered system in Figure 7.2a. The signals were obtained by convolving a Morlet wavelet with a time series containing a spike at the expected time for each mode and each frequency and then stacking on the whole frequency band (10-25 Hz). In Figure 7.2a, we show the computed responses at positions 1000 m (T1) and 1200 m (T2). The processing workflow requires a velocity limit, which separates the fundamental and the 1st higher modes. For real data, we estimate the velocity limit from the multi-channel analysis. Here, given the synthetic example, we obtained the velocity limit by averaging the phase velocities of the true fundamental and 1st higher modes at each frequency. In Figure 7.2a, we also show the velocity limit in black; the blue and red hatches below and above the velocity limit are the fundamental and 1st higher mode zones, respectively. We applied the two-station method twice to estimate the fundamental and 1st higher modes of the surface waves.

In Figure 7.2b and c, we show, as examples, the processing steps applied to estimate the 1st higher mode at 10 Hz and fundamental mode at 25 Hz, respectively. First, the velocity limit was transformed into time at the location of each trace (T1 and T2) by dividing the offsets (1000 m for T1 and 1200 m for T2) to velocity limit at the two considered frequencies (690 m/s at 10 Hz and 488 m/s at 25 Hz). Based on the arrival times (1.45 s and 1.74 s for T1 and T2 at 10 HZ, and 2.05 s and 2.46 s for T1 and T2 at 25 Hz), mutes were designed according to the intended mode estimation (first panels of Figure 7.2b for the 1st higher mode estimation at 10 Hz and Figure 7.2c for the fundamental mode estimation at 25 Hz). The traces were multiplied (×) by the muting functions. Then, the muted traces were narrow-band

filtered at the considered frequencies. We performed the filtering in the frequency domain by multiplying a narrow banded zero-phase Gaussian filter centered at the desired frequencies (10 Hz and 25 Hz) to the frequency domain representation of the traces (T1-muted and T2-muted). For a more straightforward representation of the filtering, in the second panels of Figures 7.2b and c, we show the filtering of T1-muted and T2-muted in the time domain as the convolution (*) to the 10 Hz and 25 Hz filters. Finally, the muted and filtered traces were cross-correlated (third panels in Figure 7.2b for the 1st higher mode at 10 Hz and Figure 7.2c for the fundamental mode at 25 Hz). The processing method in Figures 7.2b and c shown at 10 Hz and 25 Hz for the 1st higher and fundamental modes was repeated for all frequencies within the band 10 to 25 Hz. The cross-correlated signals were assembled to form the cross-multiplication matrices in the first panels of Figures 7.2d and e. Knowing the distance between the two receivers (200 m), we used a 3rd order interpolator to transform the cross-multiplication matrix as a function of frequency and time delay to the same matrix as a function of frequency and velocity. In the second panel of the Figures 7.2d and 7.2e, we show the estimated cross-multiplication matrices to estimate the fundamental and 1st higher modes, respectively; the trends of the true fundamental and 1st higher modes (blue and red solid lines) are well obtained by the two matrices, except for the 1st higher mode above 23 Hz (second panel in Figure7.2d).

It is noteworthy that the synthetic example in Figure 7.2 was designed to show the steps of the path-averaged DC estimation and the muting strategy used to recover the correct cross-multiplication matrix corresponding to each surface wave mode. The very close maxima obtained in the cross-multiplication matrix of the fundamental mode (second panel of Figures 7.2e) are caused by the selected parameters of the synthetic example. In the scope of seismic exploration, this issue is usually observed when the method is applied to the recording of very distant receiver couples. In these situations, unless a very accurate reference local DC is available, the DC should not be picked to mitigate the picking of the wrong maxima.

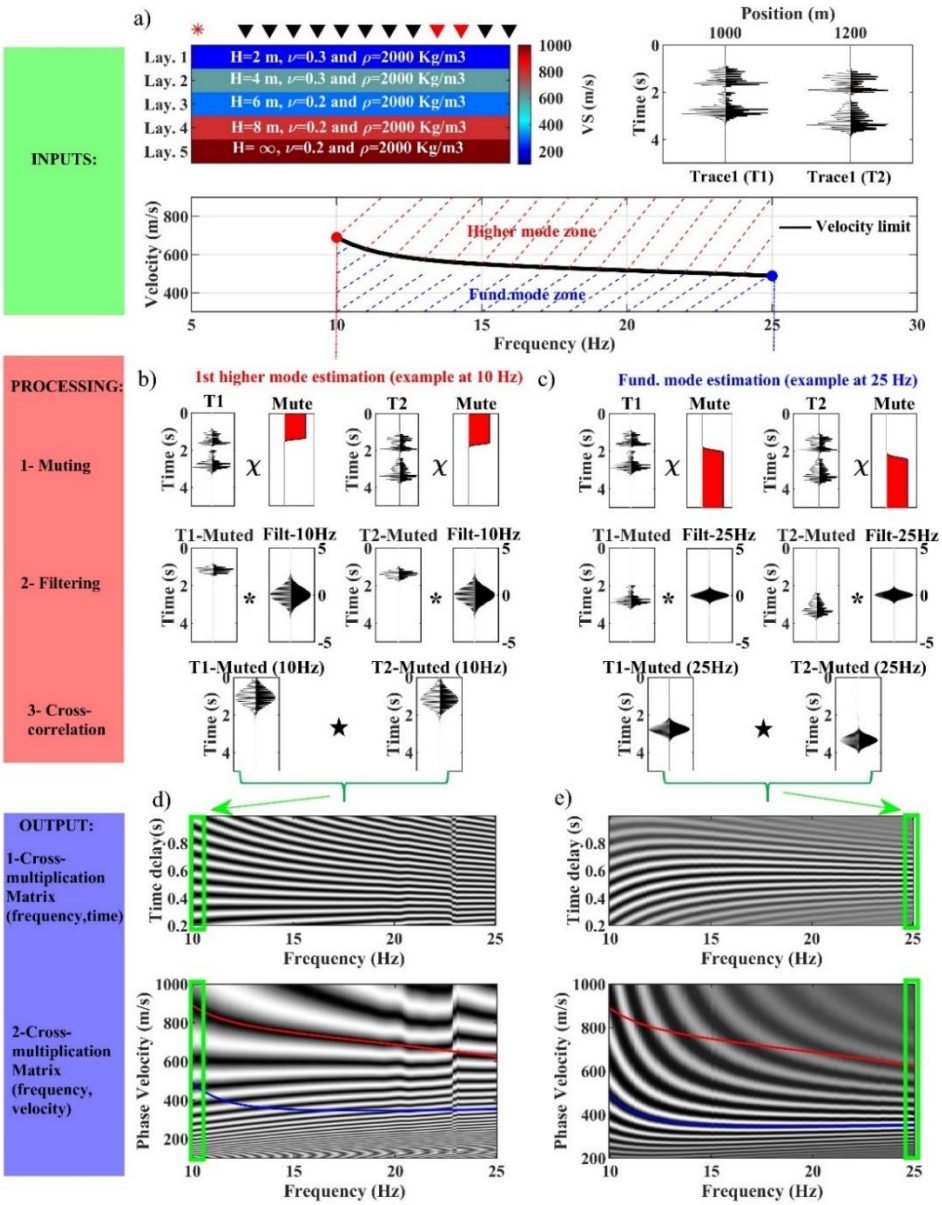

Figure 7.2: The fundamental and 1st higher mode estimation of a synthetic example. (a) The inputs of the method: the model parameters of the laterally invariant example; the computed responses at location 1000 and 1200 m from the source; the velocity limit separating the fundamental and the 1st higher mode zone. (b) The steps for phase velocity estimation of the 1st higher mode at 10 Hz. (c) The steps for the phase velocity estimation of the fundamental mode at 25 Hz. (d) The estimated cross-multiplication matrices in the frequency-time delay domain and the frequency-velocity domain aim to estimate the 1st higher mode within 10 – 25 Hz. (e) The estimated cross-multiplication matrices in the frequency-time delay domain and the frequency-velocity domain aim to estimate the fundamental mode within 10 – 25 Hz.

7.2.3 Tomographic inversion

The tomographic inversion is based on Boiero (2009). Concerning the formulation, we included higher modes and modified the algorithm to support parallel computing. Also, we introduced wavelength-based weighting of the data points, which increases the investigation depth and vertical resolution of the obtained model (Khosro Anjom and Socco, 2019). The only inputs of the tomographic inversion are the path-averaged DCs and a reference model.

7.2.3.1 Reference Model

The model is a regular grid of 1D models (model points). The parameters of the model are the thickness, VS, Poisson's ratio, and density. The only parameter that updates in the inversion is VS, while the others are fixed a priori; thus, the number of unknowns of the inversion is the number of the model points multiplied by the number of the layers plus one (the half-space). We use constant thicknesses for the layers within the investigation depth. We define the initial VS model based on the trend of the selected VS models from the Monte Carlo inversion of the reference local fundamental mode. Considering negligible lateral variations for the Poisson's ratio, we use the reference Poisson's ratio from the W/D method (explained in section 4.4) as prior information for the SWT inversion. Although the inversion is not very sensitive to Poisson's ratio, a priori Poisson's ratio helps the inversion to get a more consistent and accurate VS model. The density has a minor effect on the inversion, and it is selected based on the information available for the site's formations.

7.2.3.2 Forward operator

In this stage, the synthetic path-averaged DCs corresponding to the observed paths are obtained. The algorithm computes the local 1D synthetic DCs at each model point, using a Haskell (1953) and Thomson (1950) forward model, developed by Maraschini (2008) in MATLAB. Next, Each path is discretized to evenly spaced points. For each point and at each frequency, the slowness is computed as the bilinear interpolation between the slowness of the four adjacent model points. We then compute the path-averaged synthetic slowness as the mean slowness of all discretized points along the path at each frequency as:

$$P(f)_{AB} = \frac{\sum_{i=1}^{n} P_i(f)}{l_{AB}}, \tag{7.1}$$

where P_i is the computed slowness for the discretized point i. The n is the number of discretized points along the straight path AB with length of l_{AB}. The synthetic DC computation is performed similarly for the higher surface modes.

7.2.3.3 Inversion scheme

The experimental DCs are transformed to slowness and assembled in a single vector as:

$$\mathbf{p_{obs}} = [\mathbf{p_{fund.}}; \mathbf{p_{high.}}], \tag{7.2}$$

where $\mathbf{p_{fund.}}$ and $\mathbf{p_{high.}}$ are the estimated slowness relevant to the fundamental and the 1st higher modes. The penetration depth of the surface waves is directly related to the wavelength. The non-uniform sampling of the DC data in terms of wavelength usually drives the inversion algorithms to the shallowest parts of the subsurface (Khosro Anjom and Socco, 2019). We associate a wavelength-based weight to each DC data point, correcting this non-uniformity in depth. For the jth DC, we compute the weights of the ith data point as:

$$w_{i,j} = \frac{\Delta\lambda_{i,j}}{\Delta\lambda_{j,max}}, \tag{7.3}$$

where the $\Delta\lambda_{i,j}$ is the wavelength distance from the closest data point to data point i. The larger the wavelength distance of the data points, the higher the weight will be. The weights of each DC are normalized to the maximum registered weight $\Delta\lambda_{j,max}$. The normalization of the weights assures an equal rank of the various DCs in the inversion process. For each DC's computation, if many shots from different source locations are stacked, the individual shots can be used to compute a standard deviation for each data point, representing the uncertainty. The data uncertainties are important in inversion algorithms as they can limit the impact of the erroneous data points. We define the covariance matrix corresponding to the data points $\mathbf{p_{obs}}$ as the diagonal matrix:

$$\mathbf{C_{obs}} = \begin{bmatrix} \frac{\sigma_{1,1}^2}{w_{1,1}} & 0 & 0 & 0 & \cdots & 0 \\ 0 & \frac{\sigma_{2,1}^2}{w_{2,1}} & 0 & 0 & \cdots & 0 \\ 0 & 0 & \ddots & 0 & \cdots & 0 \\ 0 & 0 & 0 & \frac{\sigma_{1,2}^2}{w_{1,2}} & \cdots & 0 \\ \vdots & \vdots & \vdots & \vdots & \ddots & \vdots \\ 0 & 0 & 0 & 0 & 0 & \frac{\sigma_{i,j}^2}{w_{i,j}} \end{bmatrix}, \quad (7.4)$$

where the $\sigma_{i,j}$ and $w_{i,j}$ are the standard deviation and the normalized wavelength-based weights of the *i*th data point of the *j*th DC.

We use a weighted least-square method to invert the estimated DCs, which involves minimizing the misfit function Q:

$$Q = \left[(\mathbf{p_{obs}} - \mathbf{p(m)})^{\mathbf{T}}\, \mathbf{C_{obs}^{-1}}\, (\mathbf{p_{obs}} - \mathbf{p(m)}\right] + \left[\left(-\mathbf{R_p m}\right)^{\mathbf{T}} \mathbf{C_{Rp}^{-1}} (-\mathbf{R_p m})\right], \quad (7.5)$$

where the first term is related to the data misfit and the second term is the spatial regularization. The spatial regularization helps to retrieve consistent results (Auken and Christiansen, 2004; Boiero, 2009) and is obtained by imposing constraints on the variations between the VS of the adjacent 1D models (Boiero, 2009). $\mathbf{R_p}$ is the spatial regularization matrix, which relates the model parameters of the adjacent model points, and the $\mathbf{C_{Rp}}$ the regularization covariance matrix defines the strength of the spatial constraints. The $\mathbf{m}$ is the vector of the model parameters, and $\mathbf{p(m)}$ is the vector of the synthetic path-averaged DCs, corresponding to the experimental data points $\mathbf{p_{obs}}$. The $\mathbf{C_{obs}^{-1}}$ is the reciprocal of the covariance matrix shown in equation (7.4). We use the weighted damped least-square method (Marquart, 1963) to iteratively update the model as:

$$\mathbf{m_{n+1}} = \mathbf{m_n} + \Big(\left[\mathbf{G^T C_{obs}^{-1} G} + \mathbf{R_p^T C_{Rp}^{-1} R_p} + \boldsymbol{\lambda} \mathbf{I}\right]^{-1} \times \left[\mathbf{G^T C_{obs}^{-1}} (\mathbf{p_{obs}} - \mathbf{p(m)}) + \mathbf{R_p^T C_{Rp}^{-1}} (-\mathbf{R_p m_n})\right]\Big), \quad (7.6)$$

where $\mathbf{G}$ the Jacobian matrix, evaluates the sensitivity of the DCs to the model parameters. $\mathbf{m_n}$ and $\mathbf{m_{n+1}}$ are the previous and updated model vectors, respectively.

We follow the same approach explained in section 6.2.3 to select the constraints levels.

7.2.3.4 Synthetic example: The impact of higher modes and wavelength-based weights on SWT

Here, we show the application of the surface wave tomography (SWT) to a synthetic 2D model to evaluate the effect of including 1st higher mode, as well as the impact of imposing the wavelength-based weights on the tomographic inversion. In Figure 7.3, we show the true synthetic model, which consists of 101 1D models, evenly spaced. Along the 1 km line, we defined 612 DC paths with lengths ranging from 10 to 60 m.

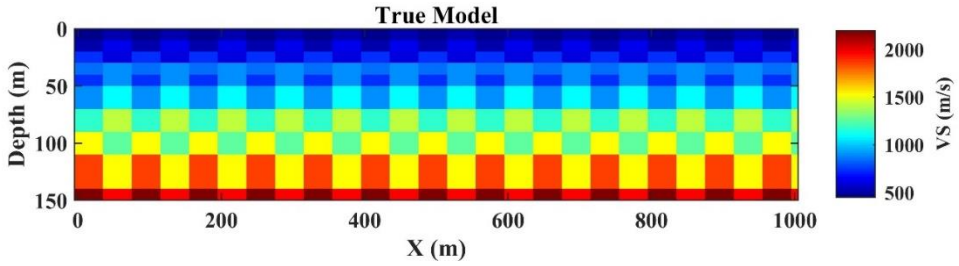

Figure 7.3: The true VS model of synthetic model.

We computed the synthetic DCs corresponding to each path within the frequency range of 5 to 30 Hz. Figure 7.4a shows the computed path-averaged surface wave fundamental and the 1st higher modes in blue and red, respectively. In Figure 7.4b and c, we show the wavelength distribution corresponding to the data points of the fundamental and 1st higher modes, respectively. The fundamental mode wavelengths are limited to 200 m of wavelength, while the 1st higher mode has wavelength coverage up to 300 m of wavelength.

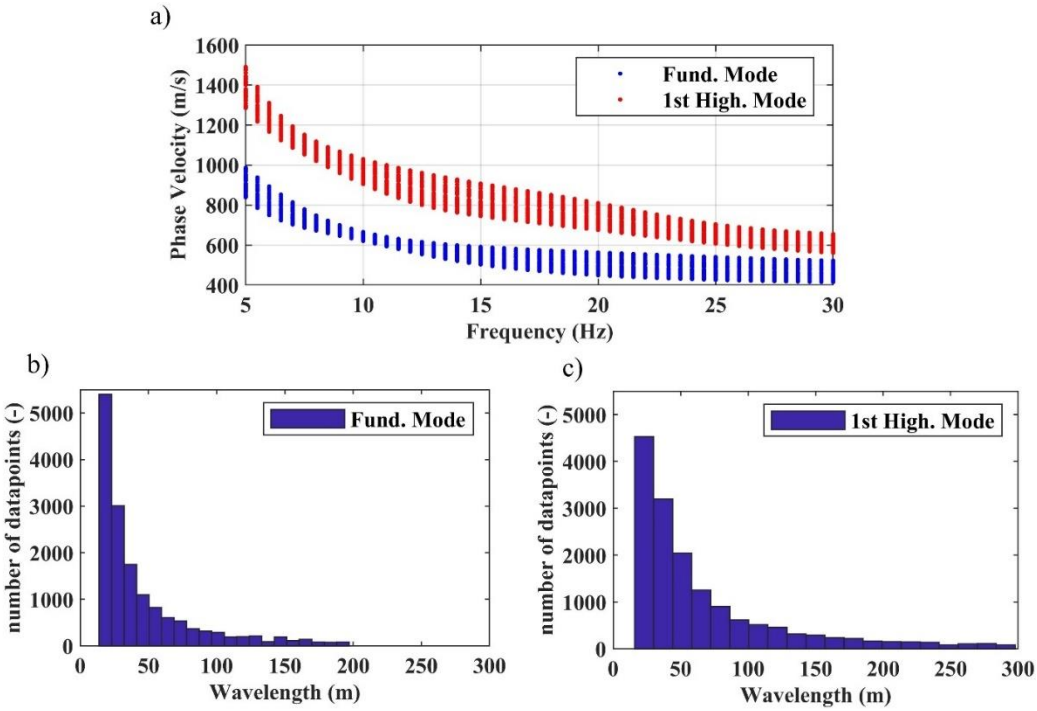

Figure 7.4: (a) The 612 computed fundamental and the 1st higher modes along the 1 km of the 2D synthetic example in Figure 7.3. All DCs are computed between 5 to 30 Hz. (b) The wavelength distribution of the computed fundamental mode DCs. (c) The wavelength distribution of the computed 1st higher mode DCs.

In Figure 7.5a, we show the initial model used for the tomographic inversion. In Figure 7.5b, we show the results of the inversion using only the fundamental mode and without imposing weights to the inversion. The results show a reasonable estimation of the first 70 m; however, the lateral and vertical variations are not fully recovered within the first 70 m of depth.

Next, we inverted the data using both the fundamental and 1st higher modes, again without imposing weights to the data points (Figure 7.5c). The inversion result shows much more accuracy in recovering the first 70 m. Also, the investigation depth is enhanced with respect to the fundamental mode inversion in Figure 7.5b. In Figure 7.5d, we show the result of the inversion using the fundamental and the 1st higher modes and by imposing wavelength-based weights, where it shows the successful recovery of the model up to 140 m in depth.

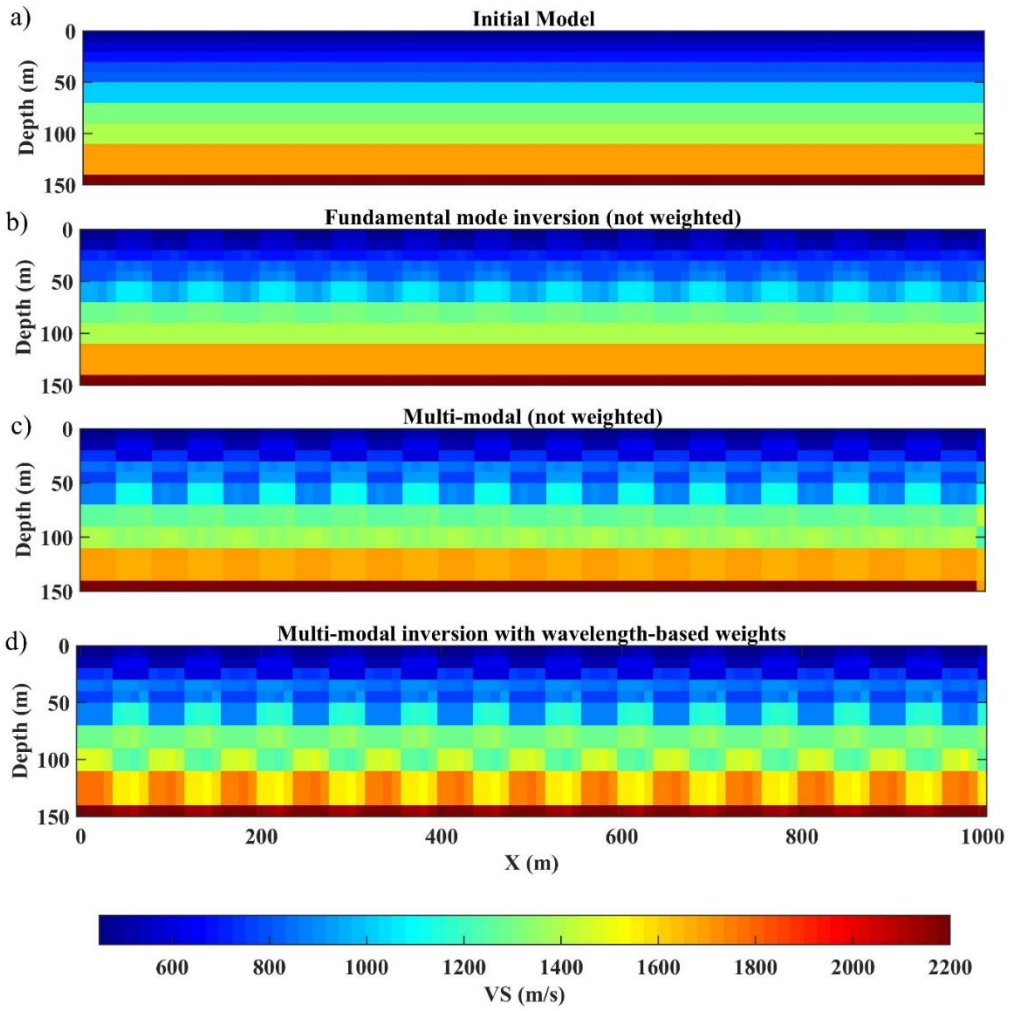

Figure 7.5: The results of the tomographic inversion performed on the synthetic model in Figure 7.3. (a) The initial model. (b) The estimated VS model from the non-weighted fundamental mode inversion. (c) The estimated VS model from the non-weighted multi-modal inversion. (d) The estimated VS model from weighted (wavelength-based) multi-modal inversion.

7.3 Application to field data sets

In this section, we show the application of the SWT to three industry data sets. For the PNG data set, we estimate and use the fundamental and 1st higher modes, while for Aurignac, we use only the fundamental mode to estimate the VS and VP models. Finally, we show the SWT application to oil and gas exploration data set to estimate the near-surface VS model.

7.3.1 PNG

7.3.1.1 Local DCs: Velocity limit and Poisson's ratio estimation

We estimated local DCs using various sets of sources and receivers of the data set. Figures 7.6a and b show the frequency-velocity spectrum corresponding to two different sources and receivers' deployment geometries. The estimated fundamental mode and the 1st higher mode are shown in blue and red, respectively.

In Figure 7.6c, we show all estimated fundamental and 1st higher modes of surface waves using the multi-channel analysis. We selected the reference fundamental and 1st higher modes amongst local DCs based on the frequency band. For the reference fundamental mode, we considered the broadband DC that also contained low-frequency elements. In Figure 7.6c, we show the reference fundamental and 1st higher modes with dashed blue and red lines, respectively. We used these DCs to manually design a velocity limit that separates the fundamental and 1st higher modes of the data (Figure 7.6c, in black). We will use the velocity limit in the SWT processing step to separate the modes of surface waves.

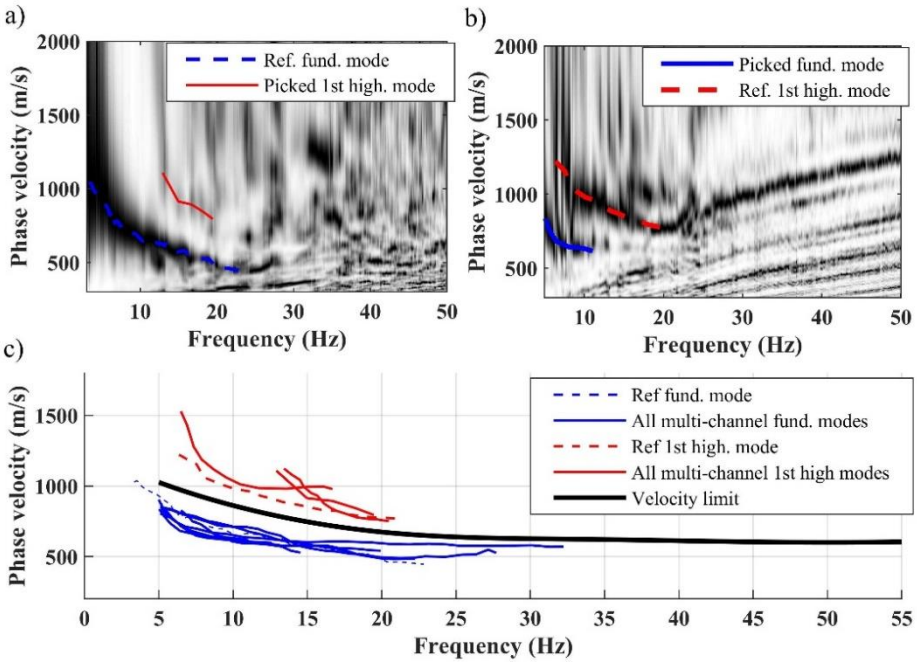

Figure 7.6: The multi-channel analysis of the PNG data set applied to the recordings of various receiver spreads. (a) The spectrum used to compute the reference fundamental mode. (b) The spectrum used to compute the reference 1st higher mode. (c) All estimated fundamental (in blue) and 1st higher modes (in red) using the multi-channel method, and the dispersive velocity limit (in black).

In Figure 7.7, we show the W/D method's steps (section 4.4) applied to the reference fundamental mode (Figure 7.6a). Considering variable Poisson's ratio in a wide range (0.1 to 0.45), we inverted the reference fundamental mode using the Monte Carlo inversion. We used the statistical Fisher test with a low level of confidence (0.05) to select all models that belong to the best-fitting model population. In Figures 7.7a and b, we show the selected DCs and the corresponding VS models. In Figure 7.7c, we show the selected and the reference VSZ models. The estimated VSZ and the reference DC were used to compute the experimental W/D relationship (Figure 7.7d). We then assessed the W/D relationship's sensitivity to Poisson's ratio, which led to VPZ estimation. Next, we used equations (4.9) and (4.10) to transform the VSZ and VPZ into interval VS and VP (Figure 7.7e). Finally, having estimated the VS and the VP model, we computed the averaged 1D Poisson's ratio (the blue curve in Figure 7.7f) corresponding to the investigation area.

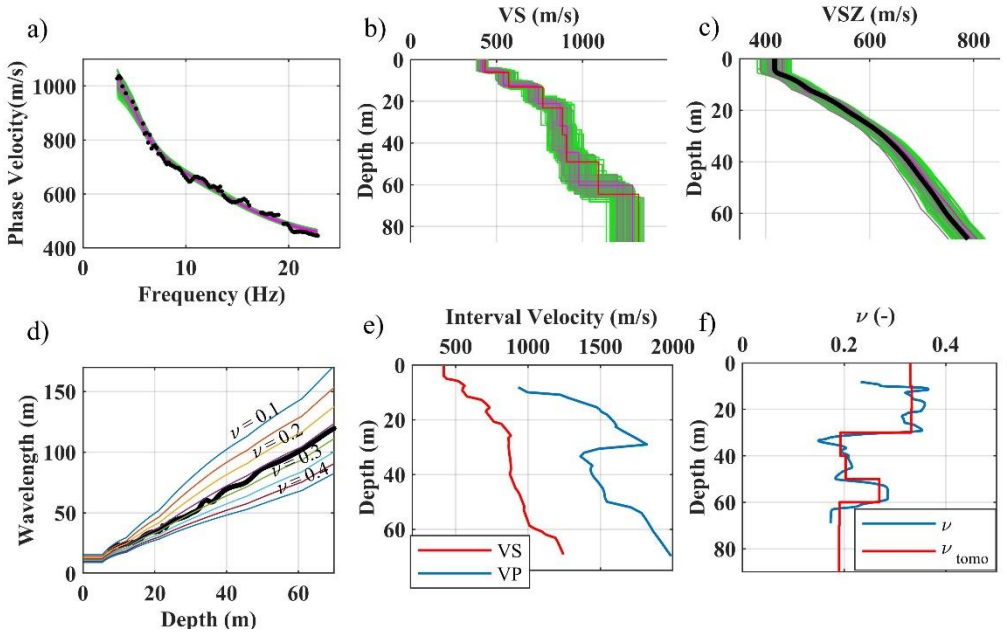

Figure 7.7: W/D method to obtain the reference Poisson's ratio corresponding to the investigation area of the PNG site. (a) the reference fundamental mode with the DCs of the selected models. (b) The VS of the selected model. (c) The VSZ of the selected models, with the reference VSZ shown in black. (d) The estimated W/D relationship shown with the synthetic W/D relationships, each obtained from a constant Poisson's ratio. (e) The estimated VS and VP models. (f) The estimated Poisson's ratio corresponding to the reference fundamental mode in blue and the adopted Poisson's ratio (averaged and extrapolated) for the tomographic inversion in red.

7.3.1.2 Path-averaged DCs

In total, 505 possible paths were registered for the data set. We used the velocity limit obtained in Figure 7.6c to isolate the fundamental and 1st higher mode of the surface wave. Figure 7.8 shows two examples of the processing method applied to the same receiver recordings from the data, for picking the fundamental mode (Figure 7.8a and b) and 1st higher mode (Figure 7.8c and d). We only picked the data points relevant to wavelengths smaller than twice the receiver pair's distance (half-wavelength rule, Heisey et al., 1982; Nazarian et al., 1983; Yao et al., 2006). In Figures 7.8a and c, we show the half-wavelength line in white. We also show the reference fundamental and 1st higher modes obtained from the multi-channel analysis; we used the reference DCs to locate the correct trend when picking the path-averaged DCs.

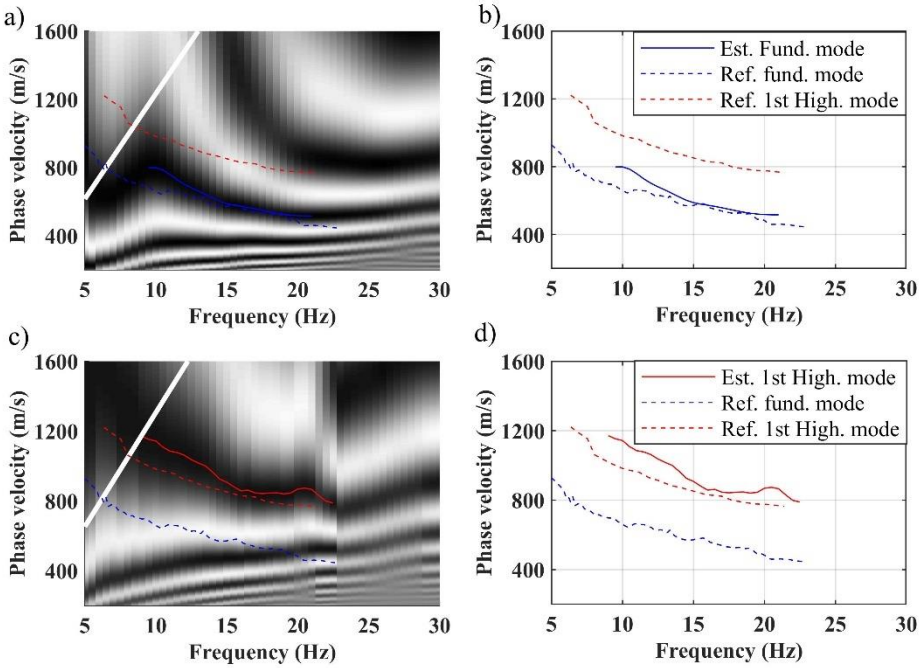

Figure 7.8: *Example fundamental and 1st higher mode estimations from the PNG data set. The dashed lines are the reference DCs obtained in the multi-channel analysis of the PNG data set (Figure 7.6). (a) The fundamental mode cross-multiplication matrix, where the white line is the half-wavelength limit. (b) The estimated fundamental mode from the cross-multiplication matrix in (a). (c) The 1st higher mode cross-multiplication matrix, where the white line is the half-wavelength limit (d) The estimated 1st higher mode from the cross-multiplication matrix in (c).*

In total, we computed 198 fundamental modes and 168 1st higher modes. The remaining paths presented a noisy cross-multiplication matrix. As a result, they were discarded from the data. In Figures 7.9a and b, we show all estimated DCs and the corresponding data coverage (paths). In Figure 7.9c, we show the azimuthal illumination of the estimated DCs as a polar plot; most of the paths show the azimuth angles between 0 to 25° and 150 to 179°.

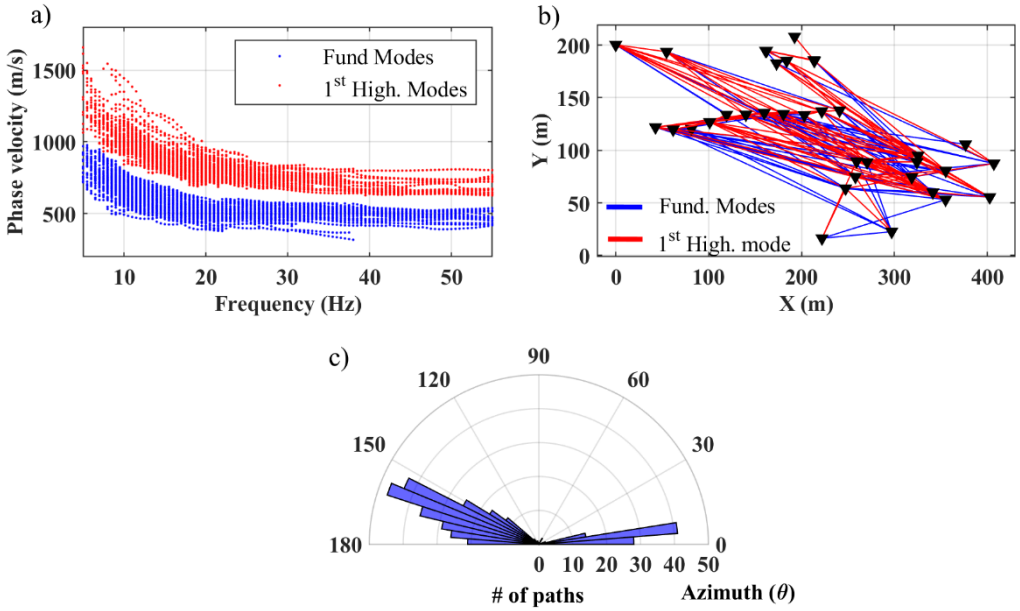

Figure 7.9: (a) The estimated path averaged DCs for the PNG data set. (b) The observed paths of the estimated DCs in (a). (c) The azimuthal illumination. In (c), the numbers around the greatest circle are the angles, and the smaller circles show the number of available paths.

The resolution and investigation depth of the inversion is directly related to the wavelength coverage of the estimated DCs. The wavelength coverage for 3D data can be evaluated as pseudo-slices (Da col et al., 2019), in which, for a wavelength range, the available paths are plotted with a color corresponding to the average phase velocity (apparent phase velocity). In Figures 7.10a to f, we show the fundamental modes' pseudo-slices corresponding to six wavelength ranges. The pseudo-slices are useful tools to locate possible lateral variations or outliers that do not corroborate with the apparent phase velocity of similar paths. For example, in Figure 7.10d, a significant velocity contrast is observed, indicating a considerable lateral variation. Figure 7.10a shows inadequate coverage for the wavelength range

of 0-20 m; thus, a low resolution should be expected in recovering the first few meters of the model. The wavelength coverage shows the highest number of paths between 20 to 150 m (Figures 7.10b to d), while the coverage vanishes for the wavelengths greater than 200 m (Figure 7.10f).

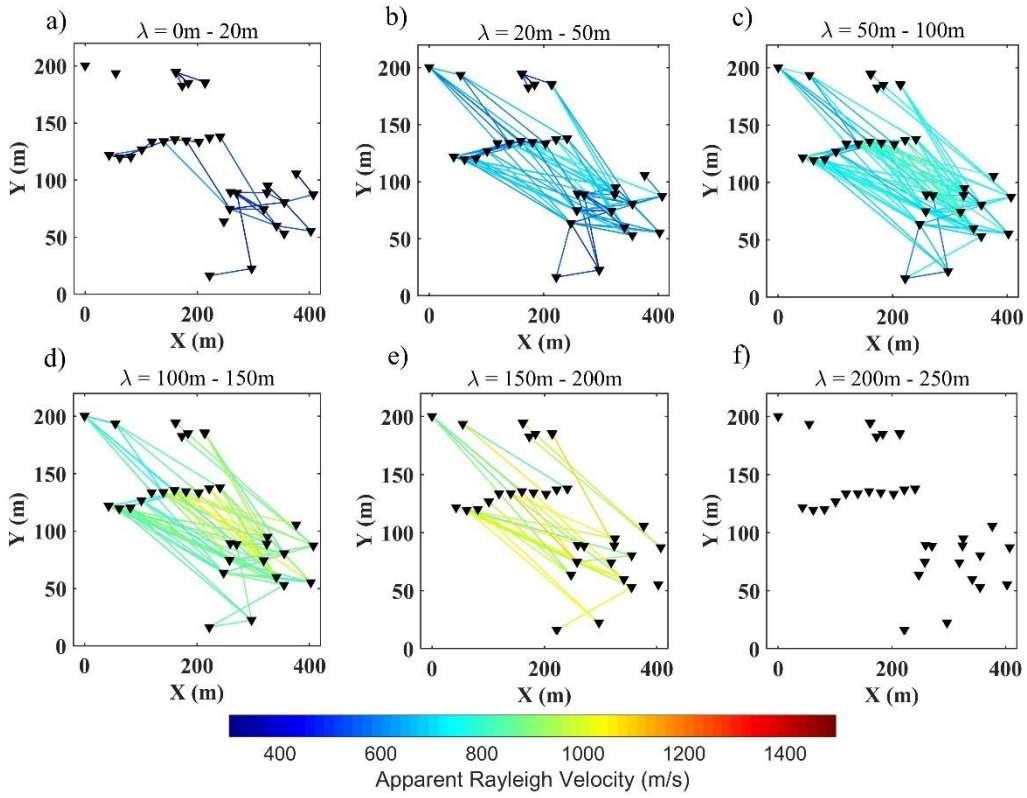

Figure 7.10: The data coverage of the estimated surface wave fundamental modes of the PNG data set (Figure 7.9a) as pseudo-slices corresponding to different wavelength intervals between: (a) 0-20 m. (b) 20 to 50 m. (c) 50 to 100 m. (d) 100 to 150 m. (e) 150 to 200 m. (f) 200 to 300 m.

In Figures 7.11a to f, we show the pseudo-slices corresponding to the 1st higher modes within the same six wavelength ranges as we used for the fundamental mode (Figure 7.10). Similar to fundamental modes, for the wavelength range between 0 to 20 m, the wavelength coverage of the 1st higher mode is limited to a few paths (Figure 7.11a). The coverage reaches its maximum between 20 to 100 m of wavelength (Figures 7.11b and c), and it declines afterward. Unlike fundamental modes, the 1st higher mode shows coverage up to 300 m of wavelength (Figure 7.11f).

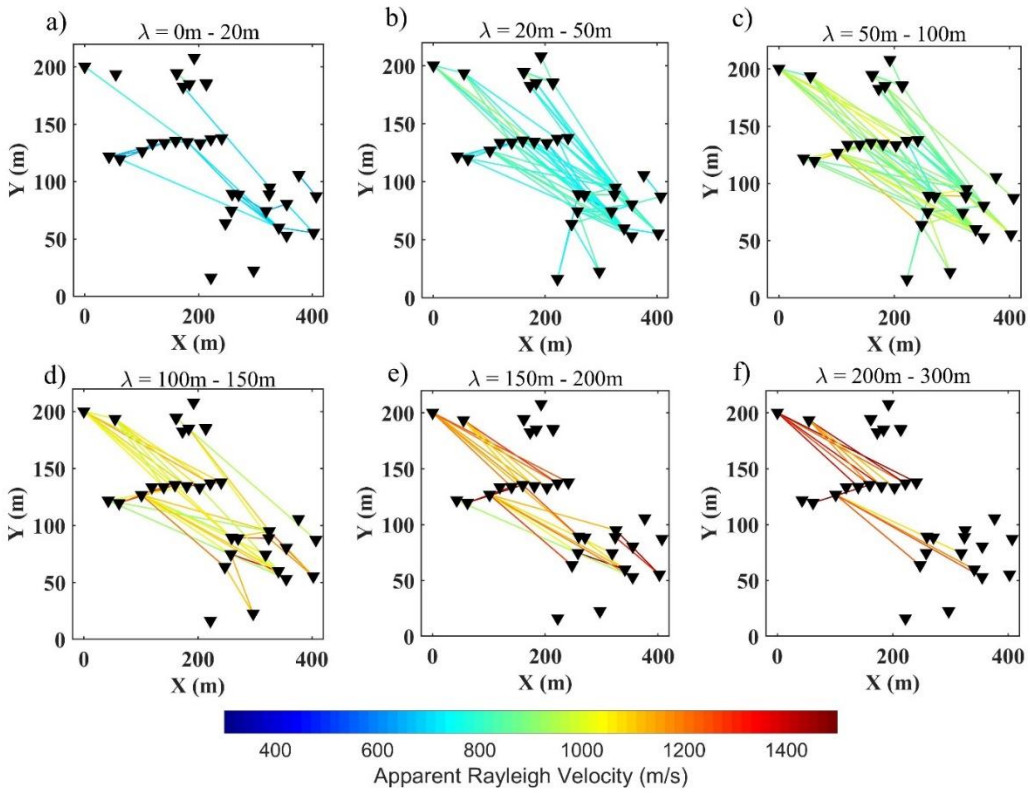

Figure 7.11: The data coverage of the estimated surface wave 1st higher modes of the PNG data set (Figure 7.9a) as pseudo-slices corresponding to different wavelength intervals between: (a) 0-20 m. (b) 20 to 50 m. (c) 50 to 100 m. (d) 100 to 150 m. (e) 150 to 200 m. (f) 200 to 300 m.

7.3.1.3 The reference model

We defined the 3D model consisting of 152 1D models. Each 1D model was consisting of 9 layers overlying the half-space with a constant thickness of 10 m. The initial model corresponds to 1520 VS unknowns. The initial VS model was selected from the estimated VS model of the MCI (Figure 7.7e). The W/D method provided the Poisson's ratio for every 10 cm depth interval between 10 to 70 m from the surface. The values were averaged within 10 m intervals to obtain Poisson's ratio corresponding to each model layer. We extrapolated the Poisson's ratio to cover the full 90 m required for the inversion. In Figure 7.7f, we show the adopted Poisson's ratio for the tomographic inversion in red. Geological properties of the very shallow sub-surface of a forest suggest very loose and unconsolidated soil. As a result, we considered a low density of 1,400 kg/m3 for the first layer of the model. The density of the rest of the layers and the half-space was set at 1,800 kg/m3.

We computed the number of DC paths crossing each model point, disregarding the wavelength range of the DCs. In Figure 7.12, we show the obtained data coverage on the model, where the white color stands for zero path crossing the model points. The maximum data coverage is obtained in the center of the model. Except for the north-west, the data coverage on the model's edges is minimal, suggesting a lower resolution in recovering the VS of these model points.

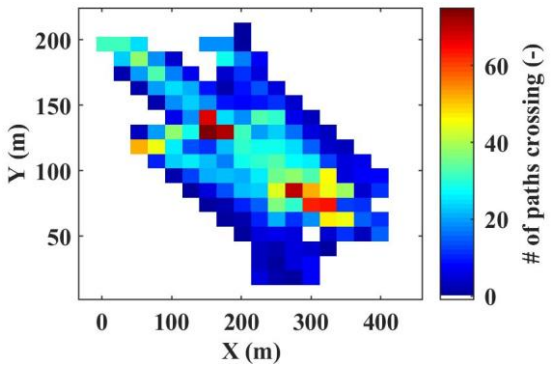

Figure 7.12 The data coverage on the selected reference model for the tomographic inversion of the PNG data set.

7.3.1.4 Results

We imposed 100 m/s lateral constraints to the inversion, which did not significantly impact the residual misfit of the DCs compared to the unconstrained inversion. In Figure 7.13, we show the horizontal slices of the estimated VS model corresponding to the different layers. In Figures 7.13d to g, the estimated VS model shows a velocity contrast between the east and the west.

We used the reference Poisson's ratio (blue curve in Figure 7.7f) to transform the estimated VS model into the VP model (Figure 7.14). The estimated VP's depth range depended on the estimated VS from SWT and the reference Poisson's ratio from the W/D method. The estimated Poisson's ratio was available in a shorter depth range (10 to 70 m) compared to the estimated VS (0 to 90 m). As a result, the estimated VP in Figure 7.14 is limited to 10 to 70 m of depth. The shallow aquifers are very common in the investigation area, given the intense rain in the region, which is usually more than 6000 mm per year (McAlpine et al., 1983). The shallow saturated media are the main reason for the high VP between 10 to 30 m of the subsurface (Figures 7.14a and b). Then, following the drop in Poisson's ratio (Figure 7.7f), the VP decreases (Figure 7.14c). This drop in Poisson's ratio and VP can be due to clay-rich soil below the aquifer, creating an unsaturated environment

below 30 m. Afterward, the VP gradually increases until it reaches the maximum velocity (Figure 7.14f) at depth 60 to 70 m, which we believe coincides the era bed formations. This formation is mainly composed of sandstone, siltstone, mudstone, conglomerates with P-wave velocity of about 2000 m/s (Craig and Warvakai, 2009). We estimated a single reference Poisson's ratio by assuming negligible lateral variations. As a result, the lateral variations of the estimated VP were solely related to the estimated VS, and the lateral variations of the Poisson's ratio were not accounted for in the VP estimation.

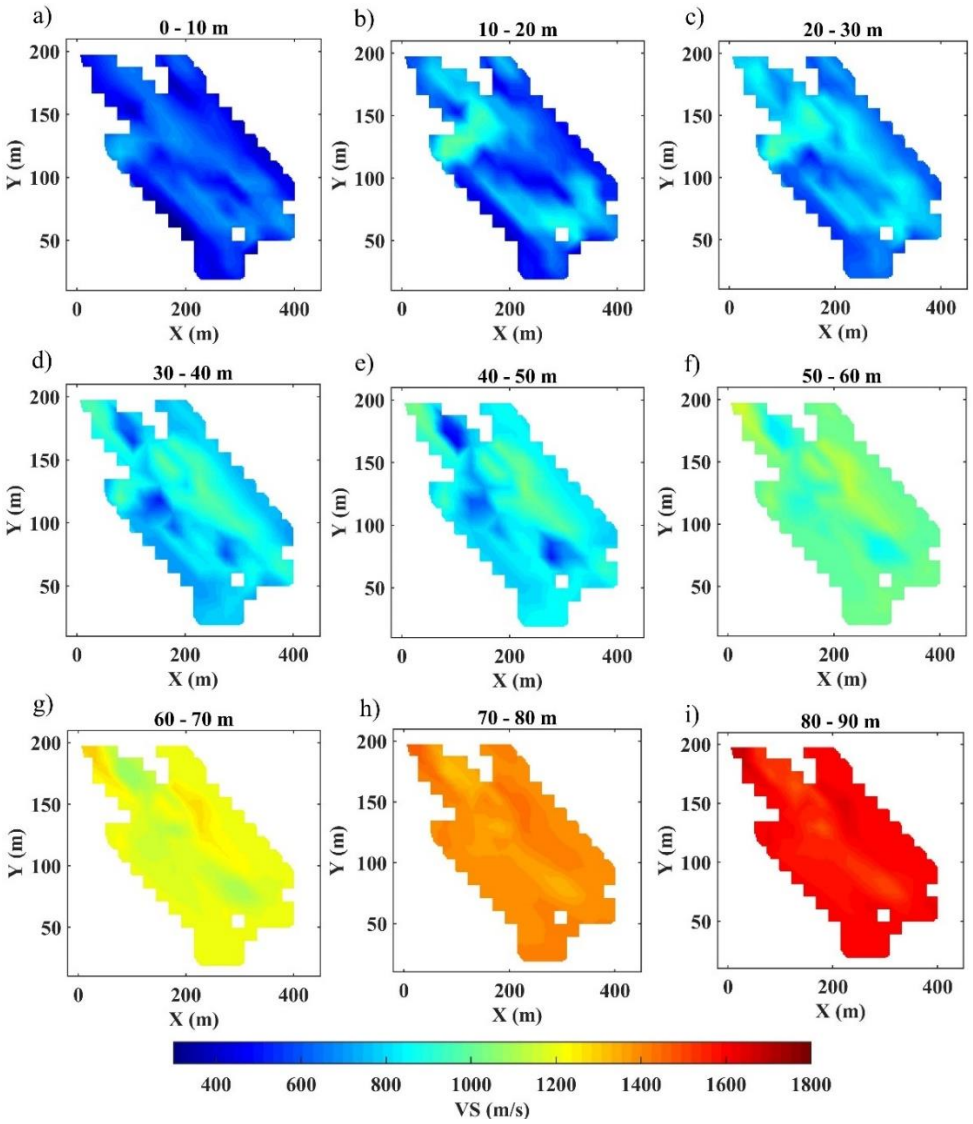

Figure 7.13 The estimated VS model for the PNG data set at depth: (a) 0 to 10 m. (b) 10 to 20 m. (c) 20 to 30 m. (d) 30 to 40 m. (e) 40 to 50 m. (f) 50 to 60 m. (g) 60 to 70 m. (h) 70 to 80 m. (i) 80 to 90 m.

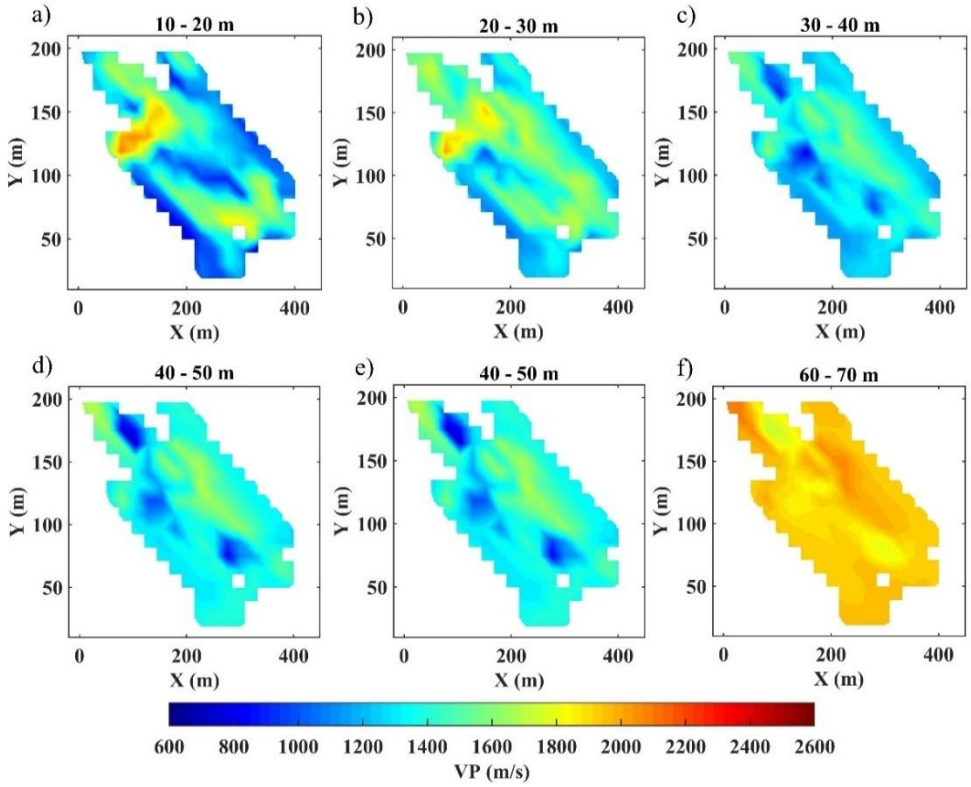

Figure 7.14 The estimated VP model for the PNG data set between 10 to 70 m using the estimated VS model in Figure 7.13 and the reference Poisson's ratio in Figure 7.7f. (a) 10 to 20 m. (b) 20 to 30 m. (c) 30 to 40 m. (d) 40 to 50 m. (e) 50 to 60 m. (f) 60 to 70 m.

The laterally constrained tomographic inversion well converged, and the synthetic DCs showed a proper fitting compared to the experimental ones. Figure 7.15 shows example comparisons between the synthetic DCs from the last iteration of the inversion and the experimental DCs, where the four fundamental modes and three 1st higher modes are displayed with distinct markers and colors.

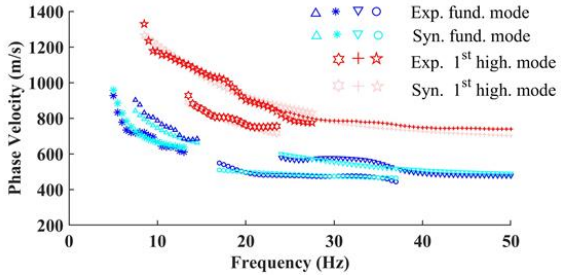

Figure 7.15 The example comparison between the experimental path-averaged and synthetic DCs from the tomographic inversion of the PNG data set. Different markers represent different DCs, while the different colors separate the synthetic and experimental data, as well as the fundamental and the 1st higher modes.

To better evaluate the impact of the wavelength-based weights on the DC fittings, we computed the residual misfit as:

$$\mathbf{r} = \mathbf{c}_{syn} - \mathbf{c}_{exp}, \tag{7.7}$$

where $\mathbf{c}_{syn}$ and $\mathbf{c}_{exp}$ are the vectors of synthetic (last iteration) and experimental phase velocities. In Figures 7.16a and b, we show the boxplot of the residuals for the non-weighted and weighted SWT, respectively. A full description of the boxplot figure was given in section 5.2.2. We divided the residuals based on the wavelengths of the experimental data points to analyze the misfit within different ranges of wavelengths.

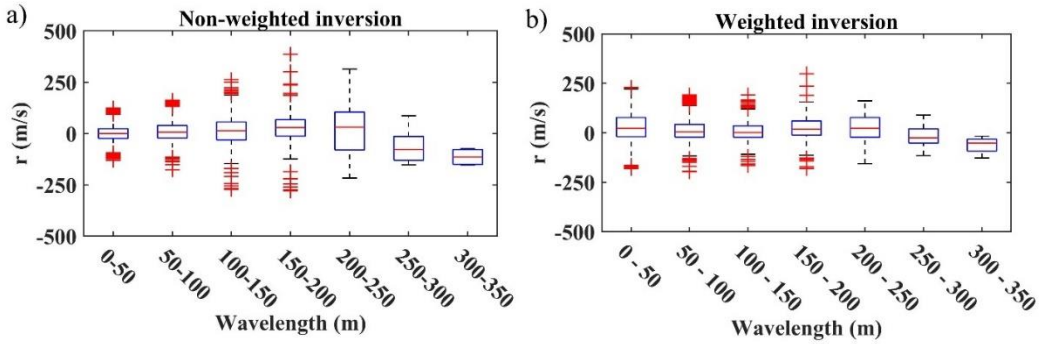

Figure 7.16: The box plot showing the residuals at the last iteration of SWT applied to the PNG data set within different wavelength ranges for: (a) non-weighted inversion, and (b) inversion with wavelength-based weights

For data points with wavelengths between 0 to 50 m, the non-weighted inversion (Figure 7.16a) shows slightly lower residuals compared to the weighted inversion

(Figure 7.16b); however, for the rest of the data points with wavelengths larger than 50 m, the weighted inversion shows considerably lower misfit. Also, the negative distribution of residuals (over-estimation) for the non-weighted inversion is significantly damped when weighted inversion is used. The outliers in both cases are mainly from the paths close to the model's edges, where inadequate data coverage was available (Figure 7.12).

7.3.1.5 Checkerboard Test

We performed the checkerboard test to assess the spatial resolution of the final model. We perturbed the estimated *VS* model (Figure 7.13) 10%, negatively and positively. In Figures 7.17a and b, we show the horizontal sections of the perturbations. The pattern of the perturbation alternated every 40 m. So, the first 40 m and the last 10 m (80-90 m) of the model were perturbed using the pattern in Figure 7.17a; the portion of the model between 40 to 80 m of depth was perturbed by the pattern in Figure 7.17b.

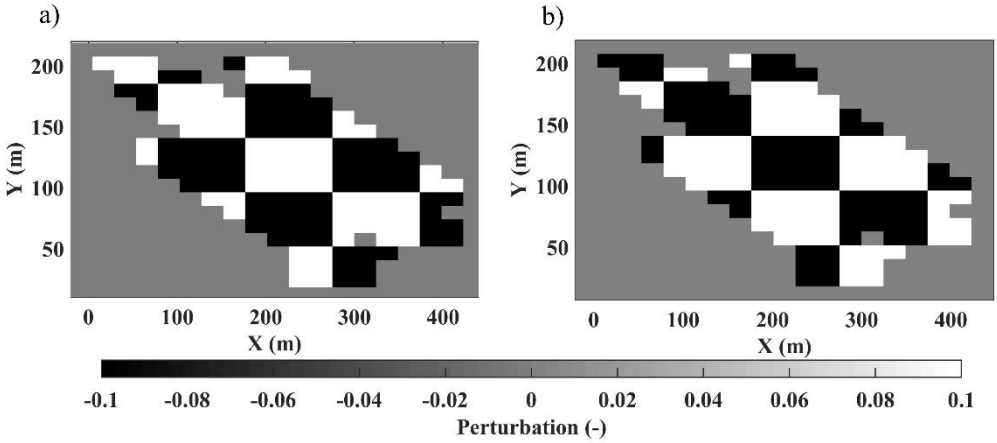

Figure 7.17 The checkerboard test's perturbation patterns applied to the estimated model for the PNG using the SWT method. (a) The pattern used to perturb the model between depth 0 to 40 m and 80 to 90 m. (b) The pattern used to perturb the model at depths 40 to 80 m.

In Figure 7.18a to d, we show the recovered perturbations at various layers. In the shallowest part of the model, the perturbations are better estimated (Figures 7.18a and b); however, the geometry of the perturbations (squares) are poorly recovered. This issue is mainly related to the acquisition scale, the obtained data coverage (Figure 7.9b), and the non-uniform azimuthal illumination (Figure 7.9c). The directionality of the azimuths is mainly due to the limited number of available receivers and the source deployment's geometry. The latter could be overcome

when more sparse locations of shots, covering multiple sides of the receivers, are available.

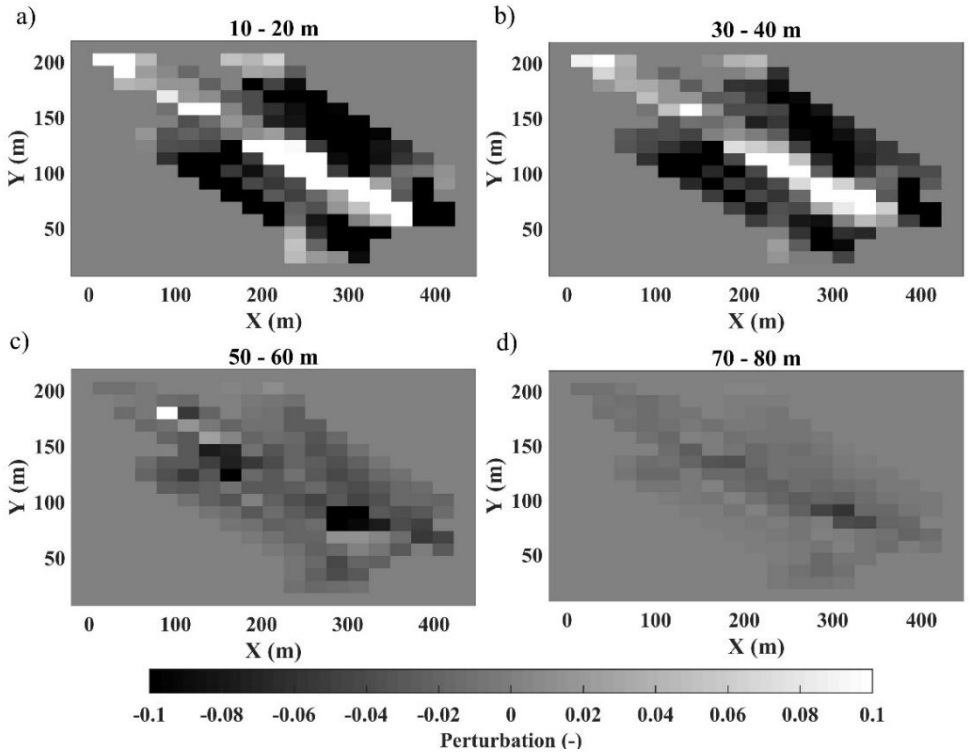

Figure 7.18: Horizontal sections of recovered perturbations for the checkerboard test on the PNG model at depth: (a) 10 to 20 m. (b), 30 to 40 m., (c) 50 to 60 m., and (d) 70-80 m.

To show this, we performed another checkerboard test, adding 10 hypothetical source locations to the PNG acquisition geometry. In Figure 7.19, we show the 10 hypothetical source locations in green.

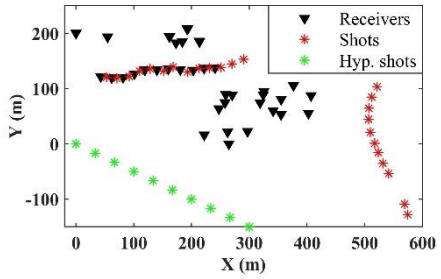

Figure 7.19: Hypothetical geometry of the PNG acquisition, where 10 hypothetical source's locations are added to the observed geometry in Figure 3.5a.

We computed the additional synthetic path-averaged DCs using the model from the last iteration of the inversion and added them to the observed ones. We repeated the checkerboard test on the new data. In Figure 7.20, we show the checkerboard test results, where the perturbations are better recovered compared to the checkerboard test in Figure 7.18, both in terms of the values and geometry of the perturbation.

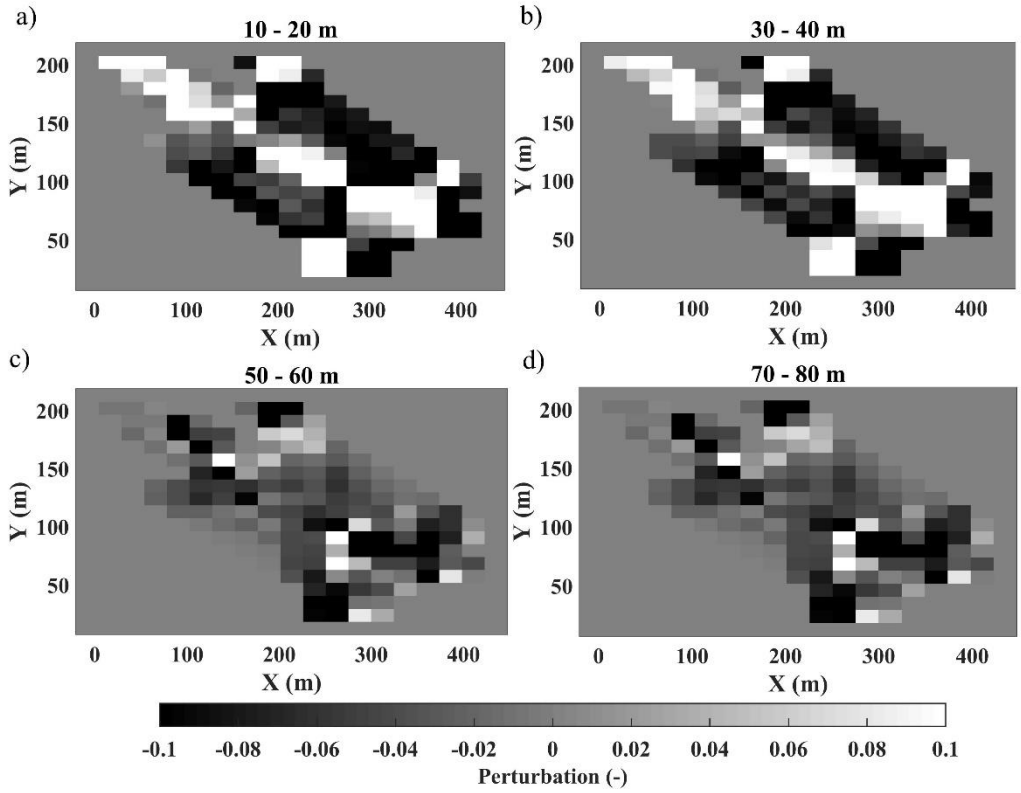

Figure 7.20 The checkerboard test performed to the hypothetical geometry of PNG acquisition in Figure 7.19. The horizontal sections showing the recovered perturbations at depths: (a) 10 to 20 m. (b) 30 to 40 m. (c) 50 to 60 m. (d) 70 to 80 m.

7.3.2 Aurignac

The Aurignac data showed a very complex propagation of the surface wave (Figure 3.8b), where multiple modes of the surface wave were excited contemporarily. The modes' indexing was very challenging, as often a merged version of the modes (effective DC) was observed. Here, we perform the SWT only to the fundamental modes of the north-west part of the data set (blue subset in Figure 3.6b).

7.3.2.1 Path-averaged DC estimations

We performed an automatic search of the receiver couples aligned with sources within 250 m offset. 4710 possible receiver couples and source settings were identified. We used the local DCs (4.19a) from the phase-shift analysis as references to locate the correct trend of the path-averaged fundamental mode DCs; for each path between the receiver couples, the local DC (Figure 4.19a) closest to the path was used as the reference DC. In total, 1301 DCs were estimated. The rest of the possible settings resulted in very noisy or inconsistent cross-multiplication matrices; as a result, they were discarded. In Figure 7.21a and b, we show the estimated path-averaged DCs and the obtained azimuthal illumination. The data show uniform data coverage with most paths showing angles between 0 to 40 and 140 to 180 degrees.

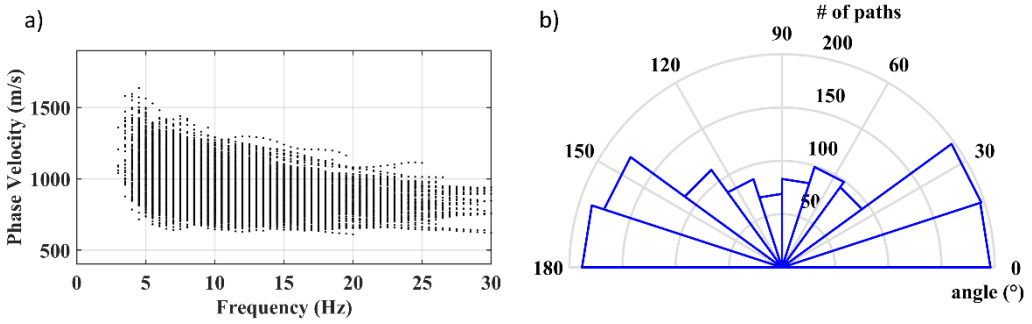

Figure 7.21: (a) The estimated path-averaged DCs corresponding to north-west part of the Aurignac site. (b) The obtained azimuthal illumination.

We computed the wavelength coverage of the estimated DCs. In Figure 7.22a to f, we show the data coverage within different wavelength ranges, where the color scale shows the apparent phase velocity. The data exhibits very high data coverage for wavelengths between 40 to 220 m. However, the wavelength coverage decreases substantially beyond this range. The pseudo-slices show sharp velocity contrast between the east and west of the investigated area, which was also observed in the estimated local DCs (Figure 4.20).

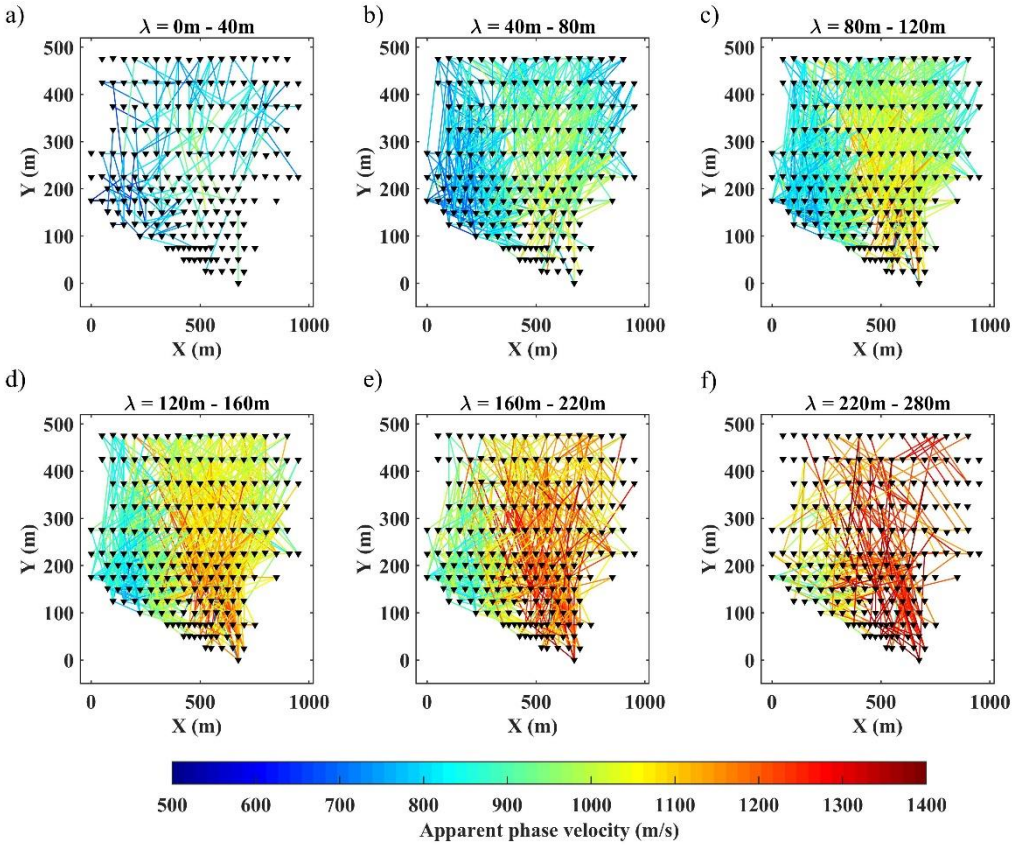

Figure 7.22: Pseudo-slices of the estimated DCs from the north-west of the Aurignac site shown within the wavelength ranges: (a) 0 to 40 m. (b) 40 to 80 m. (c) 80 to 120 m. (d) 120 to 160 m. (e) 160 to 220 m. (f) 220 to 280 m.

7.3.2.2 Reference model

We considered a 9-layer 3D reference model, consisting of 300 1D model points. Each layer's thickness was fixed at 15 m, except for the first layer (20 m), giving an investigation depth of about 140 m. We used the reference Poisson's ratio from the W/D method (section 6.3.2; red curves in Figures 6.2c and d). We defined a constant density of 2400 kg/m^3, except for the first layer (2200 kg/m^3). We considered the estimated reference VS models from the W/D method (section 6.3.2; Figures 6.2a and b).

7.3.2.3 Results

In Figure 7.23, we show the horizontal slices of the estimated VS from the unconstrained tomographic inversion. The unconstrained inversion resulted in non-realistic abrupt velocity variations (equivalence issue).

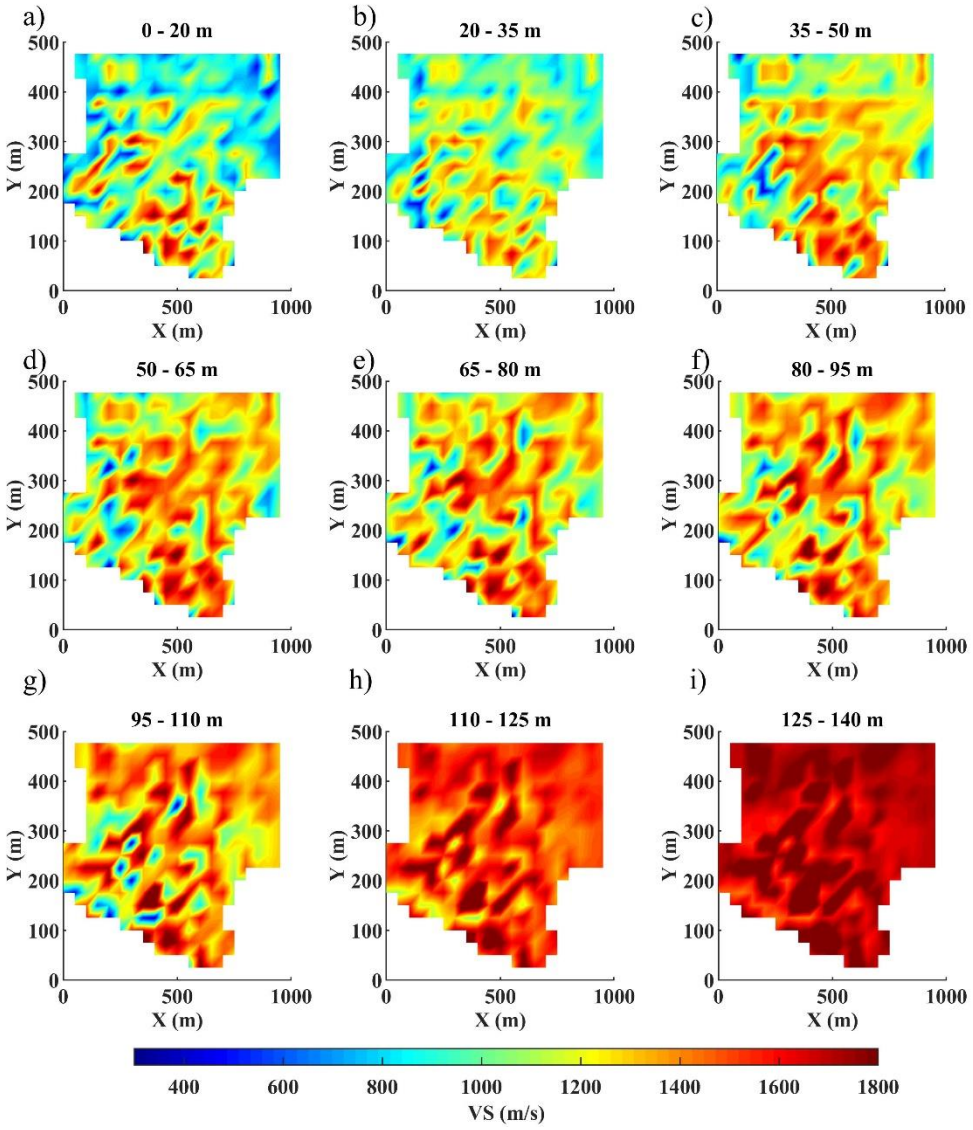

Figure 7.23: The horizontal slices of estimated VS model for the north-west of the Aurignac site using SWT method without imposing spatial constraints. The VS models within the depths: (a) 0 to 20 m. (b) 20 to 35 m. (c) 35 to 50 m. (d) 50 to 65 m. (e) 65 to 80 m. (f) 80 to 95 m. (g) 95 to 110 m. (h) 110 to 125 m. (i) 125 to 140 m.

To reach a smoother and more realistic model, we gradually increased the spatial constraints, taking into account the residual misfit of the DCs (equation 6.1). The 50 m/s constraints resulted the maximum level of constraints that did not significantly impact the residual misfit. In Figure 7.24, we compare the residuals of the unconstrained and constrained (50 m/s) inversions. The misfit shows similar values, and the average residual misfits of the two inversions are very similar

(6.64% for unconstrained and 6.7% for constrained inversion), showing that the selected constraints did not introduce over-smoothing in the model.

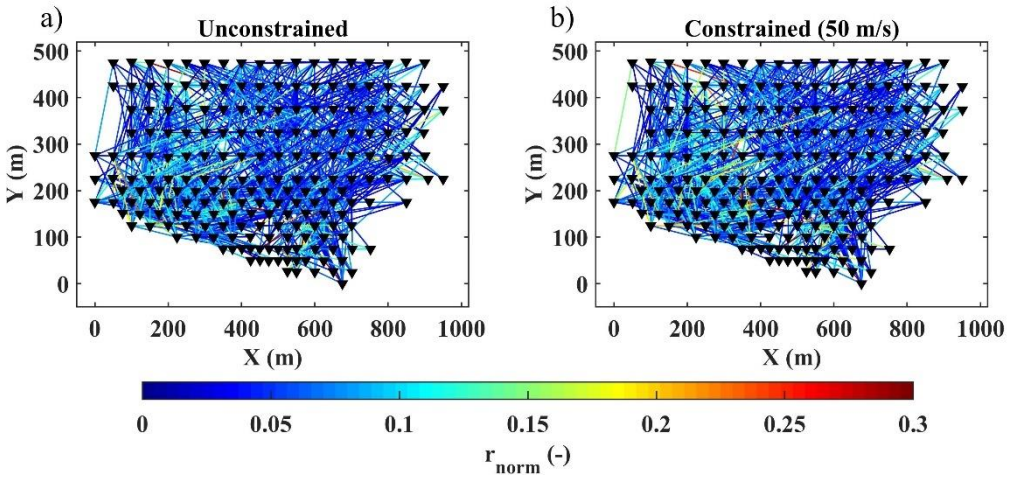

Figure 7.24: The residual misfit between the experimental and synthetic path-averaged DCs of the north-west Aurignac at the last iteration using: (a) unconstrained inversion, and (b) constrained inversion (50 m/s).

In Figure 7.25, we show the horizontal slices of the estimated VS of the constrained inversion at the last iteration (15). The estimated VS well-maps the lateral variation between the east and the west previously observed by the VS model from W/D method (Figure 4.23) and LCI (Figure 6.4) methods.

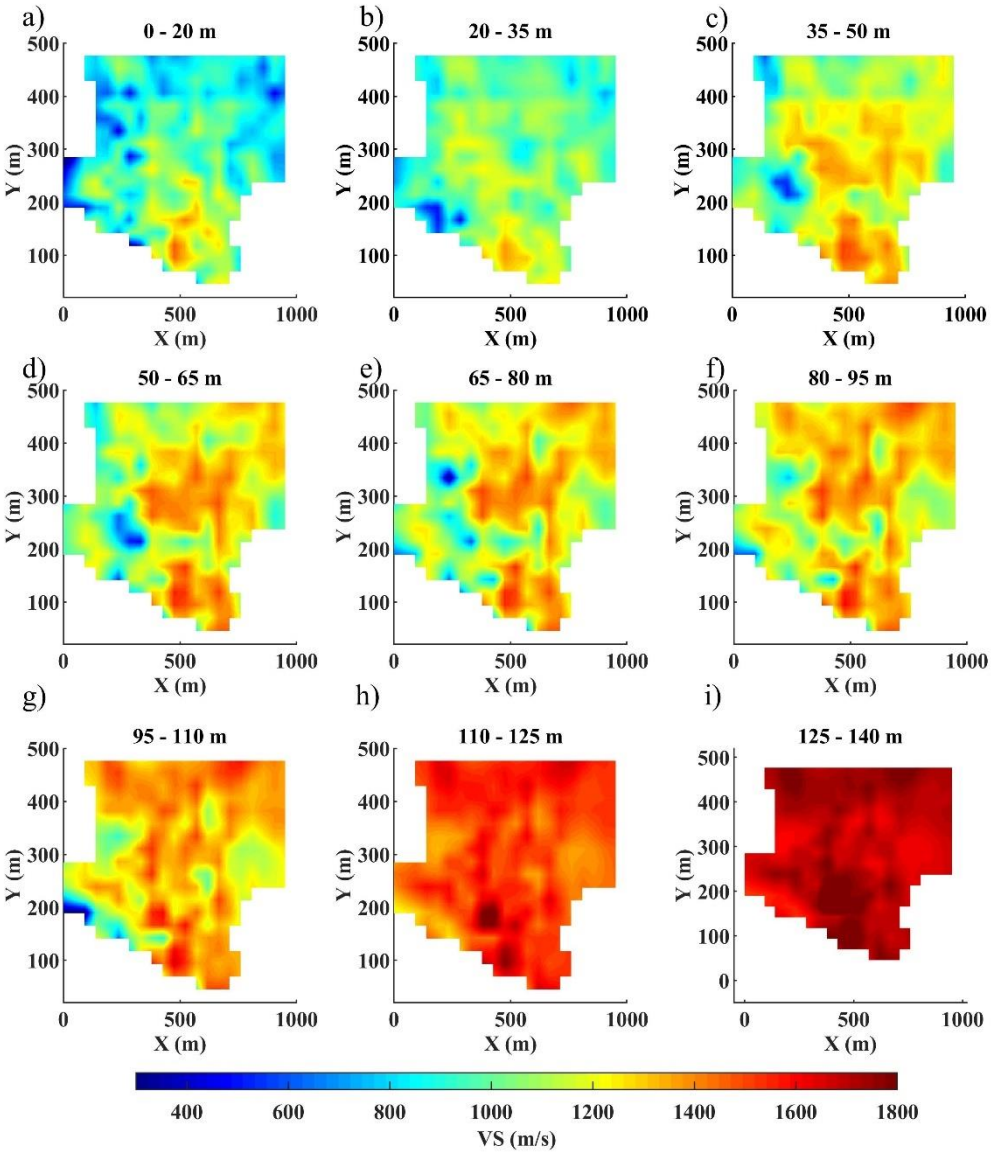

Figure 7.25: The horizontal slices of the estimated VS model for the north-west part of the Aurignac dataset using SWT with spatial constraints equal to 50 m/s. The VS models within the depths: (a) 0 to 20 m. (b) 20 to 35 m. (c) 35 to 50 m. (d) 50 to 65 m. (e) 65 to 80 m. (f) 80 to 95 m. (g) 95 to 110 m. (h) 110 to 125 m. (i) 125 to 140 m.

We used the Poisson's ratio of the two clusters shown in Figure 6.2c and d in red to transform the estimated VS model into VP. In Figure 7.26, we show the estimated VP model at different layers. The estimated Poisson's ratio of cluster A and B were limited to 20 to 128 (Figure 6.2c) and 20 to 140 (Figure 6.2d). The estimated VP is also bounded to the same depth range.

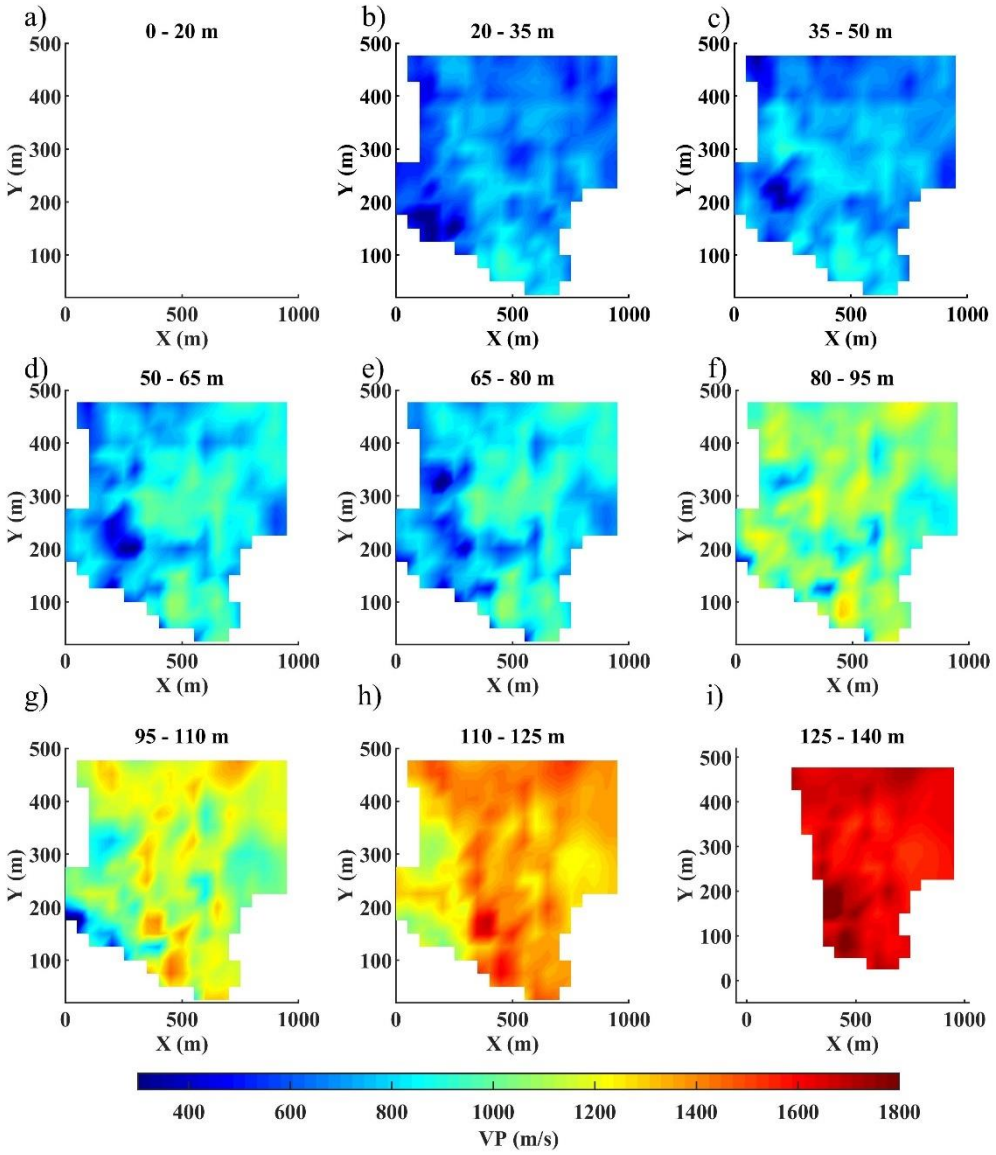

Figure 7.26: The horizontal slices of the estimated VP model for north-west part of the Aurignac site computed by applying the reference Poisson's ratios from W/D method (Figure 6.2c and d) to the estimated VS model from SWT (Figure 7.25). The VP model at depths: (a) 0 to 20 m. (b) 20 to 35 m. (c) 35 to 50 m. (d) 50 to 65 m. (e) 65 to 80 m. (f) 80 to 95 m. (g) 95 to 110 m. (h) 110 to 125 m. (i) 125 to 140 m.

7.3.2.4 Checkerboard tests

We perturbed the estimated *VS* model in Figure 7.25 by 10% negatively and positively. The pattern used to perturb the first layers of the models is shown in Figure 7.27a. The negative and positive perturbation values were alternated at each

layer. In Figure 7.27b, we show the vertical section of the perturbations at y-plain equal to 250 m.

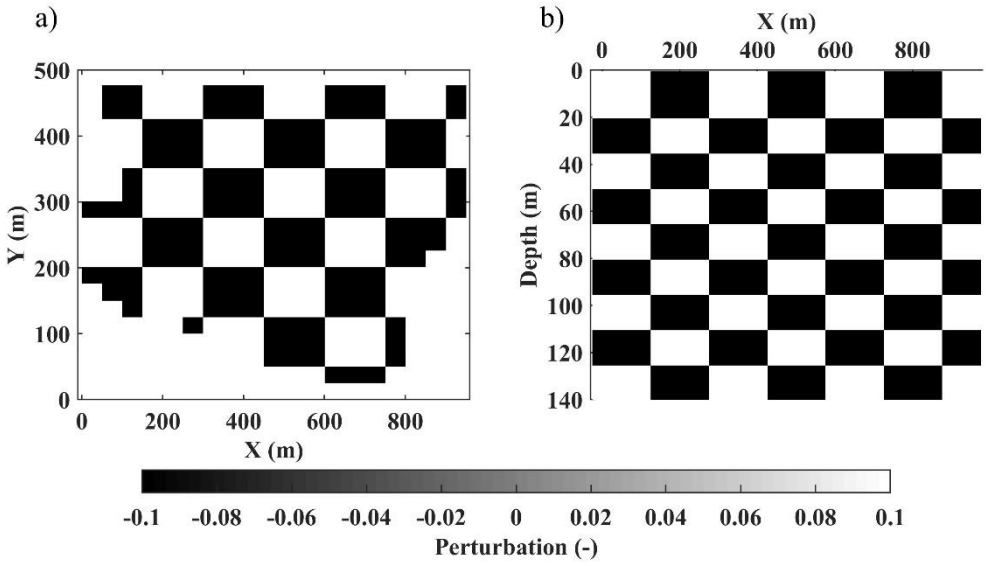

Figure 7.27:The perturbation pattern used for the application of the checkerboard test to estimated VS model of north-west Aurignac using the SWT method. (a) The pattern at the surface (1st layer). (b) The vertical section of the model perturbation at y-plain equal to 250 m. The negative and positive values are alternated for each layer.

The inversion automatically stopped at iteration 32. In Figure 7.28, we show the recovered perturbations at different layers. The geometries of the perturbations are entirely recovered for all layers. Also, the recovered values of the perturbations are satisfactory for the whole depth range.

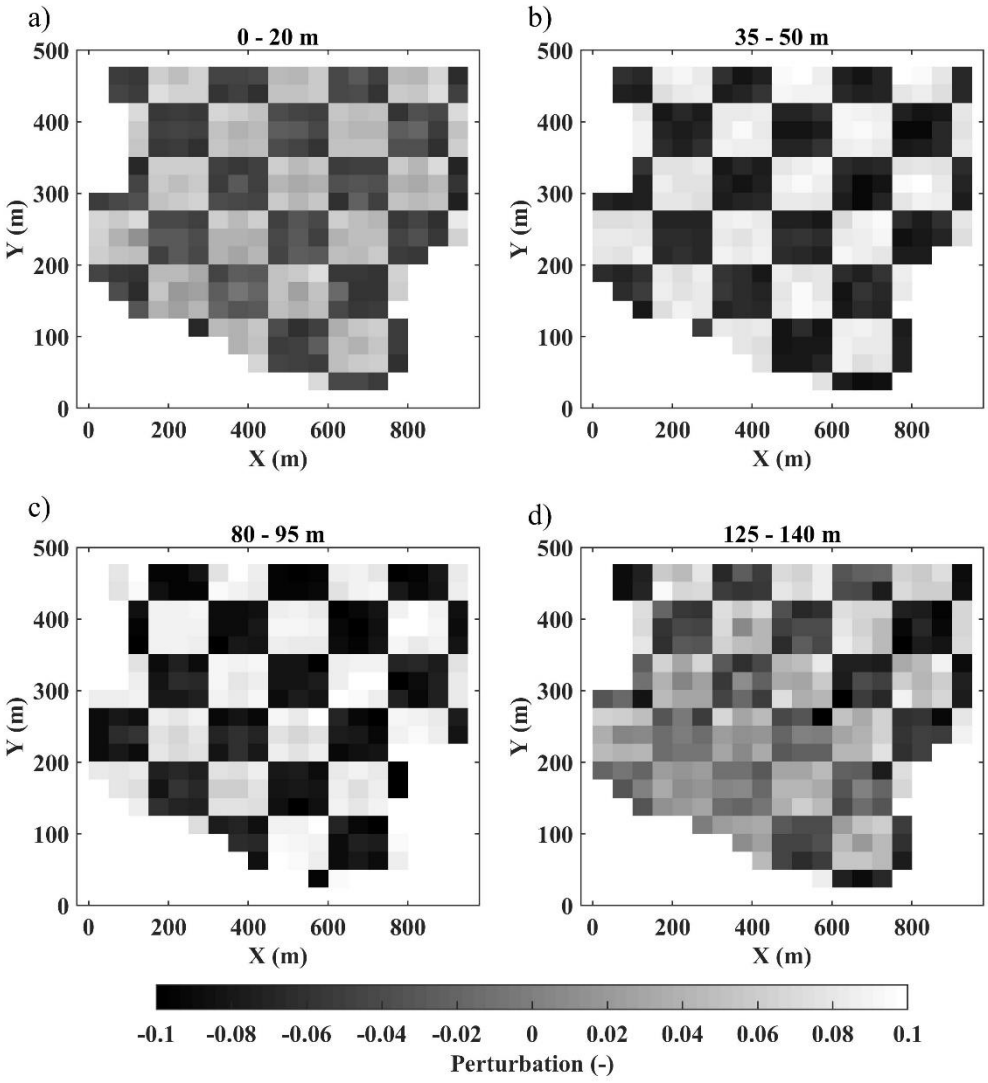

Figure 7.28: The recovered perturbations at various depths from the application of the checkerboard test to the result of the Aurignac north-west. (a) 0 to 20 m. (b) 35 to 50 m. (c) 80 to 95 m. (d) 125 to 140 m.

7.3.3 Oil and gas exploration data set

We show the application of the SWT to the oil and gas exploration data set for VS estimation (Tawil, 2019). The SWT is applied to the 2 km out of the 12 km seismic line, between positions 1 to 3 km. The previous applications of the W/D method and surface wave 1D inversion (Figure 4.31) suggested a considerable lateral variation for shallow layers at position 2 km. Given the data set is 2D, the target of the SWT is a quasi 2D estimated model.

7.3.3.1 Path-averaged DC estimations

All receivers were aligned with the source (2D line), leading to 180,300 possibilities for receiver couple selection. Since the path-averaged DCs were picked manually, a criterion should have been adopted to reduce the time required without significantly affecting the data coverage. We selected the paths between 60 to 140 m with the scheme shown in Figure 7.29.

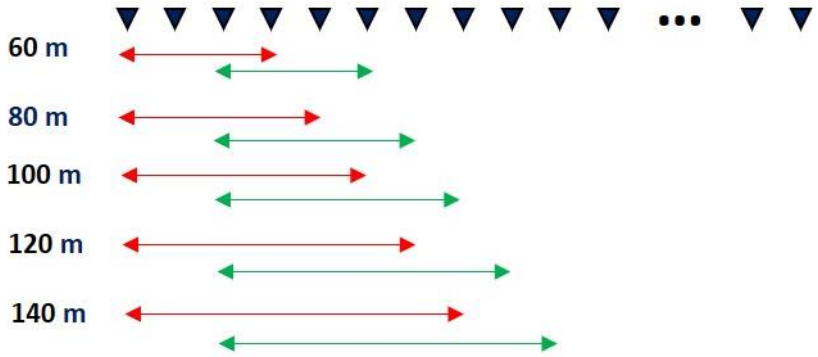

Figure 7.29: The schematic view of the DC path selection for the oil and gas exploration data set. Paths between 60 to 140 m were considered, and they were shifted by two receivers.

240 possible paths were analyzed, and the corresponding path-averaged DCs were estimated. In Figure 7.30a and b, we show the estimated DCs as a function of frequency and wavelength, respectively. The data are available mainly between 24 to 100 m of wavelength. We show the estimated curves spatial and wavelength coverage in Figure 7.30c, where the location of the paths are presented in the x-axis. The data are compartmentalized in the y-axis, showing the coverage within various wavelength ranges. The color of each path corresponds to the average phase velocity within the wavelength range. The estimated DCs show a velocity contrast between the left and right sides of the investigated line, with the transition zone at an approximate position of 2 km.

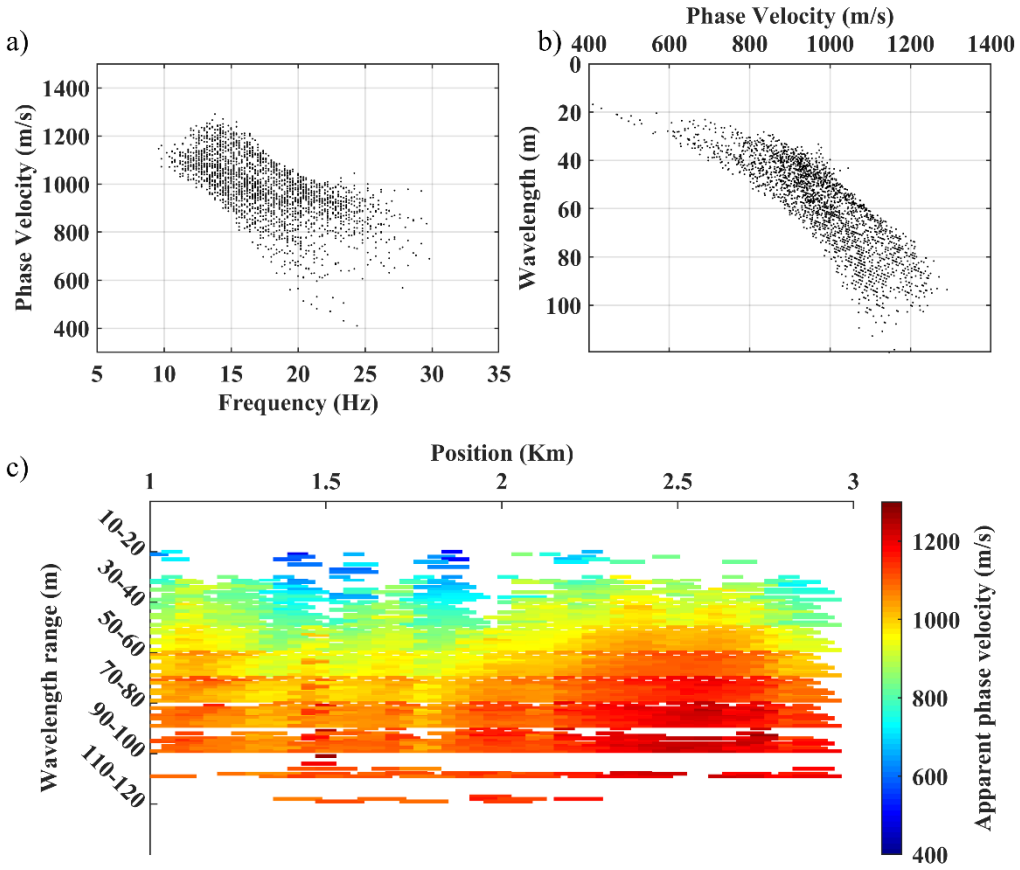

Figure 7.30 The estimated path-averaged DCs and data coverage for the 2 km (position 1 to 3 km) of the oil and gas exploration data set. (a) Estimated DCs as a function of frequency. (b) Estimated DCs as a function of wavelength. (c) The data coverage shown within various ranges of the wavelength. The color scale is the apparent phase velocity within each wavelength range.

7.3.3.2 The Reference Model

We defined a 12-layer 2D model overlying the half-space, consisting of 30 1D models. Since the data coverage is limited for wavelengths shorter than 24 m, we considered 12 m thickness for the first layer. The other layers were set at 3 m, giving an investigation depth of about 50 m. The constant density and Poisson's ratio of 1800 kg/m^3 and 0.33 were considered for all layers. We considered laterally and vertically invariant *VS* equal to 1100 m/s.

We evaluated the data coverage on the model by computing the paths crossing each model point. In Figure 7.31a and b, we show the model coverage as a function of frequency and wavelength, respectively. The model points at the two edges of the

model show the lowest coverage. The maximum data coverage is registered for the wavelengths 50 to 80 m.

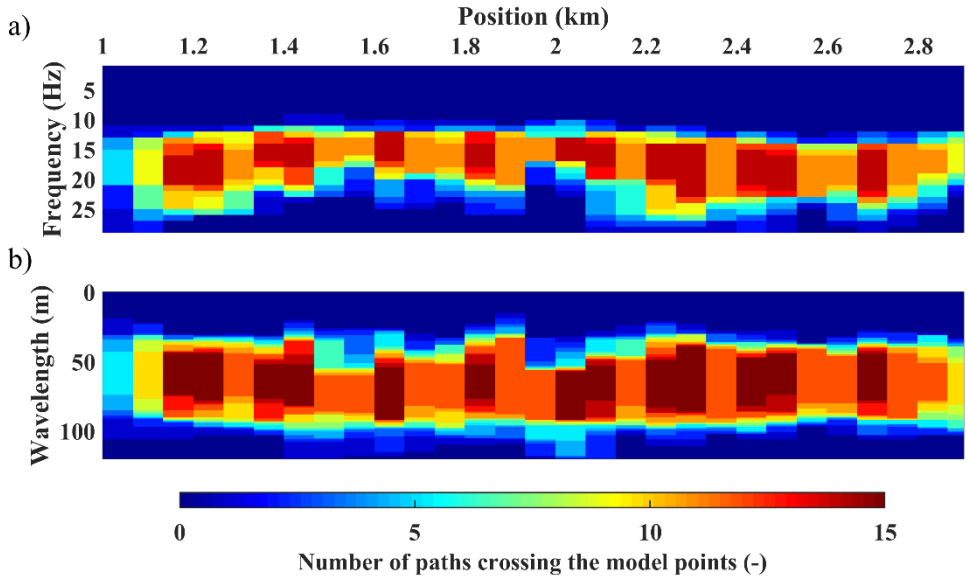

Figure 7.31 The coverage on the defined reference model for the tomographic inversion of the oil and gas exploration data set shown as a function of: (a) frequency, and (b) wavelength.

7.3.3.3 Results

We performed the inversion considering 100 m/s spatial constraints, which did not significantly impact the misfit compared to unconstrained inversion. The inversion automatically stopped at iteration 28. In Figure 7.32, we show the estimated VS model. Similar to estimated VS from the W/D method and 1D surface wave inversion (Figure 4.31), the estimated VS from SWT shows significant variations between the left and right sides of the position 2 km (Figure 7.32).

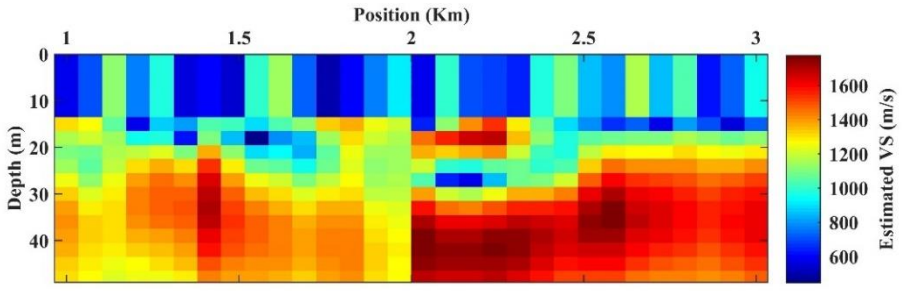

Figure 7.32 The estimated VS model for the 2 km of the oil and gas exploration data set using the SWT.

7.4 Conclusions

We developed a multi-modal SWT workflow that can be applied to data sets acquired with irregular acquisition geometries. We used the surface wave tomography to estimate the VS model and considered the W/D method to obtain the Poisson's ratio and transform the VS model into the VP. We provided a method to automatically separate the various modes of surface wave, avoiding the surface wave modal analysis for every receiver couple aligned with a source. In the 3D application of the SWT, such as the one applied to Aurignac and PNG data sets, the azimuthal illumination and data coverage are important factors that significantly affect the estimated models' resolution. The checkerboard tests proved that high-resolution models can be obtained when a large number of DCs with uniform azimuthal distribution are available.

8. Method Comparison

In this section, we analyze the velocity models estimated from the application of the W/D, LCI, and SWT methods to the Aurignac data set. We also perform a quantitative comparison between the models of the three methods. Finally, we compare the estimated models with the geological map of the area.

8.1 Model parameters

The results of the three applied methods were 1D VS and VP models corresponding to various locations. In Table 8.1, we describe the location of 1D estimated models and their characteristics in depth according to each method. The LCI algorithm was set to update also the layer thicknesses in addition to the VS model. So, the thicknesses of the obtained 1D models were various at the last iteration of the inversion, while the thicknesses of the SWT models were based on the reference model.

Table 8.1: The spatial and depth parameters of the estimated models from W/D, LCI, and SWT methods.

Method	Position of 1D models	Property in depth
W/D	at DC locations	Every 0.1 m
LCI	at DC locations	Layered model (various thickness)
SWT	Defined: reference model	Layered model (fixed thickness)

The model points for the W/D and LCI methods were determined by the location of the local DCs. We used a receiver spread over an area of 100×100 m^2 to estimate the local DCs. The receiver selection square was shifted by one receiver at a time, giving the maximum possible number of DCs. For the SWT method, a reference model consisting of 300 model points was adopted. The checkerboard test we

performed showed a good recovery of perturbations at all model points, eliminating the possibility of over-defined number of model points (Figure 7.28).

The W/D method directly estimated the VS and VP models and was performed separately to the two zones (east and west of the site). For each zone, based on the wavelength range of the reference DC, the depth range was obtained for the estimated models. In LCI and SWT scheme, the estimated VS model's investigation depths were defined by the reference model. A priori Poisson's ratio from the W/D method was used to transform the estimated VS models of LCI and SWT methods to the VP model. As a result, the estimated VP's depth range also depended on the depth range of a priori Poisson's ratios from W/D method. Table 8.2 provides the depth ranges obtained for the estimated VS and VP according to each method.

Table 8.2:The depth range of the estimated VS and VP models from the methods.

	VS depth west (m)	VS depth east (m)	VP depth west (m)	VP depth east (m)
W/D	20 to 128	20 to 140	20 to 128	20 to 140
LCI	0 to 140	0 to 140	20 to 128	20 to 140
SWT	0 to 140	0 to 140	20 to 128	20 to 140

The W/D and LCI methods' spatial resolution is the same as one obtained for estimated local DCs. The dimension of the receiver spreads used for the DC estimations can be considered as the spatial resolution ($100\times100 m^2$). The model's spatial resolution from the SWT method depends on the data coverage and azimuthal illumination, which can be recovered from the checkerboard test (in section 7.3.2.4; Figure 7.28). The tomographic inversion well recovered the 75 × 150 m^2 perturbations.

The resolution of the methods in depth is related to the sampling of the DCs in the processing step. The multi-channel DCs were used for the W/D and LCI method, while two-station DCs were the input of the SWT. In Figure 8.1a, we show the wavelength distribution of the estimated DCs from the multi-channel and two-station processing in blue and gray, respectively. Even though, the total number of DCs from multi-channel analysis was less than the two-station ones, the datapoints related to large wavelengths (>120 m) were more than the ones obtained with the

two-station analysis (Figure 8.1b), giving a better chance to retrieve the deeper portion of the model. As it was explained in section 7.2.3, to resolve this issue in scheme of SWT, we introduced wavelength-based weighting system to increase the score of large wavelength data points aiming at enhancing the resolution in depth. The checkerboard test that we performed confirmed the good recovery of the deepest layer of the model (Figure 7.28d).

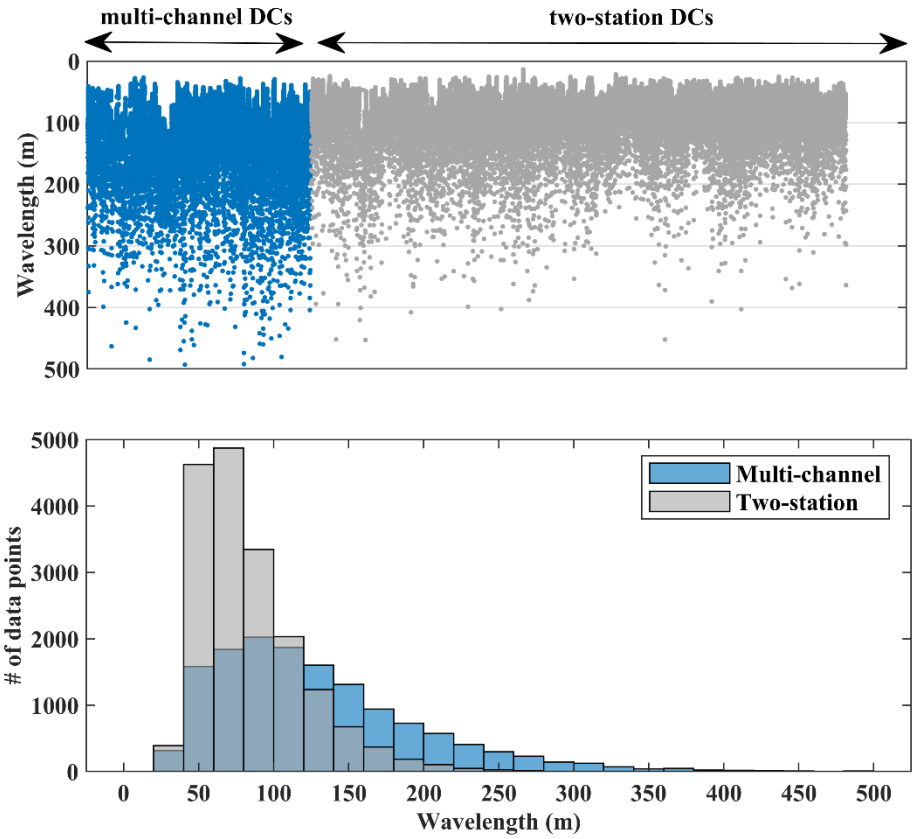

Figure 8.1: Comparison between the wavelength distributions from multi-channel and two-station processing of the Aurignac data set. (a) The distribution of the wavelength shown separately for each estimated DC. (b) The histogram showing the wavelength distribution of all DCs within 20 m wavelength bins.

8.2 Model Comparison

We interpolated the estimated models from the three methods to obtain comparable velocity models with the same spatial and depth elements. We first discretized the estimated models from LCI and SWT at every 0.1 m, matching with the depth elements of the models from W/D method. Then, we used linear interpolation to

obtain the velocity models at voxels of 10×10×0.1 m^3. In Figure 8.2 and 8.3, we show the quasi 3D estimated VS and VP models from the three methods after the interpolation. The significant lateral variation between the west and east is observed in all estimated models.

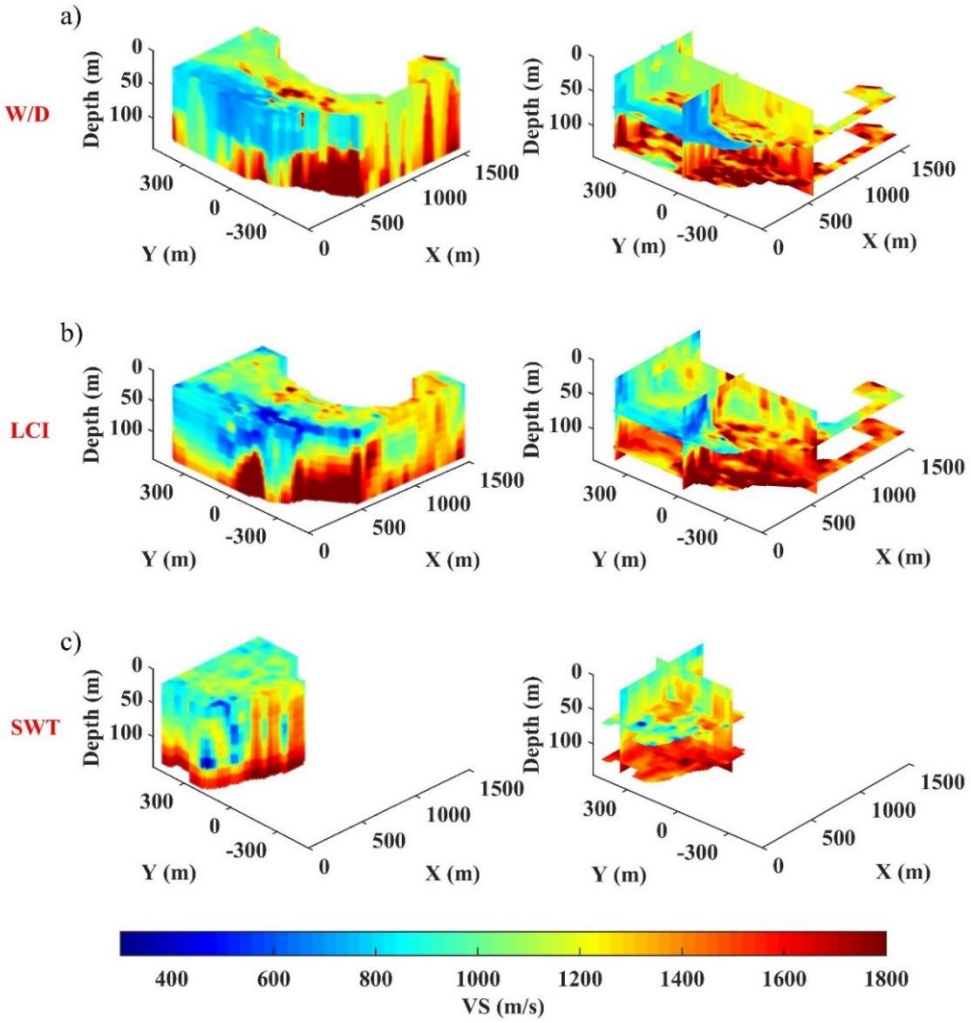

Figure 8.2: Quasi 3D estimated VS model (left panel) and corresponding slices at plains x=600 m, y=0 and 400 m, and z=70 and 125 m (right panel), for the Aurignac data using the methods: (a) W/D. (b) LCI. (c) SWT.

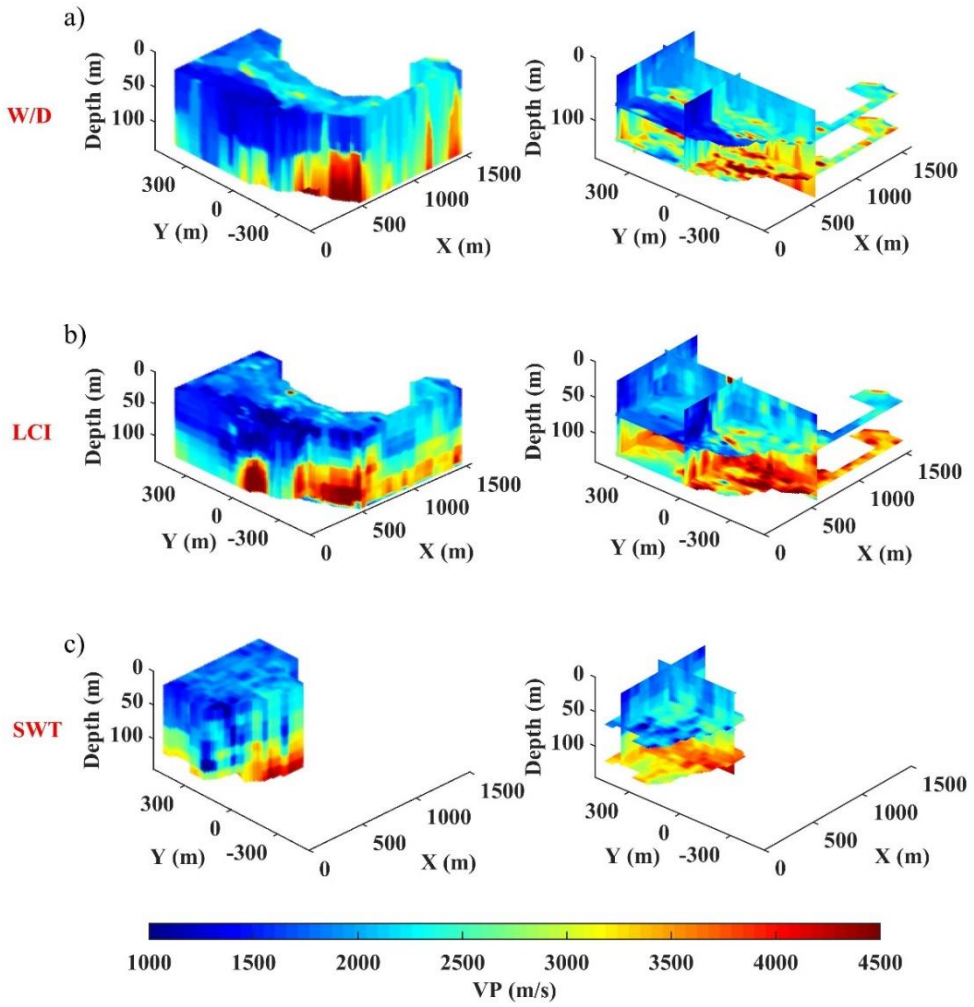

Figure 8.3: Quasi 3D estimated VP model (left panel) and corresponding slices at plains x=600 m, y=0 and 400 m, and z=70 and 125 m (right panel), for the Aurignac data set using the methods: (a) W/D. (b) LCI. (c) SWT.

At each voxel, we compute the difference between estimated VS and VP of every two methods as:

$$\varepsilon(i,j,k) = \frac{1}{2}\left[\frac{V(i,j,k)_{method.1} - V(i,j,k)_{method.2}}{V(i,j,k)_{method.1} + V(i,j,k)_{method.2}}\right], \qquad (8.1)$$

where i, j and k are the indices of the voxels in x, y, and depth directions, respectively. In Figure 8.4, we show the boxplots of the normalized differences within different depth intervals. A description of the boxplot figures was previously given in section 5.2.2. The boxplots in Figure 8.4 are all limited to the depth

between 20 and 140 m, except for the VS comparison of LCI and SWT methods (Figure 8.4e), which also includes the first 20 m (for the information about depth range of each method see Table 8.2). The significant differences of the outliers (red "+") are mainly due to the methods' different resolution in depth; the W/D method provided interval velocities every 10 cm, while the SWT and LCI provided layered models. Although we defined similar reference models for the LCI and SWT methods, the LCI was set to change also the thicknesses at each iteration, leading to different parameterization in depth compared to SWT.

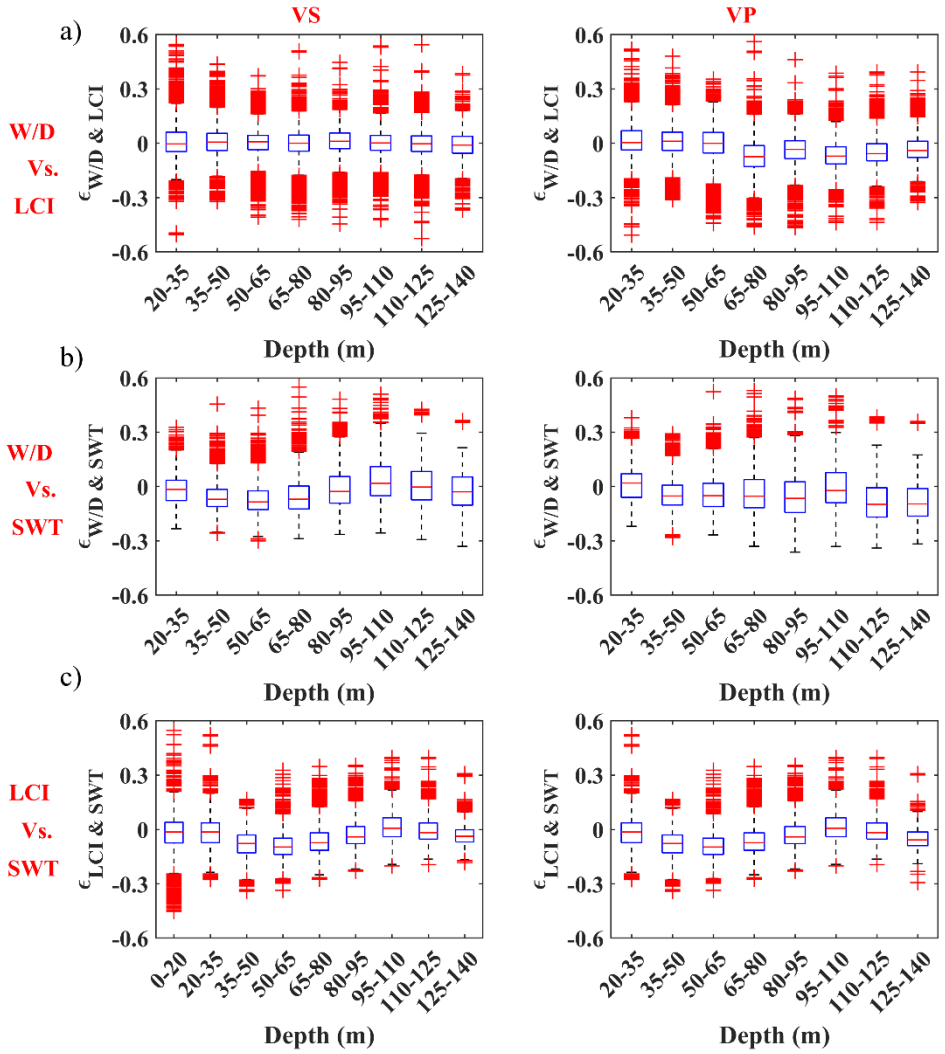

Figure 8.4: The difference between the VS (left panel) and VP (right panel) models obtained from the three methods applied to the Aurignac data set using equation (8.1). (a) W/D versus LCI. (b) W/D versus SWT. (c) LCI versus SWT.

The difference between the estimated VS and VP from W/D and LCI methods are small and uniform within different depth (Figure 8.4a). However, for the deepest layers, a slight over-estimation of the VP from the W/D method is registered compared to the VP from LCI (left panel in Figure 8.4a). The differences are increased in depth when the VS and VP of the W/D and SWT methods are compared (Figure 8.4b). The difference obtained for the estimated VS and VP using the LCI and SWT (Figure 8.4c) are very similar as the VP models of both methods were obtained from the estimated VS and same a priori Poisson's ratios; the differences show limited variations within each depth interval and are maintained within 5%.

To reflect the differences in space, we average the differences in depth as:

$$\varepsilon(i,j) = \frac{1}{n}\sum_{k=1}^{n}\varepsilon(i,j,k), \tag{8.2}$$

where n is the index of the deepest voxel at each location. In Figure 8.5, we show the difference at each location, comparing the models from every two methods. The difference between the VS of the W/D and LCI method is less than 4% in most areas (left panel Figure 8.5a). This difference slightly increases when the estimated VP of the same methods (right panel in Figure 8.5b) are compared. Higher differences are registered when the estimated VS and VP models from SWT are compared to W/D and LCI models (Figures 8.5b and c). This is expected since the same DCs were considered as inputs of the W/D and LCI methods, while the path-averaged DCs from two-station processing were used for the SWT method. The differences obtained for the estimated VP of the W/D and SWT (right panel in Figure 8.5b) are slightly higher than those obtained for the VS (left panel in Figure 8.5b), but they are still less than 5% for most of the area.

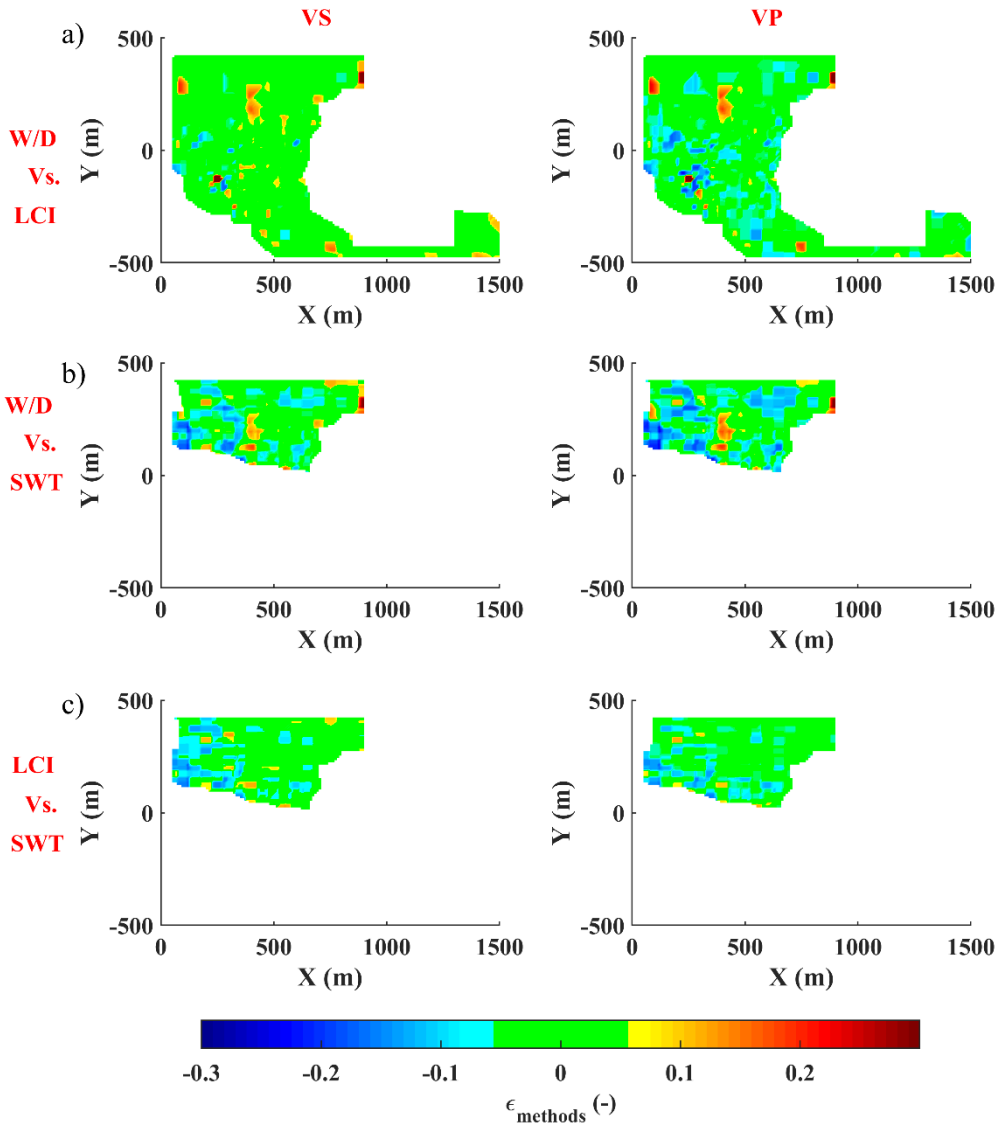

Figure 8.5: The averaged difference (in-depth) between the VS (left panel) and VP (right panel) models obtained from the three methods applied to the Aurignac data set using equation (8.2). (a) W/D versus LCI. (b) W/D versus SWT. (c) LCI versus SWT.

In Figure 8.4 and 8.5, we compared the results of the different methods both in depth and space. We also compute the overall differences between the estimated models of every two methods as:

$$\varepsilon_{tot} = \left[\frac{1}{m.q} \sum_{j=1}^{q} \sum_{j=1}^{m} \left| \varepsilon(i,j) \right| \right] \times 100, \qquad (8.2)$$

where m and q are the number of indices in x and y directions, respectively. In Table 8.3, we provide the total difference values obtained comparing the models from the three methods.

Table 8.3: The total difference between the estimated VS and VP models obtained for Aurignac data set using W/D, LCI, and SWT methods.

Total difference	VS's ε_{tot}	VP's ε_{tot}
WD vs. LCI	3.3%	4.67%
WD vs. SWT	6%	7.06%
LCI vs. SWT	4.74%	4.52%

8.3 Estimated models vs. geology of the site

Similar to the estimated VS models (Figure 8.2), the estimated VP models (Figure 8.3) from all three methods (W/D, LCI and SWT) exhibited a significant variation between the west and east. We obtained the geological map of the area from the French Geological Survey (BRGM). In Figure 8.6, we show the geological map superimposed with the satellite view of the area. Since the W/D method was involved in the VP estimation from all three surface wave methods, in Figure 8.6, for interpretation purposes, we plot also the horizontal slice of the estimated VP model from W/D for the depth interval of 35-50 m. The interpretation of the estimated VP model from W/D method above this depth cannot be comprehensively performed since the estimations were available for no or limited locations of the site (Figures 4.24a and b). The two diagonal and vertical faults at the north-west of the investigated area separate the east from the west. In the region between the two faults, a gap within the estimated model from the W/D method is observed: The complex propagation of surface waves passing through these discontinuities resulted in inadequate spectral coverage for DC estimations. The west of the area is characterized by loose materials from recent deposits (outcrop 5 in Figure 8.6). The rest of the region is known for much stiffer materials, mainly composed of

limestone and marl. The estimated VP also shows a higher velocity in the eastern region. The fastest VP is registered in the correspondence of the Sparnecian formation (outcrop 4 in Figure 8.6).

The estimated VP models from all three surface wave methods show values of 4000 to 4500 m/s at depths below 100 m (Figure 8.3). We believe the Danian formation is reached at depth below 100 m of the investigated area. The Danian formation is characterized by dense limestone with seismic P-wave velocity of approximately 5000 m/s.

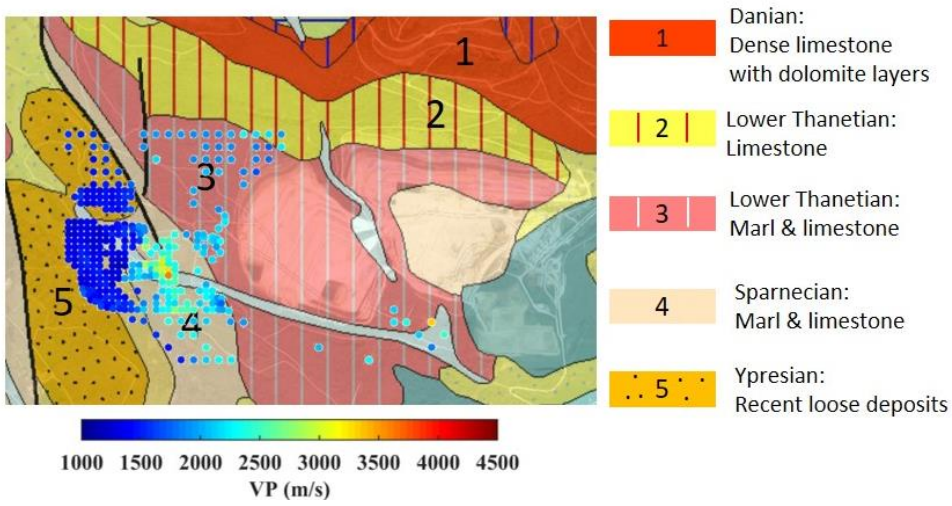

Figure 8.6: The geological map of the Aurignac site, obtained from French Geological Survey (BRGM), superimposed with the area's satellite view and the estimated VP for depth interval of 35-50 m below the surface using the W/D method.

8.4 Computational costs

The three methods involved a processing stage for DC estimation, and an inversion (for LCI and SWT) or data transformation stage (for W/D) to estimate the models. In Table 8.4, we provide the approximated computational costs for each part of the methods. The most time-consuming step of all methods is the DC estimation, which also involves expert user intervention. Compared to W/D and LCI, the SWT usually requires more DCs to reach adequate data coverage for the tomographic inversion. We estimated 1307 DCs for SWT of the north-west zone of Aurignac data set, while we obtained only 545 DCs for the W/D and LCI methods application to both zones of the data set.

Table 8.4: The approximated computational costs for each method.

	Processing (DC estimation)	Common W/D steps for the methods	Model estimation
W/D	1 min/DC	24 hrs	5 s/1D model
LCI	1 min/DC	24 hrs	5 hrs
SWT	1 min/DC	24 hrs	48 hrs

The inversion running times (for LCI and SWT) given in Table 8.4 are for a single inversion trial using 10 CPU cores. Usually, in addition to an unconstrained inversion, several constrained inversions are performed to reach a satisfactory model.

8.5 Conclusion

The estimated VS and VP models of the Aurignac data set from the three surface wave method applications were similar, with 4.7% and 5.4% difference on average. The information from the geological map of the area well supported the estimated models. The three methods' computational cost is mainly due to the DC estimation, which is usually higher for the SWT method.

9. Conclusions

9.1 Final Remarks

We investigated four surface wave methods to estimate near-surface S-wave and P-wave velocity models (VS and VP). We evaluated the performance of the methods using five data sets, out of which 3 were industry data sets, and 2 data sets were recorded in small-scale controlled sites. We provided a detailed description of the data sets in chapter 3.

In chapter 4, we introduced the W/D direct transformation method. The method is based on a wavelength-depth relationship (W/D) composed of the wavelength-depth couples corresponding to equal phase velocity and time-average VS (VSZ). The W/D relationship is sensitive to Poisson's ratio, which enables retrieving the apparent Poisson's ratio required to transform VSZ models into time-average VP (VPZ). The method directly provides the VSZ and VPZ models at the location of the local dispersion curves (DCs). We reformulated the relationship between time-average velocity and interval velocity, and with introducing regularization to the derivative term of this relationship, we provided a stable scheme to transform VSZ and VPZ models into interval VS and VP. The clustering of the data and separate application of the W/D method to different zones of the sites enabled the application of the method to laterally varying sites. The method's application to the CNR data set showed less than 5% VP difference from P-wave tomography. We provided an uncertainty propagation workflow based on W/D steps to transfer the uncertainty of the input DCs to the estimated VS and VP models. The uncertainty assessment of the CNR and Aurignac data set showed low normalized standard deviations (less than 5%) in estimating the VS and VP models in most of the areas. Similarly, the method was successfully applied to the oil and gas exploration data set, even though the data were acquired with group receivers aiming to eliminate the surface waves. The obtained velocity models from the application of the method to the remaining surface waves in the data well depicted the previously registered variations along the investigation line. We also developed a method to estimate an averaged Poisson's ratio corresponding to the area of each cluster, which we then used as prior information for the laterally constrained inversion (LCI) and surface wave tomography (SWT) methods.

We developed a joint inversion method in the scheme of Monte Carlo to estimate high-resolution VS and VP models (Chapter 5). The method considers both the W/D relationship and surface wave DC as minimization objectives. We successfully applied the method to two synthetic examples and a real data set (La Salle). The synthetic example 2 included saturated loose sand layers, which led to high Poisson's ratio for these layers. The application of the method to this example improved both VS and VP estimations compared to the DC Monte Carlo inversion. However, less accurate estimated VP for high Poisson's ratio layers were obtained, which is due to the abrupt variation of VP/VS ratio at high Poisson's ratios (>0.45). The estimated VP model for La Salle data set showed a satisfactory resemblance to the benchmark high-resolution reflection and P-wave tomography surveys from other studies.

The LCI of the surface wave DCs is a well-established method to estimate a consistent near-surface VS model. Providing the Poisson's ratio from the W/D method, we were able to estimate both VS and VP models in the context of LCI. The estimated VS and VP models from the application of the LCI to the Aurignac data set showed a good correlation with the estimated models from the W/D and SWT applications.

We also developed a SWT workflow that allowed the estimation and use of multi-modal path-averaged DCs (chapter 7). We used an automatic muting strategy to isolate and estimate the desired modes and modified the tomographic inversion algorithm to support multi-modal DCs. We defined a data weighting strategy for the inversion based on the wavelength of the DCs. The application of the method to a synthetic example revealed the impact of wavelength-based weights and the higher modes of DCs in enhancing the vertical resolution and in increasing the investigation depth of the estimated model. Using the Poisson's ratio from the W/D method, enabled estimation of both VS and VP models from the SWT applications. In the context of exploration usually large data sets are available and SWT applied to the estimated DCs along straight paths can fully retrieve the lateral variation. The significant retrieved lateral variation from the application of the method to Aurignac data set was also observed by other methods (W/D and LCI), confirming the validity of straight path assumption of surface wave propagation. However, despite the higher computational time, obtaining the curved paths for the propagation of the surface waves at different frequency can improve the accuracy of the estimated model. We successfully applied the method to the PNG data set, which was recorded with innovative acquisition methods. The applied checkerboard tests on the real and hypothetical geometry of the PNG data set showed that sparse location

of the sources can significantly enhance the azimuthal data coverage, and as a result, improves the resolution of the obtained models. Finally, we showed the application of the SWT method to the 2 km line of the oil and gas exploration data set to estimate the VS model. The sharp lateral variations in the shallow layers previously seen by the W/D method were also registered in the estimated VS model of the SWT.

In chapter 8, we compared the LCI, W/D, and SWT methods using the models from the application of these methods to the Aurignac data set. The methods provided similar spatial resolution of the model (100×100 m^2 for W/D and LCI; 75×150 m^2 for SWT). However, the SWT required a greater number of DCs (more working time) to reach the adequate data coverage for the obtained resolution. The resolution of the models in depth was related to the wavelength distribution of input DCs. The multi-channel DCs used for the W/D and LCI method provided greater number of large wavelength (>120 m) data points compared to the two-station DCs used for the SWT. To improve the resolution of the SWT models in depth, we introduced wavelength-based weights to the tomographic inversion; the checkerboard test that was performed on the SWT results of the Aurignac data set showed a good recovery of the perturbations for the whole investigation depth. The quantitative comparison of the methods showed, on average less than 4.7% total difference between the VS models and less than 5.4% between the VP models. The information available about the geology of the site suggested a contrast between the west and east of the site, which was recovered by all three surface wave methods.

According to different acquisition layouts and expectations, different methods can be adopted. The W/D method is considered a stand-alone method, providing estimated VS and VP models that can be used in various conditions. For important locations where a high vertical resolution of the estimated VS and VP models is required, the joint Monte Carlo inversion is a suitable option. Despite the high computational expectation of the method, it provides an accurate estimation of VS and VP. The LCI method is the other alternative method that provides a smooth and laterally consistent VS model with a similar spatial resolution to the W/D method. For data sets recorded in the scheme of full 3D acquisitions, the SWT provides a significant advantage. Usually, excellent data coverage with uniform azimuthal illumination and multiple cross-paths can be expected, which leads to high-resolution quasi 3D VS model. In the loose saturated environment, the application of the W/D method and Monte Carlo joint inversion are more challenging in estimating precise VP model, even though the methods still provide accurate estimation of the Poisson's ratio.

The investigation depth of the proposed surface wave methods is directly related to the maximum achievable wavelength (minimum frequency) for dispersion data. As a result, similar to what was observed for Aurignac, oil and gas exploration, La Salle and PNG data sets, the estimated models from these methods can reach much deeper portion of the subsurface compared to what is usually perceived as near-surface (first 30 m). On the contrary, lack of large wavelength dispersion data can limit the investigation depth to a few meters (e.g., CNR data set).

9.2 Future prospects

The total variation regularization parameter to transform the estimated time-average velocities into interval velocities is currently selected manually. We have already studied the relationship between the noise level and the required level of regularization for noisy synthetic data (Gomes, 2020). We are planning to expand this study to the real data and provide a data-driven procedure to select the regularization parameter based on each DC's noise level.

The proposed surface wave methods' main kernel is the estimation of the local DCs (for W/D and SWT) or path-averaged DCS (for SWT). Depending on the user's skill and experience, each DC estimation takes 1 to 3 minutes. The automation of the DC estimations is considered to be revolutionary to the surface wave methods. In literature, there are a few applications of Deep Learning algorithms for this purpose. However, the successful automation of the DC estimations using Deep Learning algorithms requires comprehensive synthetic and real training data sets, covering different geological settings.

10. References

Auken, E., and A.V. Christiansen, 2004, Layered and laterally constrained 2D inversion of resistivity data: *Geophysics,* 69, 752-761, doi: 10.1190/1.1759461

Auken, E., V. Christiansen, B.H. Jacobsen, N. Foged, and K.I. Sørensen, 2005, Piecewise 1D laterally constrained inversion of resistivity data: *Geophysical Prospecting,* 53, 497-506, doi: 10.1111/j.1365-2478.2005.00486.x

Badal, J., Y. Chen, M. Chourak, and J. Stankiewicz, 2013, S-wave velocity images of the Dead Sea Basin provided by ambient seismic noise: *Journal of Asian Earth Sciences,* 75, 26-35, doi: 10.1016/j.jseaes.2013.06.017

Bao, X., X. Song, and J. Li, 2015, High-resolution lithospheric structure beneath Mainland China from ambient noise and earthquake surface-wave tomography: *Earth and Planetary Science Letters,* 417, 132-141, doi: 10.1016/j.epsl.2015.02.024

Bardainne, T., K. Garceran, M. Retailleau, X. Duwattez, R. Sternfels, and D. Le Meur, 2017, Laterally Constrained Surface Wave Inversion: *Expanded abstract, EAGE,* 1-5, doi: 10.3997/2214-4609.201700957

Båth, M., and S. Crampin, 1965, Higher Modes of Seismic Surface Waves—Relations to Channel Waves: *Geophysical Jornal International,* 9, 309-321, doi: 10.1111/j.1365-246X.1965.tb03889.x

Bergamo, P., D. Boiero, and L.V. Socco, 2012, Retrieving 2D structures from surface-wave data by means of space-varying spatial windowing: *Geophysics,* 77, 39-51, doi: 10.1190/geo2012-0031.1#

Bergamo, P., and L.V. Socco, 2016, P- and S-wave velocity models of shallow dry sand formations from surface wave multi-modal inversion: *Geophysics,* 81, 197-209, doi: 10.1190/geo2015-0542.1

Blonk, B., 1995, Removal of scattered surface waves from seismic data: *Ph.D. thesis, TU Delft.*

Blonk, B., and G.C. Herman, 1994, Inverse scattering of surface waves: A new look at surface Consistency: *Geophysics,* 59, 963-972, doi: 10.1190/1.1443656

Boiero, D, 2009, Surface wave analysis for building shear wave velocity models: *Ph.D. thesis, Politecnico di Torino.*

Borisov, D., R. Modrak, F. Gao, and J. Tromp, 2018, 3D elastic full-waveform inversion of surface waves in the presence of irregular topography using an envelope-based misfit function: *Geophysics,* 83, 1-11, doi: 10.1190/geo2017-0081.1

Boschi, L., and G. Ekström, 2002, New images of the Earth's upper mantle from measurements of surface wave phase velocity anomalies: *Journal of Geophysical Research Solid Earth,* 107, 1-14, doi: 10.1029/2000JB000059

Brossier, R., S. Operto, and J. Virieux, 2009, Seismic imaging of complex onshore structures by 2D elastic frequency-domain full-waveform inversion: *Geophysics,* 74, 105-118, doi: 10.1190/1.3215771

Cara, M., 1978, Regional variations of higher Rayleigh-mode phase velocities: a spatial-filtering method: *Geophysical Journal International,* 54, 439-460, doi: 10.1111/j.1365-246X.1978.tb04268.x

Cercato , M., 2005, Indagini geofisiche in siti d'interesse ambientale con particolare riferimento alle onde superficiali: *Ph.D. thesis, Universita degli Studi di Roma* .

Cercato, M., 2009, Addressing non-uniqueness in linearized multichannel surface wave inversion: *Geophysical Prospecting,* 57, 22-47, doi: 10.1111/j.1365-2478.2007.00719.x

Chartrand, R., 2011, Numerical differentiation of noisy, nonsmooth data: *ISRN Applied Mathematics,* 2011, doi: 10.5402/2011/164564

Comina, C., R.M. Cosentini, S. Foti, and G. Musso, 2010, Electrical Tomography as laboratory monitoring tool: *Rivista Italiana di Geotecnica,* 44, 15-26.

Coruh, C., and J.K. Costain, 1983, Noise attenuation by Vibroseis whitening (VSW) processing: *Geophysics,* 48, 505-650, doi: 10.1190/1.1441485

Cox, M., 1999, Static Corrections for Seismic Reflection Surveys: (SEG), 546.

Craig, M.S., and K. Warvakai, 2009, Structure of an active foreland fold and thrust belt, Papua New Guinea: *Australian Journal of Earth Sciences,* 56, 719-738, doi: 10.1080/08120090903005360

Da Col, F., M. Papadopoulou, E. Koivisto, L. Sito, M. Savolainen, and L.V. Socco, 2019, Application of surface-wave tomography to mineral exploration: a case study from Siilinjärvi, Finland: *Geophysical Prospecting,* 68, 254-269, doi: 10.1111/1365-2478.12903

Dunkin, J.W., 1965, Computation of modal solutions in layered, elastic media at high frequencies: *Bulletin of the Seismological Society of America,* 55, 335-358.

Edgeworth, F.Y., 1881, Mathematical Physics: *McMaster University Archive for the History of Economic Thought.*

Embree, P., J.P. Burg, and M.M. Backus, 1963, Wide-band Velocity Filtering—The Pie-Slice Process: *Geophysics,* 28, 925-1074, doi: 10.1190/1.1439310

Ernst, F., G. Herman, and B. Blonk, 1998, Reduction of near-surface scattering effects in seismic data: *The Leading Edge,* 17, 759-764, doi: 10.1190/1.1438047

Ernst, F., G.C. Herman, and A. Ditzel, 2002, Removal of scattered guided waves from seismic data: *Geophysics,* 67, 1240-1248, doi: 10.1190/1.1500386

Fang, H., H. Yao, H. Zhang, Y. Huang, and R.D. van der Hilst, 2015, Direct inversion of surface wave dispersion for three-dimensional shallow crustal structure based on ray tracing: methodology and application: *Geophysical Journal International,* 201, 1251-1263, doi: 10.1093/gji/ggv080

Foti, S., and C. Strobbia, 2002, Some notes on model parameters for surface wave data inversion: *Symposium on the Application of Geophysics to Engineering and Environmental Problems (SAGEEP),* doi: 10.4133/1.2927179

Foti, S., C. Lai, and R. Lancellota, 2002 , Porosity of fluid-saturated porous media from measured seismic wave velocities: *Géotechnique,* 52, 359-373, doi: 10.1680/geot.2002.52.5.359

Foti, S., F. Hollender, D. Albarello, M. Asten, P.Y. Bard, C. Comina, C. Cornou, et al., 2018, Guidelines for the good practice of surface wave analysis: a

product of the InterPACIFIC project: *Bulletin of Earthquake Engineering,* 16, 2367-2420, doi: 10.1007/s10518-017-0206-7

Ganji, V., N. Gucunski, and S. Nazarian, 1998, Automated Inversion Procedure for Spectral Analysis of Surface Waves: *Journal of Geotechnical and Geoenvironmental Engineering,* 124, doi: 10.1061/(ASCE)1090-0241(1998)124:8(757)

Garofalo, F., 2014, Physically constrained joint inversion of seismic and electrical data for near-surface application: *Ph.D. thesis, Politecnico di Torino.*

Gomes, Ana Paula, 2020, Optimized Regularization of Interval S-wave Velocity Estimation from Seismic Surface Wave: *M.Sc. thesis, Politecnico di Torino.*

Halliday, D., and A. Curtis, 2008, Seismic interferometry, surface waves and source distribution: *Geophysical Journal International,* 175, 1067-1087, doi: 10.1111/j.1365-246X.2008.03918.x

Halliday, D.F., A. Curtis, P. Vermeer, C. Strobbia, A. Glushchenko, D.J. van Manen, and J.O.A. Robertson, 2010, Interferometric ground-roll removal: Attenuation of scattered surface waves in single-sensor data: *Geophysics,* 75, SA15-SA25, doi: 10.1190/1.3360948

Halliday, D., P. Bilsby, L. West, E. Kragh, and J. Quigley, 2015, Scattered ground-roll attenuation using model-driven interferometry: *Geophysical Prospecting,* 63, 116-132, doi: 10.1111/1365-2478.12165

Haskell, N., 1953, The dispersion of surface waves on multilayered media: *Bulletin of the Seimological Society of America,* 43, 17-34.

Hauksson, E., and P.M. Shearer, 2006, Attenuation models (QP and QS) in three dimensions of the southern California crust: Inferred fluid saturation at seismogenic depths: *Journal of Geophysical Research Solid Earth,* 111, doi: 10.1029/2005JB003947

Heisey, J.S., K.H. Stokoe, and A.H. Meyer, 1982, Moduli of Pavement Systems from Spectral Analysis of Surface Waves: *Transportation Research Record,* 852, 22-31.

Henley, D.C., 2003, Coherent noise attenuation in the radial trace domain: *Geophysics,* 68, 1942-2156, doi: 10.1190/1.1598134

Herrmann, R.B., 2002, "SURF."

Hwang, H.J., and B.J. Mitchell, 1986, Interstation surface wave analysis by Frequency-domain Wiener deconvolution and modal isolation: *Bulletin of the Seismological Society of America,* 76, 847-864.

Karimpour, M.K., 2018, processing workflow for estimation of dispersion curves from seismic data and QC = Extraction of Dispersion Curves from Field Data: *M.Sc. thesis, Politecnico di Torino.*

Kelamis, P.G., and A.R. Mitchell, 1989, Slant-stack processing: *First Break,* 7, doi: 10.3997/1365-2397.1989003

Kennett, B.L.N, and K. Yoshizawa, 2002, A reappraisal of regional surface wave tomography: *Geophysical Journal International,* 150, 37-44, doi: 10.1046/j.1365-246X.2002.01682.x

Khosro Anjom, F., A. Arabi, L.V. Socco, and C. Comina, 2017, Application of a method to determine S and P wave velocities from surface waves data analysis in presence of sharp lateral variations: *Expanded Abstracts, 36th GNGTS national convention.*

Khosro Anjom, F., S.M. Muriuki, C. Comina, and L.V. Socco, 2018, Joint Vp and Vs Monte Carlo Inversion from Surface Wave Data: *24th European Meeting of Environmental and Engineering Geophysics, conference proceedings, 1-5*, doi: 10.3997/2214-4609.201802638

Khosro Anjom, F., and L.V. Socco, 2019, Improved surface wave tomography: Imposing wavelength-based weights: *Extended Abstracts, 38th GNGTS national convention.*

Khosro Anjom, F., D. Teodor, C. Comina, R. Brossier, J. Virieux, and L.V. Socco, 2019, Full-waveform matching of VP and VS models from surface waves: *Geophysical Journal International*, 218, 1873-1891, doi: 10.1093/gji/ggz279

Khosro Anjom, F., T.J Browaeys, and L.V. Socco, 2021a, Multi-modal surface wave tomography to obtain S- and P-wave velocities applied to the

recordings of UAV deployed sensors: *Geophysics* (Just-Accepted), doi: 10.1190/geo2020-0703.1

Khosro Anjom, F., S.M. Muriuki, C. Comina, and L.V. Socco, 2021b, Joint Vp and Vs Monte Carlo Inversion from Surface Wave Data: *EAGE E-Lecture,* URL

Knowles, I., and R.J. Renka, 2014, Methods for numerical differentiation of noisy data: *Electronic Journal of Differential Equations,* 21, 235-246.

Lai, C.G., and G.J. Rix, 2002, Solution of the Rayleigh Eigenproblem in Viscoelastic Media: *Bulletin of the Seismological Society of America,* 92, 2297-2309, doi: 10.1785/0120010165

Liu, X., 1999, Ground roll suppression using the Karhunen–Loève transform: *Geophysics*, 64, 564-566, doi: 10.1190/1.1444562

Lowe, M.J.S., 1995, Matrix Techniques for Modeling Ultrasonic Waves in Multilayered Media: *IEEE Transactions on Ultrasonics, Ferroelectrics, and Frequency Control,* 42, 525-542, doi: 10.1109/58.393096

Luke, B.A., C. Calderón-Macías, R.C. Stone, and M. Huynh, 2003, Non-Uniqueness in Inversion of Seismic Surface-Wave Data: *Symposium on the Application of Geophysics to Engineering and Environmental Problems,* 1491, doi: 10.4133/1.2923140

Lys, P.O., the METIS team, K. Elder, and J. Archer, 2018, METIS, a disruptive R&D project to revolutionize land seismic acquisition: *SEG global meeting,* 28-31, doi: 10.1190/RDP2018-41752683.1

MacBeth, C.D., and P.W. Burton, 1985, Upper crustal shear velocity models from higher mode Rayleigh wave dispersion in Scotland: *Geophysical Journal International,* 83, 519-539, doi: 10.1111/j.1365-246X.1985.tb06501.x

Mansoor, N., L. Slater, F. Artigas, and E. Auken, 2006, High-resolution geophysical characterization of shallow-water wetlands: *Geophysics,* 71, doi: 10.1190/1.2210307

Maraschini, M., 2008, A new approach for the inversion of Rayleigh and Scholte waves in site characterization: *Ph.D. thesis, Politecnico di Torino.*

March, D.W., and A.D. Bailey, 1983, A Review of the Two-dimensional Transform and its use in seismic processing: *First Break,* 1, doi: 10.3997/1365-2397.1983001

Marquart, D., 1963, An algorithm for least squares estimation of nonlinear parameters: *Journal of the Society of Industrial Applied Mathematics,* 2, 431-441, doi: 10.1137/0111030

Marsden, D., 1993, Static corrections--a review, Part 1: *The Leading Edge,* 12, 43-49, doi: 10.1190/1.1436912

Masoni, I., 2016, Inversion of surface waves in an oil and gas exploration.

Masoni, I., R. Brossier, J. Virieux, and J.L. Boelle, 2014, Robust full waveform inversion of surface waves: *SEG Expanded Abstracts,* 1126-1130, doi: 10.1190/segam2014-1077.1

McAlpine, J.R., G. Keig, and R. Falls. 1983., Climate of Papua New Guinea: *Australian National University Press.*

McMechan, G.A., and M.J. Yedlin, 1981, Analysis of dispersive by wave field transformation: *Geophysics,* 46, 869-874, doi: 10.1190/1.1441225

McMechan, G.A., and R. Sun, 1991, Depth filtering of first breaks and ground roll: *Geophysics,* 56, 390-396, doi: 10.1190/1.1443056

Mitchel, R.G., 1980, Array measurements of higher mode Rayleigh wave dispersion: an approach utilizing source parameters: *Geophysical Journal International,* 63, 311-331, doi: 10.1111/j.1365-246X.1980.tb02623.x

Nazarian, S., 1984, In situ determination of elastic moduli of soil deposits and pavement systems by spectral-analysis-of-surface waves method: *Ph.D. thesis, University of Austin at Texas.*

Nazarian, S., H. Kenneth, K.H. Stokoe, and W.R. Hudson, 1983, Use of Spectral Analysis of Surface Waves Method for Determination of Moduli and Thicknesses of Pavement Systems: *Transport research Record,* 930, 38-45.

Nolet, G., 1975, Higher Rayleigh modes in western Europe: *Geophysical Research Letters,* 2, 60-62, doi: 10.1029/GL002i002p00060

Nolet, G., and G.F. Panza, 1976, Array analysis of seismic surface waves: Limits and possibilities: *pure and applied geophysics,* 114, 775-790.

Pagliccia, B., K. Dalton, C. Walker, K. Elder, and R. Jenneskens, 2018, METIS Hits The Ground in Papua New Guinea, a Field-Proof Innovative Method to Revolutionize Onshore Seismic Acquisition: *EAGE, Extended Abstracts,* 1-5, doi: 10.3997/2214-4609.201801402

Papadopoulou, M., D. Da Col, L.V. Socco, S. Hu, E. Bäckström, M. Schön and P. Marsden, 2018, Surface-Wave Tomography at Mining Sites - A Case Study from Central Sweden: *25th European Meeting of Environmental and Engineering Geophysics, conference proceedings*, doi: 10.3997/2214-4609.201902464

Papadopoulou, M., D. Da Col, B. Mi, E. Bäckström, P. Marsden, B. Brodic, A. Malehmir and L.V. Socco, 2020, Surface-wave analysis for static corrections in mineral exploration: A case study from central Sweden: *Geophysical Prospecting,* 68, 214-231, doi: 10.1111/1365-2478.12895

Pareto, V., 1897, Cours d'Économie Politique: *the American Academy of Political and Social Science,* 9, doi: 10.1177%2F000271629700900314

Park, C.B., R.D. Miller, and J. Xia, 1998, Imaging dispersion curves of surface waves on multi-channel record: *SEG, Expanded abstract,* 1377-1380, doi: 10.1190/1.1820161

Parolai, S., M. Picozzi, S.M. Richwalski, and C. Milkereit, 2005, Joint inversion of phase velocity dispersion and H/V ratio curves from seismic noise recordings using a genetic algorithm, considering higher modes: *Geophysical Research Letters,* 32, 1-4, doi: 10.1029/2004GL021115

Passeri, F., 2019, Development of an advanced geostatistical model for shear wave velocity profiles to manage uncertainties and variabilities in ground response analyses: *Ph.D. thesis, Politecnico di Torino.*

Perez Solano, C.A., D. Donno, and H. Chauris, 2014, Alternative waveform inversion for surface wave analysis in 2-D media: *Geophysical Journal International,* 198, 1359-1372, doi: 10.1093/gji/ggu211

Picozzi, M., S. Parolai, D. Bindi, and A. Strollo, 2009, Characterization of shallow geology by high-frequency seismic noise tomography: *Geophysical Journal International,* 176, 164-174, doi: 10.1111/j.1365-246X.2008.03966.x

Ritzwoller, M.H., and A.L. Levshin, 1998, Eurasian surface wave tomography: Group velocities: *Hournal of Geophysical Research Solid Earth,* 103, 4839-4878, doi: 10.1029/97JB02622

Rokach, L., and O. Maimon, 2005, Clustering Methods, Data Mining and Knowledge Discovery Handbook: 321-352, Springer.

Rudin, L., S. Osher, and E. Fatemi, 1992, Nonlinear total variation based noise removal algorithms: *Physica D,* 60, 259-268, doi: 10.1016/0167-2789(92)90242-F

Saatcilar, R., and N. Canitez, 1988, A method of ground-roll elimination: *Geophysics,* 53, 894-902, doi: 10.1190/1.1442526

Sabra, K.G., P. Gerstoft, P. Roux, W.A. Kuperman, and M.C. Fehler, 2005, Surface wave tomography from microseisms in Southern California: *Geophysical Research Letters,* 32, doi: 10.1029/2005GL023155

Sambridge, M., and K. Mosegaard, 2002, Monte Carlo Methods in Geophysical Inverse Problems: *Reviews of Geophysics,* 40, 1-29, doi: 10.1029/2000RG000089

Sambridge, M.S., and B.L.N. Kennett, 2001, Seismic Event Location: Nonlinear Inversion Using a Neighbourhood Algorithm: *pure and applied geophysics,* 158, 241-257, doi: 10.1007/PL00001158

Santamarina, J.C., K.A. Klein, and M.A. Fam. n.d., Soils and Waves: Particulate Materials Behavior, Characterization and Process Monitoring: *J. Wiley and Sons.*

Schmoller, R., 1982, Some Aspects of Handling Velocity Inversion and Hidden Layer Problems in Seismic Refraction Work: *Geophysical Prospecting,* 30, 735-751, doi: 10.1111/j.1365-2478.1982.tb01336.x

Shapiro, N.M., and M.H. Ritzwoller, 2002, Monte-Carlo inversion for a global shear-velocity model of the crust and upper mantle: *Geophysical Journal International,* 151, doi: 10.1046/j.1365-246X.2002.01742.x

Shapiro, N.M., L. Campillo, L. Stehly, and M.H. Ritzwoller, 2005, High resolution surface wave tomography from ambient seismic noise: *Science,* 307, 1615-1618, doi: 10.1126/science.1108339

Socco, L.V., and C. Strobbia, 2004, Surface-wave method for near-surface characterization: a tutorial: *Near Surface Geophysics,* 2, 165-185, doi: 10.3997/1873-0604.2004015

Socco, L.V., and D. Boiero, 2008, Improved Monte Carlo inversion of surface wave data: *Geophysical Journal International,* 56, 357-371, doi: 10.1111/j.1365-2478.2007.00678.x

Socco, L.V., D. Boiero, C. Comina, S. Foti, and R. Wisen, 2008, Seismic characterization of an Alpine site: *Near Surface Geophysics,* 6, 255-267, doi: 10.3997/1873-0604.2008020

Socco, L.V., D. Boiero, S. Foti, and R. Wisen, 2009, Laterally constrained inversion of ground roll from seismic reflection records: *Geophysics,* 74, 35-45, doi: 10.1190/1.3223636

Socco, L.V., D. Boiero, P. Bergamo, F. Garofalo, H. Yao, R.D. Van der Hilst, and F. Da Col, 2014, Surface wave tomography to retrieve near surface velocity models: *SEG Expanded Abstracts,* 2013-2018, doi: 10.1190/segam2014-1278.1

Socco, L.V., C. Comina, and F. Khosro Anjom, 2017, Time-average velocity estimation through surface-wave analysis: Part 1—S-wave velocity: *Geophysics,* 82, 49-59, doi: 10.1190/geo2016-0367.1

Socco, L.V., and C. Comina, 2017, Time-average velocity estimation through surface-wave analysis: Part 2—P-wave velocity: *Geophysics,* 82, 61-73, doi: 10.1190/geo2016-0368.1

Tarantola, A., 2005, Inverse Problem Theory and Methods for Model Parameter Estimation: *SIAM* (SIAM), doi: 10.1137/1.9780898717921

Tawil, M., 2019, Surface Wave Tomography Applied to Oil and Gas Data: *M.Sc. thesis, Politecnico di Torino.*

Teodor, D., C. Comina, L.V. Socco, R. Brossier, P.T. Trinh, and J. Virieux, 2017, Initial model design for full-waveform inversion—preliminary results and critical aspects: *Extended Abstract, 36th GNGTS national convention.*

Teodor, D., C. comina, F. Khosro Anjom, L.V. Socco, J. Virieux, P.T. Trinh, and R. Brossier, 2018, Building initial models for Full-Waveform Inversion of shallow targets by surface waves dispersion curves clustering and data transform: *SEG, Expanded Abstract,* 4738-4742, doi: 10.1190/segam2018-2997848.1

Teodor, D., C. Comina, F. Khosro Anjom, R. Brossier, L.V. Socco, and J. Virieux, 2021, Challenges in shallow targets reconstruction by 3D elastic full-waveform inversion — Which initial model: *Geophysics* (Just-Accepted), doi: 10.1190/geo2019-0523.1

Thomson, W.T., 1950, Transmission of elastic waves through a stratified solid medium: *Journal of applied Geophysics,* 21, 89-93.

Treitel, S., J.L. Shanks, and C.W. Fraster, 1967, Some aspects of fan filtering: *Geophysics,* 32, 789-800, doi: 10.1190/1.1439889

Trinh, P.T., R. Brossier, L. Metivier, L. Tavard, and J. Virieux, 2019, Efficient time-domain 3D elastic and visco-elastic full-waveform inversion using a spectral-element method on flexible Cartesian-based mesh: *Geophysics,* 84, 1942-2156, doi: 10.1190/geo2018-0059.1

Van Leeuwen, T., and F.J. Herrmann, 2013, Mitigating local minima in fullwaveform inversion by expanding the search space: *Geophysical Journal International,* 195, 661-667, doi: 10.1093/gji/ggt258

Virieux, J., and S. Operto, 2009, An overview of full-waveform inversion in exploration geophysics: *Geophysics,* 74, 1942-2156, doi: 10.1190/1.3238367

Warner, M., and J. Guasch, 2016, Adaptive waveform inversion: theory: *Geophysics,* 81, 429-445, doi: 10.1190/geo2015-0387.1

Wathelet, M., D. Jongmans, and M. Ohrnberger, 2005, Direct Inversion of Spatial Autocorrelation Curves with the Neighborhood Algorithm: *Bulletin of the Seismological Society of America,* 95, 1787-1800, doi: 10.1785/0120040220

Wespestad, C.E., C.H. Thurber, N.L. Andersen, B.S. Singer, C. Cardona, Z. Zeng, N.L. Bennington, et al., 2019, Magma Reservoir Below Laguna del Maule Volcanic Field, Chile, Imaged With Surface-Wave Tomography: *JGT Solid Earth,* 124, 2858-2872, doi: 10.1029/2018JB016485

Whiteley, R.J., and S.A. Greenhalgh, 1979, Velocity inversion and the shallow seismic refraction method: *Geoexploration*, 17, 125-141, doi: 10.1016/0016-7142(79)90036-X

Wisén, R., and V. Christiansen, 2005, Laterally and Mutually Constrained Inversion of Surface Wave Seismic Data and Resistivity Data: *Journal of Environmental and Engineering Geophysics,* 10, 251-262, doi: 10.2113/JEEG10.3.251

Wisén, R., E. Auken, and T. Dahlin, 2005, Combination of 1D laterally constrained inversion and 2D smooth inversion of resistivity data with a priori data from boreholes: *Near Surface Geophysics,* 3, 71-79, doi: 10.3997/1873-0604.2005002

Xia, J., R.D. Miller, and C.B. Park, 1999, Estimation of near-surface shear-wave velocity by inversion of Rayleigh waves: *Geophysics,* 64, 691-700, doi: 10.1190/1.1444578

Xia, J., R.D. Miller, C.B. Park, and G. Tian, 2003, Inversion of high frequency surface waves with fundamental and higher modes: *Journal of Applied Geophysics,* 52, 45-57, doi: 10.1016/S0926-9851(02)00239-2

Yao, H., R.D. Van der Hilst, and M.V. De Hoop, 2006, Surface-wave array tomography in SE Tibet from ambient seismic noise and two-station analysis – I. Phase velocity maps: *Geophysical Journal International,* 166, 732-744, doi: 10.1111/j.1365-246X.2006.03028.x

Yao, H., C. Beghein, and R. Van Der Hilst, 2008, Surface wave array tomography in SE Tibet from ambient seismic noise and two-station analysis - II. Crustal and upper-mantle structure: *Geophysical Journal International,* 173, 205-219, doi: 10.1111/j.1365-246X.2007.03696.x

Yilmaz, Ö., 2001, Seismic Data Analysis: Processing, Inversion, and Interpretation of Seismic Data: *Society of Exploration Geophysicists,* 10, doi: 10.1190/1.9781560801580

Yoshizawa, K., and B.L.N Kennett, 2004, Multimode surface wave tomography for the Australian region using a three-stage approach incorporating finite frequency effects: *Journal of geophysical research solid earth,* 109, doi: 10.1029/2002JB002254

Yuan, Y.O., F.J. Simons, and E. Bozdag, 2015, Multiscale adjoint waveform tomography for surface and body waves: *Geophysics,* 80, 281-302, doi: 10.1190/geo2014-0461.1